NUCLEAR SPIN RELAXATION

IN METHANE GAS

by

PETER ADRIAN BECKMANN

B.Sc., University of British Columbia, 1969

M.Sc., University of British Columbia, 1971

A THESIS SUBMITTED IN PARTIAL FULFILMENT OF

THE REQUIREMENTS FOR THE DEGREE OF

DOCTOR OF PHILOSOPHY

in the Department

of

Physics

We accept this thesis as conforming to the

required standard

THE UNIVERSITY OF BRITISH COLUMBIA

January, 1975

In presenting this thesis in partial fulfilment of the requirements for an advanced degree at the University of British Columbia, I agree that the Library shall make it freely available for reference and study. I further agree that permission for extensive copying of this thesis for scholarly purposes may be granted by the Head of my Department or by his representatives. It is understood that copying or publication of this thesis for financial gain shall not be allowed without my written permission.

Department of _____Physics_____

The University of British Columbia
Vancouver 8, Canada

Date _____January 1975_____

ABSTRACT

Nuclear spin relaxation in low density methane gas (CH_4) is investigated both experimentally and theoretically.

The 30 MHz nuclear magnetic resonance experiments were performed at temperatures of 77K, 110K, 150K and 295K over a density range of 0.0046 to 0.040, 0.008 to 2.0, 0.006 to 6.0 and 0.006 to 17 amagat, respectively. The recovery of the observed magnetization could be characterized by a single relaxation rate to within experimental error. The manner in which the relaxation rate is extracted from the data, along with a statistical and (known) systematic error is discussed in detail.

A theory is developed in which the Fermi-Dirac statistics of the nuclear spins (protons) and the centrifugal distortion of the molecule play a central role. The calculations imply that, in general, the relaxation should be non-exponential. At nuclear Larmor frequencies coincident with molecular centrifugal distortion frequencies, an observable departure from exponential relaxation is predicted by the calculations. On the other hand, at 30 MHz, which is well away from centrifugal distortion frequencies, the departure from exponential relaxation is predicted to be too small to be observed. This is consistent with the observed single decay constant. In addition, the magnitudes of the calculated longitudinal relaxation rates are shown to be consistent with experiment. Finally, new experiments are suggested, based on the theory developed, that should unequivocally show the importance of the centrifugal distortion splittings.

TABLE OF CONTENTS

LIST OF TABLES

LIST OF FIGURES

ACKNOWLEDGEMENTS

I sincerely thank Myer Bloom and Irving Ozier for their
guidance and help over the past four years.

I have learned a great deal through countless discussions
with Myer Bloom. I have benefitted from his broad experiences in the
scientific community and his tremendous insight into physical problems.
He has a concientious and fair attitude toward his students and I am
most grateful for the opportunity I have had to work under him.

Irving Ozier has played an important role in my education. A
large part of my research is due to his deep understanding of certain
problems. He gave freely of his time and as a result of his truly
unlimited patience I was able to grasp a considerable understanding
of a complicated and involved facet of methane spectroscopy.

CHAPTER I

INTRODUCTION

1.1   NUCLEAR SPIN RELAXATION IN GASES

Nuclear magnetic resonance is a useful technique for investigating
the dynamic properties of dilute gases. Using the nuclear spin system as a
probe, nuclear spin relaxation can yield information regarding the nature
and strength of spin-molecule interactions and the effects of collisions on
these interactions. If the interaction between the spin system and its
environment is well known, parameters such as correlation times (or cross-
sections) associated with various molecular reorientation processes can be
determined. In some cases, the anisotropic intermolecular potential res-
ponsible for molecular reorientation can be extracted. This is one of the
major aims in gas phase nuclear spin relaxation studies because determining
the form of the intermolecular potential has proved to be a very difficult
problem in theoretical molecular physics (1).

In pure low density gases, this has met with most success in
monatomic and diatomic gases. The simplest gas is He^3, there being only one
nuclear spin per molecule. The isolated He^3 molecule has no degree of
freedom other than translation and nuclear spin relaxation can only occur
via the intermolecular spin-spin interaction which is only effective during
collisions. Theoretical studies (2) and nuclear spin relaxation experiments

(3) in He^3 do lead to a considerable understanding of the intermolecular potential.

Many nuclear spin relaxation experiments have been performed with H_2 gas (4, 5, 6, 7), the next simplest system. In this case, nuclear spin relaxation occurs via intra-molecular interactions, namely the intra-molecular spin-rotation and dipolar interactions. The rotational structure of the molecule is relatively simple and extensive theoretical studies (8, 9) have resulted in a relatively clear picture of the intermolecular forces.

The two main classes of polyatomic gases studied to date are symmetric and spherical tops. The symmetric tops examined include CHF_3, CH_3F, BF_3, PH_3, NH_3 and $CClF_3$ (10, 11, 12, 13, 14, 15, 16, 17, 18, 19). In some cases, the interaction constants for the spin-rotation interaction are not well known which makes it difficult to determine precise information concerning correlation functions and cross-sections. In some cases, the interaction constants determined from nuclear spin relaxation measurements are in marked disagreement with the probably more precise molecular beam measurements (10). Although the characteristic times for nuclear spin systems to relax are accurately determined by the nuclear spin relaxation measurements (in most cases), it is sometimes not clear how the experimental results should be interpreted (10, 20) due to lack of theoretical investigation.

Some of the spherical tops studied using nuclear spin relaxation experiments are SF_6, CF_4, SiF_4 and GeF_4 (16, 21, 22, 23) and in much greater detail, CH_4 (16, 24, 25, 26, 27, 28). The experiments are usually interpreted in terms of "effective" spin-rotation interaction constants and "effective" cross-sections for molecular reorientation. Methane (CH_4) is the subject of this thesis although many aspects of the theory should be

applicable to other spherical tops of the form XY_4.

It should be pointed out that experimental studies involving mixtures of CH_4 and (spinless) He^4 (29, 30, 31) have met with some success at determining cross sections (29, 30) and the anisotropic part of the intermolecular potential (31).

1.2   METHANE SPECTROSCOPY

The geometry of methane is that of a tetrahedron. Normal CH_4 consists of a spinless C^{12} atom in the geometric centre of the molecule with the four spin ½ protons occupying the corners of the tetrahedron. Because the spin system (i.e., the proton spins) communicate only with the molecular rotation, nuclear spin relaxation measurements can be sensitive to the rotational structure of the molecule (25).

The form of the spin-rotation interaction for CH_4 is well known (33) and the interaction constants have been accurately measured by molecular beam spectroscopy (32). The rotational structure (i.e., energy levels) have been extensively studied both theoretically (34, 35, 36, 37, 38 39, 40, 61) and experimentally by molecular beam spectroscopy (32, 33, 41, 49), microwave spectroscopy (42), infrared spectroscopy (43, 44, 45) and in-frared-rf double resonance spectroscopy (46, 47, 48, 49). It is because of this input, coupled with the facts that ultra-high purity methane is cheap, safe and the PVT data well known (50),that nuclear spin relaxation experiments (rf spectroscopy) can provide useful qualitative and quantitative information concerning the effects of the spin-rotation interaction. As an aside, we note for completeness that the relationship between Raman spectro-scopy and nuclear spin relaxation (51) and the relationship between

dielectric relaxation and nuclear spin relaxation (52) is discussed in the literature.

It should be pointed out why CH_4 is so intensely studied. As well as being the model spherical top, it is interesting in its own right. Although CH_4 is not among the myriad of molecules found as yet in interstellar space, it may in fact be a parent molecule to many of them (53). It is known that CH_4 is a major constituent of the atmospheres of some of the outer planets and it is thought that it exists in comets (54). Also, the amount of deuterium in the universe is a test of certain cosmological models (55) and much of the detected deuterium in the solar system is in the form of deuterated methanes. Thus abundance ratios like CH_3D/CH_4 are of interest (56). It is thought that at one time, CH_4 was a major constituent of the earth's atmosphere and that, with the help of lightning, it is the origin of the basic "life" molecules. The frequency and wavelength of a certain vibrational transition has been measured with considerable accuracy result- ing in the most precise value for the speed of light (57). Finally, it has been proposed that a vibrational transition in CH_4 could serve as a very convenient secondary frequency standard (58).

1.3   NUCLEAR SPIN RELAXATION IN METHANE

Nuclear spin relaxation in methane can be conceptually divided into two aspects. The first is the isolated molecule spin-rotation inter- action responsible for the presence of a magnetic field at the proton sites. The second aspect of the problem is the modulation of this local field by collisions. Collisions modulate this field because the anisotropic inter- molecular forces acting during a collision can reorient the molecule in space

and/or produce changes of rotational quantum numbers. An excited nuclear spin system will relax via the Larmor frequency component of this time dependent local field. The Larmor frequency is the frequency at which the nuclear spins precess in an applied dc field H_0 and is given by $\nu_N = (2\pi)^{-1}\gamma H_0$, where γ is the gyromagnetic ratio.

The spin-rotation interaction for an isolated molecule (i.e., the limit of zero density) is discussed in the literature (33, 59) and the Hamiltonian is reviewed in some detail in section 3.5. The rotational structure of the molecule is such that the principal rotational J-levels are split by the centrifugal distortion of the molecule. Whereas the J-levels are split by frequencies in the range 10^{11}-10^{13} Hz, the distortion splitting are in the range 10^7-10^{10} Hz. Because nuclear spin relaxation experiments can be performed in the range 10^7-10^8 Hz, the relaxation can be influenced by the centrifugal distortion of the molecule.

The nuclear spin relaxation is dominated by the isotropic or scalar spin-rotation interaction which does not involve a change of centrifugal distortion energy. This interaction can be thought of as producing a constant local magnetic field (i.e., zero frequency) at the proton sites for the isolated molecule. The coupling constant associated with this scalar interaction is C_a.

There is also, however, a contribution to the nuclear spin relaxation from the anisotropic spin-rotation interaction. This is a tensor interaction and has associated with it the coupling constant C_d. This interaction can couple states of different distortion energy and thus produce components of the local field which fluctuate at the characteristic centrifugal distortion frequencies even in the limit of zero density. Thus the isolated molecule

sees a spectrum of local fields which is a series of δ-functions. The frequency of each δ-function is determined by the distortion frequencies of the molecule and the intensity is a measure of the strength of the coupling between the nuclear spins and the local field. One of the major theoretical tasks performed in this study is to calculate the intensities for this zero density spectrum.

It is in the calculation of this spectrum (which has been called "the nuclear spin relaxation rotational spectrum" (25)) that spin-symmetry enters the problem. As discussed in greater detail in Chapter III, the symmetry requirements of the wavefunctions (rotation plus spin) result in a one to one correspondence between the molecular rotational state and the total nuclear spin of the molecule. The latter, for four spin $\frac{1}{2}$ protons per molecule, is $I = 0, 1$ or 2. The $J = 0$ and $J = 1$ rotational states are not split by the centrifugal distortion interaction and have associated with them $I = 2$ and $I = 1$ spin states respectively. The $J = 2$ level has two distortion states, the lower of the two being associated with $I = 0$ and the higher with $I = 1$. This splitting is 8 MHz and has been observed directly (41). For a more complicated example the eleven distortion states and their respective spin states of the $J = 12$ rotational level are indicated in Figure 3.1 (Chapter III).

The existence of these spin symmetry states has also been confirmed by the study of solid CH_4 where the conversion to $I = 2$ $(J = 0)$ from $I = 0$ and 1 $(J = 2)$ and $I = 1$ $(J = 1)$ is detected as an increase in nuclear magnetization as the temperature is lowered (62, 63, 64, 65). The existence of the spin symmetry states is important in understanding the crystal field in solid CH_4 and its deuterated modifications (66, 67, 68, 69).

The effect of collisions is to broaden this zero density nuclear spin relaxation rotational spectrum. The rate at which the nuclear spin system relaxes will be a sum of all the contributions at the Larmor frequency.

As previously stated, nuclear spin relaxation in the dilute gas is dominated by the scalar spin-rotation interaction. This gives rise to a maximum in the relaxation rate at the density where the frequency of collisions which reorient the molecule is the same as the Larmor frequency. This phenomenon was first observed in H_2 gas(5). It should be pointed out that we are neglecting the dipolar interaction. This is based on a theoretical calculation (26) and it will turn out à posteriori that the experimental results are fit very well by the relaxation resulting from the spin-rotation interaction. The reason that the dipolar interaction can be neglected is because it gives very little intensity in the $\Delta J = 0$ contribution to the relaxation.

The present experiments are sufficiently precise as to be sensitive to the contribution to the relaxation of those terms in the tensor spin-rotation interaction which result in a change of centrifugal distortion state. As stated in the literature(25), the strongest conceivable test of the theory of nuclear spin relaxation in dilute gases would be to study the relaxation as a function of the Larmor frequency over a very wide range of frequencies. It is also suggested in reference (25) that when the Larmor frequency is tuned through a centrifugal distortion frequency a maximum in the relaxation rate will occur. It is now known (this work) that this would require extremely low densities, considerably lower than the lowest densities reported in this work. The effects of tuning the Larmor frequency through a distortion frequency at the densities used in this study are very complicated and involve non-exponential relaxation. This is investigated theoretically in detail in Chapter IV. The Larmor frequency is directly proportional

to the applied dc field and this study is experimentally impossible with the magnets presently available in this laboratory. Although it is less sensitive, an equivalent experiment which is reported here is to measure the nuclear spin relaxation rate as a function of density. As the density is varied, one would sweep through a maximum contribution of each distortion transition. This will occur when the frequency of collisions which are responsible for this transition is equal to the difference between the Larmor and distortion frequencies.

1.4 THESIS OUTLINE

This thesis is concerned with nuclear spin relaxation in dilute CH_4 gas, taking the isolated spin-rotation interaction into account in an exact and detailed fashion. Theoretically, the effects of collisions are then introduced in a phenomenological manner and tested against the experimental results.

The experiment involves measuring the longitudinal nuclear spin relaxation rate at various temperatures over a very wide density range. The experimental apparatus, procedures and results are presented in the next chapter (Chapter II).

The theory of nuclear spin relaxation is developed in Chapter III. Chapter IV is concerned with the predictions of the theory, especially at the Larmor frequency employed in the experiments.

CHAPTER II

EXPERIMENTAL APPARATUS, PROCEDURES AND RESULTS

2.1   PULSED NUCLEAR SPIN RELAXATION EXPERIMENTS

The nuclear spin relaxation experiments reported here were

performed using conventional pulsed nuclear magnetic resonance techniques.

In a dc magnetic field $\underline{H}_0 = H_0 \hat{Z}$, nuclear spins (nuclei having

a magnetic moment) precess about the field at the angular frequency

$\omega_N = \gamma H_0$. The "hat" denotes a unit vector, γ is the gyromagnetic ratio

and $\nu_N = \omega_N/2\pi$ is called the Larmor frequency. The Larmor frequency for

hydrogen nucleii is 30 MHz in a field of 7 kilogauss. The equilibrium value

M_0 of the nuclear magnetization is parallel to the field and is given by

$M_0 = X H_0$ where X is the nuclear magnetic susceptibility. This is the Curie

Law (70,page 2) where the high temperature approximation ($\mu H_0 \ll kT$) has been

used. The nuclear magnetic moment is μ and k is Boltzmann's constant.

In order to induce nuclear spin transitions, an rf voltage of

frequency ν_N is applied across a solenoid whose axis is perpendicular to

H_0. The resulting field which is of magnitude H_1, say, can be decomposed into two

oppositely circularly polarized fields of magntidue H_1, one with an angular

frequency ω_N and the other with an angular frequency $-\omega_N$. The field whose

motion has the opposite sense to the precession of the nuclear

spins may be neglected (70, page 21; 71). In the reference frame

rotating at the Larmor frequency, the magnetization precesses about an

effective field given by $\underline{H}_{eff} = \underline{H}_0 + \underline{H}_1$. The result is that M_z oscillates between $+M_0$ and $-M_0$. This resonance phenomenon (nuclear magnetic resonance) is explained very clearly and in considerable detail elsewhere (72, Chapter 2).

If the H_1 field is pulsed such that $M_z \neq M_0$ after the pulse, M_z will decay toward M_0 as the nuclear spin system transfers energy to the molecular degrees of freedom via various spin-molecule interactions (88). If the recovery of the magnetization is exponential, the associated rate constant is R_1, the longitudinal nuclear spin relaxation rate. The longitudinal relaxation time is $T_1 = R_1^{-1}$.

The value of $M_z(t)$, a time t after a perturbing pulse is measured by applying a second pulse, called a $\pi/2$ pulse, which takes $M_z(t)$ into the xy plane. The magnetization now precesses in the xy plane and induces a voltage in the same coil that was used to produce H_1. The resulting signal is called a free induction decay. This signal decays from a value proportional to $M_z(t)$ to zero signal at a rate $(T_2')^{-1} = (T_2)^{-1} + (T_2^M)^{-1}$ as indicated in Figure 2.1.

For ideal systems, the spin-spin or transverse nuclear spin relaxation time T_2 is the characteristic time for the spin system to approach internal equilibrium in a homogeneous dc field. This involves no energy exchange with the molecular degrees of freedom, but does destroy the magnetization in the xy plane. Under general conditions, this loss of magnetization due to the interaction between spins is irreversible although there are interesting exceptions in some solids (73).

Inhomogeneities in H_0 give rise to a spread in values of ω_N and the magnetization in the xy plane after the $\pi/2$ pulse will tend to zero because
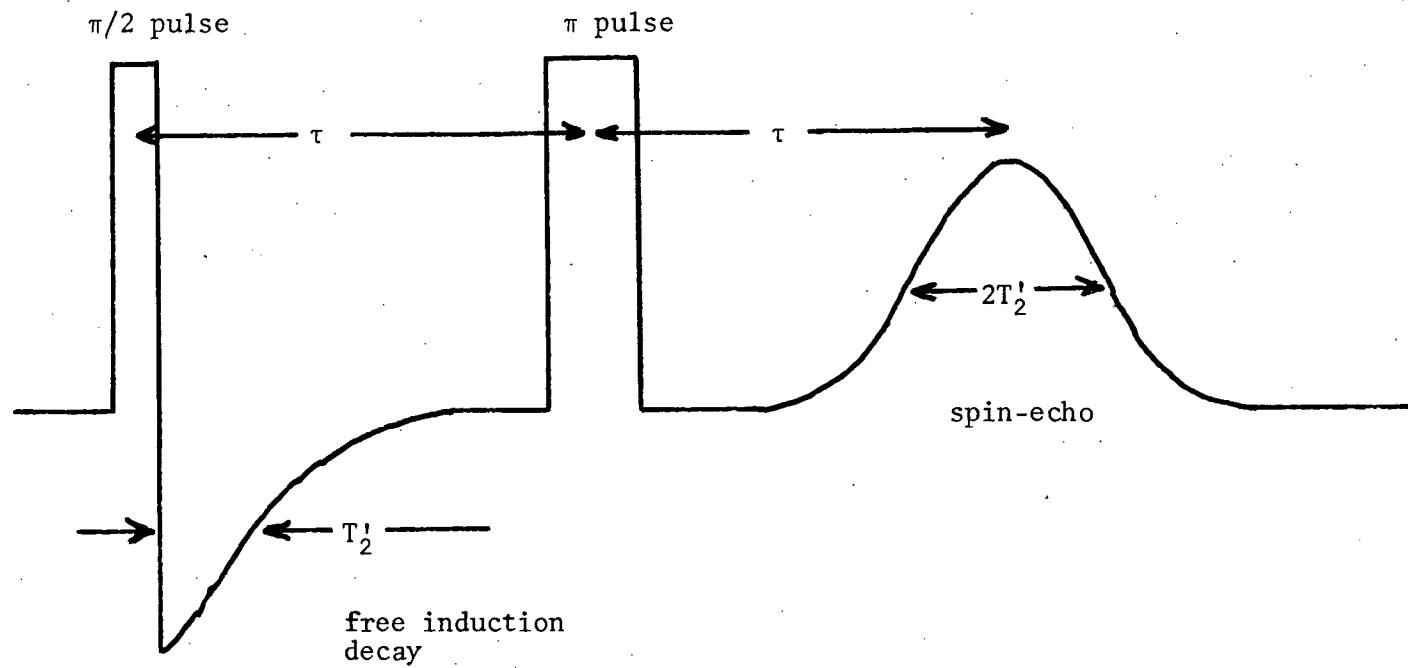
Figure 2.1. A free induction decay and spin-echo resulting from a three pulse sequence. The first π pulse is not shown.

of a dephasing effect. This process occurs with a characteristic time

constant T_2^M (M refers to magnet) and is completely reversible in the

limit of no diffusion (74, 75). Note that T_2^M is determined by the magnet

inhomogeneity and the gyromagnetic ratio γ.

Nuclear induction (76) and T_1 and T_2 processes (76, 77) were first

thoroughly understood in the 1940's. A thorough up to date treatment (70)

and a recent review article concerning only gas phase nuclear spin

relaxation (88) have been published.

A two pulse experiment involves applying a π pulse (perturbing

pulse) which takes M_0 into $-M_0$ and then a time t later applying a $\pi/2$ pulse

(measuring pulse) to observe the free induction decay. This pulse sequence

is denoted by π-t-$\pi/2$.

A three pulse experiment involves the addition of a second π pulse

a time τ after the $\pi/2$ pulse and is denoted by π-t-$\pi/2$-τ-π. The second π

pulse has the effect of reclaiming some of the phase loss of the xy

magnetization resulting from inhomogeneities in H_0. This has the consequence

of producing a spin-echo a time τ after the second π pulse which is

essentially a time reversed free induction decay and a normal free induction

decay back to back. The spin-echo was first discussed by Hahn (78) and

pictoral descriptions may be found in the literature (79). This pulse

sequence is shown in Figure 2.1 where the first π pulse is not included.

2.2 EXPERIMENTAL APPARATUS

The experimental apparatus can be conveniently divided into six

stages as indicated in Figure 2.2. We discuss the six stages separately.
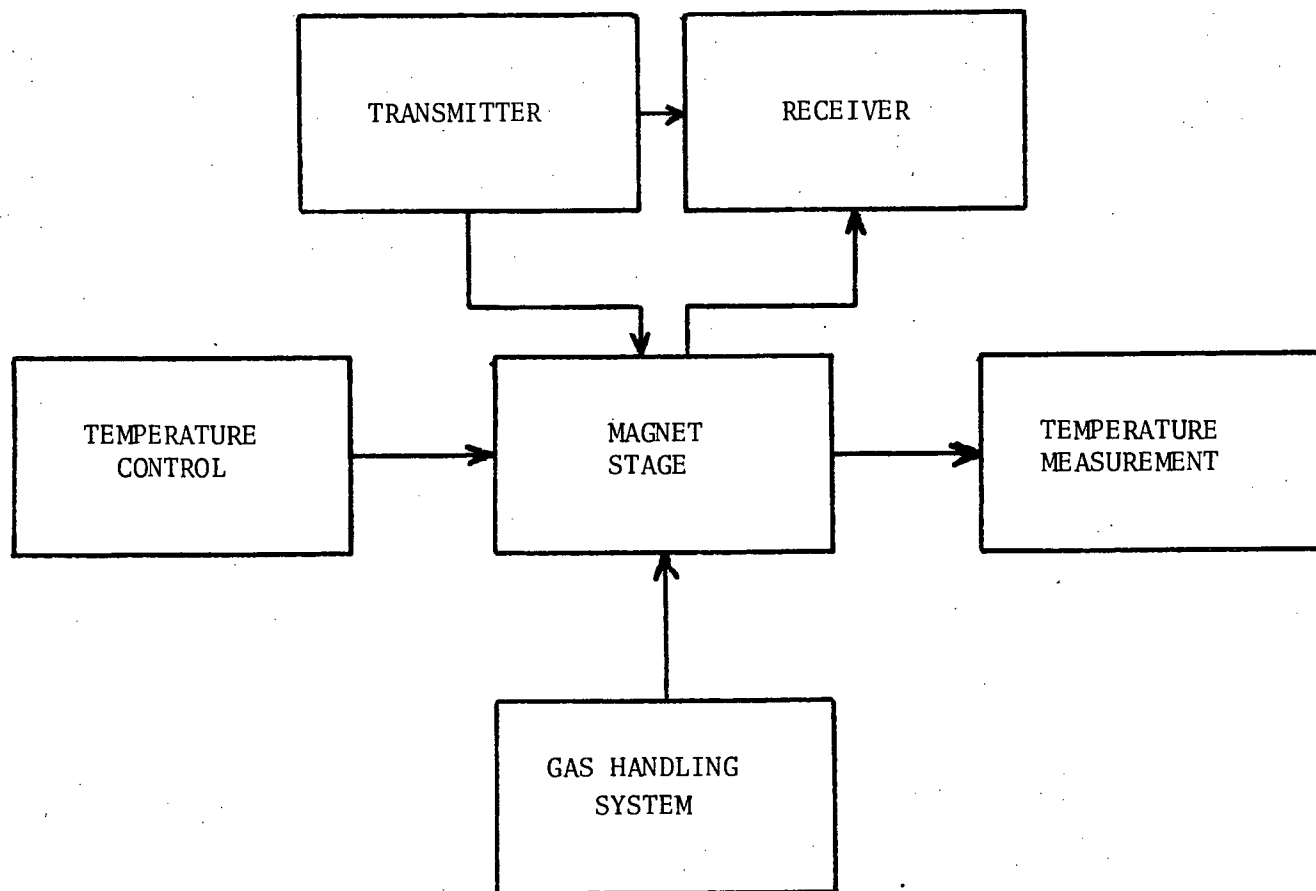
Figure 2.2. A block diagram of the six major parts of the apparatus used to measure longitudinal relaxation rates as a function of pressure and temperature.

2.2.1 TRANSMITTER STAGE

The transmitter stage supplies the rf pulses: π-t-$\pi/2$ for the two pulse experiment and π-t-$\pi/2$-τ-π for the three pulse experiment.

Gating pulses are provided by a series of Tektronix Pulse and Waveform Generators which control the repetition period of the pulse sequence and τ, both of which are fixed for a measurement. The time t is automatically varied by a modified Tektronix Waveform Generator (5, 80). These gating pulses are then used to trigger two pulse width generators (14), one for the π pulse(s) and the other for the $\pi/2$ pulse. The width (time duration) of the pulses can be accurately controlled.

The rf source is a crystal oscillator operating at 10 MHz. This frequency is tripled to obtain the desired 30 MHz. The rf pulses are amplified (about 10^3 volts peak to peak) and coupled to the tuned circuit via a one-half wavelength coaxial line.

The details of the transmitter may be found elsewhere (24) where circuit diagrams for all the non commercial components can also be found. Although improvements have been made, the transmitter stage is essentially as described by Hardy (5, 80).

2.2.2 MAGNET STAGE

The sample gas is contained in a coil inside a brass sample chamber. The coil and a tuning capacitor which is outside the sample chamber form a parallel resonant circuit which is tuned to the Larmor angular frequency: $(LC)^{-\frac{1}{2}} = \omega_N$. A general discussion of the tuned circuit stage for a nuclear magnetic resonance experiment of this type is given by

Clarke (81).

The whole assembly rests in a 7 kilogauss permanent magnet with 20 cm diameter pole faces and a gap of 4.8 cm. The field can be varied ±25 gauss by means of shim coils. The geometric arrangement is such that the axis of the coil is perpendicular to H_0 and misalignment effects are completely negligible (82). There are two sample chambers, one for room temperature experiments and one for variable temperature experiments.

Most of the room temperature measurements were taken with the room temperature sample chamber shown in Figure 2.3. This sample chamber is discussed elsewhere (24, 25) and Figure 2.3 is taken directly from reference (24).

The variable temperature arrangement is shown in Figure 2.4. Figure 2.4 is to scale and the details of the variable temperature sample chamber is shown in Figure 2.5. Figure 2.5 is twice actual size. The chamber is 7.9 cm long and has an inside diameter of 2.5 cm. The 14 turn coil was made from #14 gauge copper wire which was stripped of enamel and well cleaned. The inside diameter of the coil is 1.5 cm and the outside diameter is 1.8 cm. The coil is 4.0 cm long.

It is extremely important that the sample cell circuitry be designed to minimize losses (22, 24, 25, 81). The distance between the coil and the tuning capacitor should be as short as possible. This distance was determined by the presence of the sample chamber dewar (see Figure 2.4) and is about 5 cm.

The rf feed-through and the four diode feed-throughs (see Section 2.2.4) were made by passing #32 gauge brass wire through 0.09 cm holes and sealing with Stycast Epoxy #2850 FT (#11 catalyst). The epoxy on the rf feed-through was extended about one cm on either side of the sample chamber
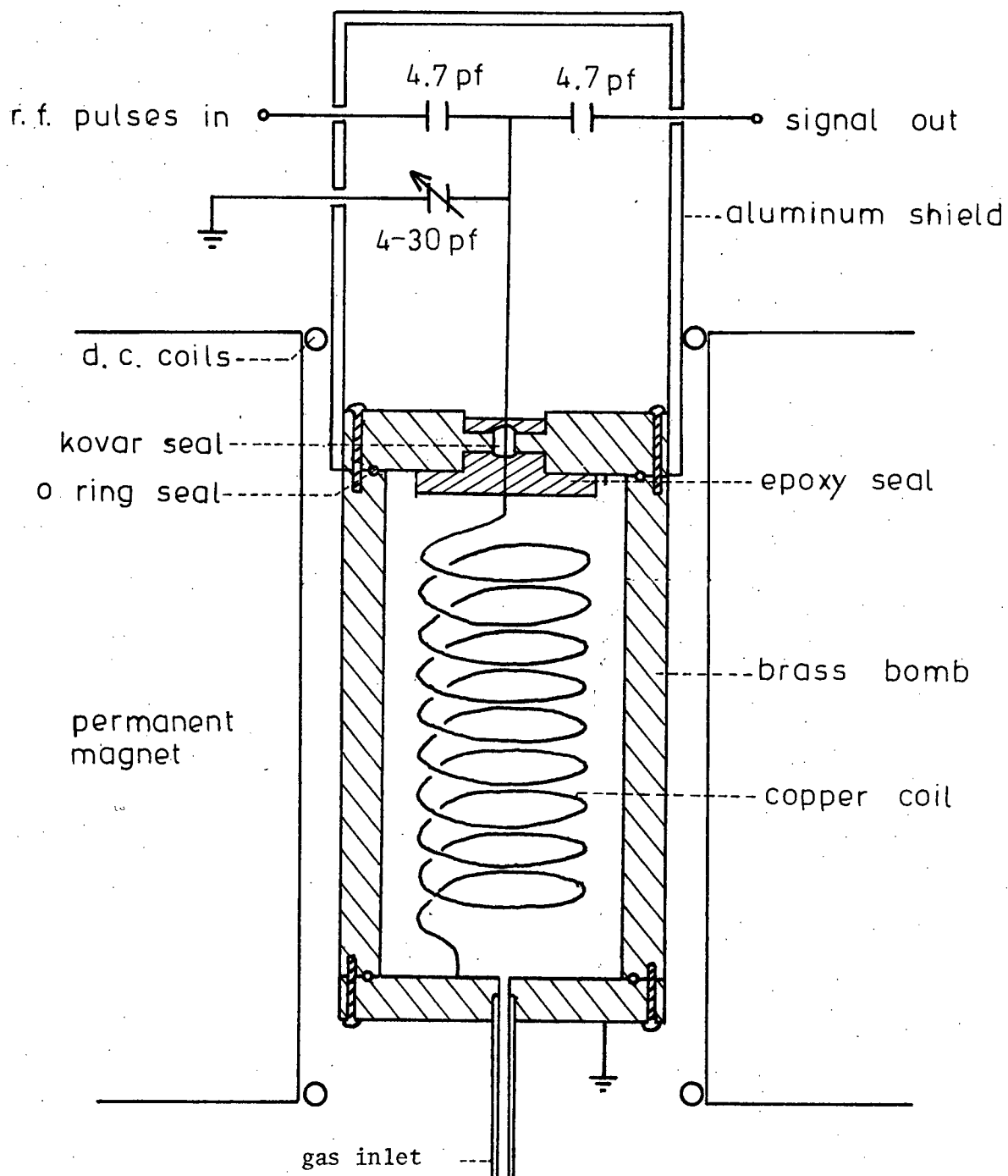
Figure 2.3. The room temperature sample chamber and parallel resonant circuit. The diagram is taken from reference (24) and is not to scale.
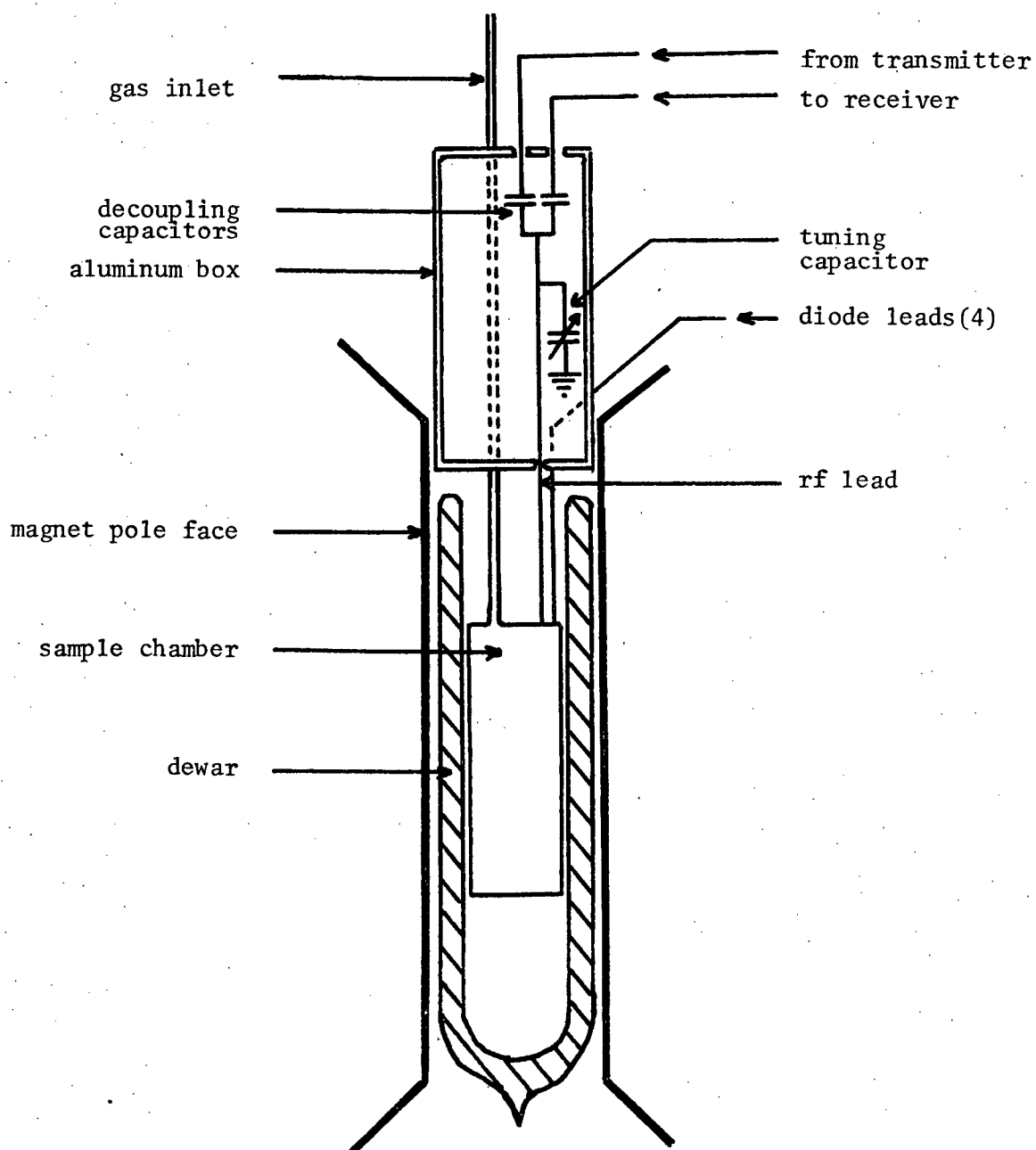
Figure 2.4. Scale diagram of the variable temperature magnet
stage. The nitrogen gas feed tubes are not shown.
The sample chamber is shown in Figure 2.5.

gas inlet

epoxy

temperature
sensing diode

rf coil

brass

Woodsmetal
joint
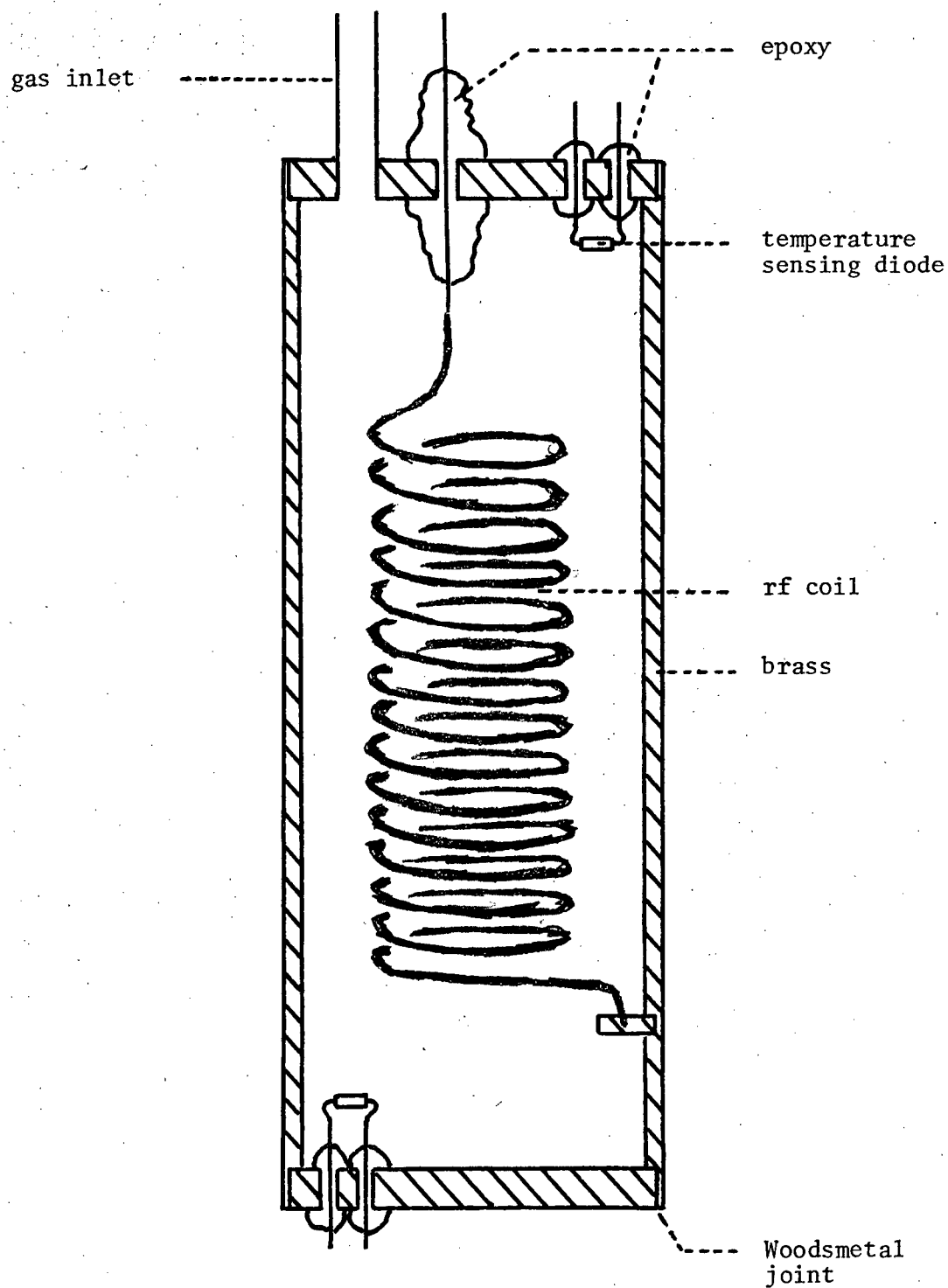
Figure 2.5.   Scale diagram (X2) of the variable temperature
            sample chamber.

to prevent "snaking" resulting from the high voltage rf pulses. Brass wire was used to match thermal expansions. Although most commercial feed throughs are leak-tight, they are often magnetic and seriously interfere with the homogeneity of the permanent magnet. Commercial non-magnetic feed throughs (ceramic) were found to leak on recycling between 77K and room temperature.

The temperature sensing diodes were placed off-centre to prevent interaction with the coil. The top diode was placed as far away as possible from the rf lead to prevent interference. Both diodes were about 1.5 cm from the coil and it was found that they did not have to be shielded as long as the outside leads were open-circuited and surrounded by aluminium foil.

The gas enters the sample chamber via a 0.32 cm (outer diameter) thin walled stainless steel tube.

The top and bottom of the variable temperature sample chamber were soldered to the body of the chamber with Woodsmetal because conventional Pb/Sn solder would require sufficient heating to destroy the epoxy feed throughs. The sample chamber was recycleable (77-300K) and would withstand pressures of at least three atmospheres. The gas handling system could be pumped down to less than 10^{-3} Torr. The sample chamber, if closed off, would then recover to less than 10^{-1} Torr in 5 weeks. Figure 2.4 does not show the temperature control parts of the magnet stage. This is discussed in Section 2.2.5.

It should be noted that whereas many experiments confine the sample gas to the interior of the coil (22, 84) this is not the case for both sample chambers. This is discussed further in Section 2.4.

2.2.3   RECEIVER STAGE

      A block diagram of the receiver stage is shown in Figure 2.6. The preamplifier (83) and the parallel resonant circuit are connected by a half wavelength coaxial cable. In the middle of this cable there is a set of crossed diodes to ground, thus the cable is a high impedance quarter wavelength lead with respect to the high voltage rf pulses but a low impedance half wavelength lead with respect to the nuclear induction signal whose voltage level is below that of the threshold voltage of a silicon diode.

      The receiver amplifier is a commercial low noise amplifier, L.E.L. Model 21BS, whose characteristics are discussed elsewhere (14, 24). A continuous rf is introduced into the amplifier for phase sensitive detection. Care was taken to operate in the linear regime (24, 85).

      The output from the amplifier is channelled to an oscilloscope for tuning the signal and placing the boxcar pulse. For a measurement, the output from the amplifier is fed into a P.A.R. model CW-1 Boxcar Integrator which samples the signal (free induction decay or spin-echo) over the desired range of time. The boxcar output is channelled to a strip chart recorder solely for the purpose of visually monitoring the signal, and to a Monsanto Model 200A Digital dc Voltmeter for recording the signal. The voltmeter samples the boxcar output at a predetermined rate and adds each successive signal a predetermined number of times. After the digital voltmeter has completed its summation, the sum is printed on paper tape along with the time t at the end of the summation. Effectively, then, the digital voltmeter provides further averaging.

      The time t in the sequences π-t-$\pi/2$ or π-t-$\pi/2$-τ-π is measured
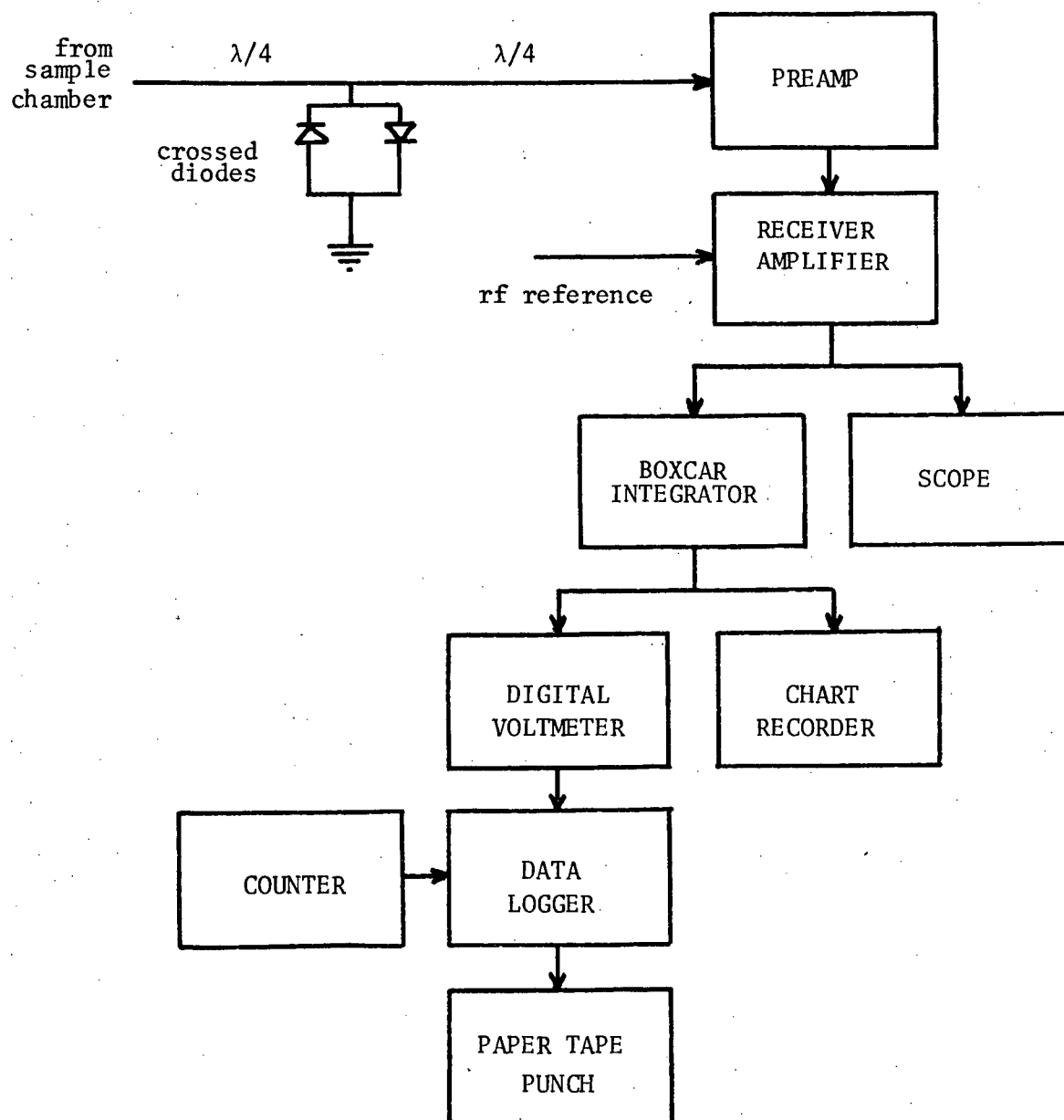
Figure 2.6. A block diagram of the receiver stage.

with a Hewlett Packard 5245 Electronic Counter with a Model 5262A Time Interval Unit Plug-in. The interfacing of the Monsanto Digital Voltmeter and the Hewlett Packard Counter with the Teletype BRPE11 High Speed Paper Punch was performed via a custom made Model 12 Datalogger manufactured by Technical Associates Ltd (Vancouver).

2.2.4   TEMPERATURE MEASUREMENT

Room temperature was measured with a standard mercury thermometer which could be read to ±0.2C. This measurement was made next to, but outside, the room temperature sample chamber. The heating effect of the rf pulses is calculated to be less than 0.5C.

The apparatus for measuring temperatures between 77K and 273K is shown in Figure 2.7. The two FD400 diodes are located at the top and bottom of the variable temperature sample chamber as indicated in Figure 2.5.

The temperature-voltage characteristics for fixed current through an FD200 silicon diode are linear between 77K and 273K (86). Because FD200 diodes are no longer manufactured, FD400 (or FDH400) diodes were used and it was found that they have temperature-voltage characteristics identical to FD200 diodes. The diodes were calibrated at 77K and 273K and temperature was calculated using $v = aT + b$. A constant current of 10 μA gave $a = 2.8$ volts/K and $b = 1.2$ volts. These values (the latter being the band gap for a silicon diode) are in good agreement with previous measurements (86). As indicated in Figure 2.7, the current was set by monitoring the voltage across 100K resistors and adjusting the dc supply until a reading of 1.0000 ± 0.0001 volts was obtained on the Monsanto digital

FD400 temperature sensing
diodes (in sample chamber)
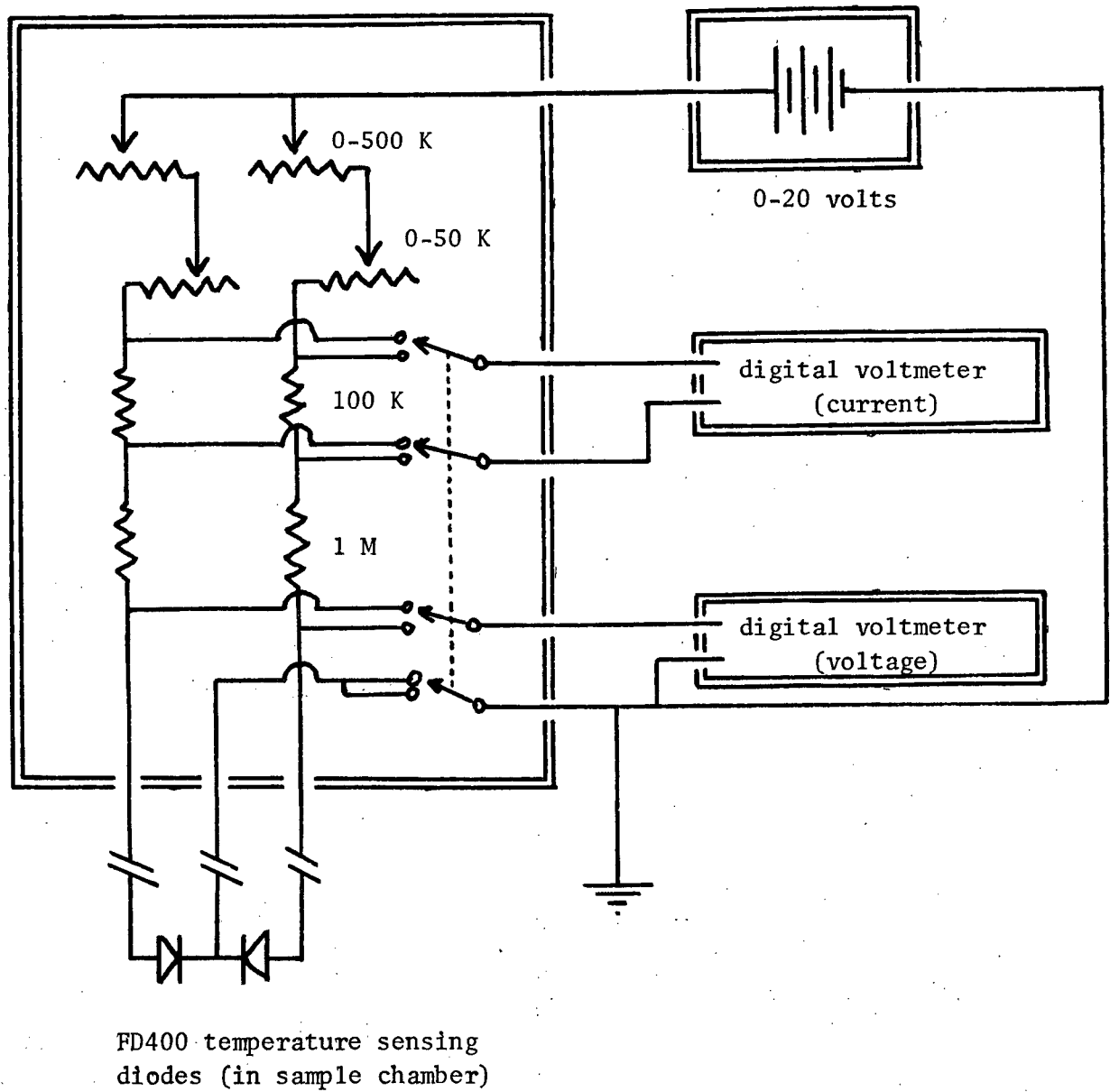
Figure 2.7.   Schematic diagram of the temperature measurement apparatus.

voltmeter. The 100K resistors (±5%) were not changed during the course of the project and the leads to the two diodes were not switched after calibration. The potential difference across the diodes is measured (at the same time the current is monitored) on an Advance Digital Multimeter Model DMM2.

Although the sensitivity of this arrangement is about 0.1K, we give an uncertainty of ±1K on all temperature measurements. This uncertainty results mainly from the difficulty of obtaining the 273K calibration point accurately. The calibration of the diodes was repeated several times during the course of the project. The Advance Voltmeter was calibrated with the considerably more accurate Monsanto Voltmeter.

2.2.5   TEMPERATURE CONTROL

The room temperature measurements were performed in a laboratory whose temperature was very well regulated.

The 77K measurements were performed by simply filling the sample chamber dewar with liquid nitrogen (see Figure 2.4).

Temperatures of 110K and 150K were achieved by blowing cold nitrogen gas to the bottom of the sample chamber dewar. Heaters were placed at the bottom of a 50 or 100 ℓ nitrogen container and the N_2 gas blown through a tube to the sample chamber dewar. Using Variac autotransformers, the voltage across the heaters could be varied with the result that the N_2 flow rate could be accurately controlled. Because of limited space between the variable temperature sample chamber and the sample chamber dewar, the 0.95 cm (outer diameter) copper tube from the nitrogen container was fed into four 0.32 cm (outer diameter) thin walled stainless steel tubes. The N_2 gas feed tube as well as the top of the sample chamber dewar were covered

with cotton batting to prevent thermal losses and to minimize temperature gradients.

There was no temperature gradient across the variable temperature sample chamber (top to bottom) to within the accuracy that the temperature could be measured absolutely (±1K). Over the time scale of an R_1 measurement, the temperature drift was usually zero but when observable, it was never more than 1K.

2.2.6   GAS HANDLING SYSTEM

The methane was purchased from Matheson and the quoted purity was 99.99%.

The gas handling apparatus is shown in Figure 2.8. Pressure was measured with a Texas Instruments Precision Pressure Gauge, Model 145. For pressures below 0.34 atm a Texas Instruments Type 1 Capsule (tube no. 11A) was used and for pressures between 0.34 and 20.4 atm a Texas Instruments Type 1 Capsule (tube no. 16) was used. The uncertainty in pressure measurement is less than 0.2% at all pressures employed in this project (0.0013 < P < 20.1 atm).

The Texas Instruments Pressure Capsules used in the Texas Gauge measure differences in pressure and the low pressure sides of the capsules were kept below 10^{-2} Torr.

As shown in Figure 2.8, pressure is monitored on (crude) gauges P_1 (0-1 atm) and P_2 (0-27 atm) before admitting gas to the very delicate low pressure and high pressure capsules respectively.

A Veeco Thermocouple Gauge Control Model TG-7 was used to monitor
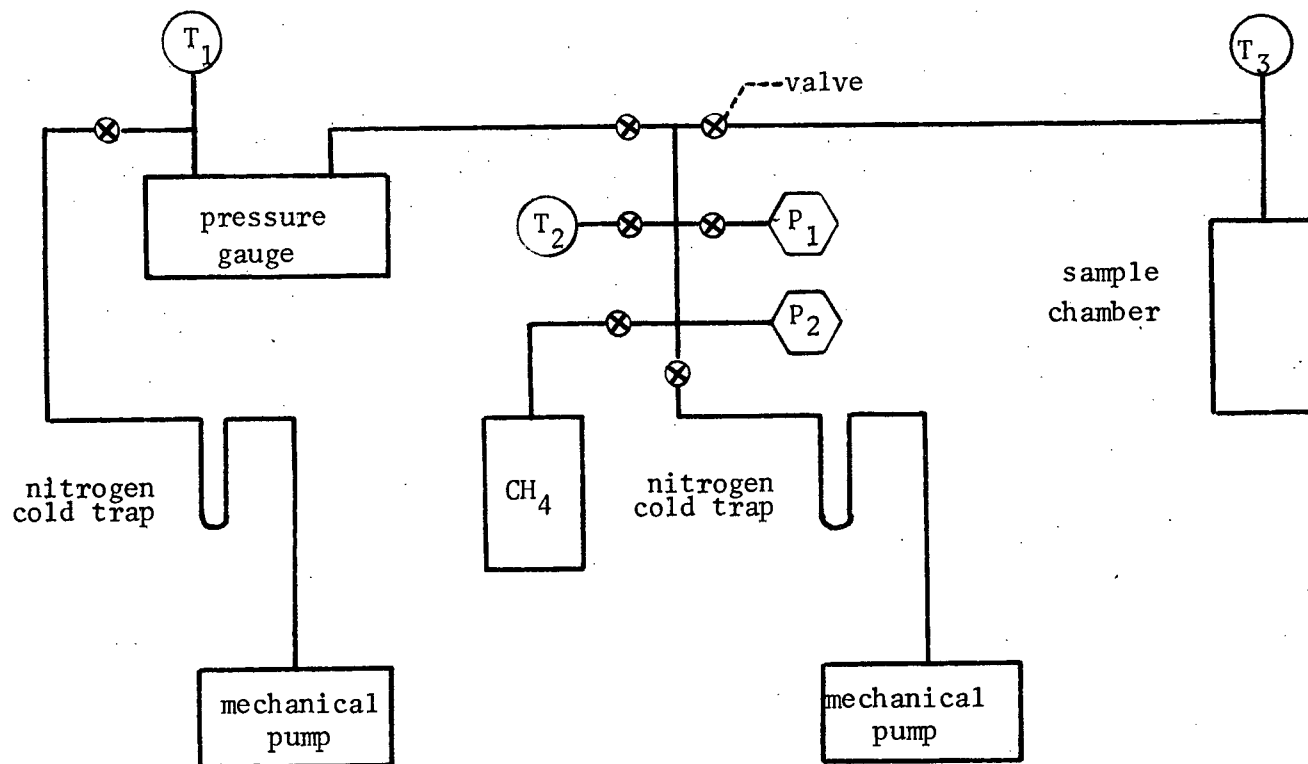
Figure 2.8. A schematic diagram of the gas handling system.

very low pressures (10^{-3} to 10^{-1} Torr) at three points in the system as indicated by T_1, T_2 and T_3 in Figure 2.9.

With a nitrogen cold trap and a Welch Duo-Seal mechanical pump, the relatively large volume system could be pumped from any pressure to 5×10^{-3} Torr in 15 minutes (30 minutes at 77K).

2.3   EXPERIMENTAL PROCEDURE

The most homogeneous region of the dc field was found by moving the sample chamber and observing the free induction decay in CH_4 at room temperature. In order to accommodate the variable temperature apparatus in the magnet gap, the variable temperature sample chamber was 2/3 the volume of the room temperature sample chamber. The ratios of the volumes of the coils is about the same. The resulting loss in signal to noise was partially compensated for by an increase of signal to noise because of an increase in T_2'. At the densities used to tune the signal, $T_2 \gg T_2^M$ and $T_2' \sim T_2^M$ with the result that the smaller variable temperature sample chamber sees a more homogeneous H_0 field.

The area in the magnet gap was cooled considerably by the process of blowing nitrogen for measurements at 110 and 150K. The magnitude of the dc field was seriously affected and required about 10 hours to come to equilibrium. The homogeneity was not visually affected.

The signal was normally maximized (i.e., the input circuit tuned) with the sample chamber at the operating temperature. However, at 77K the vapour pressure of CH_4 is only 9 Torr (0.012 atm) and the signal was too weak for tuning purposes. In this case the apparatus was tuned at room temperature. This was reasonably satisfactory because unlike blowing

nitrogen gas, filling the sample chamber dewar with liquid nitrogen did not
seriously change the temperature in the gap region and therefore did not
change the dc field appreciably.

It should be pointed out that even after the signal is maximized,
the pulses are not "perfect" or "clean" in the sense that they do not produce
pure rotations of the magnetization. This effect results from inhomogeneities
in H_0 and H_1 (see Section 2.4) and cannot be neglected in T_2 measurements
(87) and some T_1 measurements (for instance the "null" method (89)). In
our case, the determination of $R_1 = T_1^{-1}$ is not affected by this but the
signal to noise is reduced.

Having maximized the signal, a two pulse experiment was performed
in the following manner. The boxcar sampling pulse (i.e., the time during
which the boxcar samples the free induction decay) was set to a width of
approximately (0.75) T_2', starting 20 μs after the end of the π/2 pulse (as
it appears at the transmitter output). The period of the two pulse sequence
was set to about 10 T_1 to ensure the spin system had returned to equilibrium
before the start of each sequence. The time constant for the boxcar was set
to give an effective time constant of between 5 and 15 seconds. The effective
time constant is given by the repetition period times the boxcar time constant
divided by the time duration of the boxcar sampling pulse (24, 80).

For repetition periods shorter than 0.75 seconds, the Monsanto
digital voltmeter was set to sample the boxcar output every 0.75 seconds.
Under these conditions the datalogger added the signal 40 times; thus
a data "point" was measured every 30 seconds. For repetition periods greater
than 0.75 seconds, the voltmeter sampling period was increased and the number
of counts per point was reduced to keep the total time per data point at

about 30 seconds.

Between 10 and 14 data points were taken with $t \sim 10\ T_1$ which gives the equilibrium signal. Then t was varied from as close to zero as possible to nT_1. For $\rho \gtrsim 0.1$, $n \sim 3$; for $0.03 \lesssim \rho \lesssim 0.1$, $n \sim 2$ and for $\rho \lesssim 0.03$, $n \sim 1$. The density ρ is given in amagat (see Section 2.5.3). This sweep took between 15 and 20 minutes which means there are between 30 and 40 data points per measurement. The equilibrium signal was again measured with $t \sim 10\ T_1$.

A three pulse experiment was performed in the same way, the only difference being that the boxcar sampling pulse was given about twice the width and was centred symmetrically about the spin-echo.

The temperature and pressure were measured before and after each measurement of $R_1 = T_1^{-1}$.

The measurements were performed in sets of between 1 and 10 (usually 3,4 or 5) with the pressure being changed between each one. No other experimental parameters were changed with the single exception of the rate at which t was varied. At the end of each set, the sample chamber was evacuated ($P \lesssim 5 \times 10^{-3}$ Torr) and another measurement performed. This "vacuum" run was important at low densities (receiver at very high gain) because of the presence of a small (rarely visible on the chart recorder) long term recovery of the receiver-amplifier after the pulses. The signal is monitored a fixed time after the $\pi/2$ pulse (free induction decay) or a fixed time after the second π pulse (spin echo) so any recovery associated with these pulses is not important. However, as t is varied, the boxcar pulse sweeps through the recovery of the amplifier after the first π pulse. This "vacuum run" signal had to be subtracted from each experiment in the set. This was very important because small errors in determining the equilibrium

signal led to large errors in R_1. This is discussed further in Section 2.5.2.

Only the two pulse sequence was used for measurements at densities below the R_1 maximum (T_1 minimum). (See Figure A.1 in Appendix A.) Whereas $T_2' \sim T_2^M$ = constant at densities above the R_1 maximum, T_2 becomes comparable with T_2^M at very low densities and T_2' becomes shorter. At densities at and above the R_1 maximum both the two and three pulse sequences were used equally and within experimental error resulted in the same relaxation rates.

2.4   DIFFUSION EFFECTS

In order that the experimental results be a good test of the theory of nuclear spin relaxation one must make sure that the experimentally measured relaxation rate is that of the bulk gas and that there are no systematic effects associated with other possible relaxation mechanisms. One such effect which could, in principle, increase the measured relaxation rate in a systematic way is diffusion.

The effects of diffusion are extremely difficult to calculate, but one can estimate worst possible cases and perform experiments with different conditions inside the sample chamber. This will determine whether it is best to confine the sample gas to the interior region of the coil (22, 84) or to immerse the coil in the sample (25) as done in this study. One also wishes to know if cleaning the sample chamber and the sample gas is necessary. It is known that diffusion to the sample chamber walls and the subsequent relaxation by paramagnetic impurities on the wall is completely dominant in the case of He^3 if the sample gas and chamber are not carefully cleaned. This is because the intrinsic relaxation rates are

extremely small (3). Also, there is disagreement among different investigations of relaxation rates in some polyatomic gases. For instance, there is disagreement for CH_4 (25), and certain proton relaxation rates in CHF_3 (15) were questioned (20) and are now known to be about 100% too large(13) (90). Finally, spurious R_1 maximums (T_1 minimums) appear in the literature for CH_4 (27) and for BF_3 (12). Because these systematic effects can only increase the relaxation rate, one tends to have more confidence in measurements resulting in lower values for R_1. Only after these effects have been excluded can one choose a sample chamber geometry solely on the basis of signal to noise considerations.

The effect of diffusion to, and the subsequent relaxation on the walls depends on the time it takes a molecule to get to the wall and the probability that a spin will be relaxed on colliding with the wall. The worst case is obtained by assuming that each time a spin comes in contact with a wall it is relaxed. In this limit a rigorous expression for $R_{1,wall}$ can be derived. We do not do this because although this is the case for He^3 at low temperatures where the sample chamber has not been extensively cleaned, it can be shown not to apply here. This is shown further in this section.

There is another possible effect of spin diffusion other than wall relaxation which concerns the inhomogeneities in the rf H_1 field. An rf pulse may produce different rotations of the magnetization in different parts of the sample chamber. The responsiveness of the coil (i.e., the induced nuclear induction signal) will reflect this inhomogeneity. We can show how this effect could contribute to the observed relaxation by choosing two regions inside the sample chamber but not necessarily inside the coil. We

assume an rf pulse "flips" (i.e., excites) the spins in one region but not in the other as a consequence of rf inhomogeneities. If, as a result of diffusion, a certain fraction of the spins in each region "trade places" in a time comparable with or less than T_1, the observed signal will include an extra apparent relaxation because the coil is responsive in the same regions that the rf is effective. An extreme example of two such regions might be inside and outside the coil.

If wall relaxation is not negligible, its contribution to the observed relaxation rate will be reduced if the sample chamber is made as large as possible and its contribution will be increased if the gas is confined to the interior of the coil. If apparent relaxation due to the mechanism discussed in the previous paragraph is important, the opposite is true, namely its contribution will be increased if molecules are allowed to diffuse in and out of the coil.

The majority of the room temperature experiments were performed with the room temperature sample chamber with the coil immersed in the gas. Several experiments were performed with Teflon plugs at the bottom and top of the coil and a glass cylinder surrounding the coil. The remaining region outside the coil was filled with Teflon as well as possible. The results of these experiments were two-fold. First, the signal was decreased by almost a factor of two. This indicates that the coil is sensitive to the regions outside the coil. Secondly and more importantly, the relaxation rates so measured were in complete agreement with those measured with the immersion geometry. Also, seven measurements were taken at room temperature with the variable temperature sample chamber. These are also in complete agreement with the other results. These experiments indicate that relaxation due to

effects of diffusion and walls are negligible for both the "immersion"

geometry and the case of confining the sample gas to the interior region

of the coil and that the choice should be made on the basis of signal to

noise. It is, of course, assumed that all experiments involve at least

elementary cleaning precautions. It should be pointed out that the

disagreement among different investigators remains a mystery. The

relaxation rates reported here (295K) are in agreement with other measurements

(28, 91) and are systematically lower than measurements reported in reference

(16). The latter disagreement is discussed quantitatively in reference (25)

but the discussion concerning wall effects (25) seems to be incorrect.

The results of the measurements reported in this section were not

performed at very low densities nor were they performed at low temperatures.

The possibility of a small contribution to the observed relaxation rate due

to diffusion effects at densities below the R_1 maximum can not be ruled out.

At 77K, the possibility of the formation of liquid monolayers building up

on the walls (most likely the bottom) was suggested by a very slow decrease

in pressure. This phenomenon occurred during only about five of the 24

measurements performed at 77K. It was clear that liquid was not forming

on the coil because an increase in the signal would have been

observed. This was not the case. One would not expect liquid to form on

the coil because of the heating effect of the rf pulses. At the present time,

therefore, the 77K measurements must be treated with a great deal of

suspicion. Because the 77K measurements can only be performed over a

limited density range below the equilibrium vapour pressure they cannot

provide a strong test of the theory. These measurements, however, open up

the possibility of studying extremely low density gases and studying effects

associated with surface interactions.

The reason for immersing the coil in the sample gas was one of signal to noise. The "cleanliness" of the pulses can be estimated by noting the relative amplitudes of the free induction decay at $t = 0$ and $t = \infty$ for a $\pi - t - \pi/2$ sequence. If we define λ by $M(0) = -\lambda M(\infty)$ then a homogeneous rf field (i.e., clean pulses) will lead to a situation where $\lambda = 1$. Confining the sample gas to the interior of the coil results in a λ that is larger than one would obtain by immersing the coil in the sample gas. This is a direct result of the effects of inhomogeneities in H_1 and H_0. However, because the sample outside the coil contributes significantly to the signal, $M(\infty)$ will be larger for the immersion case. A measure of the total signal is $M(\infty) - M(0) = M(\infty) \{1 + \lambda\}$. In both the room temperature sample chamber ($\lambda \sim 0.4$) and the variable temperature sample chamber ($\lambda \sim 0.7$) the decrease in λ resulting from immersing the coil in the sample gas is more than compensated for by the increase in $M(\infty)$. Assuming that wall relaxation and diffusion are negligible, as seems to be the case, the effect of an inhomogeneous rf field (i.e., $\lambda < 1$) in no way affects the determination of the longitudinal relaxation rate.

In nuclear spin relaxation measurements in dilute gases, low signal to noise is the chief problem. The lowest density reported in this project was performed at 77K with a pressure of 0.99 Torr. This corresponds to a density of 0.0046 amagat or 5×10^{17} spins/cm^3. For comparison purposes, the nuclear magnetization in CH_4 of this density and temperature is down by a factor of 1.4×10^5 of that of water at room temperature.

2.5   DATA ANALYSIS

We outline the data analysis used to determine R_1, the longitudinal nuclear spin relaxation rate along with the statistical and systematic errors. Also discussed is the determination of the density from the temperature and pressure.

2.5.1   DETERMINATION OF $R_1 = T_1^{-1}$

The experimental data includes three sets of measurements. There are N_b ($N_b \sim 12$) values of the equilibrium signal which we denote by $S_{b,i}(\infty)$ where $i = 1,2, \ldots\ldots, N_b$ and where "b" refers to before. Then, there are between 30 and 40 measurements of the signal at different times t where t is varied between zero and t_f. The parameter t_f is given by $t_f = nT_1$ where $1 \lesssim n \lesssim 3$. We denote these measurements by S(t). Finally, there are N_a ($N_a \sim 12$) measurements of the equilibrium signal which we denote by $S_{a,i}(\infty)$ where $i = 1,2, \ldots., N_a$ and "a" refers to after.

The average value of the equilibrium signals, before and after the S(t) values are measured, are defined by

$$S_\alpha(\infty) = \frac{1}{N_\alpha} \sum_{i=1}^{N_\alpha} S_{\alpha,i}(\infty) \qquad \alpha = b,a \qquad (2.5.1)$$

We require the differences between the equilibrium signal and the signal at time t in order to determine the relaxation rate. The equilibrium values $S(t,\infty)$ to be associated with each value of S(t) are computed in the following way. Since there is always a finite drift in the equilibrium signal over the time of a run, a linear drift is assumed from $S(t,\infty) =$

$S_b(\infty)$ at $t = 0$ to $S(t,\infty) = S_a(\infty)$ at $t = t_f$:

$$S(t,\infty) \quad = \quad \left[\frac{S_a(\infty) - S_b(\infty)}{t_f} \right] t + S_b(\infty) \qquad (2.5.2)$$

These parameters are shown in Figure 2.9 where the drift in the baseline (equilibrium signal) is greatly exaggerated. This process is done by computer and not on the chart record as indicated in Figure 2.9.

The values of $S(t,\infty) - S(t)$ are then calculated for each experiment. For the vacuum run, we have equivalent parameters and they will be denoted by a superscript v. The parameters $V(\infty) - V(t)$ are defined by

$$V(\infty) - V(t) \quad = \quad S(t,\infty) - S(t) - [S^v(t,\infty) - S^v(t)] \qquad (2.5.3)$$

The data are in digital form so the values for the particular experiment and the vacuum run do not, in general, coincide. The computer interpolates between points in the vacuum run.

We assume that after a perturbation the magnetization decays according to

$$M(t) = M(\infty) + [M(0) - M(\infty)]e^{-R_1 t} \qquad (2.5.4)$$

The validity of interpreting the relaxation in terms of a single relaxation rate R_1 is discussed in Section 2.5.2. The measured signal resulting from this magnetization is given by

$$V(t) = AM(t) + B \qquad (2.5.5)$$
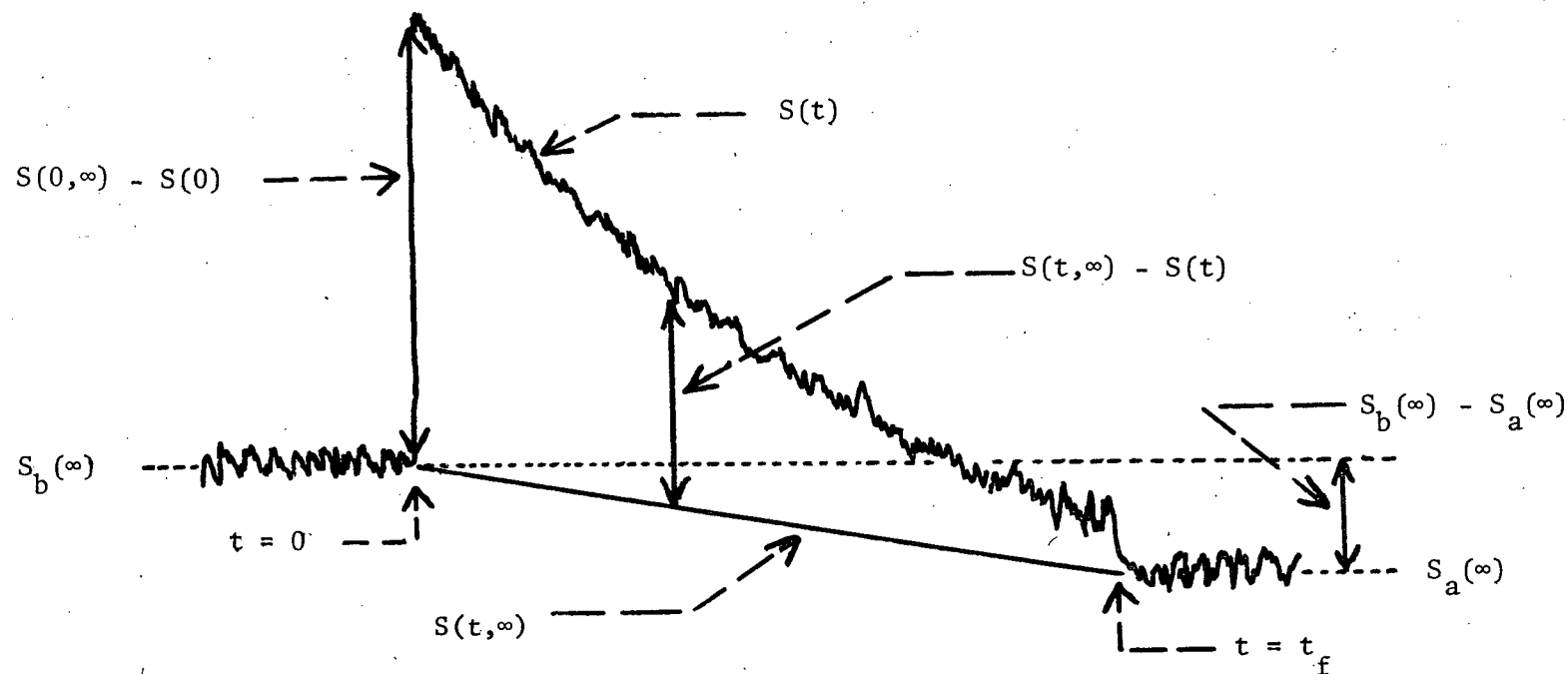
Figure 2.9. Pictorial representation of the manner in which $S(t,\infty)-S(t)$ is calculated for a finite drift in $S(t,\infty)$. The parameters are defined in the text and the drift shown here is greatly exaggerated.

where A and B reflect the amplification of the signal and any dc offset respectively.

From equations 2.5.4 and 2.5.5 we can determine R_1 by fitting the experimental values of $V(\infty) - V(t)$ to the equation

$$\ln[V(\infty) - V(t)] = -R_1 t + \text{constant} \qquad (2.5.6)$$

The slope, $-R_1$ is computed from a least squares fit of the data. The least squares fit programme (92) is based on an analysis described in the literature (93) and is discussed in somewhat more detail in the next Section. Figure 2.10 shows a plot of $\ln[V(\infty) - V(t)]$ vs t for the lowest density experiment performed. This particular experiment is discussed at the end of the previous section. The straight line results from the least squares fit of the data.

A total of 466 experiments were performed. At 295K, 123 experiments were performed in the region $0.08 < \rho < 17.0$. All densities are given in amagat. (see Section 2.5.3). These measurements are in complete agreement with others reported in the literature (25, 28). With the exception of 7 measurements performed with the variable temperature sample chamber, (see Section 2.4), the experiments reported here and those of references (24, 25) were performed with the room temperature sample chamber. The experiments reported here and those of reference (25) combine to give 293 values of R_1 in the region $0.0062 \leq \rho \leq 17.0$. These results are tabulated in Table A.1 and plotted in Figures A.1 and A.2 (the A refers to appendix A.) The data will usually be presented in two plots. Because of the nature of the R_1 vs ρ log-log plots (Figure A.1) the details of the high density results are obscured. This is rectified by plotting $R_1 \rho$ vs ρ on a semi-log (Figure A.2). This latter format, in turn obscures the details of the low density results.
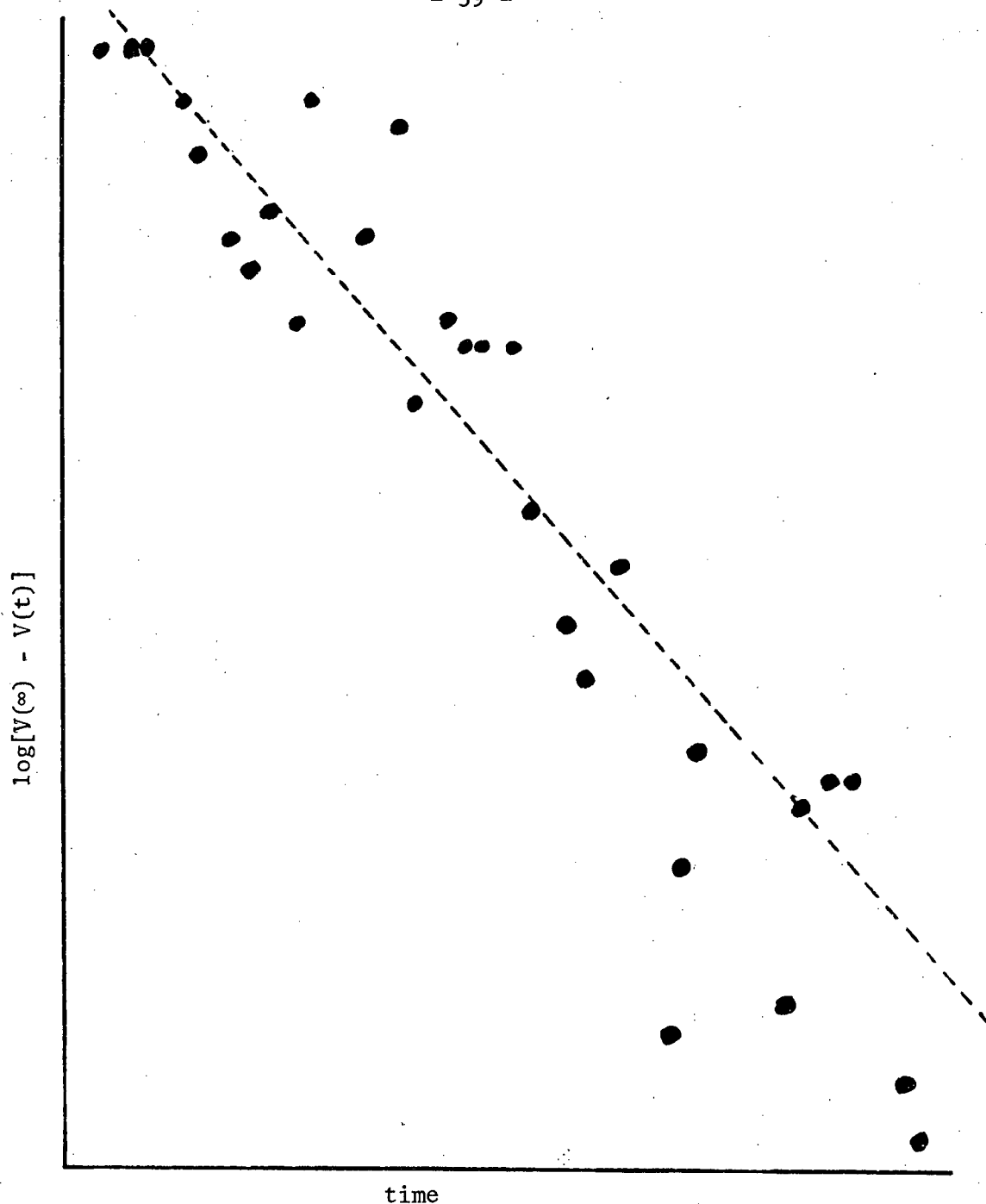
Figure 2.10. A plot of $\log[V(\infty) - V(t)]$ vs time for the lowest density relaxation measurement reported in this project. The straight line resulting from the least squares fit of the data gives $R_1 = 119$ sec^{-1} with a statistical error $E(S)$ of 17 sec^{-1}. The temperature is 77K, the pressure is 0.99 Torr and the density is 0.0046 amagat.

At 150K, 110K and 77K; 166, 152 and 25 measurements were performed in the regions $0.006 \lesssim \rho \lesssim 5.8$, $0.008 \lesssim \rho \lesssim 2.2$ and $0.0046 \lesssim \rho \lesssim 0.040$, respectively. The upper limits on the density at 77K and 110K correspond to the vapour pressure of CH_4 at each temperature. The 150K results appear in Table A.2 and Figures A.3 and A.4. The 110K results appear in Table A.3 and Figures A.9 and A.10. The 77K results appear in Table A.4 and Figure A.15.

For comparison purposes, all the measurements reported here are given in Figures A.18 and A.19.

2.5.2   ERROR ANALYSIS

A thorough investigation of both statistical and (known) systematic errors has been made for the experiments at 150, 110 and 77K. The R_1 values at 295K (this work – not that of reference 25) have been computed as indicated in the previous section but have not been subjected to statistical tests by computer. Random errors have been estimated however (24) and the result of this procedure is that the scatter in the R_1 values for the 295K measurements is representative of the total error. One can only assume that even though the following discussion has been applied only to the 77, 110 and 150K results that the resulting error bars (%) will be typical of the 295K measurements.

The least squares fit with which R_1 is determined is linear (equation 2.5.6)

$$Z(t) = -R_1 t + \text{constant} \qquad (2.5.7)$$

where

$$Z(t) = \ln[V(\infty) - V(t)]$$

$$= \ln[S(t,\infty) - S(t) - S^V(t,\infty) + S^V(t)] \qquad (2.5.8)$$

These parameters are defined in the previous section (Section 2.5.1). The actual fitting procedure (92, 93) is a relatively complicated χ-squared fit, the details of which we shall not discuss. The important point is that the observed parameters $Z(t)$ are weighted by $[\Delta Z(t)]^{-2}$ where $\Delta Z(t)$ is the statistical uncertainty in $Z(t)$. Thus very small uncertainties result in greater weights and vice versa, as would be expected.

We wish, then, to determine a statistical uncertainty for each value of $S(t,\infty) - S(t)$ and $S^V(t,\infty) - S^V(t)$. Because there are N_b measurements of $S_{b,i}(\infty)$ and N_a measurements of $S_{a,i}(\infty)$ we can calculate an uncertainty (one standard deviation) for the equilibrium signal before and after the measurements of $S(t)$. We call these uncertainties σ_b and σ_a. These two standard deviations are nearly equal because they are computed from measurements made under the same conditions with respect to noise. As a result, we define the average value of σ_b and σ_a as ΔS.

$$\Delta S = \frac{1}{2}[\sigma_b + \sigma_a] \qquad (2.5.9)$$

Because the measured quantities $S(t)$ are also measured under the same conditions with respect to noise, we can associate ΔS with the uncertainty in each $S(t)$. We are not able to compute an uncertainty for each $S(t)$ directly because the time t is being continuously varied. Thus ΔS is to be associated with the uncertainty in all the measured quantities, namely the $S_{b,i}(\infty)$, the $S(t)$ and the $S_{a,i}(\infty)$, each of which involve a summation over the same length of (real) time by the digital voltmeter (see Section 2.3).

In order to compute a statistical error in $S(t,\infty) - S(t)$ we would also have to compute an uncertainty in $S(t,\infty)$. If each value of $S(t,\infty)$ were measured independently between each successive $S(t)$ measurement and, if the equilibrium signal were measured N times (or any signal for that matter) solely to obtain the uncertainty ΔS, then the statistical uncertainty in $S(t,\infty)$ would be ΔS. This is, however, not the case. In the present situation if the noise fluctuations have a correlation time much shorter than the time between samples then the statistical uncertainty in $S(t,\infty)$ would be $\Delta S/\sqrt{N}$. In fact, slow drifts in the gain of the spectrometer and in certain D.C. voltages, or for example a 1/f component in the noise spectrum, do not satisfy this criterion. In this case the value of ΔS will not converge in general and may get larger as the number of samples is increased. This also means that the uncertainty in $S(t,\infty)$ may get worse as the number of samples is increased. In practise, for $N = N_a \sim 12$ the uncertainty in $S(t,\infty)$ falls between the values ΔS and $\Delta S/\sqrt{N}$. We will assume the worst possible case, namely that the uncertainty in $S(t,\infty)$ is ΔS.

The least squares fit programme used to calculate R_1 and statistical uncertainties in R_1 assumes the uncertainties for each value of $V(\infty) - V(t)$ are uncorrelated. The statistical uncertainties described in the previous paragraphs are, however, correlated and it is clear that there is a systematic component to the error. This systematic error comes about because we are subtracting the quantities $S(t,\infty)$ (the uncertainties of which are correlated because they are all based on the same measured quantities) from the quantities $S(t)$ (the uncertainties of which are not correlated). We assume the possible correlations between all measured quantities which may come about as a result of the nature of the noise (previous paragraph) are negligible compared with the correlations which result from subtracting these two quantities. Because

of this effect, the uncertainty in R_1 generated by the least square fit

programme will underestimate the total error.

As a result of this analysis, we compute two errors which we shall

call statistical and systematic. In order to determine what we are referring

to as the statistical error in R_1, we assume the uncertainty in $S(t)$ is ΔS

as previously discussed, and that the error in $S(t,\infty)$ is identically zero.

In order to determine the systematic error in R_1, we assume the uncertainty

in $S(t)$ is zero and that the uncertainty in $S(t,\infty)$ is ΔS. Including the

vacuum run, the total uncertainty in $V(\infty) - V(t)$ for use in the least squares

fit is $\sqrt{2} \, \Delta S$. The total uncertainty in $V(\infty) - V(t)$ for use in the systematic

error analysis will also be $\sqrt{2} \, \Delta S$.

In order to compute $\Delta Z(t)$ for use in the least squares fit, we

define the following:

$$[Z(t)]_{MAX} = \ln[V(\infty) - V(t) + \sqrt{2} \, \Delta S]$$

$$(2.5.10)$$

$$[Z(t)]_{MIN} = \ln[V(\infty) - V(t) - \sqrt{2} \, \Delta S]$$

The difference between these two parameters represents the length of the

error bar in the linear plot and the final statistical uncertainty is given by

$$\Delta Z(t) = \frac{1}{2} [\ln\{V(\infty) - V(t) + \sqrt{2} \, \Delta S\} - \ln\{V(\infty) - V(t) - \sqrt{2} \, \Delta S\}]$$

$$= \frac{1}{2} \ln \left(\frac{V(\infty) - V(t) + \sqrt{2} \, \Delta S}{V(\infty) - V(t) - \sqrt{2} \, \Delta S} \right) \qquad (2.5.11)$$

Each point, then, is weighted by $[\Delta Z(t)]^{-2}$ where $\Delta Z(t)$ is given in equation

2.5.11. It is clear from equation 2.5.11 that because $V(\infty) - V(t)$ is a

decreasing function of time and ΔS a constant, $\Delta Z(t)$ is an increasing function

of time and thus the weights a decreasing function of time.

The X-squared fit of equation 2.5.7 with the weights given by equation 2.5.11 results in a computation of R_1 along with two statistical errors. The algebraic expressions for these errors (93) are complicated and we will discuss them qualitatively.

Roughly speaking, the first statistical error, E_1 is determined by the goodness of fit. E_1 is a measure of how well the values of $Z(t)$ constitute a straight line without regard to the error bars.

The second statistical error, E_2, takes into account the error bars on each point. For a fixed set of data points, increasing the length of the error bars will increase E_2 but not E_1.

The relative size of E_1 and E_2 is significant. For example, if one is measuring a quantity $y(x)$ (with measured uncertainties $\Delta y(x)$) which is known to be linear, one must always obtain $E_2 \geq E_1$. If $E_2 \gg E_1$ then $\Delta y(x)$ is being overestimated. If $E_2 = E_1$, the implication is that $\Delta y(x)$ are as small as possible (i.e., the uncertainties have been accurately estimated) whereas if $E_2 < E_1$, the errors $\Delta y(x)$ are clearly being under-estimated.

This example serves to show that if the random errors $\Delta Z(t)$ in the nuclear spin relaxation measurements are reasonably determined, the relative sizes of E_1 and E_2 indicate how well the data is represented by a straight line (i.e., $V(\infty) - V(t)$ by a single exponential).

In all the experiments performed at 77, 110 and 150K, upon evaluating the $\Delta Z(t)$ as prescribed above, we obtained E_2 ranging from about 1.2 to 1.8 E_1. Because of the way we have divided the error into a statistical and systematic component, we are probably underestimating E_2. The implication

is that the observed relaxation process is well represented by a single exponential to within experimental accuracy. This does not imply that the data may not be better fit (i.e., a smaller X-squared) by some other function such as, say, the sum of 2 exponentials. Unless there is a specific reason to fit the data to some other function, it seems a fruitless computational exercise to fit the results with a function more complicated than need be. This point will be discussed further in Chapter IV.

The statistical errors are labelled by $E(S) = E_2$ and are indicated in Table A.2 and Figures A.5 and A.6 for the 150K results, Table A.3 and Figures A.11 and A.12 for the 110K results and Table A.4 and Figure A.16 for the 77K results.

In order to accurately determine what we are referring to as the systematic error, a lengthy numerical study was performed with a computer. Using a function of the form

$$y(t) = 1 - 2 \exp(-R_1 t) + \Delta y \qquad (2.5.12)$$

the function

$$\ln\{1 - y(t)\} = \ln\{2 \exp(-R_1 t) + \Delta y\} \qquad (2.5.13)$$

was fit using the same programme used to fit the experimental data, i.e., equation 2.5.13 was forced into the form

$$\ln\{1 - y(t)\} = -R_1' t + \text{constant} \qquad (2.5.14)$$

and the resulting R_1' compared with the known R_1. The parameter

$$E(B) = \frac{|R_1' - R_1|}{R_1} \qquad (2.5.15)$$

was computed as a function of Δy and Δt (the time duration of the experiments). The value of Δy appropriate to the experiment is

$$\Delta y \quad = \quad \frac{\sqrt{2} \ \Delta S}{V(\infty)-V(0)} \qquad\qquad (2.5.16)$$

which is just the fraction uncertainty in $V(\infty) - V(0)$ resulting from the uncertainty in $V(\infty)$.

It was found that to a very good approximation only $\Delta t = t_f - t_s$ was relevant and not t_f or t_s independently. It was also interesting to note that $E(B)$ could be significant (5%) with no visually detected departure from linearity when equation 2.5.13 was plotted. This is interesting in that this simulated data has, of course, no noise superimposed. The departure from linearity was clear (visually) for $E(B) \sim 8\%$ resulting from $\Delta t \sim 2.5 \ R_1^{-1}$ and $\Delta y \sim 2\%$.

For a fixed Δy, the error $E(B)$ increases with increasing Δt. This explains, perhaps, why the higher density R_1 measurements are greatly affected by this systematic error. At the higher densities, signal to noise is greater and larger Δt values could be used.

Because of the nature of the log function, the error is different depending on the sign of Δy. The error was assumed to be the average of that computed for Δy positive and that computed for Δy negative. Analytical formulae were arrived at through trial and error by fitting the artificial data. This resulted in several algebraic formulae expressing $E(B)$ as a function of Δy and Δt, the choice of which one being based on the size and sign of Δy. These formulae are algebraically complex and are only of relevance to the particular way the data has been handled by the specific least squares fit programme used in this study. We do not reproduce them here but they accurately predicted

this (known) error in the artificially produced data. The artificial data covered the entire range of Δy and Δt values realized in the experiments.

The computer then calculated the error E(B) by choosing the relevant "error formulae" on the basis of Δy. It should be noted that this analysis is consistent with a procedure presented in the literature (94) where, under the conditions chosen, an error of 1% in $y(\infty)$ (i.e., $\Delta y = 0.01$) results in about a 3% error in R_1.

The systematic errors in R_1 resulting from this analysis are tabulated in Appendix A. They appear in Tables A.2, A.3 and A.4 for the 150K, 110K and 77K experiments respectively.

It should be noted that whereas this error E(B) is systematic with respect to an individual measurement, its effect on the R_1 vs ρ plot (or $R_1\rho$ vs ρ) is to give rise to more scatter than one would expect if the error were eliminated. It does not result in a systematic shift of all the experimental data. It is quite clear that a far superior method for measuring R_1 would be to jump back and forth between measurements of S(t) and S(∞) thus eliminating the dependence on the long term stability of the apparatus which is clearly the origin of this systematic error. The method employed in this experiment is widely used in gas phase nuclear spin relaxation experiments and it is not at all clear that this systematic error is always fully appreciated.

The total error E in an R_1 measurement is then given by

$$E = [\{E(S)\}^2 + \{E(B)\}^2]^{\frac{1}{2}} \qquad (2.5.17)$$

These errors appear in Tables A.2, A.3 and A.4 for the 150K, 110K and 77K measurements respectively. They are plotted in Figures A.7 and A.8 for the

150K results, Figures A.13 and A.14 for the 110K results and Figure A.17 for the 77K results.

2.5.3   DETERMINATION OF DENSITY

The measured parameters, temperature T and pressure P are related by

$$PV = znkT \qquad (2.5.18)$$

where z is the compressibility factor, V is the volume, k is Boltzmann's constant and n is the number of molecules. The compressibility factor z (95, page 114) corrects for the inadequacies of the Perfect Gas Law and is defined by equation 2.5.18. The compressibility factor has been measured (by measuring P, V and T) over a wide range of pressure and temperature for methane gas (50). The density in real amagat units is given by

$$\rho = \frac{n/V}{n_0/V_0} = \frac{z_0 P T_0}{z P_0 T} \qquad (2.5.19)$$

where the subscript zero refers to NTP. A real amagat is a dimensionless unit and is the ratio of the density in any units to the density at NTP (in the same units). If z_0 (which is 0.9977 for CH_4) is set to unity, the units are called ideal amagat . The error in the density calculated via equation 2.5.19 is determined by the uncertainty in the temperature and is less than 1%. Although the difference between real and ideal amagat is clearly negligible, real amagat were used in this project. Real amagat can be converted to molecules/cm^3 by multiplying by 2.69×10^{19}.

CHAPTER III

THE SPIN SYMMETRY THEORY OF NUCLEAR SPIN RELAXATION IN METHANE GAS

3.1   THEORETICAL OUTLINE

The aim of the spin-symmetry theory of nuclear spin relaxation in low density CH_4 is to calculate the longitudinal nuclear spin relaxation rate observed in the experiment.

The time rate of change of the magnetization is expressed in terms of the nuclear spin transition probabilities in Section 3.2. These transition probabilities involve the total rotation plus spin transition probabilities which are then summed over the rotational degrees of freedom. These sums are performed in Section 3.8 where the final nuclear spin transition probabilities can be found.

The problem of calculating the total transition probabilities is simplified by dividing the problem into time dependent and time independent or free molecule parts as discussed in Section 3.3.

In calculating the free molecule total transition probabilities, the matrix elements of the spin-rotation interaction are needed. It is here where spin-symmetry plays an important role and the calculations are simplified by the extensive use of group (representation) theory. The wavefunctions (Section 3.4) and spin-rotation interaction (Section 3.5) and the total transition probabilities are calculated (Section 3.7). The algebra involved in these calculations is straightforward but tedious and heavy use

is made of appendices for mathematical manipulation.

The time rate of change of the magnetization is given in Section 3.9 in terms of relaxation functions. The theoretical predictions of the theory require numerical computation of these relaxation functions and are described in the next Chapter.

3.2   GENERAL RELAXATION THEORY

The observed magnetization is given by

$$M^{obs} = \sum_{I=0}^{2} M^{(I)} = \sum_{I=0}^{2} \text{Trace } (\rho I_z) \qquad (3.2.1)$$

where $M^{(I)}$ is the magnetization of the I species. Writing the nuclear spin

density matrix ρ in the I m_I representation, this becomes

$$M^{(I)} = \sum_{m_I'} \sum_{m_I} \rho_{m_I m_I'} <m_I'|I_z|m_I>$$

$$= \sum_{m_I} m_I \rho_{m_I m_I} \qquad (3.2.2)$$

The time derivative of the density matrix is calculated by utilizing the re-

laxation matrix theory of Redfield (70, 72, 96, 97).

$$\frac{d}{dt} \overset{\sim}{\rho}_{m_I m_I} = \sum_{\substack{I' \quad I'' \\ m_I', \ m_{I''}''}} \sum R_{m_I m_I, m_I', \ m_{I''}''} \overset{\sim}{\rho}_{m_I', m_{I''}''} \qquad (3.2.3)$$

where $\overset{\sim}{\rho}$ denotes the difference between $\rho(t)$ and $\rho(\infty)$, the equilibrium value.

The rate of change of $M^{(I)}$ is then (utilizing 3.2.2 and 3.2.3)

$$\frac{d\tilde{M}^{(I)}}{dt} = \frac{dM^{(I)}}{dt} = \sum_{m_I} m_I \sum_{\substack{I' \quad I'' \\ m_I', \ m_{I''}''}} \sum R_{m_I m_I, m_I', m_{I''}''} \overset{\sim}{\rho}_{m_I', m_{I''}''} \qquad (3.2.4)$$

As discussed in references (70), page 277 and (72), page 143, we need only be concerned with those terms in the relaxation matrix for which the frequency associated with $m''_{I''} - m'_{I'}$ is the same as the frequency associated with $m_I - m_I$ which, in this case, is zero. The relaxation matrix in equation 3.2.4 involves matrix elements of the spin-rotation interaction. Because the spin-rotation Hamiltonian is linear in the total nuclear spin operators, we must satisfy the selection rules $\Delta I = 0, \pm 1$ and $\Delta m = 0, \pm 1$.

The diagonal elements of R are (97)

$$R_{m_I m_I, m_I m_I} = - \sum_{\substack{I' \\ m'_{I'} \neq m_I}} R_{m_I m_I, m'_I, m'_I} \qquad (3.2.5)$$

Further, the elements of R given by $R_{m_I m_I, m'_I, m'_I}$ are the transition probabilities.

$$R_{m_I m_I, m'_I, m'_I} = W_{m_I m'_{I'}} \qquad (3.2.6)$$

There are other properties of R which are useful when equation 3.2.4 is expanded. The high temperature approximation (72) implies

$$R_{m_I m'_{I'}, m''_{I''}, m'''_{I'''}} = R_{m''_{I''}, m'''_{I'''}, m_I m'_{I'}} \qquad (3.2.7)$$

Performing the summations in equation 3.2.4 and invoking conditions 3.2.5 to 3.2.7 leads to many individual terms for both $I = 1$ and 2 involving 18 density matrix elements. About one-half of these terms are diagonal in

the sense that they are expressible through transition probabilities as indicated in equation 3.2.6. These are the terms one would obtain by expressing the relaxation problem in terms of populations of the nine m_I levels, 5 for I = 2, 3 for I = 1 and 1 for I = 0. In this approach, the equivalent of equation 3.2.4 is

$$\frac{d\tilde{M}^{(I)}}{dt} = \sum_{m_I} m_I \sum_{\substack{I' \\ m_I'}} W_{m_I m_I'} (\tilde{n}_{m_I'} - \tilde{n}_{m_I}) \qquad (3.2.9)$$

where the n refers to the population and the tilda has the same meaning as in the density matrix. Equation 3.2.9 is a special case of equation 3.2.4 and is valid if the relaxation process is describable through rates of changes of populations. We will assume this to be the case here although it is not at all clear that the requirements needed to justify using this approximation are rigorously satisfied. All that can be said is that the off-diagonal density matrix elements are zero at equilibrium (t = ∞) and because of the nature of the experiment, at t = 0.

It is appropriate to mention here that a complete density matrix treatment of a system of four spin - ½ nuclei has been given by Hubbard (98) who has applied it to the case of liquid methane. The theory of Hubbard, though probably valid for liquid CH_4, cannot be used for gaseous CH_4 or for solid CH_4. The reason for this is that Hubbard explicitly neglects any correlation between nuclear spin states and molecular rotational states which is central to the calculations presented in this work. As a result of the permutation symmetry of the protons, such correlations are important in the dilute gas where the rotational (centrifugal distortion) states do not overlap appreciably and in the solid for similar reasons. In our treatment, the

proper molecular and spin states will be introduced from the start. The inclusion of off-diagonal terms of the density matrix remains to be done, however, and our presumption that these terms have only a small influence on the relaxation must be treated as a conjecture. A complete treatment would involve a combination of the calculations performed in this work and those of Hubbard (98).

The problem we set before us, then, is to calculate the $W_{m_I m_I'}$ in equation 3.2.9. (the sums in equation 3.2.9 are performed in Section 3.8). The conditions imposed on the molecule by the existence of spin symmetry as discussed in the introduction necessitate the calculation of total (spin plus rotation) transition probabilities. In order to calculate the probability that a molecule in the state $I'm_I'$ will make a transition to the state Im_I, we compute the probability that the total system (rotation plus spin) will make a transition from the state $R'I'm_I'$ to the state RIm_I and then perform a weighted sum over R' and R.

$$W_{m_I', m_I} = \sum_{R'} P_{R'} \sum_{R} W_{R'I'm_I', RIm_I} \qquad (3.2.10)$$

The parameter R refers to the rotational degrees of freedom. $P_{R'}$ is the probability of finding the molecule in the state R' and is calculated in Section 3.8 where the details of equation 3.2.10 are discussed.

3.3 THE TIME DEPENDENCE OF THE PROBLEM

The effects of collisions are introduced in a phenomenological manner through the use of correlation functions. This is convenient, mainly because it allows us to make use of previous studies, in particular references (16) and (26) . An alternate approach, that of the kinetic equation is mentioned for completeness but not discussed in any detail whatsoever.

3.3.1 CORRELATION FUNCTIONS AND SPECTRAL DENSITIES

We follow closely the analysis of Gordon (99), the present discussion being somewhat more complicated. The molecular degrees of freedom are divided into three categories: S refers to the nuclear spin energy, R refers to the centrifugal distortion energy and L refers to the rotational and translational energy. Thus, for example a change of state L' → L can involve a change in the translational kinetic energy, a change in J, the principle rotational quantum number, and a reorientation of the molecule - the latter being described by a change in the direction of $\overline{J}$ with $\Delta J = 0$.

With these conventions in mind, we can use the result of time dependent perturbation theory to express the probability per unit time that a transition takes place from the state $|R'S'\rangle$ to the state $|R\,S\rangle$ (99, page 4)

$$W_{R'S'RS} = 2\pi\hbar^{-2} \sum_{L'} \sum_{L} P_{L'} |\langle L'R'S'|H_1|LRS\rangle|^2 \delta(\omega_{L'R'S'LRS}) \qquad (3.3.1)$$

Equation 3.3.1 is simply the Golden Rule (100) where the Dirac δ-function conserves the energy of the total system. H_1 is the perturbation Hamiltonian

whose eigenvalues are small when compared with the difference in the eigenvalues of the unperturbed Hamiltonian from whence the states $|LRS\rangle$ are obtained. H_1 is discussed in greater detail in the following pages. $P_{L'}$ is the probability that the system is in the state L'. The parameter $\omega_{L'R'S'LRS}$ is given by

$$\omega_{L'R'S'LRS} = \omega_L + \omega_R + \omega_S - (\omega_{L'} + \omega_{R'} + \omega_{S'})$$

$$= (\omega_L - \omega_{L'}) + (\omega_R - \omega_{R'}) + (\omega_S - \omega_{S'}) \qquad (3.3.2)$$

where ω refers to the energy in units of angular frequency. The differences $\omega_R - \omega_{R'}$ are the differences of centrifugal distortion energies discussed in the introduction (Chapter I). The ω_R will be discussed in considerably greater detail in the latter sections of this chapter. The difference $\omega_S - \omega_{S'}$ equals $-(m_I - m_I')\omega_0$ which is $+\omega_0$, $-\omega_0$ or zero. The parameter ω_0 is the difference between the nuclear and molecular Larmor frequencies. This is discussed further in reference (5). Both Larmor frequencies are proportional to the applied dc field and the ratio of the two is equal to the ratio of the gyromagnetic ratios. This ratio has been measured (59) and is 0.056. Thus $\omega_0 = 0.944\omega_N$ where ω_N is the nuclear Larmor angular frequency.

Using the integral form (Fourier expansion) of the Dirac δ-function:

$$\delta(\omega) = \frac{1}{2\pi} \int_{-\infty}^{\infty} e^{-i\omega t} dt \qquad (3.3.3)$$

equation 3.3.1 can be written

$$W_{R'S'RS} = \hbar^{-2} \int_{-\infty}^{\infty} \sum_{L'} \sum_{L} P_{L'} \ |\langle R'S'L'|H_1|RSL\rangle|^2 e^{-i\omega_{L'R'S'LRS}t} dt \qquad (3.3.4)$$

We can now cast equation 3.3.4 into the Heisenberg form with respect to the system L by the following

$$W_{R'S'RS} = \hbar^{-2} \int_{-\infty}^{\infty} \sum_{L'} \sum_{L} P_{L'} \langle R'S'L'|H_1|RSL\rangle \times$$

$$\langle RSL|e^{+i\omega_L t} H_1^\dagger e^{-i\omega_L' t}|R'S'L'\rangle e^{-i\omega_{S'R'SR} t} dt \qquad (3.3.5)$$

where the notation $\omega_{S'R'SR}$ is obvious from equation 3.3.2. If the exponentials $e^{\pm i\omega_L t}$ are expanded, $\omega_L|L\rangle$ can be identified with $H_L|L\rangle$ the unperturbed Hamiltonian for the system L. If the exponentials are then reformed we can rewrite equation 3.3.5

$$W_{R'S'RS} = \hbar^{-2} \int_{-\infty}^{\infty} \sum_{L} \sum_{L'} P_{L'} \langle R'S'L'|H_1|RSL\rangle \langle RSL|H_1^\dagger(t)|R'S'L'\rangle e^{-i\omega_{S'R'SR} t} dt$$

$$(3.3.6)$$

where

$$H_1^\dagger(t) = e^{iH_L t} H_1^\dagger e^{-iH_L t} \qquad (3.3.7)$$

The correlation function G(t) is defined by

$$G_{R'S'RS}(t) = \sum_{L'} \sum_{L} P_{L'} \langle R'S'L'|H_1(0)|RLS\rangle \langle RLS|H_1^\dagger(t)|R'S'L'\rangle \qquad (3.3.8)$$

and the transition probability is given by

$$W_{R'S'RS} = \hbar^{-2} \int_{-\infty}^{+\infty} G_{R'S'RS}(t) e^{-i\omega_{R'S'RS} t} dt \qquad (3.3.9)$$

For completeness, we note that the spectral density $J(\omega)$ is defined as the Fourier transform of $G(t)$ with the result that

$$W_{R'S'RS} = \hbar^{-2} J(\omega_{R'S'RS}) \tag{3.3.10}$$

The centrifugal distortion (R) and the nuclear spin (S) energy levels are known exactly and the problem reduces to one of determining the form of the correlation function $G_{R'S'RS}(t)$. This has not been done from first principle for any system in the gaseous state other than hydrogen gas (9). It is clearly an important but difficult exercise in statistical mechanics to do this for polyatomic gases and we do not attempt it. A general discussion of correlation functions is given in Abragam (70).

We can simplify the problem by assuming the Hamiltonian H_1 can be decomposed into a sum of terms, each of which is the product of a time independent operator H_{sr} acting on the systems S and R and the other a time dependent random interaction $F(t)$ acting on the system L (70, page 278).

$$H_1(t) = \sum_i H_{sr}^i F^i(t) \tag{3.3.11}$$

where H_{sr}^i is a term in the isolated molecule spin-rotation interaction. The random interaction $F^i(t)$ is time dependent because it includes the effect of the anisotropic intermolecular potential V_a, which until now has not been included in the discussion. It should be noted that although equation 3.3.11 appears to be a reasonable assumption, it has not been put on a solid theoretical footing. The randomness of $F(t)$ allows us to treat the collisions in a phenomenological manner.

From equations 3.3.8 and 3.3.11 we have

$$G_{R'S'RS}(t) = \sum_i \sum_{L'} \sum_L P_{L'} \langle R'S'|H_{sr}^{i}|RS\rangle \langle RS|H_{sr}^{+i}|R'S'\rangle \times$$

$$\langle L'|F^i(0)|L\rangle \langle L|F^{i\dagger}(t)|L'\rangle \qquad (3.3.12)$$

where we have made the additional assumption that cross correlation effects
are negligible (i.e., in equations 3.3.12, the sum over i' does not appear
because we have invoked a δ-function in i and i').

Equation 3.3.12 can be expressed

$$G_{R'S'RS}(t) = \sum_i |\langle R'S'|H_{sr}^{i}|RS\rangle|^2 g_i(t) \qquad (3.3.13)$$

where the reduced correlation function $g_i(t)$ is given by

$$g_i(t) = \sum_{L'} \sum_L P_{L'} \langle L'|F^i(0)|L\rangle \langle L|F^{i\dagger}(t)|L'\rangle \qquad (3.3.14)$$

Equation 3.3.14 is just an average over an equilibrium ensemble of molecules.
It should be noted that the translational degree of freedom is considered
an infinite heat sink and as such is always in equilibrium. It is also
assumed that the energy exchange between the molecular rotation and the trans-
lation is very fast compared with the nuclear spin relaxation time. This is
an excellent approximation.

The effects of collisions are now completely contained in $g_i(t)$.
The factors $|\langle L'|F^i(0)|L\rangle|^2$ are normalized such that $g_i(0) = 1$.

Because $F^i(t)$ is a random operator, all correlations will be lost in a characteristic time τ_i which is the time between collisions which effectively reorient the molecule. The spectral lines in dilute gases are completely motionally narrowed (70, Chapter X). The reduced correlation function $g_i(t)$ usually adopted in gas phase nuclear magnetic resonance which both a) satisfies the above restrictions and b) leads to the Lorentzian line shape of a motionally narrowed line is given by (16, 26)

$$g_i(t) \quad = \quad e^{-|t|/\tau_i} \tag{3.3.15}$$

As an aside, it should be pointed out that the situation in very dense gases is much more complex than our present discussion allows for (101, 102). Using equations 3.3.9, 3.3.12, 3.3.13 and 3.3.15 and performing the integration over t, we obtain the result

$$W_{R'S'RS} \quad = \quad \sum_i \hbar^{-2} |<R'S'|H_{sr}^i|RS>|^2 \quad \frac{2\tau_i}{1 + \tau_i^2 \omega_{R'S'RS}^2} \tag{3.3.16}$$

The reduced spectral density $j(\omega)$ is the Fourier transform of the reduced correlation function and is given in this case by the Lorentzian factor in 3.3.16. We write the transition probability in the convenient form

$$W_{R'S'RS} \quad = \quad \sum_i \hbar^{-2} |<R'S'|H_{sr}^i|RS>|^2 j_i(\omega_{R'S'RS}) \tag{3.3.17}$$

3.3.3   KINETIC EQUATION APPROACH

As an aside, it should be pointed out for completeness that the
kinetic equation approach has also been used to describe nuclear spin re-
laxation in dilute gases. In this method (103, 104, 105) the time depend-
ence in the relaxation problem is introduced through the use of collision
integrals. The kinetic theory approach has been applied to H_2 (4, 6, 106),
diatomics with $I > \frac{1}{2}$ (119), symmetric tops (19, 107) and CH_4 (108). Refer-
ence (119) contains an error and the conclusions regarding different relaxa-
tion rates for different spin symmetry species are incorrect (122). There
are several errors in reference (108) which involve a misunderstanding of
the role of spin symmetry. These errors have been pointed out (109) and
a correction published (110) but the authors have underestimated the im-
portance of centrifugal distortion in methane nuclear spin relaxation. The
results of this project are in contradiction to footnote 4 of reference (110).

3.4 THE WAVEFUNCTIONS

In order to calculate the matrix elements $\langle S'R'|H_{sr}|SR\rangle$, the wavefunctions $|SR\rangle$ are required. They are computed in a basis which is diagonal in the unperturbed free molecule Hamiltonian, $H_0 = H_0{}^S + H_0{}^R$ where $H_0{}^S = -\gamma h\bar{I}\cdot\bar{H}_0$ and $H_0{}^R = B\bar{J}^2 + W_d$. The centrifugal distortion Hamiltonian W_d is (33)

$$W_d = \tfrac{1}{4}D_t[5J_+^4 + 5J_-^4 + 70J_z^4 - 60\bar{J}^2J_z^2 + 6\bar{J}^4 - 12\bar{J}^2 + 50J_z^2] \qquad (3.4.1)$$

where the components of $\bar{J}$ are referred to the molecular fixed frame (MFF).

Because the energy eigenvalues associated with W_d are, in general, large compared with those associated with $H_0{}^S$, the wavefunctions $|SR\rangle$ must be diagonal in W_d. This leads to computational difficulty in that this can be performed only numerically.

The wavefunctions are cast into forms which transform according to the symmetry requirements of the molecule. This leads to the use of group (representation) theory. Finally, the total wavefunctions are obtained by appropriately contracting spin and rotational functions.

3.4.1 SPIN FUNCTIONS

Protons are fermions and the wavefunctions must exhibit Fermi-Dirac statistics. Adding the wavefunctions of the four individual protons in the usual way (111) using the Clebsch-Gordan and/or the Racah coefficients results in 16 linearly independent wavefunctions. Further, using group

theory (112), one can ascribe to each of the 16 functions an irreducible representation (and component) of the tetrahedral point group T_d. Such a set of functions is taken directly from reference (33) and appears in Table 3.1[1]. We note that these functions are not unique. The set we have chosen (33) differs from those in reference (59)[2]. The wavefunctions used in reference (59) have also been used in reference (114)[2].

As indicated in Table 3.1, the spin functions are written $\chi(\beta\zeta:Im_I)$ where the total nuclear spin per molecule is $I = 0$, 1 or 2 and the projection on the magnetic field axis is m_I. The function χ transforms according to the ζ component of the β representation of T_d.

3.4.2   ROTATIONAL FUNCTIONS

The rotational wavefunctions for spherical tops are constructed by taking linear combinations of symmetric top wavefunctions, namely the $D_{m_J K}^{J*}(\Omega)$ as defined by Rose (111). Having decided on a particular set of spin wavefunctions, there is one and only one set of rotational wavefunctions such that the total wavefunctions are diagonal with respect to the centrifugal distortion Hamiltonian. This process is discussed in detail in reference (33). The resulting wavefunctions are then cast into a form which manifests the tetrahedral symmetry of the spherical top. The resulting rotational wavefunctions can then be written

---

[1] The $\sqrt{8}$ in the second to last function in Table V of reference (33) should be $\sqrt{12}$ (113). Also, we use F where T is used in reference (33).

[2] The spin functions in reference (59) are in error. The corrections appear in reference (33).

TABLE 3.1 SPIN FUNCTIONS

I	m_I	β	ζ	$\chi(\beta,\zeta;I,m_I)$
2	2	A1		aaaa
	1			½(baaa + abaa + aaba + aaab)
	0			√6̄/6(abab + baba + baab + abba + aabb + bbaa)
	-1			½(abbb + babb + bbab + bbba)
	-2			bbbb
1	1	F2	x	½(aaab + abaa - aaba - baaa)
	0			√2̄/2(abab - baba)
	-1			½(abbb + bbab - babb + bbba)
	1		y	½(aaab + baaa - aaba - abaa)
	0			√2̄/2(baab - abba)
	-1			½(babb + bbab - abbb - bbba)
	1		z	½(aaab + aaba - abaa - baaa)
	0			√2̄/2(aabb - bbaa)
	-1			½(abbb + babb - bbab - bbba)
0	0	E	1	√3̄/6(abab + baba + baab + abba - 2aabb - 2bbaa)
			2	½(abab + baba - baab - abba)

where a ⟹ I = ½ m_I = ½

       b ⟹ I = ½ m_I = -½

$$R(\gamma\xi;J,m_J;t,\rho) \quad = \quad \sum_K A(\gamma\xi;J,K;t,\rho) \ P(\gamma,\xi;J,K,m_J;\rho) \qquad (3.4.2)$$

The primitive functions (the P's) are functions of the $D^J_{m_J K}$ and are given in Table 3.2. Table 3.2 is based on Table IV of reference (115) with the phases being provided by Ozier (113). The angle $\Omega = \alpha\beta\gamma$ of which the $D^J_{m_J K}$ are functions, are measured with respect to the space fixed frame.

In equation 3.4.2, J is the usual principal rotation quantum number and m_J is the projection of J on the magnetic field axis. The function R transforms according to the ξ component of γ irreducible representation of T_d. If the γ representation occurs more than once for a particular J, the levels are labelled by the t quantum number which takes on the values 1, 2, 3... beginning with the lowest energy state.

There is no preferred molecular axis for spherical tops so there is no quantum number corresponding to the projection of J on the molecular axis (i.e., K). One can think of t in a spherical top as replacing K in a symmetric top. Finally, ρ is a parity index equalling 1 or 2 depending on whether the true parity operator has eigenvalues $(-1)^J$ or $(-1)^{J+1}$ respectively. Because this choice of ρ must be conserved in a spin-rotation interaction, it is a convenient parity index. It should be noted that we are, in effect, using the group $T_d \otimes i$ where i is the inversion group whose elements are 1 for $\rho = 1$ and -1 for $\rho = 2$. The various quantum numbers and indices that occur in equation 3.4.2 are explained in detail elsewhere (33, 116). See also section 3.6 on notation.

The A-constants in equation 3.4.2 involve the diagonalization of

TABLE 3.2   PRIMITIVE ROTATIONAL WAVEFUNCTIONS

				range of K	
$\underline{\gamma}$	$\underline{\xi}$	$\underline{\rho}$	$\underline{P(\gamma,\xi;J,K,m_J;\rho)}$	$\underline{J\ even}$	$\underline{J\ odd}$
F1	x	1	ϕW	1,3,5...	1,3,5...
	y		$-i\phi U$	1,3,5...	1,3,5...
	z		ϕU	4,8,12..	2,6,10..
F2	x	2	ϕW	1,3,5...	1,3,5...
	y		$-i\phi U$	1,3,5...	1,3,5...
	z		ϕU	2,6,10..	0,4,8,...
E	2	1,2	W	0,4,8...	2,6,10..
	1	1,2	$-(-1)^J W$	2,6,10..	4,8,12..
A1	-	2	W	0,4,8...	2,6,10..
A2	-	1	$-W$	2,6,10..	4,8,12..

$$\phi \quad = \quad -i \quad \text{if J is even}$$

$$\phi \quad = \quad i \quad \text{if J is odd}$$

$$W(J,K,m_J) \quad = \quad \left(1 + \delta(K,0)\right)^{-\frac{1}{2}} \left(\frac{2J+1}{16\pi^2}\right)^{\frac{1}{2}} \left(D^J_{m_J,K} + (-1)^J D^J_{m_J,-K}\right)^*$$

$$U(J,K,m_J) \quad = \quad \left(1 + \delta(K,0)\right)^{-\frac{1}{2}} \left(\frac{2J+1}{16\pi^2}\right)^{\frac{1}{2}} \left(D^J_{m_J K} - (-1)^J D^J_{m_J,-K}\right)^*$$

the centrifugal distortion Hamiltonian and can only be computed numerically.
The computer programme which generates the A-constants was provided by
Irving Ozier of the U.B.C. Physics Department. This programme also gives
the energy eigenvalues of the rotational functions. These centrifugal
distortion energies have the $BJ(J + 1)$ subtracted off and thus are both
positive and negative (see Figure 3.1). Thus the ω_R in equation 3.3.2
should now be written

$$\omega_R \quad = \quad \omega(J,\gamma,t,\rho) \tag{3.4.3}$$

3.4.3 TOTAL WAVEFUNCTIONS

We have only to contract the spin and rotational wavefunctions to
obtain the total wavefunctions. In general, this gives

$$\Psi(I,m_I;\beta:J,m_J;\gamma,t,\rho) \quad = \quad \underset{\zeta}{\Sigma} \underset{\xi}{\Sigma} \, B(\beta\zeta;\gamma\xi;\rho)\chi(\beta,\zeta;I,m_I)R(\gamma\xi;J,m_J;t,\rho) \tag{3.4.4}$$

It should be noted that for a given $\gamma\rho$, the normalization constants
$B(\beta\zeta;\gamma\xi;\rho)$ can be expressed as δ-functions in ζ and ξ with the result that the
expression of Ψ simplifies considerably. The values of $B(\beta\zeta;\gamma\xi;\rho)$ are
given in Table 3.3 (113) and can be obtained by normalizing Ψ. We note
from Table 3.1 that there is a 1-1 correspondence between I and β and thus
we need not specify both in Ψ. (Note that this is not true for CD_4 (33).)

TABLE 3.3   NORMALIZATION CONSTANTS $B(\beta,\zeta;\gamma,\xi;\rho)$

β	γ	ρ	B
A1	A1	2	$\delta(\zeta,\xi)$
A1	A2	1	$-\delta(\zeta,\xi)$
F2	F1	1	$\sqrt{3}/3\,\delta(\zeta,\xi)$
F2	F2	2	$\sqrt{3}/3\,\delta(\zeta,\xi)$
E	E	1	$(-1)^{\xi}\sqrt{2}/2[-1 + \delta(\zeta,\xi)]$
E	E	2	$\sqrt{2}/2\,\delta(\zeta,\xi)$

TABLE 3.4   POSSIBLE COMBINATIONS OF I, β, γ, ρ
IN $\Psi(I,m_I;J,m_J;\gamma, t, \rho)$

I	β	γ	ρ
2	A1	A1	2
2	A1	A2	1
1	F2	F1	1
1	F2	F2	2
0	E	E	2
0	E	E	1

The fact that the basis we are using includes the centrifugal distor-
tion Hamiltonian means that there are no degeneracies in a magnetic
field. We are excluding possible degeneracies in ρ. This will not affect
any perturbation calculation because ρ is conserved in matrix elements of
the spin-rotation Hamiltonian. We are also excluding the possibility of level
crossings, the existence of which have important consequences for some ex-
periments at carefully chosen magnetic fields (41). For a particular
value of J, the centrifugal distortion states are labelled by $\gamma t \rho$. Further,
for a given $\gamma \rho$, I is uniquely determined. It is, in fact, the presence of
the distortion operator in the rotational Hamiltonian which make I a "good"
quantum number.

Knowing that the total wavefunctions Ψ must be antisymmetric
(Fermi-Dirac Statistics) we can say that the representation product $\gamma \otimes \beta \otimes i$
must contain the antisymmetric one dimensional representation of T_d, namely
A2. The products $\gamma \otimes \beta$ are contained in Table III of reference (59) and the
product $(\otimes i)$ is trivial. The possible combinations of indices that result
from such a process are listed in Table 3.4.

As an example of the energy level diagram resulting from the
computation of the wavefunctions and their energies (eigenvalues), the J = 12
levels are given to scale in Figure 3.1. We choose J = 12 because it can be
compared with the identical Figure 1 of reference (42) where the observation
of the E $\leftrightarrow$ E transition ($\sim$ 10 Ghz) was reported. It should be noticed that
the transition frequencies resulting from a change of centrifugal distortion
state cover a very wide range. The spacing of the bottom three levels for
instance give rise to frequencies of tens of MHz whereas there are, in the
same J = 12 manifold, centrifugal distortion frequencies in the range of 10 GHz.

I	γ	t	ρ	E(GHz)
2	A1	2	2	6.62
1	F1	3	1	6.25
1	F2	3	2	5.78
2	A2	1	1	4.95
1	F2	2	2	2.55
0	E	2	1,2	2.10
				0
1	F1	2	1	-1.23
1	F2	1	2	-1.75
0	E	1	1,2	-8.40
1	F1	1	1	-8.43
2	A1	1	2	-8.48

J = 12
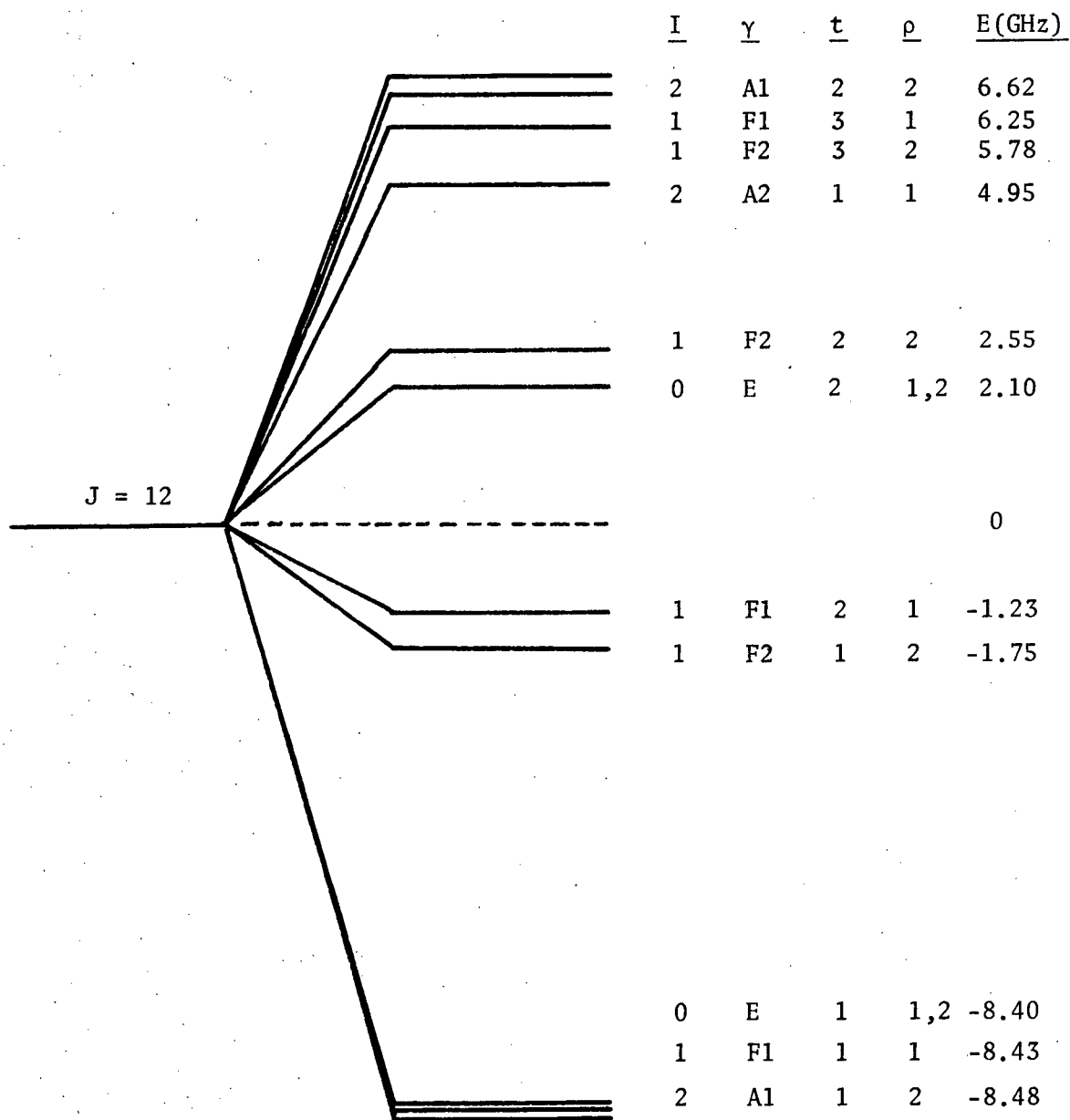
Figure 3.1. The rotational energy level diagram of the J = 12 state of methane. The group theoretical indices $\gamma t \rho$ which label each centrifugal distortion state are discussed extensively in Chapter III. The diagram is to scale and the energies have the rotational energy B(J)(J + 1) subtracted off. The total nuclear spin of a molecule in each rotational state is indicated by I. This diagram is equivalent to Figure 1 in reference (42).

The energy level diagram for J between zero and 5 is given in reference (25) but not to scale. The $(2J + 1)(2I + 1)$ degeneracy of the levels in Figure 3.1 is removed in a magnetic field.

3.5 SPIN ROTATION-INTERACTION

The spin-rotation interaction for an isolated CH_4 molecule is

$$H_{sr} = - h \sum_{S=1}^{4} \bar{I}_S \cdot \bar{\bar{C}}_S \cdot \bar{J} \tag{3.5.1}$$

where the sum is over the 4 spin ½ protons. A single bar denotes a vector and a double bar denotes a tensor. The local field experienced by the Sth proton is $\bar{H}_S \sim \bar{\bar{C}}_S \cdot \bar{J}$. If one chooses the $C-H_1$ bond as the z axis, then (59),

$$\bar{\bar{C}}_1 = \begin{pmatrix} C_\alpha & 0 & 0 \\ 0 & C_\alpha & 0 \\ 0 & 0 & C_\beta \end{pmatrix} \tag{3.5.2}$$

which simply says that the x and y directions are equivalent. By rotating the molecule and bringing the other 3 P_S into the position previously held by P_1, one can determine the other 3 $\bar{\bar{C}}_S$.

Equation 3.5.1 is then transformed into a coordinate system where all 4 protons are on equivalent sites. This corresponds to the xyz axes coming out of cube faces and the protons situated at diagonally opposite corners of the cube (33). Performing this operation on the $\bar{\bar{C}}_S$, one has, in the new molecular reference frame:

$$\bar{\bar{C}}_S = C_\alpha \bar{\bar{E}} + \frac{1}{3} C_d \bar{\bar{\epsilon}}_S \tag{3.5.3}$$

$$C_a = \tfrac{2}{3}C_\alpha + \tfrac{1}{3}C_\beta \qquad\qquad\qquad (3.5.4)$$

$$C_d = C_\alpha - C_\beta$$

$\overline{\overline{E}}$ is the unit matrix and the $\overline{\overline{\epsilon}}_S$ contain +1's or -1's in all the off-diagonal places and zeroes on the diagonal. These matrices, as well as careful definitions of the molecular fixed reference frames (MFF), appear in the literature (33, 59[1]). Substituting equation 3.5.3 into 3.5.1 gives

$$H_{sr} = -hC_a\{\sum_{S=1}^{4}\overline{I}_S\}\cdot\overline{J} - \tfrac{1}{3}hC_d\sum_{S=1}^{4}\overline{I}_S\cdot\overline{\overline{\epsilon}}_S\cdot\overline{J} \qquad\qquad (3.5.5)$$

The first term in equation 3.5.5 is simply $\overline{I}\cdot\overline{J}$ where $\overline{I}$ is the total nuclear spin operator. This is the scalar, or average, or isotropic part of the interaction. The second term is the tensor or anisotropic interaction.

Equation 3.5.5 is cast into a form in which all the operators are invariant under the operations of T_d.

$$H_{sr} = -hC_a\overline{I}^{A1}\cdot\overline{J}^{A1} - \tfrac{1}{3}hC_d\sum_{i=xyz}\overline{I}_i^{F2}\cdot\overline{\overline{\epsilon}}_i^{F2}\cdot\overline{J}^{A1} \qquad\qquad (3.5.6)$$

---

where the superscripts refer to the irreducible representations of T_d and the subscripts to the components. The x, y and z are simply convenient labels because they indicate the symmetry axis in each case. The $\bar{I}_i^{F2}$ and $\overline{\overline{\varepsilon}}_i^{F2}$ are given in reference (33) as is the necessary algebra and group theory in going from equation 3.5.5 to equation 3.5.6.

For convenience, equation 3.5.6 is cast into spherical tensor form. In general

$$H_{sr} = \sum_{\gamma} \sum_{\xi} \sum_{\mu=-\omega}^{+\omega} (-1)^{\omega} \{f(\bar{I})\}_{\omega\mu}^{\gamma\xi} \{g(\bar{J})\}_{\omega,-\mu}^{\gamma\xi} \qquad (3.5.7)$$

where, for instance, $\{f(\bar{I})\}_{\omega\mu}^{\gamma\xi}$ is the μth component of a tensor of rank ω formed from $f(\bar{I})$. It transforms according to the ξ component of the γ representation of T_d.

One now equates 3.5.6 and 3.5.7 (33) to obtain

$$H_{sr} = H_{sr}^{S} + H_{sr}^{T} \qquad (3.5.8)$$

$$H_{sr}^{S} = \sqrt{3} \, hC_a \, [\bar{I}^{A1}, \bar{J}^{A1}]_{00} \qquad (3.5.9)$$

$$H^T_{sr} = -\frac{1}{3}hC_d \sum_{\xi} \sum_{\mu=-2}^{+2} (-1)^{\mu} C^{F2,\xi}_{2,-\mu} [\bar{I}^{F2,\xi} \bar{J}^{A1}]_{2,\mu} \qquad (3.5.10)$$

where $[\bar{I}^{\gamma\xi}\bar{J}^{A1}]_{\ell\mu}$ is the μth component of a tensor of rank ℓ formed from the components of $\bar{I}^{\gamma\xi}$ and $\bar{J}^{A1}$. The $C^{F2,\xi}_{2,-\mu}$ (33) are numerical constants and are given in Table 3.5. Before defining these tensors we transform from the MFF to the SFF (space fixed frame) because the wavefunctions of the previous Section are given in the SFF.

$$[\bar{I}^{\gamma\xi},\bar{J}^{A1}]'_{\ell\mu} = \sum_{\mu'} D^{\ell}_{\mu'\mu} [\bar{I}^{\gamma\xi},\bar{J}^{A1}]_{\ell,\mu'} \qquad (3.5.11)$$

The D's are the transformation matrices of the full-rotation group and are functions of the Euler angles as are the D's in the primitive functions in Table 3.2. The transformation does not affect the scalar interaction H^S_{sr} and from equations 3.5.9 to 3.5.11 we have

$$H^S_{sr} = \sqrt{3} \, hC_a \, \theta^S_{sr} \qquad (3.5.12)$$

$$H^T_{sr} = -\frac{1}{3}hC_d \, \theta^T_{sr} \qquad (3.5.13)$$

TABLE 3.5   VALUES OF $C_{2,-\mu}^{F2,\xi}$

ξ $\quad$ $-\mu$	2	1	0	-1	-2
x	0	-i	0	-i	0
y	0	-1	0	1	0
z	i	0	0	0	-i

TABLE 3.6 $\bar{I}^{\gamma\xi}$

γ	ξ	$\bar{I}^{\gamma\xi}$
A1		$\bar{I}^{(1)} + \bar{I}^{(2)} + \bar{I}^{(3)} + \bar{I}^{(4)}$
F2	x	$\bar{I}^{(1)} - \bar{I}^{(2)} + \bar{I}^{(3)} - \bar{I}^{(4)}$
F2	y	$-\bar{I}^{(1)} + \bar{I}^{(2)} + \bar{I}^{(3)} - \bar{I}^{(4)}$
F2	z	$\bar{I}^{(1)} + \bar{I}^{(2)} - \bar{I}^{(3)} - \bar{I}^{(4)}$

$\bar{I}^{(i)}$ is the normal nuclear spin operator for the ith proton, (i = 1, 2, 3, 4)

$$\theta^S_{sr} = [\bar{I}^{A1}, \bar{J}^{A1}]_{0,0} \tag{3.5.14}$$

$$\theta^T_{sr} = \sum_\xi \sum_\mu \sum_{\mu'} (-1)^\mu C^{F2,\xi}_{2,-\mu} \; D^2_{\mu'\mu} [\bar{I}^{F2,\xi}, \bar{J}^{A1}]_{2,\mu} \tag{3.5.15}$$

where the contracted tensors are given by

$$[\bar{I}^{\gamma\xi}, \bar{J}^{A1}]_{\ell,\mu'} = \sum_{\nu=1}^{+1} C(1,1,\ell;\nu,\mu'-\nu,\mu') \bar{I}^{\gamma,\xi}_{1,\nu} \bar{J}^{A1}_{1,\mu'-\nu} \tag{3.5.16}$$

$I^{\gamma\xi}_{1,\nu}$ is the ν component of a spherical tensor of rank 1 (i.e., a vector) which transforms according to the ξ component of the γ representation of T_d. The $J^{A1}_{1,\mu'-\nu}$ are simply the normal $\bar{J}$ operators in spherical tensor form (A1 is the 1-dimensional representation). The $\bar{I}^{\gamma\xi}$ are given in Table 3.6 which is taken directly from reference (33).

In order to calculate matrix elements of H_{sr} it is convenient to perform one more transformation. We rewrite equation 3.5.14 and 3.5.15 as

$$\theta^S_{sr} = \sum_\nu I^{A1}_{1,\nu} H^{A1}_{1,-\nu} \tag{3.5.17}$$

$$\theta_{sr}^{T} = \sum_{\xi} \sum_{\nu} (-1)^{\nu} I_{1,\nu}^{F2\xi} B_{1,-\nu}^{F2\xi} \qquad (3.5.18)$$

where

$$H_{1,\nu}^{A1} = C(1, 1, 0; \nu, -\nu) J_{1,-\nu}^{A1} \qquad (3.5.19)$$

and the $B_{1,-\nu}^{F2\xi}$ are given in Table 3.7 which is taken directly from reference (117)[1].

The final form of H_{sr} is given by equation 3.5.8, 3.5.12, 3.5.13, 3.5.17, 3.5.18, 3.5.19 and Tables 3.5, 3.6 and 3.7. The outline presented here is very compact because the calculations appear in the literature. We reproduce the various functions and tables mainly for convenience but also because of slight changes in notation. We have, wherever possible, retained the same notation as in references (33) and (117). The results quoted in this Section have been independently computed and the results are in agreement with the (corrected (113)) computations of references (33) and (117).

---

[1] The expression for $B_{1,0}^{T\eta}$ on page 68 of reference (117) contains a $\sqrt{3}/\sqrt{2}$. It should be $\sqrt{2}/\sqrt{3}$. (113)

$$\text{TABLE 3.7} \quad B_{1,-\nu}^{F2,\xi}$$

$$B_{1,1}^{F2,\xi} = -\sum_{\mu} (-1)^{\mu} C_{2,-\mu}^{F2,\xi} \left(\frac{\sqrt{6}}{6} D_{0\mu}^{2} J_{+1} + \frac{\sqrt{2}}{2} D_{-1\mu}^{2} J_{0} + D_{-2\mu}^{2} J_{-1} \right)$$

$$B_{1,0}^{F2,\xi} = \sum_{\mu} (-1)^{\mu} C_{2,-\mu}^{F2,\xi} \left(\frac{\sqrt{2}}{2} D_{1\mu}^{2} J_{+1} + \frac{\sqrt{6}}{3} D_{0\mu}^{2} J_{0} + \frac{\sqrt{2}}{2} D_{-1\mu}^{2} J_{-1} \right)$$

$$B_{1,-1}^{F2,\xi} = -\sum_{\mu} (-1)^{\mu} C_{2,-\mu}^{F2,\xi} \left(D_{2\mu}^{2} J_{+1} + \frac{\sqrt{2}}{2} D_{1\mu}^{2} J_{0} + \frac{\sqrt{6}}{6} D_{0\mu}^{2} J_{-1} \right)$$

TABLE 3.8   ALLOWED TRANSITIONS

Coupling Constant	I'	β'	γ'	ρ	I	β	γ
C_a	2	A1	A1	2	2	A1	A1
C_a	2	A1	A2	1	2	A1	A2
C_a, C_d	1	F2	F2	2	1	F2	F2
C_a, C_d	1	F2	F1	1	1	F2	F1
C_d	2	A1	A1	2	1	F2	F2
C_d	2	A1	A2	1	1	F2	F1
C_d	1	F2	F2	2	0	E	E
C_d	1	F2	F1	1	0	E	E

$C_a = 10.4 \pm 0.1$ kHz; $C_d = 18.5 \pm 0.5$ kHz (32)

3.6 NOTATION

The notation involving the irreducible representations, their components and the parity index ρ can be confusing mainly because of the different conventions adopted in the literature. It has been pointed out (118) that there are three main notation schemes presently being used. The convention adopted here is originally due to Jahn (38).

T and F are both used to denote the three-dimensional representations of the group T_d. We have adopted F so as to not confuse it with the temperature T and the longitudinal and transverse nuclear spin relaxation times T_1 and T_2.

Whereas the three-dimensional spin functions transform only according to the F2 representation, the rotational wavefunctions transform according to F1 or F2. We are able to label the rotational wavefunctions by F because of the one to one relationship between the representation and ρ. Thus for $\rho = 1$, F uniquely implies F1 and for $\rho = 2$, F uniquely implies F2 (see Table 3.4). The same holds for the rotational wavefunctions that transform according to the A representation, only in this case for $\rho = 1$, A uniquely implies A2 and, for $\rho = 2$, A uniquely implies A1. The one-dimensional spin functions transform only according to A1 and not A2. It should be noted the numbers 1 and 2 following A and F have different meanings in the different notations systems. These differences have been pointed out and are discussed in the literature (37, 118, 120).

The E representations of T_d is the seat of most of the confusion. In general, the components of a representation γ will be labelled by ξ or ζ. Thus the notation Fξ implies Fx, Fy or Fz. However, when referring specifi-

cally to the E representation, we will label the components by σ instead of ξ or ζ. Thus E,σ implies E,1 or E,2. The reader is cautioned against confusing, for instance, F1 which refers to the F1 representation with no component given with E,1 which is the $\sigma = 1$ component of the E representation. This is clarified if F1 is written F_1 which it usually is. In writing F1 we are simply appeasing the typist. The rotational wavefunctions that transform according to the E representation have either $\rho = 1$ or $\rho = 2$ associated with them. The confusion arises because it can be convenient to label the components of E by ρ instead of σ. In this thesis, this is not done and ρ will have the same meaning for the E representation as it does in the A and F representations. The result is that when E and σ are specified, ρ will be superfluous, but nevertheless included. As a result, it is noted that the E-type primitive rotation functions in Table 3.2 are independent of ρ. However, in Table II of reference (121) (or the identical Table IV of reference (115)),it is noted that these functions depend on ρ. This is because $\rho = 1$ in these Tables is equivilent to $\sigma = 2$ here and $\rho = 2$ in these tables is equivalent to $\sigma = 1$. This point is made clear in equation (54) of Section C in reference (121) where the E-type functions are given explicitly. This notation problem is discussed further in footnote 32 of reference (115) where it is pointed out that $\sigma = 1$ and 2 are often called f and e respectively.

The confusion over the labelling of the E representation comes to a head at this time because until now the $I = 0 \leftrightarrow I = 1$ (E $\leftrightarrow$ F) matrix elements of the tensor spin-rotation interaction have not been calculated.

Finally, we note that Hougen has written a recent review article titled a "Catalog of Explicit Symmetry Operations for the Vibrational, Rotational and Nuclear Spin Functions of Methane, and the Use of These Operations in Determining Symmetry Labels and Selection Rules". (37)

3.7 SPIN-ROTATION MATRIX ELEMENTS

In calculating the matrix elements $\langle S'R'|H_{sr}|SR\rangle$ we first note that the spin-rotation interaction conserves the parity index ρ as we have chosen it (33). Also, we are only concerned with matrix elements diagonal in J. (i.e., $\Delta J = 0$). The transition probabilities $W_{R'S'RS}$ with $\Delta J \neq 0$ are extremely small because the frequencies $\omega_{R'} - \omega_R$ are in the infrared as discussed in the introduction. That is to say the rotational lines described by $j(\omega_{R'S'RS})$ are extremely small because of the denominator in equation 3.3.16. It should be pointed out that we are not excluding the possibility that J can change because of collisions. This effect is incorporated in the reduced correlation function in equation 3.3.14.

The required matrix elements will be of the form $L(\gamma)O^{\gamma'}M(\gamma'')$ where the functions L and M involve spin and rotation functions and O the spin-rotation Hamiltonian. The γ's refer to the irreducible representation. Because a matrix element is a scalar it must transform according to the totally symmetric A1 representation. This implies that the representation product $\gamma \otimes \gamma' \otimes \gamma''$ must contain A1 or equivalently $\gamma \otimes \gamma'$ must contain γ''. For a given I' and I, β' and β are uniquely determined and by using the representation product rules it is easily determined which sets of matrix elements must be calculated. These are listed in Table 3.8.

For convenience the matrix elements of the spin-rotation interaction will be written using the following notation.

$$\langle H_{sr}(I' \to I)\rangle \quad = \quad \langle S'R'|H_{sr}|SR\rangle \tag{3.7.1}$$

3.7.1   SCALAR MATRIX ELEMENTS

From equations 3.4.4, 3.5.12, 3.5.17 and 3.5.19 the scalar spin-rotation matrix elements are,

$$\langle H^S_{sr}(I' \to I) \rangle = [\sum_{\zeta'\xi'} \sum B^*(\beta',\zeta';\gamma',\xi',\rho)X^*(\beta',\zeta';I',m'_I)R^*(\gamma',\xi';$$

$$J,m'_J;t',\rho)] [\sqrt{3}C_\alpha h \sum_\nu C(1,1,0;\nu,-\nu,0) I^{A1}_{1,\nu} J^{A1}_{1,-\nu}]$$

$$[\sum_{\zeta\xi} B(\beta,\zeta;\gamma,\xi;\rho)X(\beta,\zeta;I,m_I)R(\gamma,\xi;J,m_J;t,\rho)] \quad (3.7.2)$$

Because both operators transform according to A1, $\beta' = \beta$ which implies that $I' = I$ and $\gamma' = \gamma$. Table 3.3 indicates that $\xi' = \zeta'$ and $\xi = \zeta$ because we are not concerned with the E (I = 0) representation. Equation 3.7.2 becomes

$$\langle H^S_{sr}(I' \to I) \rangle \propto \sum_{\xi'\xi} \sum_\nu \sum B'B\{X'IX\}\{R'JR\} \quad (3.7.3)$$

Equations such as equation 3.7.3, where all the indices and quantum numbers have been omitted, will be used frequently for obvious reasons. These equations are only meaningful on inspection of a preceding equation. There are two types of matrix elements, namely $I = 1 \to I = 1$ and $I = 2 \to I = 2$. The only non-zero matrix elements occur for $\xi' = \xi$. There is one term for $\beta = A1$ and 3 equal terms for $\beta = F2$. Thus equation 3.7.3 becomes

$$\langle H^S_{sr}(I \to I) \rangle \propto n(\beta) \sum_\nu B'B\{X'IX\}\{R'JR\} \quad (3.7.4)$$

where $n(\beta)$ is the dimensionality of β which appears in X. Equation 3.7.4 is written explicitly in Appendix B where the computation is performed by calculating the X'IX and R'JR and summing over ν.

The results from Appendix B are

$$\langle H^S_{sr}(2 \to 2)\rangle \quad = \quad -hC_a[\Gamma(J,m'_J,m_J;2,m'_I,m_I)]\delta(t',t) \qquad (3.7.5)$$

$$\langle H^S_{sr}(1 \to 1)\rangle \quad = \quad -hC_a[\Lambda(J,m'_J,m_J;1,m'_I,m_I)]\delta(t',t) \qquad (3.7.6)$$

with Γ and Λ given by

$$\Gamma(J,m'_J,m_J;2,m'_I,m_I) \quad = \quad \frac{1}{2}[(2-m_I)(3+m_I)]^{\frac{1}{2}}L_+(J,m_J)\delta(m'_I,m_I+1)\delta(m'_J,m_J-1)$$

$$+ \quad m_I L_0(J,m_J)\ \delta(m'_I,m_I)\ \delta(m'_J,m_J)$$

$$+ \quad \frac{1}{2}[(2+m_I)(3-m_I)]^{\frac{1}{2}}L_-(J,m_J)\delta(m'_I,m_I-1)\delta(m'_J,m_J+1)$$

$$(3.7.7)$$

$$\Lambda(J,m'_J,m_J;1,m'_I,m_I) \quad = \quad \frac{\sqrt{2}}{2}L_+(J,m_J)\ \delta(m'_J,m_J-1)\ \delta(m'_I,m_I+1)$$

$$+ \quad m_I L_0(J,m_J)\ \delta(m'_J,m_J)\ \delta(m'_I,m_I)$$

$$+ \quad \frac{\sqrt{2}}{2}L_-(J,m_J)\ \delta(m'_J,m_J+1)\ \delta(m'_I,m_I-1) \qquad (3.7.8)$$

with the L functions given by

$$L_+(J,m_J) \quad = \quad [(J+m_J)(J-m_J+1)]^{\frac{1}{2}}$$

$$L_0(J,m_J) \quad = \quad m_J$$

$$L_-(J,m_J) \quad = \quad [(J-m_J)(J+m_J+1)]^{\frac{1}{2}} \qquad (3.7.9)$$

As expected for an $\bar{I} \cdot \bar{J}$ interaction, these matrix elements are diagonal in all the magnetic field independent quantum numbers. This interaction cannot connect different distortion states and leads therefore to $\Delta I = 0$. In fact, were it not for the matrix elements of the tensor interaction, finding the wavefunctions in a basis which is diagonal in the distortion Hamiltonian would have been unnecessary. The value of C_a is 10.4 ± 0.1 kHz(32).

3.7.2 TENSOR MATRIX ELEMENTS

Using equations 3.4.4, 3.5.13 and 3.5.18 and grouping the spin and rotational parts, the tensor spin-rotation matrix elements are

$$\langle H^S_{sr}(I' \to I) = -\frac{1}{3} h C_d \sum_{\varsigma' \varsigma \xi' \xi \eta \nu} \sum \sum \sum \sum (-1)^\nu [B^*(\beta', \varsigma'; \gamma', \xi'; \rho) B(\beta, \varsigma; \gamma, \xi; \rho)] \quad x$$

$$[X^*(\beta', \varsigma'; I', m'_I) I^{F2, \eta}_{1, \nu} X(\beta, \varsigma; I, m_I)] \quad x$$

$$[R^*(\gamma', \xi'; J, m'_J; t', \rho) B^{F2, \eta}_{1, -\nu} R(\gamma, \xi; J, m_J; t, \rho)] \quad (3.7.10)$$

There are 3 types of transitions with respect to $I' \to I$: $1 \to 1$, $1 \to 2$ and $0 \to 1$. In particular, we note that there are no matrix elements of the type $2 \to 2$ for the tensor spin-rotation interaction. The calculation of the spin matrix elements are not difficult but considering the form of $B^{F2, \eta}_{1, -\nu}$ (Table 3.7) and R (equation 3.4.2 and Table 3.2) the calculation of the rotational matrix elements could be extremely complicated. It is worth considerable effort in choosing parameters such that only one rotational matrix element need be calculated. This in fact can be done and the procedure is outlined in Appendix C. The results for the 3 types can be conveniently expressed by,

$$\langle H^T_{sr}(1 \to 1)\rangle = - \frac{1}{3}hC_d \sum_{\nu K'K}^{\Sigma\Sigma'\Sigma'} (-1)^{\nu}[V(F,x,K',t';F,z,K,t;J,\rho)] \quad x$$

$$[\chi^*(F2,x;1,m'_I) \, I^{F2,y}_{1,\nu} \chi(F2,z;1,m_I)] \quad x$$

$$[W^*(J,m'_J,K') \, B^{F2,y}_{1,-\nu} \, U(J,m_J,K)] \qquad (3.7.11)$$

$$\langle H^T_{sr}(2 \to 1)\rangle = - \frac{1}{3}hC_d \sum_{\nu K'K}^{\Sigma\Sigma'\Sigma'} (-1)^{\nu}[V(A,K',t';F,y,K,t;J,\rho)] \quad x$$

$$[\chi^*(A;2,m'_I) \, I^{F2,y}_{1,\nu} \, \chi(F2,y;1,m_I)] \quad x$$

$$[W^*(J,m'_J,K') \, B^{F2,y}_{1,-\nu} \, U(J,m_J,K)] \qquad (3.7.12)$$

$$\langle H^T_{sr}(0 \to 1)\rangle = - \frac{1}{3}hC_d \sum_{\nu}\sum_{K'K}^{\Sigma'\Sigma'}(-1)^{\nu}[V(E,1,K',t';F,y,K,t;J,\rho)] \quad x$$

$$[\chi^*(E,1;0,0) \, I^{F2,y}_{1,\nu} \, \chi(F2,y;1,m_I)] \quad x$$

$$[W^*(J,m'_J,K') \, B^{F2,y}_{1,-\nu} \, U(J,m_J,K)] \qquad (3.7.13)$$

where $C_d = 18.5 \pm 0.5$ kHz (32), and

$$V(\gamma',\xi',K',t';\gamma,\xi,K,t;J,\rho) = a(\gamma',\gamma;\rho) \, B^*(\gamma') \, B(\gamma)$$

$$A^*(\gamma',\xi';J,K';t',\rho) \, A(\gamma,\xi;J,K;t,\rho) \quad (3.7.14)$$

where $B(A) = 1$, $B(F) = \sqrt{3}/3$ and $B(E) = \sqrt{2}/2$.

The $a(\gamma',\gamma;\rho)$ are normalizations made necessary by the fact that all three

sets of V- functions have been cast into a general form. They are:

$$a\,(F,F;\rho) \quad = \quad 6\,\phi^{*}\,\phi$$

$$a\,(A,F;\rho) \quad = \quad 3\,\{(-1)^{\rho}\}^{*}\{-i\phi\} \tag{3.7.15}$$

$$a\,(E,F;\rho) \quad = \quad 12\,(1)^{*}(-i\phi)\,[\delta(\rho,2) + \frac{1}{\sqrt{3}}\,\delta(\rho,1)]$$

In equations 3.7.15, $\phi^{*}\,\phi = 1$ (see Table 3.2). Also, the complex congugates are not required, but we leave them in order that their source may be identified.

In going from equation 3.7.10 to equations 3.7.11, 3.7.12 and 3.7.13, (Appendix C) the rotational functions have been written out explicitly using equation 3.4.2 and Table 3.2. It has been designed such that the matrix element R'BR, involves R' $\sim$ A'P' $\sim$ A'W' and R $\sim$ AP $\sim$ AU with the result that the matrix element W'BU (and not U'BW) occurs in each of equations 3.7.11, 3.7.12 and 3.7.13. The A- constants are contained in the V- functions as indicated in equation 3.7.14. The primes over the sums on K' and K mean that K' and K are restricted as indicated in Table 3.2

The spin matrix elements are calculated in a straightforward manner as outlined in Appendix D. The spin matrix element in equations 3.7.11, 3.7.12 and 3.7.13 are

$$\{\chi'(1)I\,\chi(1)\} \quad = \quad \sqrt{6}\,(-1)^{1-m'_{I}}\begin{pmatrix} 1 & 1 & 1 \\ -m'_{I} & \nu & m_{I} \end{pmatrix} \tag{3.7.16}$$

$$\{\chi'(2)I\,\chi(1)\} \quad = \quad \sqrt{10}\,(-1)^{2-m'_{I}}\begin{pmatrix} 2 & 1 & 1 \\ -m'_{I} & \nu & m_{I} \end{pmatrix} \tag{3.7.17}$$

$$\{\chi'(0)I\,\chi(1)\} \quad = \quad -\sqrt{2}\,(-1)^{0-0}\begin{pmatrix} 0 & 1 & 1 \\ 0 & \nu & m_{I} \end{pmatrix} \tag{3.7.18}$$

The single rotational matrix element can be expressed as in the case of the spin matrix elements, via the Wigner-Eckart Theorem. This is done in Appendix E where the lengthy calculation of the reduced matrix element is outlined. The result, from Appendix E, is

$$W^{*}(J,K',m_J')B_{1,-\nu}^{F2,y} U(J,K,m_J) = \frac{1}{2}(-1)^{J-m_J'} \{\frac{(2J+1)}{J(J+1)}\}^{\frac{1}{2}} \begin{pmatrix} J & 1 & J \\ -m_J' & -\nu & m_J \end{pmatrix} Q(J,K',K)$$

$$(3.7.19)$$

where $Q(J,K',K)$ is given by

$$Q(J,K',K) = [\{1+\delta(K',0)\}\{1+\delta(K,0)\}]^{-\frac{1}{2}} [(1+2K)\{(J+K+1)(J-K)\}^{\frac{1}{2}} \quad x$$

$$\delta(K',K+1) - (1-2K) \{(J-K+1)(J+K)\}^{\frac{1}{2}} \quad x$$

$$\{\delta(K',K-1) + (-1)^{J} \delta(K',1-K)\}] \qquad (3.7.20)$$

Equations 3.7.16 and 3.7.19 are substituted into equation 3.7.11 to give $<H_{sr}^{T}(1-1)>$. Equations 3.7.17 and 3.7.19 are substituted into equation 3.7.12 to give $<H_{sr}^{T}(2 \rightarrow 1)>$ and equations 3.7.18 and 3.7.19 are substituted into equation 3.7.13 to give $<H_{sr}^{T}(0 \rightarrow 1)>$. This results in sums over ν of products of 3-j symbols, one from the spin matrix element and one from the rotational matrix element. These sums are all of the form

$$\sum_{\nu} (-1)^{\nu} \begin{pmatrix} J & 1 & J \\ -m_J' & -\nu & m_J \end{pmatrix} \begin{pmatrix} I' & 1 & 1 \\ -m_I' & \nu & m_I \end{pmatrix} \qquad (3.7.21)$$

where $I' = 0$, 1 or 2. Because the second row of the 3-j symbol must add to zero, the 3-j symbols can be written in terms of a 3-j symbol involving

the unprimed quantities only, multiplied by a δ-function in m' and m as indicated for a different part of the problem in equation E.12. This calculation is not outlined because in principle it is straightforward even though, in practice, it is very lengthy. The resulting expressions for $\langle H^T_{sr}(I' \rightarrow I)\rangle$ can be conveniently divided into two parts; one part involving the magnetic field dependent quantum numbers (and J) and the other part the remaining quantum number and group theoretical indicies.

Thus, equations 3.7.11, 3.7.12 and 3.7.13 in their final form become

$$\langle H^T_{sr}(1 \rightarrow 1)\rangle = -\tfrac{1}{3}hC_d[\Lambda(J,m'_J,m_J;1,m'_I,m_I)][\Pi(F;F;J,t',t,\rho)] \qquad (3.7.22)$$

$$\langle H^T_{sr}(2 \rightarrow 1)\rangle = -\tfrac{1}{3}hC_d[\Omega(J,m'_J,m_J;2,m'_{I'},m_I)][\Pi(A;F;J,t',t,\rho)] \qquad (3.7.23)$$

$$\langle H^T_{sr}(0 \rightarrow 1)\rangle = -\tfrac{1}{3}hC_d[\theta(J,m'_J,m_J;0,\ 0,m_I)][\Pi(E;F;J,t',t,\rho)] \qquad (3.7.24)$$

The function Λ in equation 3.7.22 is the same function required in the scalar $I = 1 \rightarrow I = 1$ matrix element and is given in equation 3.7.8. The functions Ω and θ in equations 3.7.23 and 3.7.24 are as follows.

$$\Omega(J,m'_J,m_J;m'_{I'},m_I) = -\tfrac{1}{2}[(3+m_I)(2+m_I)]^{\frac{1}{2}}L_+(J,m_J)\delta(m'_J,m_J-1)\delta(m'_{I'},m_I+1)$$

$$+ [(2+m_I)(2-m_I)]^{\frac{1}{2}}L_0(J,m_J)\delta(m'_J,m_J)\delta(m'_{I'},m_I)$$

$$+ \tfrac{1}{2}[(3-m_I)(2-m_I)]^{\frac{1}{2}}L_-(J,m_J)\delta(m'_J,m_J+1)\delta(m'_{I'},m_I-1)$$

$$(3.7.25)$$

$$\theta(J,m_J',m_J;0,m_I) \quad = \quad \frac{1}{\sqrt{2}} L_+(J,m_J)\delta(m_J',m_J-1)\delta(m_I,-1)$$

$$+ \quad L_0(J,m_J)\delta(m_J',m_J)\delta(m_I,0)$$

$$- \frac{1}{\sqrt{2}} L_-(J,m_J)\delta(m_J',m_J+1)\delta(m_I,+1) \qquad (3.7.26)$$

The L-functions have been previously used and are given in equations 3.7.9. The V-functions of equations 3.7.11 to 3.7.13 are now incorporated in the Π-functions. The latter are given by

$$\Pi(\gamma';\gamma;J,t',t,\rho) \quad = \quad b(\gamma',\gamma)[J(J+1)]^{-1}$$

$$\sum_{K'K}'\sum V(\gamma',\xi',K',t';\gamma,\xi,K,t;J,\rho) \; Q(J,K',K) \qquad (3.7.27)$$

where $Q(J,K',K)$ is defined in equation 3.7.20 . The $b(\gamma',\gamma)$ are normalizations made necessary by virtue of the fact that all three sets of Π-functions are given in a general form.

$$b(F,F) \quad = \quad \frac{1}{2}; \quad b(A,F) \quad = \quad \frac{\sqrt{3}}{6}; \quad b(E,F) \quad = \quad \frac{\sqrt{6}}{6} \qquad (3.7.28)$$

The components of the representations need not be specified in Π because of the manner in which the matrix elements were calculated. Once γ and γ' are chosen, ξ and ξ' are unique (see equations 3.7.11 to 3.7.13).

The final matrix elements appearing in equations 3.7.22 to 3.7.24 represent a great deal of applied group theory and complicated algebra. These results were checked and rechecked in the following manner.

New equations were derived by using different choices of quantum numbers in calculating the reduced spin-rotation matrix elements. That is to say, the entire operation presented in this Section and Appendices C, D, and E were redone in a different "form". The resulting equations were sufficiently different in appearance (because of the extensive algebra involved) that showing their equivalence would have been very tedious. Instead, equations 3.7.22 to 3.7.24 were shown to be equivalent to their independently derived counterparts by choosing numerical values for all the quantum numbers involved and performing the calculations. These equations were then checked again by computing these same specific matrix elements from the "ground up" by using equations 3.4.2, 3.4.4, 3.5.13 and 3.5.18 and inserting the specific quantum numbers from the outset.

The matrix elements $\langle H_{sr}^T (1 \rightarrow 1) \rangle$ have been calculated in reference (117) for the specific case of $t' = t$. The special case of $t' = t = 1$, $\rho = 2$ and $J = 5$ was calculated from equation 3.7.22 and from equation 27 of reference (117) and the two agree. These two independent calculations even involve different rotational basis functions. Further, the same matrix element was calculated from the "ground up" (see previous paragraph) for particular choices of m_J', m_J, m_I', and m_I.

It should be pointed out that although all these checks confirm the reliability of equations 3.7.22 to 3.7.24, the final numbers will depend on the reliability of the rotational A-constants (discussed in Section 3.4.2) which result from the diagonalization of the centrifugal distortion Hamiltonian. These A-constants have been extensively used in interpreting experiments involving molecular beams and infrared spectroscopy and their reliability seems to be firmly established.

3.8.1   NUCLEAR SPIN TRANSITION PROBABILITIES

The nuclear spin transition probabilities are given in terms of the total spin plus rotation transition probabilities in equation 3.2.10. These total transition probabilities are, in turn, given in equation 3.3.16. These two equations give

$$
W_{m'_I, m_I} \;=\; \sum_{i} \sum_{R'(I')} P_{R'} \sum_{R(I)} \hbar^{-2} \left| \langle H^{i}_{sr}(I' \rightarrow I) \rangle \right|^2 j_i(\omega_{R'm'_I, Rm_I}) \qquad 3.8.1
$$

with the reduced spectral density given by

$$
j_i(\omega_{R'm'_I, Rm_I}) \;=\; \frac{2\,\tau_i}{1 + \tau_i^{2}\omega_{R'm'_I, Rm_I}} \qquad 3.8.2
$$

We postpone for the moment the meaning of the parameter i in equation 3.8.1 other than to remind the reader it is an index introduced phenomenologically via equation 3.3.11 in order to relate the systems L and R discussed in Section 3.3. (Note that the system $S = Im_I$ interacts with the system R via the spin-rotation interaction but does not interact directly with the system L.) The matrix elements required in equation 3.8.1 are as follows. $I' = I = 2$ is the scalar matrix element given by equation 3.7.5, $I' = I = 1$ is the scalar matrix element given by equation 3.7.6 plus the tensor matrix element given by equation 3.7.22, $I' = 2$ and $I = 1$ is the tensor matrix element given by equation 3.7.23 and $I' = 0$ and $I = 1$ is the tensor matrix element given by equation 3.7.24.

In equation 3.8.1, the sums over R and R' are written as R(I) and R'(I') because of the restrictions imposed by spin symmetry. That is to say, once I' and I are specified, the sums over the rotational centrifugal distor-

tion states are restricted through the dependence of the representation γ

on I and the parity index ρ (see Table 3.4). The centrifugal distortion

states are uniquely specified by J, γ, ρ and t. The 2J+1 degeneracy of

each state is lifted in a magnetic field and the sum over R(I) can be

replaced by;

$$\sum_{R(I)} \longrightarrow \sum_{J=0}^{\infty} \sum_{m_J=-J}^{+J} \sum_{\rho=1}^{2} \sum_{t=1}^{N\{\gamma(I,\rho),J,\rho\}} \qquad 3.8.3$$

The sum over γ does not appear because once I and ρ are specified,

γ is unique. (See Table 3.4). The information concerning which γ is

involved in each term in 3.8.3 is not lost, however, because of the

dependence of $N\{\gamma(I,\rho),J,\rho\}$ on γ. This number N is simply the number of

times a given γρ appears in a given J state. (i.e., the number of centrifugal

distortion states of the same symmetry type.) This is explained further in

reference (115) where algebraic expressions for $N(\gamma,J,\rho)$ are given. The

index t counts these states in order of increasing energy.

The weight $P_{R(I)}$ in equation 3.8.1 are given by

$$P_{R(I)} = [U(I,T)]^{-1} [\exp\{-\frac{BJ(J+1)}{kT}\}] \qquad 3.8.4$$

where the approximation $E_R = BJ(J+1)$ has been used. The next term involves

the distortion energy and is very much smaller. The functions $U(I,T)$,

where T is the temperature, represent, in some sense, the partition

function for that part of the system in the I spin state. $U(I,T)$ is

just the sum over J, m_J, γ, t and ρ of $\exp[-BJ(J+1)/kT]$. Again,

the sum over γ reduces to a single term. The sum over m_J is just

2J+1 and U(I,T) is given by

$$U(I,T) \quad = \quad \sum_{J=0}^{\infty} (2J+1) \exp\{-\frac{BJ(J+1)}{kT}\} \sum_{\rho=1}^{2} \sum_{t=1}^{N\{\gamma(I,\rho),J,\rho\}} (1) \qquad 3.8.5$$

The sum over t is clearly $N(\gamma,J,\rho)$. If we define

$$N(I,J) \quad = \quad \sum_{\rho=1}^{2} N\{\gamma(I,\rho),J,\rho\} \qquad 3.8.6$$

then equation 3.8.5 becomes

$$U(I,T) \quad = \quad \sum_{J=0}^{\infty} [2J+1][N(I,J)][\exp\{-\frac{BJ(J+1)}{kT}\}] \qquad 3.8.7$$

Using a computer the functions U(I,T) have been computed from the algebraic expressions for $N(\gamma,J,\rho)$ (115). They have been evaluated at the temperatures corresponding to the temperatures at which the measurements were performed. The upper limits, J_{MAX}, for the sum over J in equation 3.8.7 were chosen to give U(I,T) to an accuracy of better than 0.1%. They are J_{MAX} = 23, 18, 18 and 12 for T = 295K, 150K, 110K and 77K respectively. These values appear in Table 3.9.

As an aside, it is noted that the partition function Z(T) is given by

$$Z(T) \quad = \quad \sum_{I} U(I,T) \qquad 3.8.8$$

The numerical values for U(I,T) which appear in Table 3.9 are consistent with an approximate algebraic expression for Z(T) found in reference (60). Also, as an aside, the ratios U(0,T):U(1,T):U(2,T) are 2:3:1 as expected.

Having calculated the parameters $P_{R(I)}$, we again focus our attention

Table 3.9

Numerical Values for U(I,T)

		I		
		0	1	2
T(K)	77	9.87	14.81	4.94
	110	16.74	25.11	8.37
	150	26.54	39.80	13.27
	295	72.73	109.09	36.36

Table 3.10 Summary of Transition Probability Functions

Function	coupling constant	I' → I	change of centrifugal distortion energy
$A(T:C_a^2)$	C_a^2	2 → 2	no
$F(T:C_a^2)$	C_a^2	1 → 1	no
$G(T:C_aC_d)$	C_aC_d	1 → 1	no
$B(T:C_d^2)$	C_d^2	1 → 1	no
$E(T:C_d^2;m_1'-m_1)$	C_d^2	1 → 1	yes
$C(T:C_d^2;m_2'-m_1)$	C_d^2	2 → 1	yes
$D(T:C_d^2;0-m_1)$	C_d^2	0 → 1	yes

on equation 3.8.1, which we write in the following form, noting the only

dependence on m_J and m_J' is contained in the matrix elements. The dependence

of $\omega_{R'm_I',Rm_I}$ on m_J' and m_J has been taken care of by using the difference ω_0

between the nuclear and molecular Larmor angular frequencies rather than

just the nuclear Larmor angular frequency ω_N (see Section 3.3).

$$W_{m_I',m_I} = 2\hbar^{-2}[U(I,T)]^{-1} \sum_{iJ}\sum_{\rho}\sum_{t't}\sum \left[[\exp -\{\frac{BJ(J+1)}{kT}\}] \right. \times$$

$$\left. [\sum_{m_J'}\sum_{m_J} |<H_{sr}^i(I'\rightarrow I)>|^2][\frac{1}{2} j_i(\omega_{R'm_I',Rm_I})] \right] \qquad 3.8.9$$

The double sums over m_J' and m_J are performed in Appendix F. The results

are:

$$\sum_{m_J}\sum_{m_J'} |<H_{sr}(2\rightarrow2)>|^2 = \frac{1}{6}h^2 C_a^2 J(J+1)(2J+1)\delta(t',t)f^{22}(m_I',m_I) \qquad 3.8.10$$

with $f^{22}(m_I',m_I)$ given by

$$f^{22}(m_I',m_I) = [(2-m_I)(3+m_I)]\ \delta(m_I',m_I+1)$$

$$+\ [2m_I^2]\ \delta(m_I',m_I) + [(2+m_I)(3-m_I)]\ \delta(m_I',m_I-1)$$

$$3.8.11$$

$$\sum_{m_J'}\sum_{m_J} |<H_{sr}(1\rightarrow1)>|^2 = \frac{1}{6}h^2 J(J+1)(2J+1)$$

$$[C_a\ \delta(t',t) + \frac{1}{3}\ \Pi\ C_d]^2\ f^{11}(m_I',m_I) \qquad 3.8.12$$

with $\Pi(F;F;J,t',t,\rho)$ given by equation 3.7.27 and $f^{11}(m_I',m_I)$ given by

$$f^{11}(m_I',m_I) = 2 [\delta(m_I',m_I+1) + m_I^2\delta(m_I',m_I) + \delta(m_I',m_I-1)] \quad 3.8.13$$

$$\sum_{m_J'}\sum_{m_J} |<H_{sr}(2\rightarrow1)>|^2 = \frac{1}{27}h^2C_d^2 J(J+1)(2J+1)[\Pi]^2 f^{21}(m_I',m_I) \quad 3.8.14$$

where $\Pi(A;F;J,t',t,\rho)$ is given by equation 3.7.27 and $f^{21}(m_I',m_I)$ is given by

$$f^{21}(m_I',m_I) = [\frac{1}{2}(3+m_I)(2+m_I)] \delta(m_I',m_I+1)$$

$$+ [(2+m_I)(2-m_I)] \delta(m_I',m_I) + \frac{1}{2}[(3-m_I)(2-m_I)]\delta(m_I',m_I-1)$$

$$3.8.15$$

$$\sum_{m_J'}\sum_{m_J} |<H_{sr}(0\rightarrow1)>|^2 = \frac{1}{27}h^2C_d^2J(J+1)(2J+1)[\Pi]^2 f^{01}(0,m_I) \quad 3.8.16$$

where $\Pi(E;F;J,t',t,\rho)$ is given by equation 3.7.27 and $f^{01}(0,m_I)$ is included only for completeness because it is equal to 1 for all three cases.

$$f^{01}(0,m_I) = \delta(m_I,+1) + \delta(m_I,0) + \delta(m_I,-1) \quad 3.8.17$$

We note that the $f^{I'I}(m_I',m_I)$ are just sums of products of two terms, a δ-function and a number proportional to the square of a Clebsch-Gordan coefficient.

As a result of squaring the matrix elements, there arises three different types of nuclear spin transition probabilities. The first type of transition probability involves only C_a^2 which does not involve a change in centrifugal distortion energy. Using equations 3.3.2 and 3.4.3 to write the angular frequencies $\omega_{R'm_I',Rm_I}$ explicitly gives

$$\omega_{R'm_I',Rm_I} = \{\omega(J,\gamma,t,\rho) - \omega(J,\gamma',t',\rho)\} -\{m_I-m_I'\}\omega_0 \qquad 3.8.18$$

For transition probabilities in C_a^2, equation 3.8.18 reduces to $\pm\omega_0$ (zero does not occur). We will associate with this interaction the correlation time τ_1. That is to say, in summing equation 3.8.9 over i, this is the term i = 1. The reduced spectral density, in this case, is

$$j_i(\omega_0) = \frac{2\tau_i}{1 + \tau_i^2\omega_0^2} \qquad 3.8.19$$

with i = 1.

Although it is negligible as discussed later in this section, the second type of term is the cross term in $C_a C_d$. This term of the I = 1 → I = 1 transition probability does not involve a change in distortion energy because of the $\delta(t',t)$ in equation 3.8.12. The correlation time associated with this process is τ_{12} (i = 12) and $j_{12}(\omega_0)$ is given by equation 3.8.19 with i = 12.

For transition probabilities involving C_d^2 there are two kinds of terms, both of them having the correlation time τ_2 associated with them. There are transition probabilities involving no change in distortion state (i.e., elastic) for 1' = 1 → I = 1. For these terms, $j_2(\omega_0)$ is given by equation 3.8.19 with i = 2. For those transition probabilities involving a change in centrifugal state (i.e., inelastic), the spectral density is given by

$$j_2\{\omega(J,\rho;\gamma',\gamma;t',t;m_I',m_I)\}$$
$$= \frac{2\tau_2}{1 + \tau_2^2 [\{\omega(J,\gamma,t,\rho)-\omega(J,\gamma',t',\rho) - (m_I-m_I')\omega_0\}]^2} \qquad 3.8.20$$

The fact that in the denominator of j_2 in the previous equation, the distortion and nuclear frequencies add or subtract depending on the sign of Δm has important consequences on the nuclear spin relaxation at certain Larmor frequencies. This point will be discussed further. Finally, we note that Δm can be zero in this case.

We have now introduced the effect of the thermal bath or reservoir (i.e., system L) by allowing the different types of matrix elements (i.e., C_a^2, $C_a C_d$ and C_d^2) to have associated with them, different correlation times (τ_i where i = 1, 12 and 2). The molecular rotation is also part of the system L, and we may wish to allow τ_i to be dependent on J. This is discussed further in Chapter IV.

The transition probabilities in equation 3.8.9 appear very complicated and because the rotational sums can only be performed numerically, it is convenient to write each nuclear spin transition probability as a product of two parts: one containing the complex sums over the rotational quantum numbers and the other a simple function proportional to the square of a Clebsch-Gordan coefficient containing the nuclear spin quantum numbers. When this is done the nuclear spin transition probabilities of equation 3.8.9 can be expressed in the following way.

$$W_{m_2' m_2} = f^{22}(m_2' m_2) \, A \, (T:C_a^2) \qquad\qquad 3.8.21$$

$$W_{m_1' m_1} = f^{11}(m_1' m_1) \, [F(T:C_a^2) + G(T:C_a C_d)$$

$$+ \, B(T:C_d^2) + E(T:C_d^2 \, ; \, m_1' - m_1)] \qquad\qquad 3.8.22$$

$$Wm_2'm_1 = f^{21}(m_2'm_1) \, C(T:C_d^2; \, m_2'-m_1) \qquad\qquad 3.8.23$$

$$Wo_0m_1 = f^{01}(o_1m_1) \, D(T:C_d^2; \, o-m_1) \qquad\qquad 3.8.24$$

The functions A, F, G, B, E, C and D are derived in Appendix G. The notational form in which they appear in the above equations imply that F, B, G and A are functions of T only and E, C and D are functions of T and Δm. The coupling constants are included as a reminder. The distinguishing features of these functions are listed in Table 3.10. Before writing out these functions explicitly, (they appear in Appendix G) we first discuss them.

If the correlation times are independent of J, then the reduced spectral density, j_i given by equation 3.8.19 can be factored out of the A, F, G and B terms. A and F involve $j_1(\omega_0)$, G involves $j_{12}(\omega_0)$ and B involves $j_2(\omega_0)$. (See Table 3.10, the exact expressions for these functions are not necessary for this discussion.) This is not true for the E, C and D terms since the spectral density given by equation 3.8.20 depends on the rotational distortion quantum numbers through the centrifugal distortion frequencies. The primed functions are defined as follows

$$X = X' \{j_i(\omega_0)\} \qquad\qquad 3.8.25$$

for X = A, F, G and B but not for C, D and E. Equation 3.8.25 is written explicitly for the four cases in Appendix G. This is a convenient transformation It allows an evaluation of A', F', G' and B' because they are all independent of correlation time. These primed functions are given in Table 3.11 in absolute units (S^{-2}) for the temperatures at which the experiments were performed.

Table 3.11 Tabulation of A', B' and G'

T(K)	J_{MAX}	A' (T:C_a^2)	B' (T:C_d^2)	G' (T:C_aC_d)
295	23	$8.316 \times 10^{10}s^{-2}$ (0.498)[1]	$8.429 \times 10^9 s^{-2}$ (0.180)	$<2.4 \times 10^6 s^{-2}$
150	18	4.211×10^{10} (0.496)	5.244×10^9 (0.220)	$<3.3 \times 10^5$
110	18	3.078×10^{10} (0.496)	4.401×10^9 (0.251)	not calculated
77	12	2.142×10^{10} (0.492)	3.696×10^9 (0.302)	not calculated

[1] bracketed values for A' are in units of $\frac{4\pi^2}{\alpha} C_a^2$ and for B' are in units of $\frac{4}{45} \frac{4\pi^2}{\alpha} C_d^2$. $C_a = 10.4 \pm 0.1$ kHz and $C_d = 18.5 \pm 0.5$ kHz (32).

Table 3.11 does not contain the value of $F'(T:C_a^2)$ because it is equal to $A'(T:C_a^2)$. This actually presents a check on the calculation because this must be so. If C_d is set to zero then B, G, E, C and D in equations 3.8.21 to 3.8.24 are identically zero and only A and F remain, the former being proportional to the transition probability for the I = 2 species and the latter for the I = 1 species. In this limit $(C_d \rightarrow 0)$, the interaction responsible for the nuclear spin relaxation becomes $\bar{I} \cdot \bar{J}$ and the two species must relax with the same rate constants which in this case are simply the transition probabilities. This is shown in reference (70, p.308).

A further check on the A' term will involve a comparison with a previous theory of nuclear spin relaxation in methane to be discussed in the next chapter.

The functions A, F, G and B are;

$$A(T:C_a^2) \quad = \quad \sum_J \ [W(T:C_a^2;A,J)] \ [\tfrac{1}{2} j_1(\omega_0)] \qquad\qquad 3.8.26$$

$$F(T:C_a^2) \quad = \quad \sum_J \ [W(T:C_a^2;F,J)] \ [\tfrac{1}{2} j_1(\omega_0)] \qquad\qquad 3.8.27$$

$$G(T:C_a C_d) \quad = \quad \sum_J \sum_\rho \sum_t \ [X(T:C_a C_d;F,J,\rho,t)][\tfrac{1}{2} j_{12}(\omega_0)] \qquad 3.8.28$$

$$B(T:C_d^2) \quad = \quad \sum_J \sum_\rho \sum_t \ [Y(T:C_d^2;F,J,\rho,t)][\tfrac{1}{2} j_2(\omega_0)] \qquad 3.8.29$$

with W, X and Y given by

$$W(T:C_a{}^2;\gamma,J) \;=\; [\tfrac{4}{3}\,\pi^2\,C_a{}^2][U(I,T)]^{-1} \quad x$$

$$[J(J+1)(2J+1)][N(I,J)][\exp\{-\tfrac{BJ(J+1)}{kT}\}\,] \qquad 3.8.30$$

$$X(T:C_aC_d;F,J,\rho,t) \;=\; [\tfrac{8}{9}\,\pi^2 C_aC_d][U(1,T)]^{-1} \quad x$$

$$[J(J+1)(2J+1)][\exp\{-\tfrac{BJ(J+1)}{kT}\}][\Pi(F;F;J,t,t,\rho)]$$

$$3.8.31$$

$$Y(T:C_d{}^2;F,J,\rho,t) \;=\; [\tfrac{4}{27}\,\pi^2\,C_d{}^2][U(1,T)]^{-1} \quad x$$

$$[J(J+1)(2J+1)][\exp\{-\tfrac{BJ(J+1)}{kT}\}][\Pi(F;F;J,t,t,\rho)]^2$$

$$3.8.32$$

Note that X and Y contain the same Π function (equation 3.7.27) but that in Y it is squared and in X it is not. The complicated Π functions can be thought of as replacing the $N(I,J)$.

The remaining functions are as follows

$$E(T:C_d{}^2;m_1'-m_1) \;=\; \sum_J \sum_\rho \sum_{t'} \;\underset{\neq t}{\sum}\; [Z(T:C_d{}^2;F,F;J,t',t,\rho)] \quad x$$

$$[\tfrac{1}{2}\,j_2\{\omega(J,\rho;F,F;t',t;m_1',m_1)\}] \qquad 3.8.33$$

$$C(T:C_d{}^2;m_2'-m_1) \;=\; \sum_J \sum_\rho \sum_{t'} \sum_t [Z(T:C_d{}^2;A,F;J,t',t,\rho)] \quad x$$

$$[\tfrac{1}{2}\,j_2\{\omega(J,\rho;A,F;t',t;m_2',m_1)\}] \qquad 3.8.34$$

$$D(T:C_d^2;0-m_1) = \sum_J \sum_\rho \sum_{t'} \sum_t [Z(T:C_d^2;E,F;J,t',t,\rho)]$$

$$[\frac{1}{2} j_2\{\omega(J,\rho;E,F;t',t;o,m_1)\}] \qquad 3.8.35$$

where the Z functions are given by

$$Z(T:C_d^2;\gamma',\gamma;J,t',t,\rho) = [d(\gamma')\pi^2C_d^2][U(I',T)]^{-1}$$

$$\qquad 3.8.36$$

$$[\exp\{-\frac{BJ(J+1)}{kT}\}][J(J+1)(2J+1)][\Pi(\gamma',\gamma;J,t',t,\rho)]^2$$

The functions $d(\gamma')$ are

$$d(F) = \,^4/_{27} \;;\quad d(A) = \,^8/_{27} \;;\quad d(E) = \,^8/_{27} \qquad 3.8.37$$

The functions E, C and D can not be immediately evaluated because the sum over the rotational centrifugal distortion states involves the spectral density. Thus the terms A, F, B and G represent the nuclear spin relaxation rotational spectrum at zero frequency (see Table 3.10) and are broadened by the spectral densities $j_1(\omega_0)$, $j_1(\omega_0)$, $j_2(\omega_0)$ and $j_{12}(\omega_0)$ respectively. The terms E, C and D on the other hand involve the same reduced spectral density j_2 but centered around non-zero frequencies. Each individual contribution must be evaluated for a particular correlation time τ_2 and then summed over the rotational parameters (J,t',t,ρ).

All terms involve squares of matrix elements <u>except</u> G which is the cross term in C_aC_d. This term is, at least, very much smaller than the other terms and it may be identically zero. The reason that $G(T:C_aC_d)$ in equation 3.8.28 is very small is that the matrix elements can be positive or negative.

If τ_{12} is independent of J then equation 3.8.25 is valid and G' can be computed. When the sum over J is performed from J = 0 to J = J_{MAX} (having performed the sums of ρ and t) in equation 3.8.28, the individual J contributions add destructively. $G'(T:C_aC_d)$ was computed as a function of J_{MAX} and the results are shown in Table 3.12. It is quite clear that even though each of the individual matrix elements can be quite large, the absolute value of G' is a decreasing function of J_{MAX}, the upper limit in the sum over J. An interesting theoretical exercise would be to establish whether G' is identically zero in the limit $J_{MAX} \to \infty$. In any case, it is completely negligible and will be dropped. Even if τ_{12} is dependent on J, $G(T:C_aC_d)$ will be extremely small. This is an important point because one of the purposes of the theory was to determine whether or not such a cross term was important. In an existing theory (16), to be discussed in Section 4.1.2 this term is identically zero.

In equations 3.8.33 to 3.8.35 there are simply too many terms to tabulate. For example, in J = 12 alone, the eleven distortion levels (see Figure 3.1) lead to approximately 30 transitions. In total there are 806 transitions (0<J<23). Some are extremely small and some although not so small are at such high frequency (compared with the nuclear Larmor frequency) that even though Z in equations 3.8.33 to 3.8.35 may be large, the denominator of j_2 (equation 3.8.20) is also very large. A convenient way to obtain an idea of the magnitude of these terms is to plot the $Z(T:C_d^2;\gamma',\gamma;J,t',t,\rho)$ as a function of the centrifugal distortion frequency at which they occur, namely the $\{\omega(J,\gamma,t,\rho) - \omega(J,\gamma',t',\rho)\}$ in the denominator of j_2. Such a plot represents the zero density ($\tau_2 \to \infty$) nuclear spin relaxation rotational spectrum discussed in the introduction of this thesis as well as other places (25).

These plots are given in Appendix G. Figures G1 to G5 are presented

Table 3.12 Tabulation of $G'(T:C_aC_d)$

J_{MAX}	150K (x10^8)	295K (x10^8)
1	- 2.3 s^{-1}	- 0.88 s^{-1}
2	-12.	- 4.9
3	18.	9.5
4	9.1	4.5
5	-28.	-24.
6	12.	17.
7	8.2	12.
8	- 9.2	-26.
9	1.8	11.
10	1.3	8.5
11	- 0.81	-12.
12	0.088	3.5
13	0.066	2.8
14	- 0.020	- 2.9
15	0.0047	0.57
16	0.0043	0.46
17	0.0031	- 0.40
18	0.0033	0.030
19		0.020
20		- 0.055
21		- 0.024
22		- 0.024

only to give an overview. Figures G1 and G2 indicate how $Z(\gamma' = E, \gamma = F)$

changes as a function of temperature. Figures G1 and G2 being Z(295K;E,F)

and Z(110K;E,F) respectively. All the transitions present in Figure G1

are, in principle, present in Figure G2 but in the latter many are so small

as not to be given on the second plot[1]. The reason the spectrum is

"narrower" at the lower temperature results from the fact that the higher

distortion frequencies tend to be associated with the higher J states[2].

For comparison purposes, the largest Z value is given as a percent[3] of the

parameter $A'(T:C_a^2)$, (see Equations 3.8.21, 3.8.25, 3.8.26 and 3.8.30). Thus

the contribution of centrifugal distortion to the nuclear spin transition

probabilities may become more pronounced at lower temperatures. Figures G3

and G4 represent the same plots for $Z(A,F)$[4]. Each of these lines could be

labelled by J,t',t,ρ which would completely specify them.

An important point which should be clarified is the fact that these

plots are not symmetric with respect to $\omega = 0$. This results from the defini-

tions of the frequencies. The calculations for the spin conversion transition

probabilities involved calculating $I' = 2 \to I = 1$ (A $\to$ F) and $I' = 0 \to I = 1$

(E $\to$ F) and not F $\to$ A and F $\to$ E. Thus the sum over R(I) in equation 3.8.1

is different from the sum over R'(I') because spin symmetry dictates that I'

involves a different rotational system than does I. We do not need to

1. Figures G1 through to G13 include all transitions whose weights Z are
   greater than or equal to 1% of the largest Z value. In the final numerical
   computation, all Z's are used, however.
2. The range of J (i.e. from zero to J_{MAX}) used at each temperature is
   indicated in Table 3.11.
3. It must be remembered that whereas Figures G1 to G13 have the same scale
   on the y-axis, the functions $A'(T:C_d^2)$ are proportional to temperature.

4. It cannot be deduced from these plots that the E $\to$ F transitions are
   going to play a more important role than the A $\to$ F transitions since the
   functions $f^{I'I}(m_I', m_I)$ have to be taken into account (see equations 3.8.21
   to 3.8.24).

calculate the $F \to A$ and $F \to E$ transition probabilities because the high temperature approximation require that $Wm'_I, m_I = Wm_I m'_I$. If the unprimed distortion state occurs at a higher energy than the primed distortion state then the frequency is defined as positive and vice versa.

It should be noted that with the exception of $I' = I = 2$ which involves the scalar spin-rotation interaction only, the high temperature approximation does not imply $Wm'_I, m_I = Wm_I, m'_I$. This is an incorrect application of the high temperature approximation. This amounts to keeping the same sums over $R'(I')$ and $R(I)$ in equation 3.8.1 and therefore involves the same centrifugal distortion frequency. However, Δm changes sign and the denominator in equation 3.8.20 will involve adding (subtracting) the distortion and nuclear frequencies for Wm'_I, m_I but subtracting (adding) them for Wm_I, m'_I. The 72 MHz centrifugal distortion splitting (-72 MHz) in $J = 3$ serves as a useful example. The reduced spectral density involves (-72 - 30) MHz = -102 MHz (squared) for the contribution to $W_{0_2 1_1}$ but it involves (-72 + 30) MHz = -42 MHz for the contribution to $W_{1_2 0_1}$. See the arrows in Figure 3.2. Of course, the high temperature approximation is valid because both frequencies change sign in this case.

Just as the high temperature approximation must be applied carefully, so must time reversal symmetry. The latter requires that the matrix element $|<H_{sr}(I' \to I)>|$ be the same if m_I and m'_I are replaced by $-m_I$ and $-m'_I$ respectively but it does not imply, in general, that $Wm'_I, m_I = W-m'_I, -m_I$. This involves interchanging m'_I and m_I in the denominator of equation 3.8.20 and thus changing the sign of ω_0. We note that if no centrifugal distortion transitions are involved or if $m'_I, -m_I = 0$ then the high temperature approximation does imply $Wm'_I, m_I = Wm_I, m'_I$ and reversal symmetry does imply $Wm'_I, m_I = W-m'_I, -m_I$.
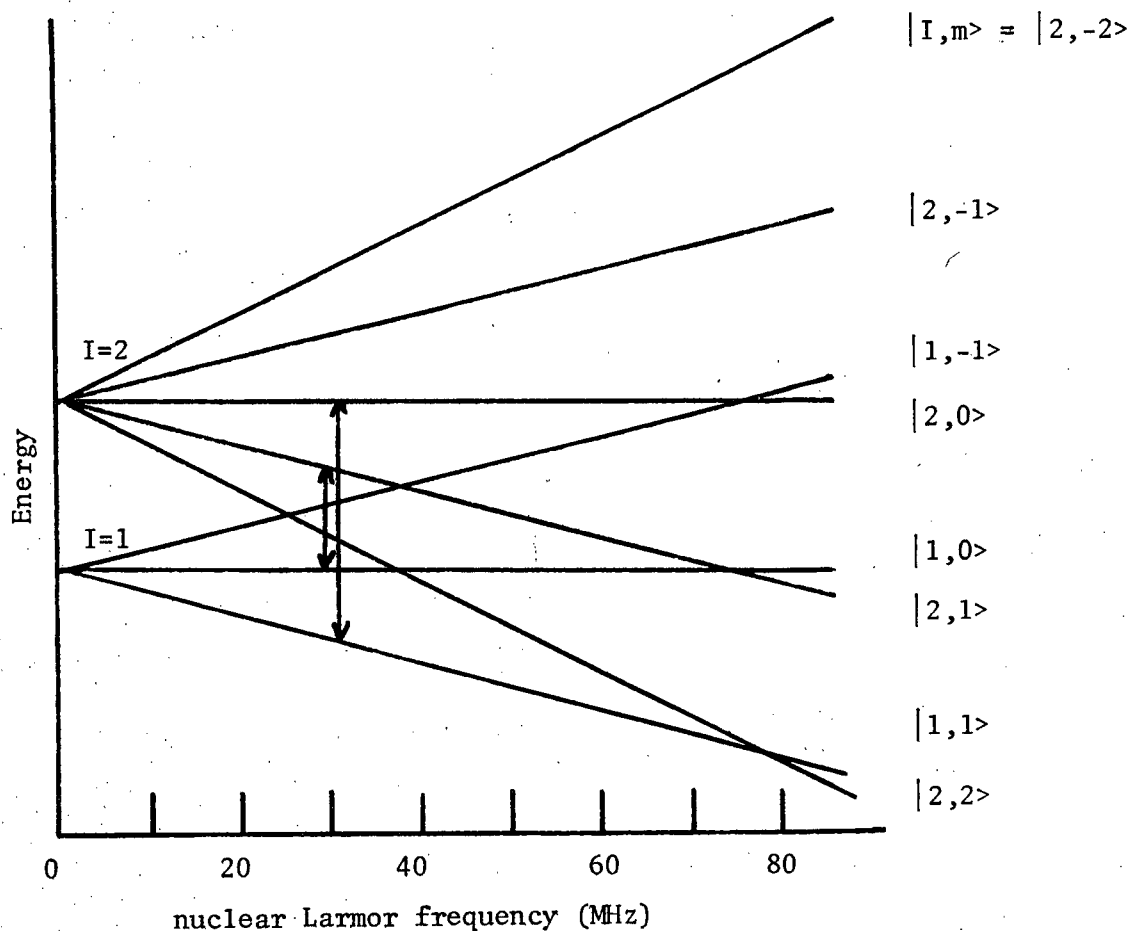
Figure 3.2. The nuclear Zeeman energy levels as a function of nuclear
Larmor frequency in the J = 3 rotational state. The zero
field centrifugal distortion splitting is 72 MHz. (See Table
4.3 for a complete classification of the low frequency dis-
tortion splittings of importance to the nuclear spin relaxation.)
The crossing of the six of the eight nuclear
spin states at a nuclear Larmor frequency of 76 MHz (nuclear
minus rotational Larmor frequency of 72 MHz) results in non-
exponential relaxation at sufficiently low densities as dis-
cussed in Chapter IV. All other level crossings involve pairs
of states with $\Delta m > 1$ and thus do not interact via the spin-
rotation interaction. The arrows represent possible spin
conversion transitions at 30 MHz as discussed in the text.

Figure G5 shows $Z(295K; C_d^2; F, F)$. These transitions will contribute very little to the nuclear spin transition probabilities for two reasons. First they are small in magnitude (i.e. Z is small) and secondly they occur only at relatively high frequencies, (i.e., j_2 is small).

It is convenient to rewrite equations 3.8.21 to 3.8.24 for the two cases; τ_i a function of J and τ_i independent of J. If τ_i is a function of J, we can not use equation 3.8.25 and

$$W_{m_2'm_2} = f^{22}(m_2'm_2) \, A(T:C_a^2) \qquad\qquad 3.8.38$$

$$W_{m_1'm_1} = f^{11}(m_1'm_1)[F(T:C_a^2) + B(T:C_d^2) + E(T:C_d^2;m_1'-m_1)] \qquad 3.8.39$$

$$W_{m_2'm_1} = f^{21}(m_2'm_1) \, C(T:C_d^2;m_2'-m_1) \qquad\qquad 3.8.40$$

$$W_{o_0m_1} = f^{01}(o_0m_1) \, D(T:C_d^2;o-m_1) \qquad\qquad 3.8.41$$

where the $f^{I'I}$ are defined in equations 3.8.11, 3.8.13, 3.8.15 and 3.8.17. A, F and B appear in equations 3.8.26, 3.8.27 and 3.8.29 and E, C and D in equations 3.8.33, 3.8.34 and 3.8.35.

If τ_i is independent of J then equations 3.8.40 and 3.8.41 remain unchanged (in form) but equations 3.8.38 and 3.8.39 may be expressed (using equation 3.8.25)

$$W_{m_2'm_2} = f^{22}(m_2'm_2) \, A'(T:C_a^2)\{\tfrac{1}{2} j_1(\omega_0)\} \qquad\qquad 3.8.42$$

$$W_{m_1'm_1} = f^{11}(m_1'm_1)[A'(T:C_a^2)\{\tfrac{1}{2} j_1(\omega_0)\}$$

$$+ B'(T:C_d^2)\{\tfrac{1}{2} j_2(\omega_0)\} + E(T:C_d^2; m_1'-m_1)] \qquad 3.8.43$$

where A' and B' are given by equations 3.8.26 and 3.8.29 without the factors j_1 and j_2 respectively. A' and B' are tabulated in Table 3.11.

Whereas Figures G1 to G5 are plotted over the range - 4000 to + 4000 MHz, Figures G6 to G13 show Z vs frequency for the A → F and E → F transitions over the range - 800 MHz to + 800 MHz. It is of interest to note the centrifugal distortion transitions in the very low J states increase in magnitude as temperature is lowered and the transitions in the higher J states decrease in magnitude as temperature is lowered. Of particular interest is the J = 2 8 MHz line[1] which grows from 4.7 x 10^8 s^{-2} (0.6% of A'(295:C_a^2)) at 295K to 2.3 x 10^9 s^{-2} (11% of A'(77:C_a^2)) at 77K as illustrated in Figures G6 to G9, (see footnote 3 on page 109). Also of interest is the 51 MHz line in J = 5 whose absolute magnitude does not vary considerably but whose relative contribution grows from 3.1% of A'(295K:C_a^2) to 9.9% of A'(77K:C_a^2) as indicated in Figures G6 and G9. The final important transition is the 71 MHz transition in J = 3 (Figures G10 to G13) which increases from 0.9% of A'(295:C_a^2) to 10% of A'(77K:C_a^2) (see footnote 4 on page 109).

As an aside, it should be noted that at level crossings corresponding to Δm = ±2, the intramolecular dipolar interaction may have an effect on the relaxation (see Figure 3.2) because it may dominate. It is not expected to be important for level crossings involving Δm = ±1 because the spin-rotation interaction will dominate.

---

[1] Characterized by Z(T:C_d^2;E,F,1,1,1).

3.9   RELAXATION FUNCTIONS

Having calculated the nuclear spin transition probabilities we can now evaluate the magnetization as a function of time

$$M^{obs}(t) = \sum_I M^{(I)}(t) \qquad 3.9.1$$

$$M^{(I)}(t) = \sum_{m_I} m_I n_{Im_I}(t) \qquad 3.9.2$$

where the populations obey the equations

$$\frac{d}{dt} \tilde{n}_{Im_I} = \frac{d}{dt} n_{Im_I} = \sum_{I'} \sum_{m'} W_{ImI'm'} \{\tilde{n}_{Im} - \tilde{n}_{I'm'}\} \qquad 3.9.3$$

When the subscript on m and m' is omitted, it is understood to mean m_I and m_I', respectively. When equation 3.9.3 is expanded, it can be written

$$\frac{d}{dt} \tilde{n}_{Im_I} = \sum_{I'} \sum_{m'} S_{ImI'm'} \tilde{n}_{I'm'} \qquad 3.9.4$$

The $S_{ImI'm'}$ are found by simply equating 3.9.3 and 3.9.4. The diagonal members of S are sums of W's and the off diagonal terms are in single W (with a minus sign) or zero subject to the conditions $\Delta I = 0, \pm 1$ and $\Delta m = 0, \pm 1$. The S matrix is given explicitly in Table 3.13 where the following notation is used for convenience[1].

$$W(I'm'Im) = W_{I'm_I', Im_I} \qquad 3.9.5$$

---

[1] In Table 3.13, we have used the fact that W(2m'2m) = W(2-m'2-m) as discussed for a different calculation on page 118.

Table 3.13 Matrix $S_{I'm'_I, Im_I}$

I'	m'$_{I'}$	\\ I → 2	1	0	-1	-2	1	0	-1	0
		m$_I$ → 2	1	0	-1	-2	1	0	-1	0
2	2	W(2221) +W(2211)	-W(2221)	0	0	0	-W(2211)	0	0	0
	1		W(2221) +W(2120) +W(2111) +W(2110)	-W(2120)	0	0	-W(2111)	-W(2110)	0	0
2	0			2W(2120) +W(2011) +W(2010) +W(201-1)	-W(2120)	0	-W(2011)	-W(2010)	-W(201-1)	0
	-1				W(2221) +W(2120) +W(2-11-1) +W(2-110)	-W(2221)	0	-W(2-110)	-W(2-11-1)	0
	-2					W(2221) +W(2-21-1)	0	0	-W(2-21-1)	0
	1						W(1110) +W(2211) +W(2111) +W(2011) +W(0011)	-W(1110)	0	-W(0011)
1	0							W(1110) +W(1-110) +W(2110) +W(2010) +W(1000) +W(2-110)	-W(1-110)	-W(0010)
	-1								W(1-110) +W(2-21-1) +W(2-11-1) +W(201-1) +W(001-1)	-W(001-1)
0	0									W(0011) +W(0010) +W(001-1)

$$S^\dagger = S$$

The nine coupled differential equations given by equation 3.9.4 (one for each nuclear spin state) can be conveniently expressed in matrix notation as

$$\frac{d}{dt} \underset{\sim}{\underline{n}} = \underline{\underline{S}} \; \underset{\sim}{\underline{n}} \qquad\qquad 3.9.6$$

In principle, we should diagonalize $\underline{S}$ and find the linear combinations of n_{Im} that correspond to each of the nine eigenvalues. However, great care must be taken in this procedure because $\underline{n}$ is not a vector that satisfies the condition that the scalar product $\underline{n} \cdot \underline{n}$ is conserved when the basis (i.e., "coordinate system") of $\underline{n}$ is changed. It is in fact the sum of the components of $\underline{n}$ that must be conserved when the basis of $\underline{n}$ is changed.

This is simply a reflection of the fact that the total number of spins is constant. This problem will be discussed further in the following paragraphs where a 2 x 2 matrix is diagonalized in the appropriate manner. The nine coupled differential equations 3.9.4 or 3.9.6 can be solved by using an iterative procedure which essentially expresses the $n_{Im}(t)$ in a Taylor expansion.

$$\underset{\sim}{n}_{Im} \{(\ell+1)\Delta t\} = \underset{\sim}{n}_{Im} \{(\ell)\Delta t\}$$

$$+ \Delta t \sum_{I'm'} S_{ImI'm'} \; \underset{\sim}{n}_{I'm'} \{(\ell)\Delta t\} + O(\Delta t)^2 \qquad 3.9.7$$

Starting with known initial conditions, the time evolution of n_{Im} can be evaluated quite accurately as long as Δt is sufficiently small. The reason that this technique works is because the $n_{Im}(t)$ are "smooth" functions of

time. That is to say, $n_{Im}(t)$ is a monotonically increasing or decreasing function of time whose slope does not change sign. When the $n_{Im}(t)$ have been calculated, $M^{obs}(t)$ can be determined numerically as a function of time via equations 3.9.1 and 3.9.2. There are 45 non zero $S_{ImI'm'}$ involving different linear combinations of 16 values of $W_{ImI'm'}$ most of which in turn involve sums over hundreds of centrifugal distortion states. Although this procedure is sufficient, it is very expensive (in computer dollars) and not aesthetically inviting.

An approximate closed form solution to the problem can be found under certain conditions. We outline the solution and clearly state when it is valid. Substituting equation 3.9.4 into the time derivative of equation 3.9.2 gives

$$\frac{d\tilde{M}^{(I)}}{dt} = \sum_m m \sum_{I'} \sum_{m'} S_{ImI'm'} \tilde{n}_{I'm'}$$

$$= \sum_{I'} \sum_{m'} \left[\sum_m m S_{ImI'm'} \right] \tilde{n}_{I'm'} \qquad 3.9.8$$

If we now define the relaxation function $R^I(I'm')$ by

$$R^I(I'm') = [m' + \delta(m',0)]^{-1} \sum_m m S_{ImI'm'} \qquad 3.9.9$$

then equation 3.9.8 can be written

$$\frac{d\tilde{M}^{(I)}}{dt} = \sum_{I'm'} [m' + \delta(m',0)] R^I(I'm') \tilde{n}_{I'm'} \qquad 3.9.10$$

If, for example, $R^I(I'm')$ is a constant for $I' = I$ and $m' \neq 0$

simultaneously, and zero otherwise equation 3.9.10 reduces to

$$\frac{dM^{(I)}}{dt} = R \sum_m m \, \tilde{n}_{Im} = R \, \tilde{M}^{(I)} \qquad \qquad 3.9.11$$

and the observed relaxation is exponential with a rate constant R.

We note that although $R^I(I'm')$ and $S_{ImI'm'}$ are related via equation 3.9.9., it is far simpler to evaluate the $R^I(I'm')$ by equating 3.9.10 with the result of substituting equation 3.9.3 into the time derivative of equation 3.9.2 to give equation 3.2.9. This has been done because we will want to discuss the $R^I(I'm')$ in detail, they are given explicitly in Table 3.14.

In calculating the $R^I(I'm')$ that appear in Table 3.14, the following relationships have been incorporated. For $I' = I = 2$, time inversion symmetry implies $W(2m'2m) = W(2-m'2-m)$ because no distortion frequencies are involved. As a result of the high temperature approximation, we can reduce the number of terms through the relation $W(I'm'Im) = W(ImI'm')$.

In expressing $R^2(2,m)$ we have utilized the relationship between the $W(2m'2m)$ using the functions $f^{22}(m_2'm_2)$ given in equation 3.8.11. Further we note that $W(2111) = W(2-11-1)$ because the Larmor frequency does not enter and we needn't be concerned whether the distortion frequency is positive or negative since it is squared (denominator of equation 3.8.20).

On investigating Table 3.14, it is clear that in general $R^I(I'm') \neq R^I(I'-m')$ and that $R^I(I'0) \neq 0$. This is a direct consequence of the effects of spin symmetry. As discussed in the previous section spin

Table 3.14 Functions $R^I(I'm')$

$\underline{I}$	$\underline{I'}$	$\underline{m'}$	$\underline{R^I(I'm')}$
2	2	2	$-\frac{1}{2}W(2221)-W(2211)$
2	2	1	$-\frac{1}{2}W(2221)-W(2111)-W(2110)$
2	2	0	0
2	2	-1	$-\frac{1}{2}W(2221)-W(2111)-W(2-110)$
2	2	-2	$-\frac{1}{2}W(2221)-W(2-21-1)$
2	1	1	$2W(2211)+W(2111)$
2	1	0	$W(2110)-W(2-110)$
2	1	-1	$2W(2-21-1)+W(2111)$
1	2	2	$\frac{1}{2}W(2211)$
1	2	1	$W(2111)$
1	2	0	$W(2011)-W(201-1)$
1	2	-1	$W(2111)$
1	2	-2	$\cdot\frac{1}{2}W(2-21-1)$
1	1	1	$-W(1110)-W(2211)-W(2111)-W(2011)-W(0011)$
1	1	0	0
1	1	-1	$-W(1-110)-W(2-21-1)-W(2111)-W(201-1)-W(001-1)$
1	0	0	$W(0011)-W(001-1)$

symmetry manifests itself in the relative signs of the distortion and nuclear frequencies. It is of interest to investigate the two different regimes of experiments; those whose Larmor frequency is near a distortion transition frequency and those whose nuclear Larmor frequency is not near a distortion frequency.

Nuclear spin relaxation measurements can be performed in the range of from zero (T_2 measurements) to about 100 MHz. In this region there are four centrifugal distortion frequencies discussed at the end of the previous section. For experiments performed near one of these frequencies, the relaxation is not exponential as discussed in the next chapter and the iterative procedure which solves the nine coupled differential equations for the populations must be used to give the observed magnetization as a function of time. This is done in the next chapter.

As it turns out, the experiments at 30 MHz fall in the category of being "far away" from a distortion transition. This means that $R^I(I',0)$ is small for $I' \neq I$. The reason that this is so is because $R^I(I',0)$ for $I' \neq I$ is the difference between two transition probabilities (see Table 3.14) which are nearly equal. They in fact differ only by the sign of Δm in the denominator of j_2 (equation 3.8.20). Also, the difference between $R^I(I'm')$ and $R^I(I'-m')$ for $I = I'$ and $m' \neq 0$ is small compared with their absolute values because they both have the same dominant $\Delta I = 0$ transition probability and differ only by a considerably smaller spin conversion ($\Delta I \neq 0$) transition probability(s). Finally, the difference between $R^I(I'm')$ and $R^I(I'-m')$ for $I' \neq I$ and $m' \neq 0$ may not necessarily be small compared with each absolute value but R is small compared with

the same function having $I' = I$. This discussion is only true if the Larmor frequency is sufficiently far removed from all important centrifugal distortion frequencies.

If we can satisfy the conditions that $R^I(I'm')$ is not strongly dependent on m' for $m' \neq 0$ and is very small for $m' = 0$, we can define the function $R^{II'}$ as

$$R^{II'} = \frac{1}{2I'} \sum_{m' \neq 0} R^I(I'm') \qquad 3.9.12$$

Equation 3.9.12 just represents an average where $2I'$ is the number of terms in the sum. With this approximation, equation 3.9.10 becomes

$$\frac{dM^{(I)}}{dt} = \sum_{I'} \sum_{m'_{I'}} m'_{I'} R^{II'} \tilde{n}_{I'm'}$$

$$= \sum_{I'} R^{II'} \tilde{M}^{(I')} \qquad 3.9.13$$

We note that it is not at all intuitively obvious whether or not this approximation is justified.

In the next chapter, it will be shown that at $\omega_N = (2\pi)$ 30 MHz, this is an excellent approximation.

Writing equation 3.9.13 in matrix formulation, gives

$$\frac{d}{dt} \underline{\tilde{M}} = \underline{\underline{R}} \, \underline{\tilde{M}} \qquad 3.9.14$$

Equation 3.9.14 (or 3.9.13) can now be treated as an eigenvalue problem. One diagonalizes $\underline{\underline{R}}$ with the result that one linear combination of $M^{(1)}$ and

$M^{(2)}$ relaxes with a rate constant λ_α and another linear combination relaxes with a second rate constant λ_β. The 2 x 2 matrix which takes $\underline{M}$ into a basis that relaxes with the two time constants is $\underline{\underline{\Lambda}}^{-1}$. In performing this matrix algebra, care must be taken that the correct restraints be put on $\underline{\underline{\Lambda}}$ (or $\underline{\underline{\Lambda}}^{-1}$) because $\underline{M}$ is not a vector in the conventional sense as discussed previously for $\underline{n}$. The sum of the components (i.e., the observed magnetization) must be conserved. The necessary matrix algebra is given in Appendix H and the solution of equation 3.9.14 for the observed magnetization is

$$M^{obs}(t) = \sum_{I'=2,1} \sum_{j=\alpha,\beta} \sum_{I=2,1} \Lambda_{I'j} \Lambda_{jI}^{-1} [M^{(I)}(\infty) - \{M^{(I)}(\infty)$$

$$-M^{(I)}(0)\} e^{-\lambda_j t}] \qquad\qquad 3.9.15$$

For the particular case of the measurements reported in Chapter II, we can put

$$M^{(I)}(0) = -M^{(I)}(\infty) \qquad\qquad 3.9.16$$

which is to say that the π pulse inverts the magnetization. It is clear that the r.f. field treats both spin species equivalently.

Also, the equilibrium contribution of $M^{(I)}(\infty)$ to $M^{obs}(\infty)$ is

$$M^{(I)}(\infty) = f(I) M^{obs}(\infty) \qquad\qquad 3.9.17$$

$$f(I) = \frac{[I(I+1)][2I+1]\sum_J [N(I,J)]}{\sum_I [I(I+1)][2I+1]\sum_J [N(I,J)]} \qquad\qquad 3.9.18$$

N(I,J) is given in equation 3.8.6. The sum over J of N(I,J) is the degeneracy of the Ith species. The m_I degeneracy is $2I+1$ and $I(I+1)$ is the contribution to the equilibrium magnetization of a molecule in the Ith state. (i.e., via Curie's Law). Equation 3.9.18 is easily evaluated with the results

$$f(1) = 0.375 ; \qquad f(2) = 0.625 \qquad\qquad 3.9.19$$

Using equations 3.9.16 to 3.9.18, equation 3.9.15 can be expressed

$$M^{obs}(t) = M^{obs}(\infty) \sum_{I'=2,1} \sum_{j=\alpha,\beta} \sum_{I=2,1} \Lambda_{I'j} \Lambda_{jI} f(I)[1-2e^{-\lambda_j t}]$$

$$3.9.20$$

The validity of equation 3.9.20 rests on the relative sizes of the $R^I(I'm')$ which define the averages $R^{II'}$ through equation 3.9.12. Only by comparing the time evolution of the magnetization given in equation 3.9.20 with the equivalent quantity generated iteratively from equations 3.9.2 and 3.9.7 can the validity of equation 3.9.20 be determined.

CHAPTER IV

THEORETICAL PREDICTIONS AND COMPARISON WITH EXPERIMENT

4.1   SUMMARY OF CHAPTER III

The time evolution of the observed magnetization can be obtained by iteratively solving the nine coupled differential equations for the populations given by equations 3.9.7. This requires the initial populations and the relaxation functions $S_{I'm'Im}$ given in Table 3.13.

If the nuclear Larmor frequency is "far" from a centrifugal distortion frequency, the relaxation problem can be solved in closed form by calculating the relaxation functions $R^{I'I}$. This then leads at most to two relaxation rates which are computed by solving the eigenvalue problem. The $R^{I'I}$ are related to the $S_{I'm'Im}$ via the relaxation functions $R^{I}(I'm')$. See equation 3.9.12. The meaning of the word "far" is to be determined by comparing this method with that of the previous paragraph.

All these relaxation functions are linear combinations of nuclear spin transition probabilities. These transition probabilities are expressed in terms of the functions A, F, B, C, D and E. Each of these functions are sums of products of two factors; the sums running over the centrifugal distortion states. The first factor contains the square of the spin-rotation matrix element and the second factor contains the reduced spectral density. The former is a measure of the strength of the interaction and the latter is

a measure of the broadening due to collisions. The terms A and F involve the scalar ($\Delta I = 0$) spin rotation interaction for $I = 2$ and $I = 1$ respectively. B, C, D and E involve the tensor ($\Delta I = o, 1$) spin-rotation interaction for $I' \rightarrow I$ of $1 \rightarrow 1$, $1 \rightarrow 1$, $2 \rightarrow 1$, and $0 \rightarrow 1$ respectively. C, D and E involve a change in centrifugal distortion energy whereas B does not. The qualitative features of these functions are to be found in Table 3.10.

If the correlation times are independent of J, the situation is somewhat simpler and the reduced spectral density can be factored out of the functions A, F and B. The remaining functions are given by A', F' and B' as indicated in equation 3.8.25. These primed functions are independent of correlation time and although they involve non-trival sums over the rotational parameters, they can be evaluated independently of correlation time. If the correlation times are made J-dependent, the transformation to the primed functions is not possible.

The reduced spectral densities for the functions C, D and E as defined in equation 3.8.20 contain the correlation time τ_2 as well as the centrifugal distortion frequencies associated with the particular transitions. Thus each term must be evaluated for a particular correlation time before the summation over the rotational indices can be performed, even if τ_2 is independent of J. The square of the tensor spin-rotation matrix elements are contained in the Z-functions which are essentially a temperature dependent weight times a Π-function squared as indicated in equation 3.8.36. The Π-functions are defined in terms of V-functions and Q-functions (equation 3.7.27). The Q-functions as given in equation 3.7.20 contain that part of the matrix element that can be expressed in closed form and the V-functions

in equation 3.7.14 contain that part of the matrix element that must be
calculated numerically, namely the rotational A-constants as defined in
equation 3.4.2.

4.2   NUMERICAL COMPUTATIONS

There are basically two non-trivial computer programmes used to investigate the relaxation process in a quantitative way. These computations were performed with the I.B.M. 370/168 computer at the University of British Columbia. The Figures in this chapter and all the appendices were generated by a Calcomp Plotter on line to the I.B.M. 370.

The first programme calculates the functions $W(T:C_a^2;\gamma,J)$, $X(T:C_aC_d;F,J)$, $Y(T:C_d^2;F,J)$ and $Z(T:C_d^2\gamma',\gamma;J,t',t,\rho)$ as given in equations 3.8.30, 3.8.31, 3.8.32 and 3.8.36. These functions, which are needed in the calculation of A, F, B, C, D and E are all independent of correlation time or, equivalently, density. W, X and Y only require subroutines to calculate $U(I,T)$ and $N(I,T)$ given by equations 3.8.7 and 3.8.6 before the rotational sums can be performed. As discussed in the previous section, the more than 700 values of $Z(T:C_d^2;\gamma',\gamma;J,t',t,\rho)$ contain several functions, all of which can be expressed algebraically except the rotational A-constants. The 3,476 non-zero A-constants were calculated using a computer programme based on subroutines provided by Irving Ozier of the Physics Department at the University of British Columbia. The calculation of the A-constants is expensive but need be done only once and stored on magnetic tape. The programme which calculates the Z-functions then simply calls the numbers from the magnetic tape.

The second programme provides a variety of functions. It calculates all the transition probabilities $W_{I'm'Im}$ for a fixed correlation time by; a) reading the W, X, Y and Z-functions and the appropriate centrifugal distortion frequency for each Z-function, b) reading the temperature, c) multi-

plying by the appropriate $j_i(\omega)$, d) summing over the distortion states, and, e) multiplying by the appropriate $f^{I'I}(m',m)$. Great care was taken in determining the relative signs of the nuclear (minus molecular) Larmor frequency and the centrifugal distortion frequencies in calculating $j_i(\omega)$. From this point the programme had several branches.

If the iterative procedure is used, the $S_{I'm'Im}$ are calculated from the transition probabilities via Table 3.13 and the time evolution of the populations of the spin states are calculated (equation 3.9.7). The initial $(t = 0)$ populations were calculated using $n_{Im}(0) = n_{I,-m}(\infty)$ and Curie's Law. The steps Δt in the iterative procedure were reduced until the resulting expressions changed by less than 0.5%. This did not require as small steps as may be thought since $n_{Im}(t)$ are smoothly varying and monotomically increasing or decreasing functions of time. The magnetization was calculated at each step of Δt as was the total number of spins to ensure it remained constant. The fact that it did so is a useful check because it implies that the rows and columns of $S_{I'm'Im}$ (Table 3.13) must add to unity.

The programme then determines whether or not the relaxation is well represented by a single relaxation rate (i.e., by a single exponential function). We must define the term "well represented". First we define the times t' by $\tilde{M}(t') = 0.75 \, \tilde{M}(0)$, t'' by $\tilde{M}(t'') = 0.2 \, \tilde{M}(0)$ and t''' by $t''' = t'' + t'$. Thus the range of times Δt from zero to t' and from t'' to t''' are equal. If the relaxation rate calculated on the basis of $\tilde{M}(t)$ over the range from $t = 0$ to $t = t'$ and the relaxation rate calculated on the basis of $\tilde{M}(t)$ over the range from $t = t''$ to $t = t'''$ differ by less than 3%, we say the relaxation is well represented by a single exponential. The tilda refers to the departures from the equilibrium magnetization. These relaxation rates were computed

using the same programme used to interpret the experimental data, the only difference being the points were weighted equally. If the relaxation is well represented by a single rate constant it is then calculated on the basis of all the $\tilde{M}(t)$ values.

The output, then, of this branch of the programme is a single relaxation rate if the relaxation is well represented by a single rate or, if not, the two relaxation rates discussed above. The latter will be used in Section 4.7. This branch of the programme is very costly.

The other way the programme can be used is to solve the eigenvalue problem. This was only used if the procedure discussed in the previous two paragraphs resulted in the relaxation being well represented by a single rate constant. By making spot checks for the limiting values of the relevant parameters (namely frequency, temperature and correlation times) it was determined where this procedure could be used. Solving the 2 x 2 eigenvalue problem is far less costly than the iterative procedure and provides considerably more information. The $R^{II'}$ are computed from the $R^I(I'm')$ (equation 3.9.12) which in turn are computed from the $W_{I'm'Im}$ (Table 3.14). A consistency check was made by comparing the $R^I(I'm')$ so obtained with those computed from the $S_{ImI'm'}$ (equation 3.9.9). The $R^{II'}$ matrix is then diagonalized and the relaxation rates λ_α and λ_β are obtained as is the matrix $\underline{\underline{A}}$. The matrix $\underline{\underline{A}}$ relates the basis $\underline{M}^{(1)}$, $\underline{M}^{(2)}$ (the magnetization associated with each nuclear spin species) with the basis N_α, N_β (the magnetizations that relax with the rate constants λ_α and λ_β). This is discussed in Section 3.9. Also, the percentage of the observed magnetization (= $\underline{M}^{(1)} + \underline{M}^{(2)}$) associated with each rate constant is calculated. Finally, a single relaxation rate is computed using the least

squares fit with equal weights. (See equation 3.9.20) This was satisfactory (where it was used) because at higher densities essentially 100% of the magnetization relaxes with one of the rate constants. At low densities (long correlation times) where the two independent magnetizations are often comparable in magnitude, the two relaxation rates were nearly equal.

Finally, the second programme performed all these calculations as a function of either density (correlation time) for fixed nuclear Larmor frequency or as a function of nuclear Larmor frequency for fixed density. The correlation times τ_1 used in j_1 (A and F functions) and τ_2 used in j_2 (B, C, D and E functions) could be made different and, if desired, J dependent.

4.3   THE $R^I(I'm')$ AS A FUNCTION OF FREQUENCY

In this section the relaxation functions $R^I(I'm')$ are computed as a function of frequency. Doing so will serve two purposes. First, we can get an idea when calculating the relaxation rate from the diagonalization of the 2 x 2 matrix $R^{I'I}$ should be valid, and secondly, we will get a qualitative and quantitative feeling for the effects of centrifugal distortion. We assume that the correlation times τ_1 and τ_2 are both equal and independent of J. We choose this simple case because it turns out à posteriori to fit the experimental results quite well. Further, we choose $\tau = \tau_1 = \tau_2 = 2.36 \times 10^{-8}$ S. This corresponds to a density at room temperature of 0.01 amagat. The relationship between correlation time and density is developed in Section 4.5 but does not concern us here. This is a convenient τ because it is well within the experimental range and it corresponds to about the highest density where the effects of single centrifugal distortion transitions are clearly visible.

The $R^I(I'm')$ are expressed in terms of the nuclear spin transition probabilities in Table 3.14. Figure 4.1 is a plot of the seven non-zero values of $R^2(Im)$ as a function of the nuclear Larmor frequency $\nu_N = (2\pi)^{-1}\omega_N$ at T = 295 K and $\tau = 2.36 \times 10^{-8}$S (or 10^{-2} amagat). Figure 4.2 is a similar plot for the nine non-zero values of $R^1(Im)$, only five of which appear to be non-zero on the vertical scale employed. We use the nuclear Larmor frequency ν_N and not the seemingly more relevant difference ν_0 between the nuclear and molecular Larmor frequencies because the nuclear spin relaxation measurements are performed at the frequency ν_N. On these plots there are two distinct regions, namely below and above about 40 MHz.

Below about 40 MHz, all the values of $R^I(I'm')$ have essentially

coalesced into two values. In Figure 4.1, the single non-zero line cor-

responds to the 4 values of $R^2(2,m')$ with $m' = -2, -1, 1, 2.$ The average

value of these four functions, namely R^{22} as defined in equation 3.9.12, will

be a satisfactory representation of the $I = 2$ to $I = 2$ relaxation. The line

at zero corresponds to all the other $R^2(Im)$. Although on the scale of Fig-

ure 4.1 they are zero, the largest at 30 MHz is $R^2(1,1)$ which is about 3% of

R^{22}. Although the two functions $R^2(1,m)$ for $m = -1, 1$ are considerably dif-

ferent, the procedure involved with taking their average (namely R^{21}) is

satisfactory because they are so small. The reason we can say it is satis-

factory is that the resulting relaxation rates have been compared with those

calculated using the iterative procedure and they agree to within less than

2%. If we were to plot the equivalent of Figure 4.1 at 10 amagat, the mag-

nitude of R^{21} would be about 18% of that of R^{22} but the $R^2(1,m)$ with $m = -1, 1$

used to define the average R^{21} would be equal to better than one part in a

thousand.

The same discussion follows for $R^1(Im)$ in Figure 4.2. The single

non-zero line below 40 MHz corresponds to $R^1(1m)$ for $m = 1, 1,$ the average

of the two becoming R^{11}. The line which is zero on the scale of Figure 4.2

corresponds to the other seven values of $R^1(Im)$, four of which will be aver-

aged to give R^{12} (namely $R^1(2,m)$, $m = -2, -1, 1, 2$)).

It should be pointed out that although R^{12} and R^{21} are small com-

pared with R^{11} and R^{22}, this does not mean that centrifugal distortion effects

are negligible at this low density because their contributions to R^{11} and R^{22}

are not negligible. Further, spin symmetry effects are evident in that R^{11}

and R^{22} differ by about 12%. The origin of this difference at 0.01 amagat is the term $B'(T;C_d^2)$ (see Table 3.10) which contributes to R^{11} and not to R^{22}. At this density, the process could be adequately described by setting $R^{12} = R^{21} = 0$. At higher densities, R^{12} and R^{21} will be appreciable, but the $R^1(2m)$ which determine R^{12} will be independent of m to about one part in a thousand. The same comments are true for R^{21}.

Thus, below about 40 MHz, instead of solving the relaxation problem via the evolution of the populations of the nine spin states, the relaxation can be characterized by the evolution of the magnetizations associated with the $I = 1$ and $I = 2$ spin species.

Above about 40 MHz the situation is quite different and the procedure leading to the evaluation of $R^{I'I}$ and the ensuing eigenvalue calculations are clearly not justified. In this regime the iterative procedure will have to be used and near centrifugal distortion frequencies, the relaxation can not be well represented by a single exponential. The structure at 76 MHz in Figure 4.1 and at 55, 76, 127, 159 and 177 MHz in Figure 4.2 corresponds to centrifugal distortion transitions at 52, -72, 120, 150, and -167 MHz. All the quantum numbers and group theoretical indices associated with these transitions are given in Table 4.1. The definitions concerning the signs of these frequencies are discussed in Section 3.8. The ratio of the distortion frequencies to the nuclear Larmor frequency at which the structure occurs is 0.944 which is the ratio ν_0/ν_N (see Section 3.3). In order to understand this structure we investigate the situation at 55 and 76 MHz.

The distortion transition at 52 MHz is E→F ($I = 0 \rightarrow I = 1$) and therefore does not affect any of the $R^2(Im)$ which involve only $A \rightarrow A$ and $A \rightarrow F$ transition probabilities. The top line at 55 MHz in Figure 4.2 is $R^1(1, 1)$

TABLE 4.1 LOW FREQUENCY CENTRIFUGAL DISTORTION TRANSITIONS

Frequency (MHz)	J	ρ	γ'	γ	t'	t	I'	I
7.97	2	2	E	F2	1	1	0	1
51.8	5	2	E	F2	1	2	0	1
-71.7	3	2	A1	F2	1	1	2	1
119.5	4	2	E	F2	1	1	0	1
150.0	8	2	E	F2	2	2	0	1
-167.3	7	1	E	F1	1	2	0	1

which is considerably affected whereas $R^1(1,-1)$ is not affected very much. There are five transition probabilities $W(I'm'Im)$ that contribute to $R^1(1,-1)$ and $R^1(1,1)$. Of the five, the one that is affected by the 52 MHz transition for $R^1(1,1)$ is $W(0011)$ and for $R^1(1,-1)$ it is $W(001-1)$. Further, from equation 3.8.17 we note that $f^{01}(01) = f^{01}(0-1)$ so the difference between $W(0011)$ and $W(001-1)$ is due to the difference between $D(T;0-(+1):C_d^2)$ and $D(T;0,-(-1):C_d^2)$ in equation 3.8.24. In the sum over J, t', t and ρ in equation 3.8.35 one term is completely dominant for $m = 1$ but $\underline{not}$ for $m = -1$. This term is the $J = 5$, $t' = t = 1$, $\rho = 1$ transition with $(2\pi)^{-1}[\omega(5,E,1,1) - \omega(5,F1,1,1)] = 52$ MHz. The difference in this term's contribution to $D(T;0-(1):C_d^2)$ and $D(T;0-(-1):C_d^2)$ is in the denominator of j_2 in equation 3.8.20. The function j_2 for this term's contribution to $D(T;0-(1):C_d^2)$ is

$$\tfrac{1}{2}j_2 \quad = \quad \frac{\tau_2}{1 + \tau_2^2 (2\pi)^2 [52 \times 10^6 - (1-0) \, 52 \times 10^6]^2}$$

$$= \quad \tau_2 \quad = \quad 2.36 \times 10^{-8} \text{ s} \qquad\qquad (4.3.1)$$

and the function j_2 for this term's contribution to $D(T;0-(-1):C_d^2)$ is

$$\tfrac{1}{2}j_2 \quad = \quad \frac{\tau_2}{1 + \tau_2^2 (2\pi)^2 [52 \times 10^6 - (-1-0) \, 52 \times 10^6]^2}$$

$$= \frac{\tau_2}{1 + \tau_2 \, (2\pi)^2 \, [103.6 \times 10^6]^2}$$

$$= 3.93 \times 10^{-10} \text{ S} \qquad\qquad (4.3.2)$$

As a result, $D(T;0-(1):C_d^2)$ is larger than $D(T;0-(-1):C_d^2)$, $W(0011)$ is larger than $W(001-1)$ and $R^1(1,1)$ is larger than $R^1(1,-1)$. The effect of this single contribution is simply the difference between $R^1(1,1)$ and $R^1(1,-1)$ in Figure 4.2 (except for the tail of the structure at 76 MHz). This difference is exactly $R^1(0,0)$ because (from Table 3.14)

$$R^1(0,0) \quad = \quad -W(0011) + W(001-1) \qquad\qquad (4.3.3)$$

$R^1(0,0)$ is not influenced by the tail of the structure at 76 MHz because that transition is A → F. Thus $R^1(0,0)$ is the dip at 55 MHz in Figure 4.2.

The structure at the other frequencies can be analyzed in the same way. In particular, the 76 MHz transition involves all the $R^I(I'm')$ except $R^1(2,\pm1)$ because they are independent of Larmor frequency (i.e., $\Delta m = 0$, see Table 3.14).

The previous discussion concerning the effects of individual distortion splittings on the $R^I(I'm')$ may appear relatively complex. A simpler, perhaps somewhat more intuitive picture involves level crossing. Using

the 76 MHz splitting as an example, it can be seen that at a magnetic field

where the nuclear (minus molecular) Larmor frequency is the same as the

centrifugal distortion splitting, some nuclear spin states will cross. This

is shown in Figure 3.2. The $n_{2,-2}$ and $n_{2,-1}$ levels are unaffected by any n_{1m}

levels with the result that $R^2(2,-2)$ and $R^2(2,-1)$ in Figure 4.1 are unaffected

by the 72 MHz distortion line at a nuclear Larmor frequency of 76 MHz (nuclear

minus molecular Larmor frequency of 72 MHz). The $n_{2,2}$ and $n_{1,1}$ levels, how-

ever, cross at this magnetic field. This crossing manifests itself by the bump

at 76 MHz for $R^2(2,2)$ in Figure 4.1 and $R^1(1,1)$ in Figure 4.2 and the valleys

in the cross relaxation functions $R^2(1,1)$ in Figure 4.1 and $R^1(2,2)$ in Fig-

ure 4.2. The qualitative features of the other $R^I(I'm')$ can be analyzed in

terms of the energy level diagram in Figure 3.2.

The relaxation process is very complicated at these distortion

frequencies and there is no way of estimating the effects on the time evolution

of the magnetization - it simply must be calculated using the iterative pro-

cedure discussed previously.

Figures 4.3 to 4.8 contain similar plots (i.e., all correspond to

10^{-2} amagat) for 150, 110 and 77 K. We note that as temperature is decreased

the effect at 76 MHz (J = 3) become very pronounced and the effects at 55 MHz

(J = 5), less so. It is also noted that the tail of the 8 MHz line (J = 2) is

becoming larger - far too small however even at 77 K to have much effect on the

relaxation at 30 MHz.

Before fitting the 30 MHz measurements we will attempt to determine

the predictions of the theory in the limit that spin-symmetry effects are

negligible. The resulting relaxation rates will not be compatible with the

measurements but will allow a comparison with the theory of Dong and Bloom (16). This serves two useful purposes. First, it presents a check on the present theory for that part of the relaxation resulting from the scalar spin-rotation interaction. Secondly, it serves as a numerical example of the matrix algebra developed in Appendix H and discussed in Section 3.9.

Finally, before comparing the theoretical predictions with the measured relaxation rates at 30 MHz we must relate the correlation times with the density, the latter being the experimentally measured parameter.
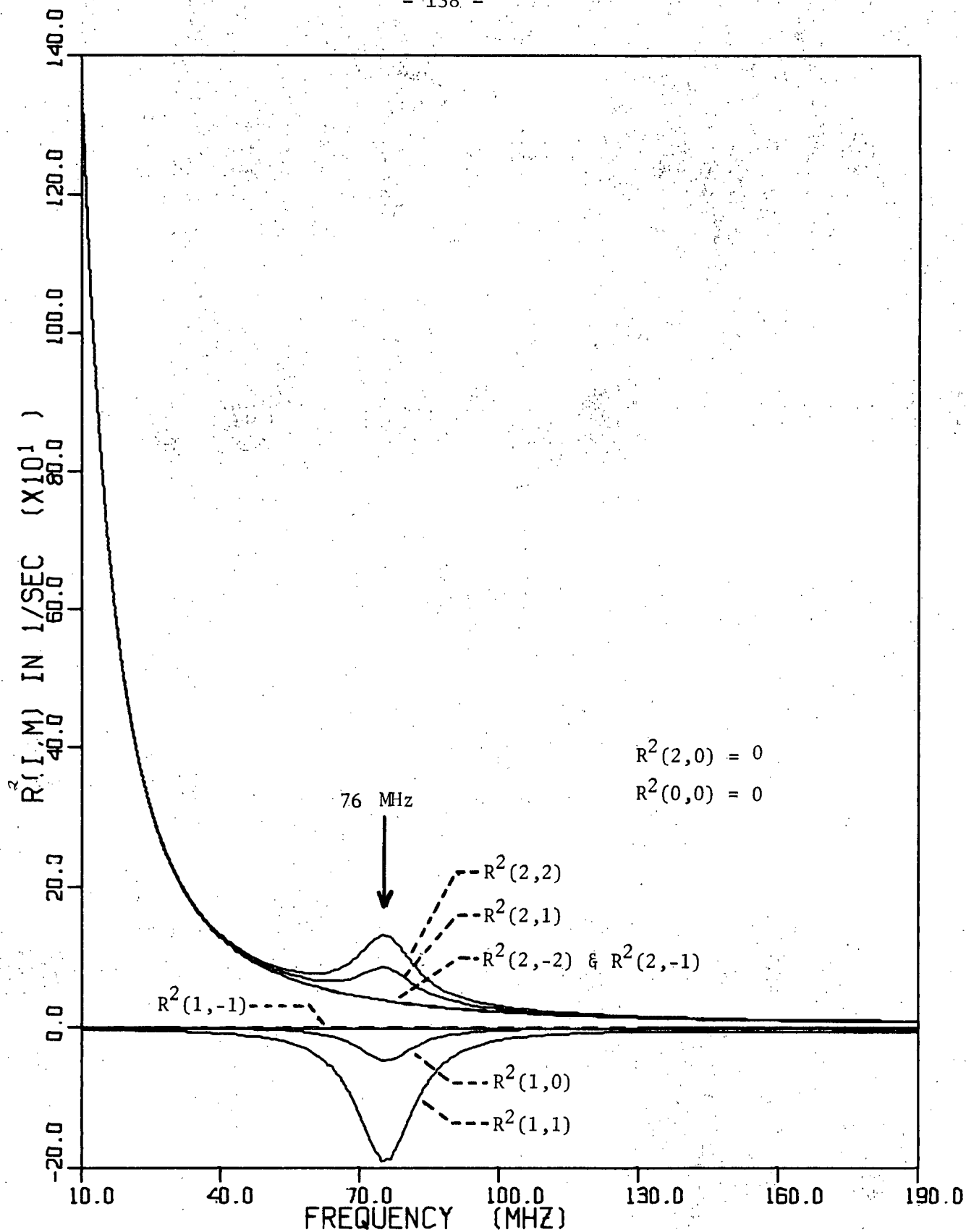
Figure 4.1. The relaxation functions $R^2(I,m)$ evaluated as a function of nuclear Larmor frequency for T = 295K and ρ = 0.01 amagat.
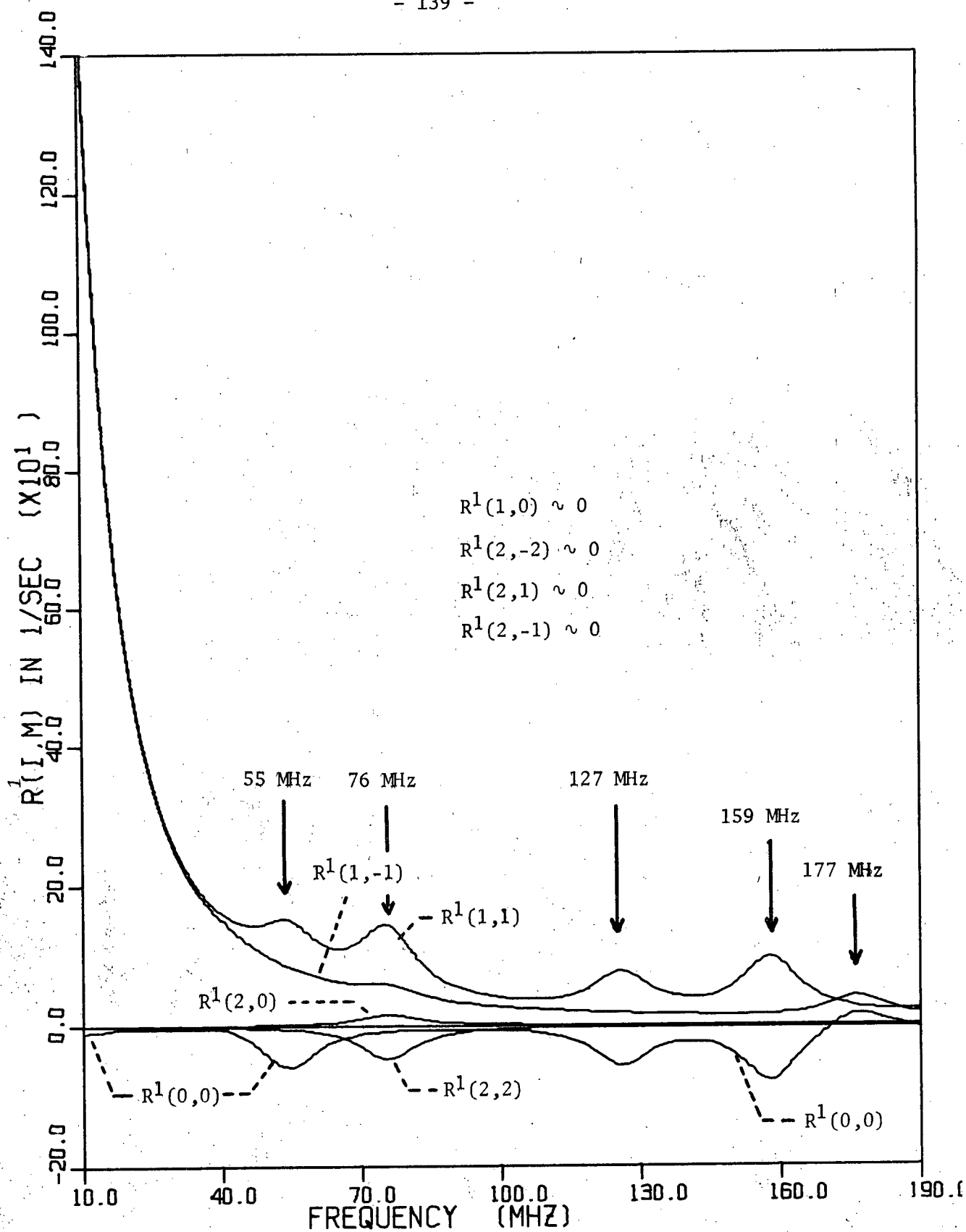
Figure 4.2. The relaxation functions $R^1(I,m)$ evaluated as a function of nuclear Larmor frequency for T = 295K and ρ = 0.01 amagat.

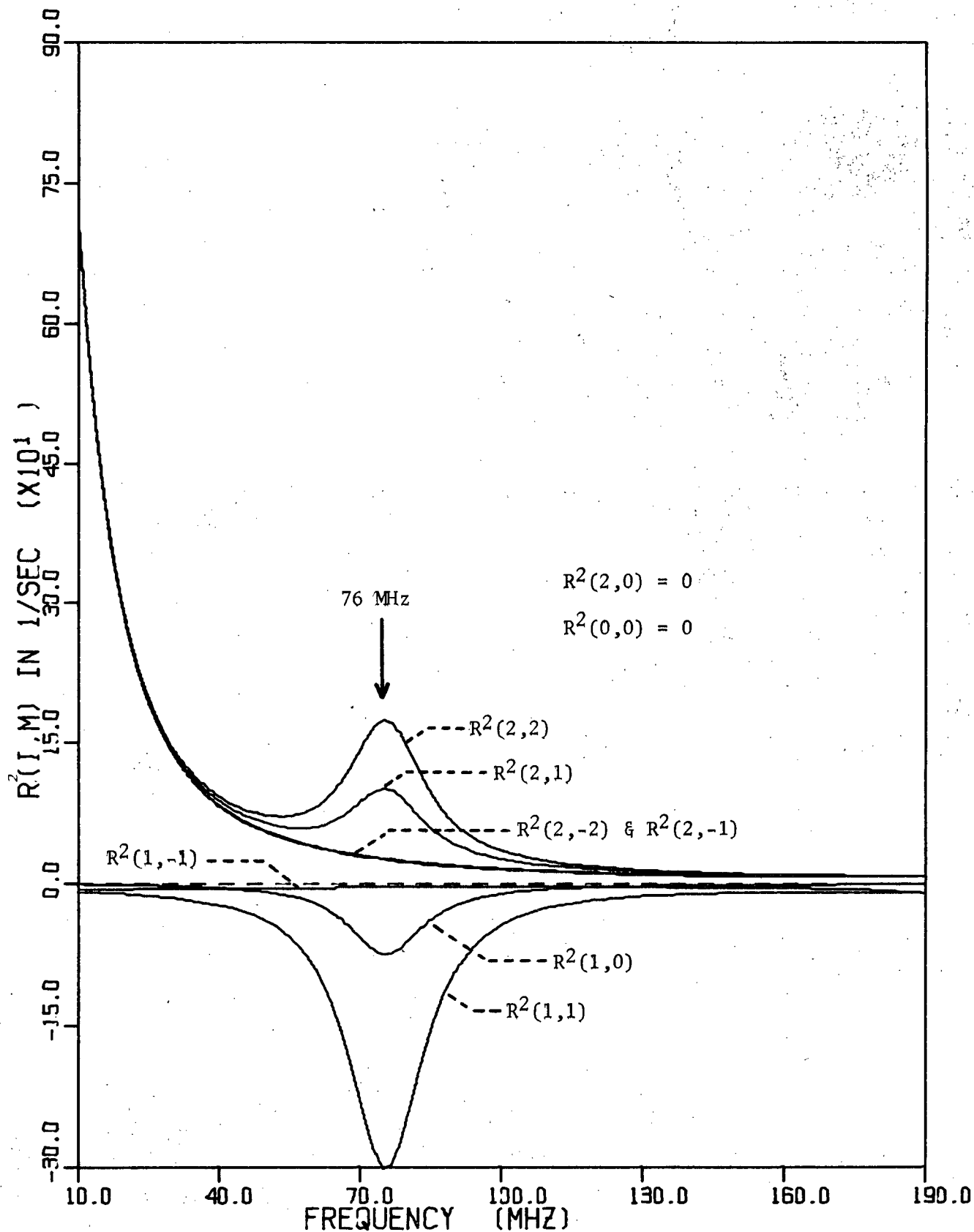Figure 4.3. The relaxation function $R^2(I,m)$ evaluated as a function of nuclear Larmor frequency for T = 150K and ρ = 0.01 amagat.

Figure 4.4. The relaxation functions R^1 (I,m) evaluated as a function of nuclear Larmor frequency for T = 150K and ρ = 0.01 amagat.
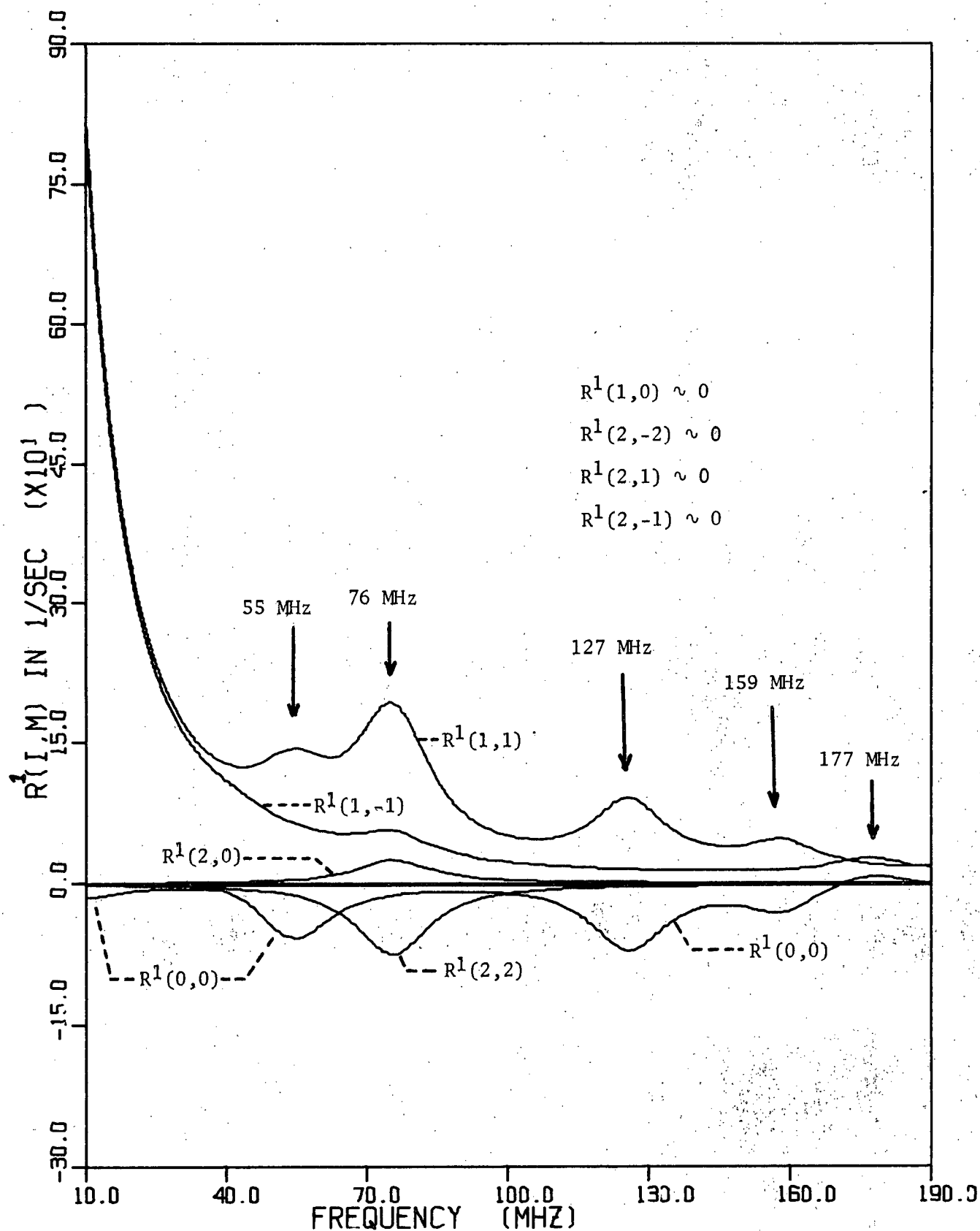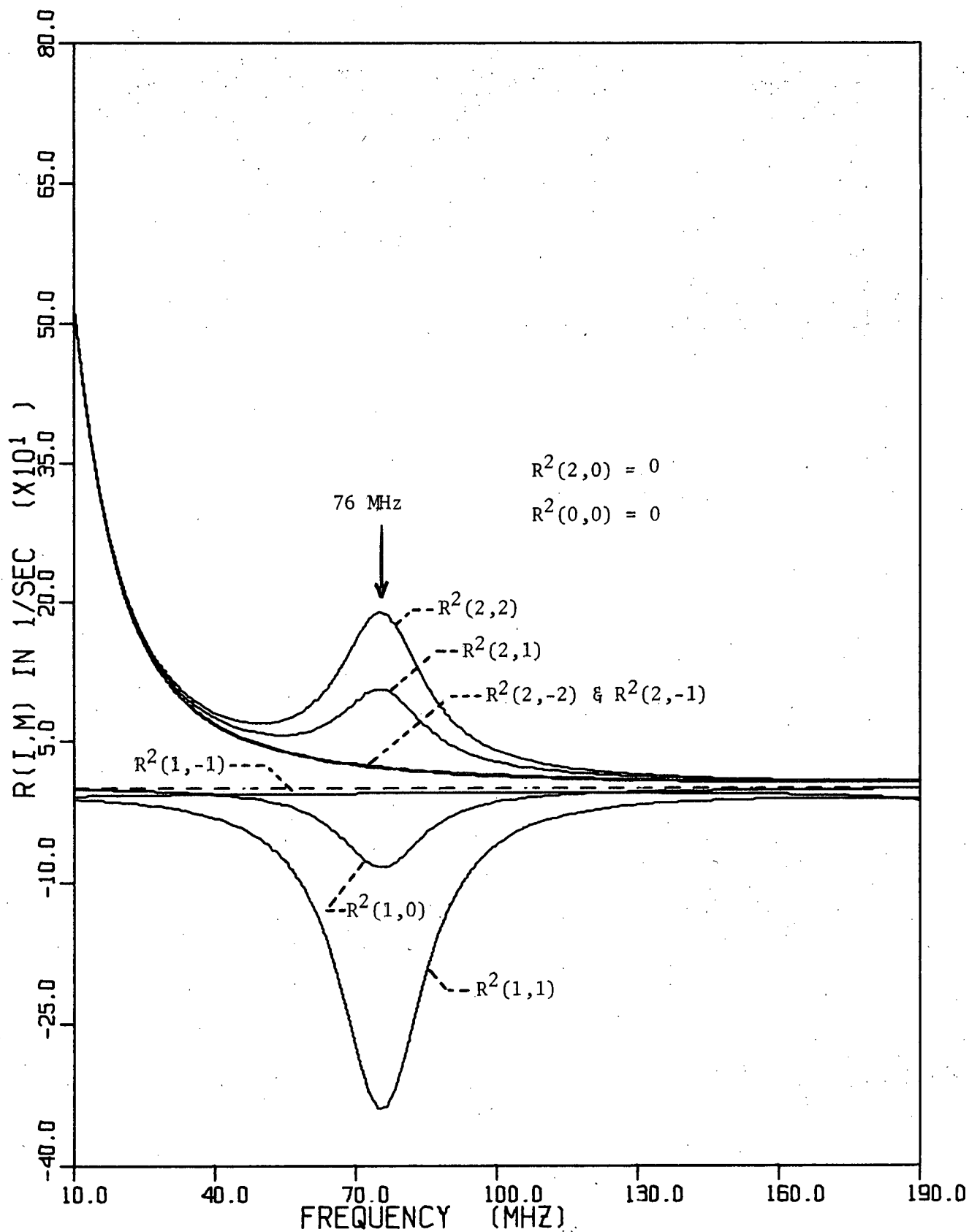
Figure 4.5. The relaxation functions $R^2(I,m)$ evaluated as a function of nuclear Larmor frequency for $T = 110K$ and $\rho = 0.01$ amagat.
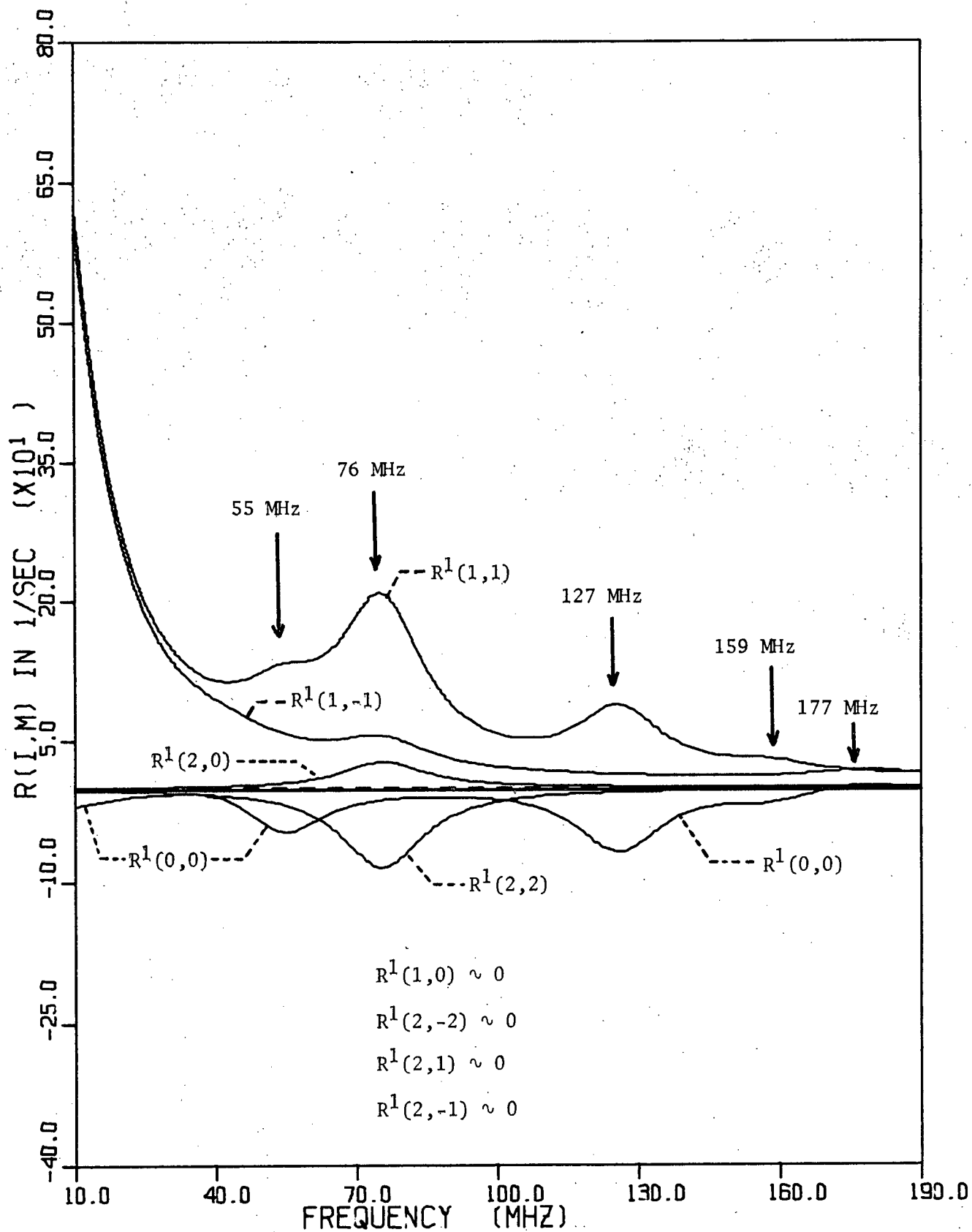
Figure 4.6. The relaxation functions $R^1(I,m)$ evaluated as a function of nuclear Larmor frequency for $T = 110K$ and $\rho = 0.01$ amagat.

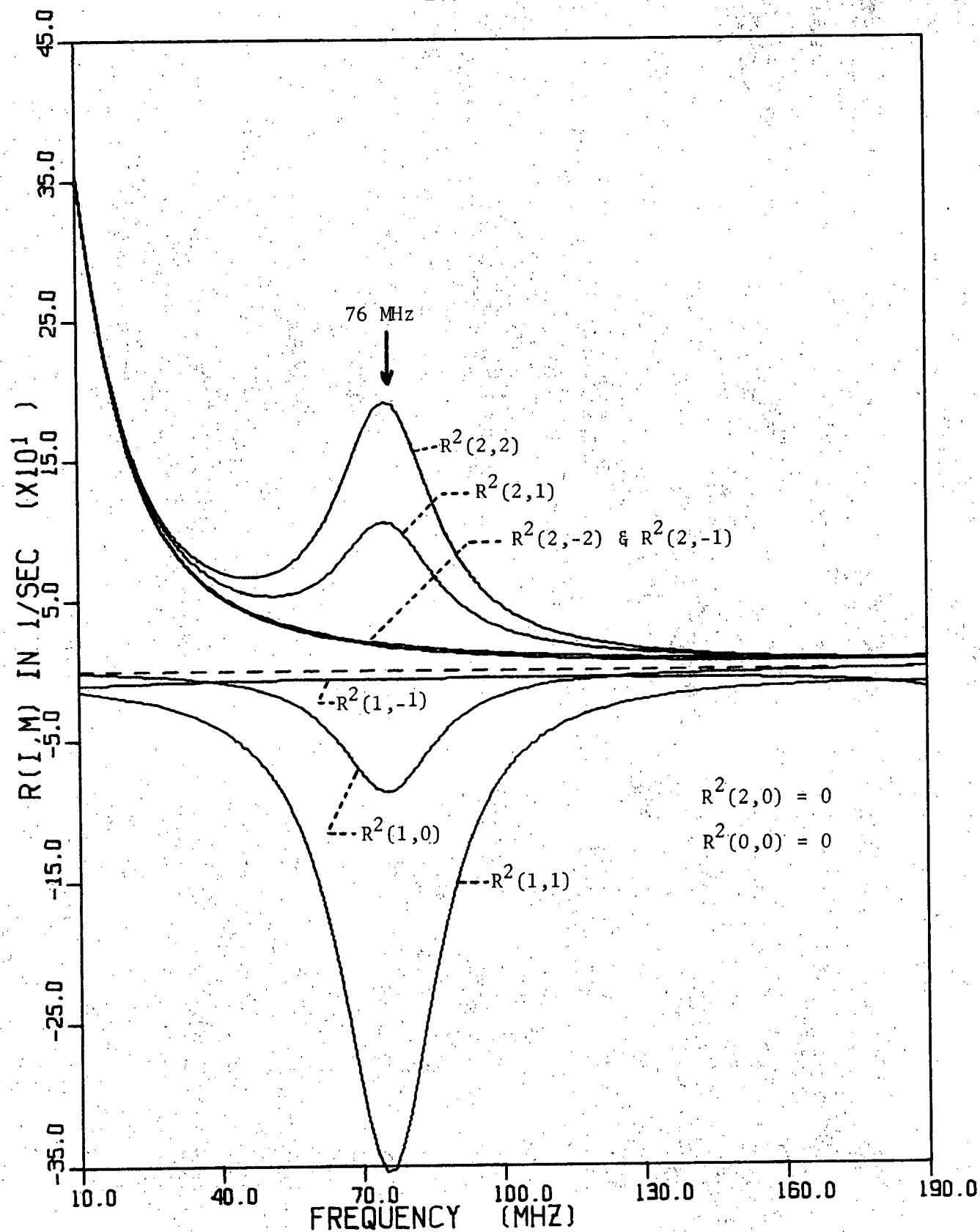Figure 4.7.   The relaxation functions $R^2(I,m)$ evaluated as a function of nuclear Larmor frequency for T = 77K and ρ = 0.01 amagat.

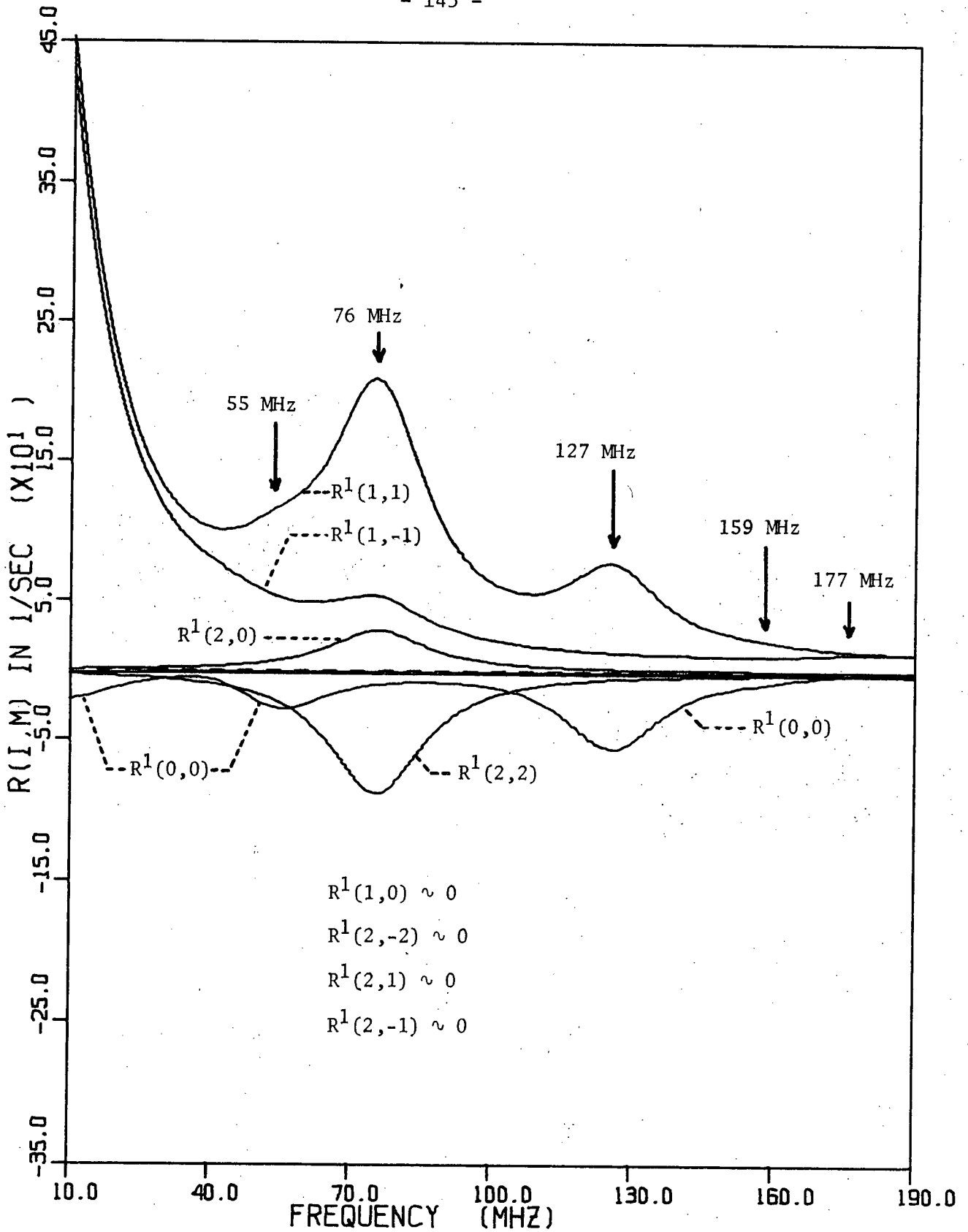Figure 4.8. The relaxation function $R^1(I,m)$ evaluated as a function of nuclear Larmor frequency for T = 77K and ρ = 0.01 amagat.

4.4 COMPARISON WITH THE THEORY OF DONG AND BLOOM

The theory of Dong and Bloom (16)[1] neglects spin symmetry effects and assumes further that the influence of the distortion transitions to the nuclear spin relaxation are negligible. As a result, the sums over the rotational degrees of freedom are much simplified and can be expressed in closed form in terms of moments of inertia of the molecule (or the rotational constant B) and the spin-rotation coupling constants. Further, DB develop the theory for symmetric tops and extend it in a perfectly natural way to spherical tops. Because spherical tops have only one distinct moment of inertia whereas symmetric tops have two, this extension leads to the disappearance of any terms in $C_a C_d$. Although it is not clear from the outset of the present spin-symmetry calculations that there are no contributions to the $I' = 1 \rightarrow I = 1$ nuclear spin transition probabilities involving terms in $C_a C_d$, one of the numerical results of this analysis is that such a term is at least completely negligible and possibly identically zero (see section 3.8). Thus we are in agreement with DB on this point.

The theory of DB is reviewed in the literature (16) and we do not discuss the details. They find the relaxation is exponential with the relaxation rate given by[2]

$$R_1 = \frac{4\pi^2}{\alpha} C_a^2 \{\tfrac{1}{2} j_1(\omega_0)\} + \frac{4}{45} \frac{4\pi^2}{\alpha} C_d^2 \{\tfrac{1}{2} j_2(\omega_0)\} \qquad (4.4.1)$$

---

[1] Referred to as DB

[2] ω_0 in DB = ω_N here so ω_0 here = $\omega_0 - \omega_J$ in DB where ω_J is the molecular Larmor angular frequency. Also j_1 here is the same as in DB, but j_2 is labelled by j_{12}' in DB. Equation 4.41 is in our notation.

with $\alpha = B(kT)^{-1}$. Further, DB find no evidence from fitting the measurements that j_1 is different from j_2 and set $j_1 = j_2$ which yields

$$R_1 = \frac{4\pi^2}{\alpha} C_{eff}^2 \{\tfrac{1}{2}j_1(\omega_0)\} \qquad (4.4.2)$$

$$C_{eff}^2 = C_a^2 + \frac{4}{45} C_d^2 \qquad (4.4.3)$$

On inspection of the DB theory, it is clear that if C_d is set to zero the present theory and that of DB should agree. The reason for this is related to the fact that with this assumption spin symmetry plays no role. That the two theories are in complete agreement in this limit is indicated in Appendix I.

A comparison of the two theories for the terms in C_d involves interpreting the present theory in the limit that spin symmetry effects are negligible. It is assumed that this implies all the non-zero frequency centrifugal distortion transitions should be assigned to zero frequency. This process is discussed in detail in Appendix I and it is remarkable how well the theories agree in this limit. The general result of Appendix I is that if all the centrifugal distortion transitions are assigned to zero frequency, the relaxation is indeed exponential and is given by equation 4.4.1 where the factor 4/45 is, perhaps, about 15% too large.

The important point, however, is that the DB theory or equivalently the present theory in the limit where spin-symmetry effects are neglected is

incompatible with the experimental results. This is clear from Figure I.1 to I.6 where an attempt to fit equation 4.4.2 to the data is made. The fitting procedure used and the various alternatives are discussed in Appendix I.

The coupling constants C_a and C_d are 10.4 ± 0.1 kHz and 18.5 ± 0.5 kHz, respectively (32). This gives a C_{eff} of 11.8 kHz.

4.5   RELATING DENSITY AND CORRELATION TIME

In order to compare theory and experiment we must relate the correlation times to the density ρ. In general, at low density,

$$\tau_i^{-1} \quad = \quad \rho <\sigma v>_i \quad = \quad \rho \bar{\sigma}_i \bar{v} \quad\quad\quad (4.5.1)$$

where $<\ >$ denotes a Canonical Ensemble average, $\bar{v}$ is the average relative velocity of a colliding pair and equation 4.5.1 defines $\bar{\sigma}_i$, the average or effective cross section.

We can now use equation 4.5.1 to rewrite the reduced spectral density $j_1(\omega_0)$ associated with the scalar spin-rotation interaction and given in equation 3.8.19.

$$\tfrac{1}{2} j_1(\omega_0) \quad = \quad \frac{\dfrac{1}{\bar{\sigma}_1 \bar{v} \rho}}{1 + \dfrac{\omega_0^2}{\bar{\sigma}_1^{\,2} \bar{v}^2 \rho^2}} \quad\quad\quad (4.5.2)$$

The maximum contribution to the relaxation rate for terms involving $j_1(\omega_0)$ will occur at a density ρ_1 given by

$$[j_1(\omega_0)]_{MAX} \quad = \quad \frac{1}{\bar{\sigma}_1 \bar{v} \rho_1} \quad\quad\quad (4.5.3)$$

where

$$\frac{\omega_0}{\bar{\sigma}_1 \bar{v} \rho_1} = 1 \qquad (4.5.4)$$

This is simply the density at which the frequency of collisions which re-orient the molecule is equal to ω_0 (i.e., $\tau_1^{-1} = \omega_0$). In other words, ρ_1 is the density at which the nuclear spins "see" the largest ω_0 component of those local fields that have their origin in the scalar spin-rotation interation.

Because the parameter ρ_1 is more convenient than $\bar{\sigma}_1$ for inter-preting the nuclear spin relaxation measurements, $\bar{\sigma}_1 \bar{v}$ is eliminated from equation 4.5.2 by using equation 4.5.4. The result is;

$$\tfrac{1}{2} j_1(\omega_0) = \frac{\frac{1}{\omega_0} \left[\frac{\rho_1}{\rho}\right]}{1 + \left[\frac{\rho_1}{\rho}\right]^2} \qquad (4.5.5)$$

The parameter ρ_1 (i.e., i = 1) will correspond, or nearly correspond to the density at which R_1 goes through a maximum. If the scalar interaction were the only interaction, the correspondence would be exact.

In complete analogy with the treatment of j_1, we can define $\rho_2(J,\rho,\gamma',\gamma,t',t;m_{I'}',m_I)$ as the density at which j_2 in equation 3.8.20 has its maximum value. The reduced spectral density j_2 is associated with the tensor spin-rotation interaction. With each centrifugal distortion fre-quency there is a particular density at which it will have its maximum

contribution to the relaxation rate. The assumption that all distortion transitions are associated with the same correlation time τ_2 is equivalent to the assumption that all "lines" in the non-zero centrifugal distortion spectrum (Figures G.1 to G.13) are equally broadened. Thus the densities ρ_2 scale with the frequencies in the denominator of equation 3.8.20 and we have in analogy with equation 4.5.4,

$$\bar{\sigma}_2\bar{v} = \frac{[\{\omega(J,\gamma,t,\rho) - \omega(J,\gamma',t',\rho)\} - \{(m_I-m_I')\omega_0\}]}{\rho_2(J,\rho,\gamma',\gamma,t',t;m_I',m_I)} \qquad (4.5.6)$$

Thus, if one of the densities ρ_2 is fixed, they all are fixed. Rather than keep one of the ρ_2 as a parameter, it is convenient to define δ by

$$\delta = \frac{\tau_2}{\tau_1} = \frac{\bar{\sigma}_1}{\bar{\sigma}_2} \qquad (4.5.7)$$

With this definition, τ_2 becomes

$$\tau_2 = \frac{\delta\rho_1}{\omega_0\rho} \qquad (4.5.8)$$

and equation 3.8.20 can be expressed

$$j_2\{\omega(J,\rho;\gamma',\gamma,t',t;m_{I'}',m_I)\} = \frac{\dfrac{\delta\rho_1}{\omega_0\rho}}{1 + \delta^2 \dfrac{[\{\omega(J,\gamma,t,\rho) - \omega(J,\gamma',t',\rho)\} - \{(m_I-m_{I'}')\omega_0\}]^2}{\omega_0^2}\dfrac{\rho_1^2}{\rho^2}}$$

(4.5.9)

In summary, the correlation times τ_1 and τ_2 are transformed into convenient parameters ρ_1 and δ. These transformations have not invoked any new assumptions (except that equation 4.5.1 is valid) but hopefully make it clearer what is implicitly assumed when the relaxation is assumed to be characterized by these two parameters.

The above discussion represents the simplest procedure for relating correlation times and density. We shall, following reference (8) allow the cross-section to be a function of J

$$\bar{\sigma}_i (J) = \bar{\sigma}_i^0 \left(\frac{J}{J_{avg}}\right)^{-N}$$

(4.5.10)

It has been suggested (8) that in the limit of weak collisions N is two and in the limit of strong collisions N is zero. In general, there is no

physical basis for equation 4.5.10, however. The author has no physical intuition concerning the dependence of $\bar{\sigma}$ on J. We simply use N as a fitting parameter and if a better fit is obtained for non-zero N than for N = 0, the physics of equation 4.5.10 will have to be reviewed. J_{avg} is included so as to define $\bar{\sigma}_i^0$ as the effective cross section for the average J state. We will permit N to be both positive and negative.

With this extension, ρ_1 in equations 4.5.5 and 4.5.9 is replaced with;

$$\rho_1(J) \quad = \quad \rho_1^0 \left(\frac{J}{J_{avg}} \right)^N$$

$$(4.5.11)$$

4.6   RELAXATION AT 30 MHz

We compare the predictions of the theory developed in Chapter III and discussed in the first part of this chapter with the measurements reported in Chapter II. On obtaining the best numerical values for the parameters in the theory based on this comparison, the general features of the relaxation at 30 MHz are discussed. Finally the spectral density (relaxation rate vs. frequency) for methane gas at 0.01 amagat is predicted.

4.6.1   NUMERICAL FITS OF THE EXPERIMENTAL RESULTS

At each temperature, the relaxation rate R_1 is calculated as a function of density. This calculation is performed on a computer as outlined in Section 4.2. There are three parameters in the theory; ρ_1, δ and N. If N is set to zero, the correlation times are independent of J and if δ is set to unity, the correlation times τ_1 and τ_2 are equal. Under these conditions, ρ_1 is varied and this is referred to as a one parameter fit. If N is set to zero and δ and ρ_1 are varied, or, if δ is set to unity and N and ρ_1 are varied, it is referred to as a two parameter fit. If ρ_1, δ and N are all allowed to vary, we have, clearly, a three parameter fit.

The fitting procedure involves estimating values for the parameter or parameters and "zeroing in" on a good fit. Rather than generating some numbers with well defined errors, the primary purpose of this project is to point out general features of nuclear spin relaxation in methane and this method of curve fitting is more than adequate for our purposes. This is discussed further in Appendix J, Section J.1.

(i) One Parameter Fits

The low density regime is relatively insensitive to small changes in ρ_1 ($\sim 5\%$) so the theoretical predictions are presented on the $R_1\rho$ vs. log ρ plots. Examples of one parameter fits for the best value of ρ_1, and ρ_1 values which are 5% larger and smaller are shown in Figures 4.9 to 4.11 for T = 110 K, 150 K and 295 K respectively. In turn, the best value of ρ_1 is used in Figures 4.12 to 4.14 where the log R_1 vs. log ρ plots are presented. The 77 K results will be discussed separately.

The relaxation measurements are well represented by the theoretical predictions at 110 K and 150 K and not so well represented at 295 K.

It should be noted that the theoretical predictions for the value of R_1 at the density $\rho = \rho_1$ is independent of the value of ρ_1. The ratio ρ_1/ρ in j_1 (equation 4.5.5) and j_2 (equation 4.5.9) is unity at this density and the theory provides $(R_1)_{MAX}$ with no adjustable parameters. In terms of Figures 4.12 to 4.14, changing ρ_1 will shift the curve horizontally and will change the shape slightly, but not the value of $(R_1)_{MAX}$. As can be seen, the agreement between theory and experiment is very good in the immediate vicinity of the R_1 maximum.

On inspecting Figures 4.12 to 4.14, it is seen that the theoretical line is consistent with the measurements at very low densities in that it passes through most of the error bars but it is clear the experimental results are too high, or, the theoretical predictions are too low. We feel that the theory is more accurate than the measurements in this region. In Section 2.4, it was stated that although diffusion effects are completely negligible at densities above the R_1 maximum, they could

become important at very low densities. It can be ruled out that a few distortion lines are causing this effect. In the same way the maximum contribution of the relaxation resulting from the scalar spin-rotation interaction occurs at a density ρ_1, the maximum contribution of each centrifugal distortion transition occurs at two densities, namely

$$\rho_{\pm} = \frac{|\omega_d \pm \omega_0|}{\omega_0} \rho_1 \qquad (4.6.1)$$

The frequency ω_d is short hand notation for $\omega(J,\gamma,t,\rho) - \omega(J,\gamma',t',\rho)$ and equation 4.6.1 results from maximizing j_2 in equation 4.5.9. ($\delta = 1$). The only candidates that could possibly affect the relaxation at densities near and below the density of the R_1 maximum are the 8 MHz line with $\rho_+ = 2.6\rho_1$ and $\rho_- = 0.73\rho_1$, the 47.5 MHz line with $\rho_+ = 2.6\rho_1$ and $\rho_- = 0.58_1$, the 51 MHz line with $\rho_+ = 2.7\rho_1$ and $\rho_- = 0.72\rho_1$ and the 71 MHz line with $\rho_+ = 3.4\rho_1$ and $\rho_- = 1.4\rho_1$. The quantum numbers and group theoretical indices involved with these transitions are given in Table 4.1 These transitions could not explain the low density discrepancy between theory and experiment unless their weights were increased by orders of magnitude. Even this would be unacceptable because it would lead to too great a relaxation at the R_1 maximum (note, this would not be a one parameter fit). This discrepency is consistent with the discussion of wall relaxation and apparent diffusion relaxation given in Section 2.4. This affects the majority of the 77 K measurements since the theoretical prediction (later in this section) for the density at which R_1 is a maximum

is near the equilibrium vapour density.

The important point concerning the discrepancy for the 295 K results above the density of the R_1 maximum is not the absolute value of R_1 at any particular density because it can be shifted up and down by varying ρ_1, but the relative magnitude of R_1 in one density region to that in another density region. For any reasonable choice of ρ_1 based on the vicinity of the R_1 maximum and densities above 5 amagat, the theoretical prediction in the region from about 0.05 to 0.1 amagat is too large. Also, above about one amagat, the theoretical prediction of $R_1\rho$ is increasing too quickly with increasing ρ. (Figure 4.11). If the centrifugal distortion transitions are neglected, the value of $R_1\rho$ becomes constant at higher densities. This is clear from Figure I.2 (Appendix I) where the prediction of the theory which neglects these transitions is plotted. Figure I.2 also makes it clear that we can not neglect these transitions but it does suggest that the one parameter fit puts too much emphasis on the higher frequency distortion transitions which in turn are associated with the higher J-states.

These single parameter fits (N = 0, δ = 1) of the data lead to the following values of ρ_1

$$\rho_1 = 0.0275 \pm 0.0008 \text{ amagat} \quad (T = 110 \text{ K})$$

$$\rho_1 = 0.0310 \pm 0.0012 \text{ amagat} \quad (T = 150 \text{ K})$$

$$\rho_1 = 0.040 \pm 0.004 \text{ amagat} \quad (T = 295 \text{ K})$$

$$(4.6.2)$$

The uncertainties in ρ_1 in equations 4.6.2 are estimates whose origin is discussed in Appendix J, section J.2.

When these three values of ρ_1 are subjected to a least square fit of $\ln\rho_1$ α $\ln T$, the result is

$$\ln\rho_1 \quad = \quad (0.38)\ln T - 5.4 \quad\quad\quad (4.6.3)$$

The errors in the slope and intercept in equation 4.6.3 resulting from the least squares fit are 0.02 and 0.4 respectively. There are, however only three points and it should be kept in mind that these errors may not be very meaningful because the number of points exceeds the number of parameters by only one. We only wish to gain some feeling for the temperature dependence of ρ_1 and eventually the effective cross section. For completeness, it is noted that the statistical errors in the slope and intercept in equation 4.6.3 result solely from the estimated error in ρ_1 given by equation 4.6.2. (see Section 2.5.2) This is because the difference $\Delta\rho_1$ between the three values given in equation 4.6.2 and the values resulting from equation 4.6.3 are very much smaller than the uncertainties in ρ_1 given by equation 4.6.2. Because there are only three values of ρ_1, this must be considered to be a coincidence.

The slope 0.38 ± 0.02 in equation 4.6.3 can be compared with a related parameter measured in reference (26). The "classical" theory of nuclear spin relaxation predicts a constant value of $R_1\rho$ at sufficiently high density, (see Figure I.2, I.4 and I.6). Under these conditions the

limiting value of $R_1\rho$ can be related to the parameter ρ_1 by substituting

equation 4.5.5 for $j(\omega_0)$ into equation 4.4.2 and using $\alpha = B/kT$ to give

$$(R_1\rho)_{lim} = \frac{4\pi^2 kTC^2_{e\delta\delta}}{B\omega_0} \rho_1 \qquad (4.6.4)$$

The details leading to equation 4.6.4 can be found elsewhere (24). It was

found experimentally (26) that

$$(R_1\rho)_{lim} \propto T^{1.45 \pm 0.09} \qquad (4.6.5)$$

From equation 4.6.4 and 4.6.5 we have

$$\rho_1 \propto T^{0.45 \pm 0.09} \qquad (4.6.6)$$

Thus the slope 0.38 ± 0.02 in equation 4.6.3 is in agreement with the

equivalent parameter 0.45 ± 0.09 taken from reference (26).

We can use equation 4.6.3 with equations 4.5.4 to

estimate the temperature dependence of the effective cross section. The

parameter ρ_1 is converted to molecules per $(cm)^3$ by multiplying by $2.69 \times$

10^{19}, (see Section 2.5.3), and we assume the kinetic theory value for the

average relative velocity which is,

$$\bar{v} = \sqrt{\frac{8kT}{\pi\mu}} = 4\sqrt{\frac{kT}{\pi m}} \qquad (4.6.7)$$

The reduced mass of the colliding pair is μ and m is the mass of a methane molecule. The result of these transformations is

$$\ln\bar{\sigma} = (-0.88) \ln T - 28.9 \qquad (4.6.8)$$

This leads to cross sections of 19 $\overset{o}{A}{}^2$ at 295 K, 34 $\overset{o}{A}{}^2$ at 150 K and 61 $\overset{o}{A}{}^2$ at 77 K. It is extremely difficult to give a reliable estimate of the error in these quantities but it would be surprising if they were not accurate to better than 15%. The value of 19 $\overset{o}{A}{}^2$ at 295 K is to be compared with 46 $\overset{o}{A}{}^2$ which is the kinetic cross section at 295 K (124). The "strength" of the collisions, therefore, seems to be intermediate between weak $(\bar{\sigma} << \sigma_{KIN})$ and strong $(\bar{\sigma} = \sigma_{KIN})$. It must be remembered that this discussion is valid only within the framework of the one parameter model.

On the basis of the satisfactory agreement between the one parameter theoretical prediction and the measurements at 110 K (Figure 4.9) and at 150 K (Figure 4.10) one would expect the single parameter fit to reliably reproduce the 77 K measurements. The 77 K theoretical prediction is presented in Figure 4.15. The value of $\rho_1 = 0.024$ amagat is based on equation 4.6.3. The large discrepancy between theory and experiment is completely consistent with the disagreement at 110 K and 150 K at densities

below the density of the R_1 maximum. Most of the 77 K measurements are at, or below, the theoretically predicted value of ρ_1 and at the very low densities the discrepancy is almost certainly due to wall effects and diffusion effects. (Varying ρ_1 would not improve the fit because it would only shift the theoretical line horizontally.) There is also the possibility that the discrepancy at the density of the R_1 maximum (which we consider more relevant than the discrepancy at the very low densities) is due to intrinsic relaxation mechanisms (i.e., not diffusion effects) other than the spin-rotation interaction. One such possibility is the relaxation resulting from the rotational and vibrational degrees of freedom associated with $(CH_4)_2$ Van der Waals complexes. Finally, we are very near the equilibrium vapour pressure and relaxation due to liquid monolayers on surfaces can not be ruled out. (See also Section 2.4.)

At 77 K, the effects of centrifugal distortion are small in the sense that only a few transitions are important. In fact the only transition of any consequence is the J = 3, 71 MHz line (see Table 4.1) which has its maximum contribution at 0.033 amagat. This will be discussed further in Section 4.6.2.

Employing 2 or 3 parameter fits may raise the relaxation rates very slightly at the highest densities ($\sim$0.04 amagat). As discussed in Chapter II, the 77 K measurements are to be treated with a great deal of suspicion and we do not consider the effort required to perform 2 and 3 parameter fits worthwhile.

It is reassuring that the theoretical prediction for the relaxation at 77 K resulting from the spin-rotation interaction is not higher than the measured relaxation rates.
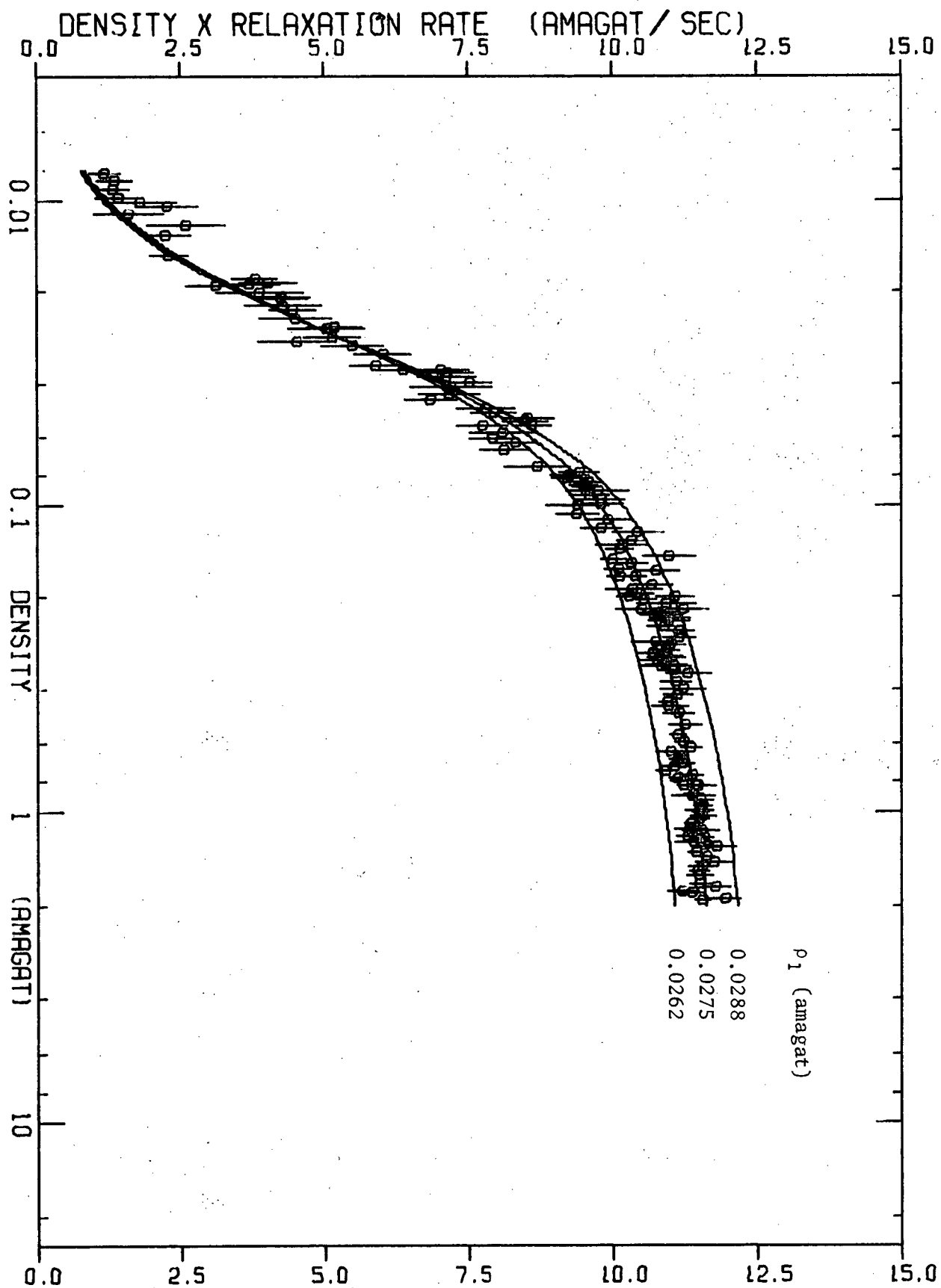
Figure 4.9. Plot of $R_1\rho$ vs ρ for T = 110K. The parameters in the theoretical line are $\delta = 1$, $N = 0$ and ρ_1 as shown.
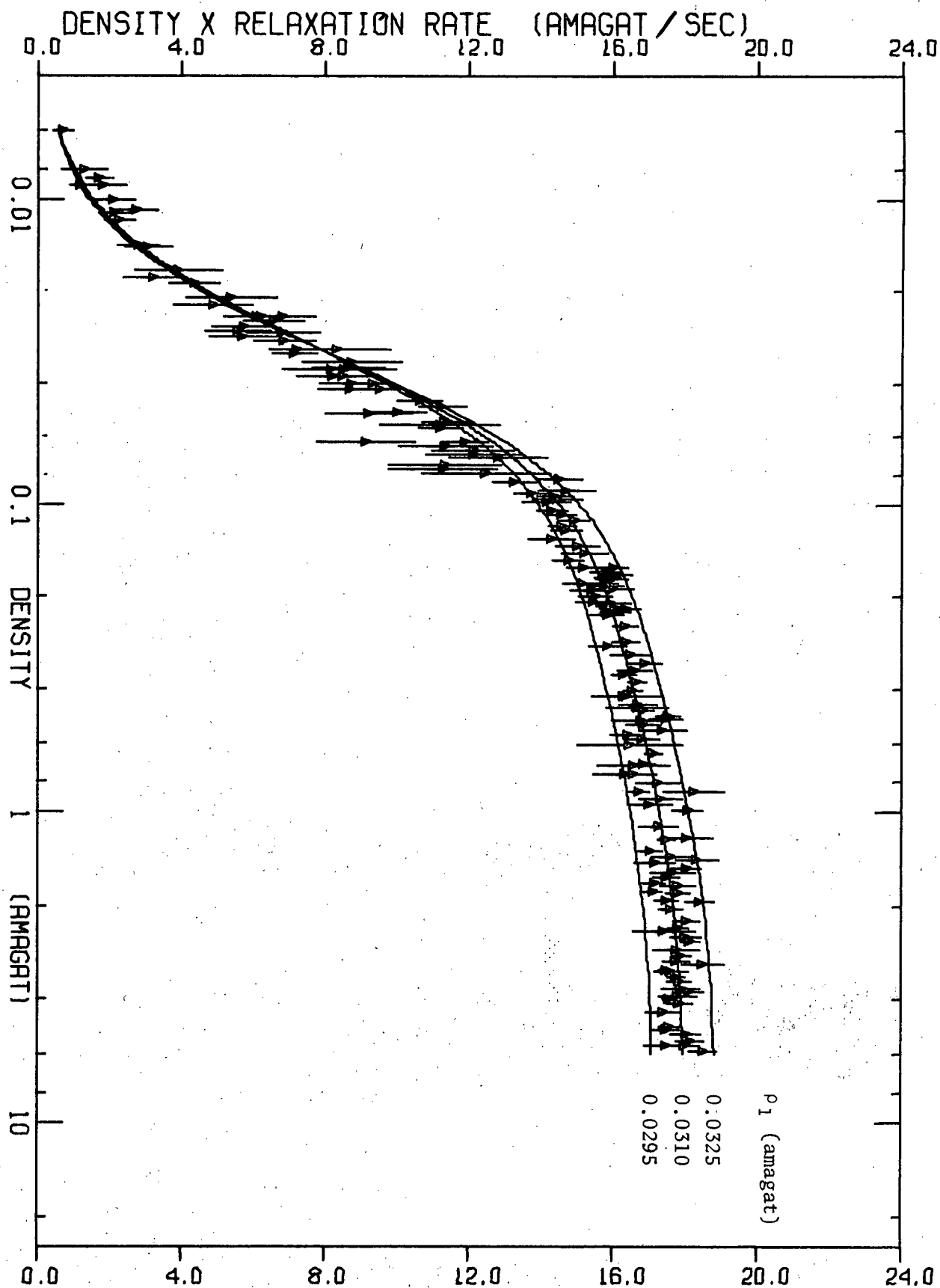
Figure 4.10. Plot of $R_1\rho$ vs ρ for T = 150K. The parameters in the theoretical line are $\delta = 1$, N = 0 and ρ_1 as indicated.
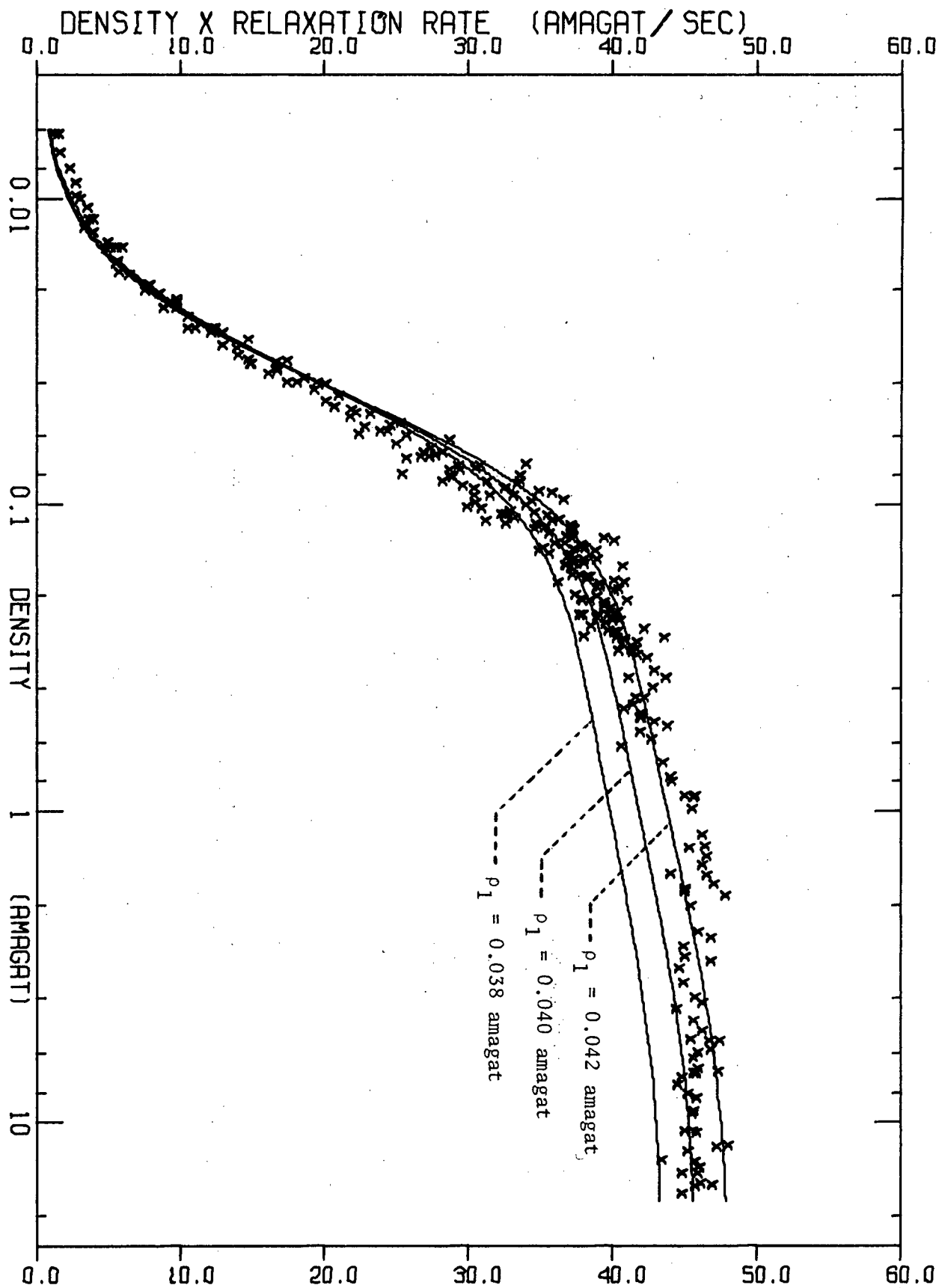
Figure 4.11. Plot of $R_1 \rho$ vs ρ for T = 295K. The parameters in the theoretical line are $\delta = 1$, $N = 0$ and ρ_1 as shown.
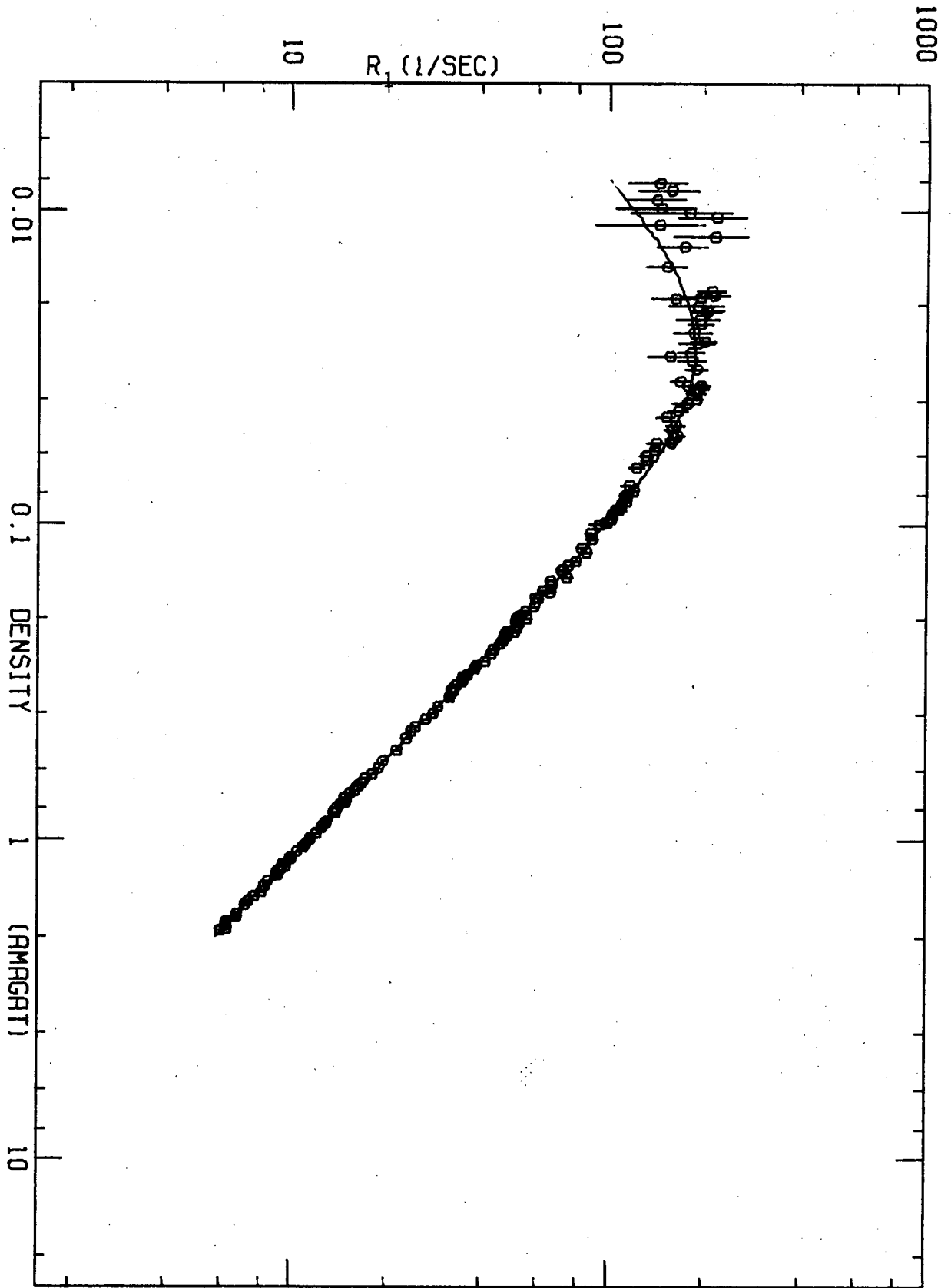
Figure 4.12. Plot of R_1 vs ρ for T = 110K. The theoretical parameters are $\delta = 1$, N = 0 and $\rho_1 = 0.0275$ amagat.
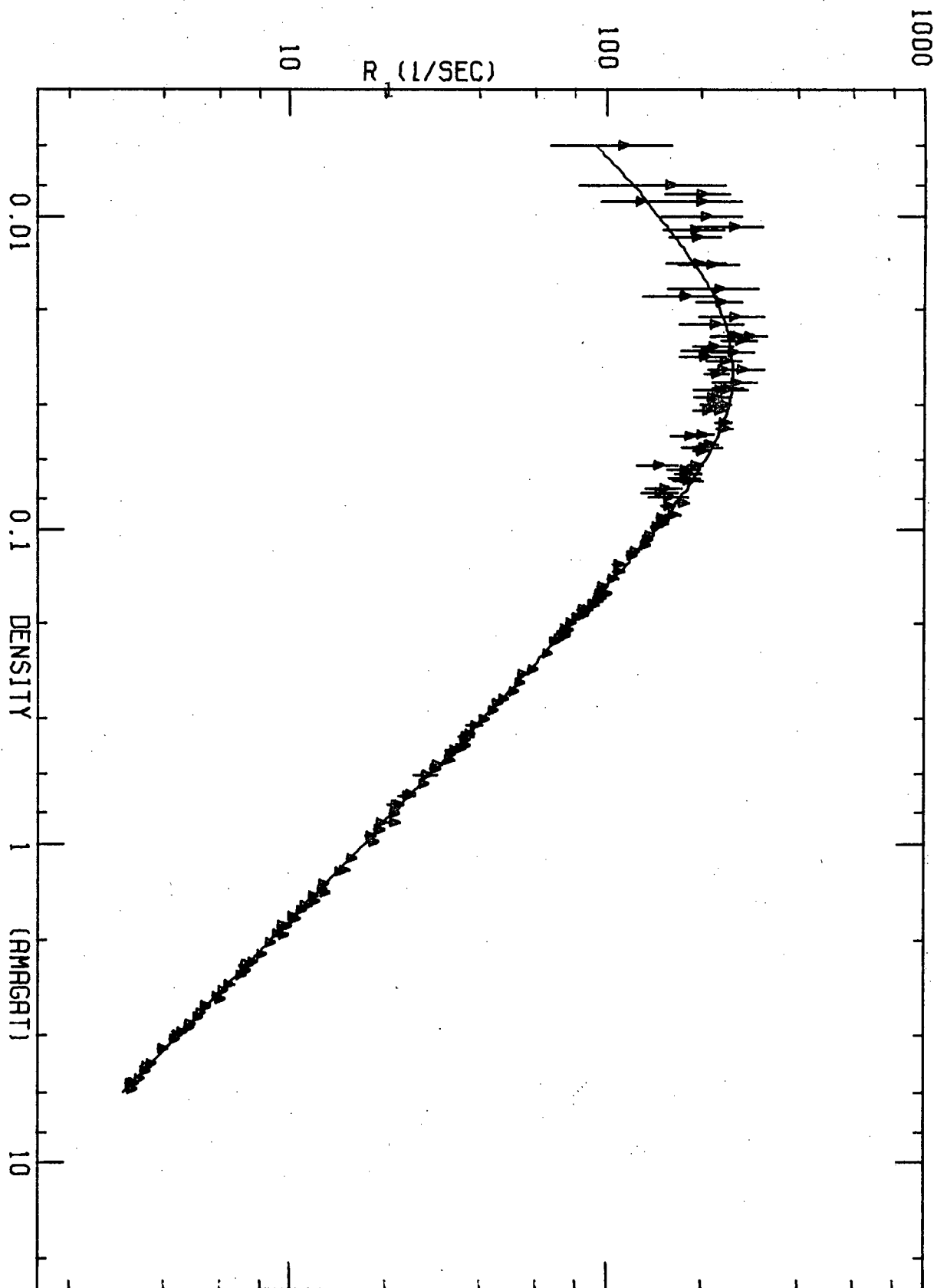
Figure 4.13.   Plot of R_1 vs ρ for $T = 150K$. The parameters in the theoretical
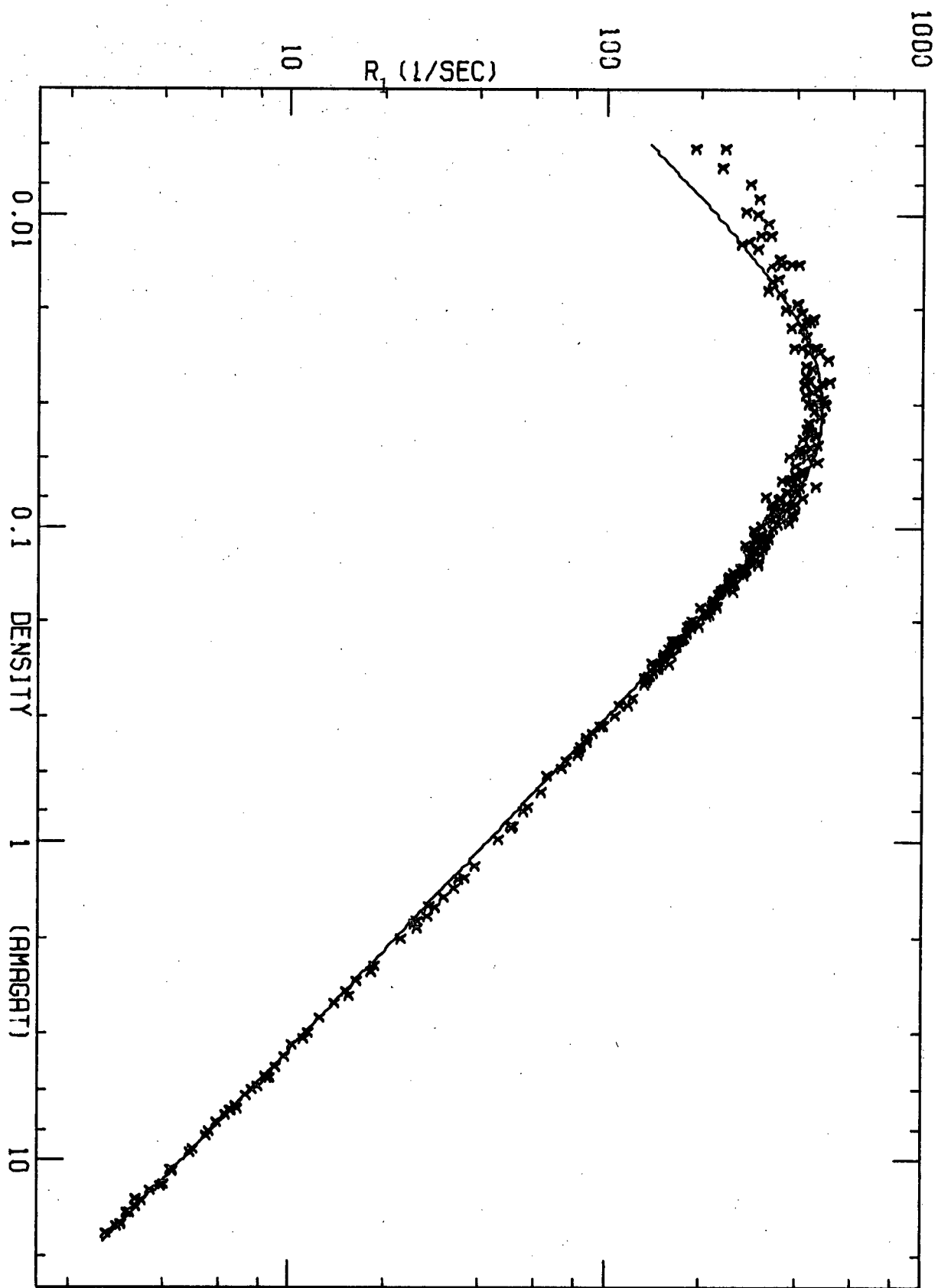line are $\delta = 1$, $N = 0$ and $\rho_1 = 0.031$ amagat.

Figure 4.14. R_1 vs ρ for T =295K. The parameters in the theoretical line are $\delta = 1$, N = 0 and ρ_1 = .04 amagat.
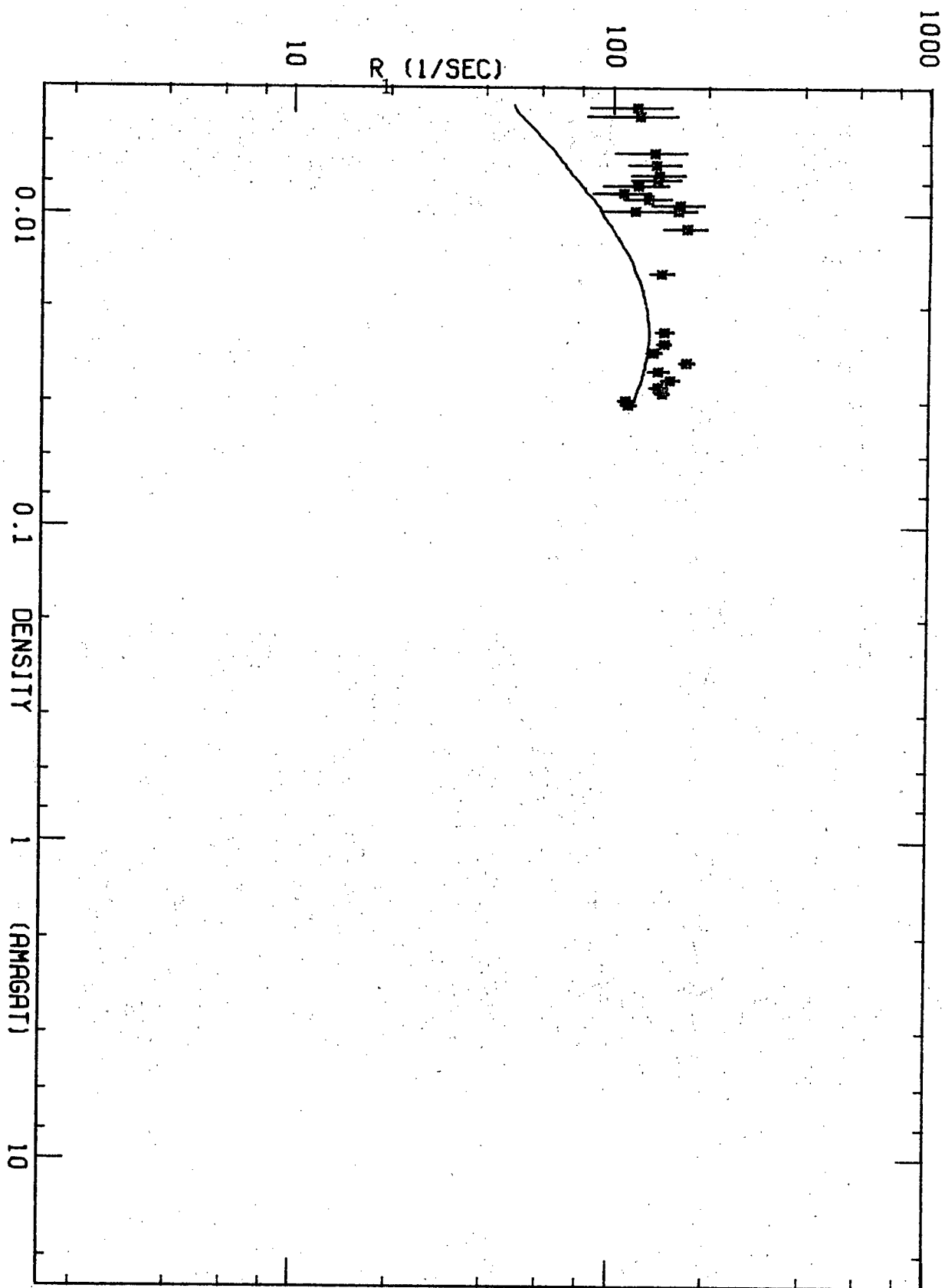
Figure 4.15. Plot of R_1 vs ρ for T = 77K. The parameters in the theoretical line are $\delta = 1$, N = 0 and ρ_1 = 0.024 amagat.

(ii) Two Parameter Fits

Were it not for the disagreement between theory and experiment at 295 K discussed in the preceding Section, we would not require the use of two parameters. The two parameter fits do, however, give some insight into the possible implications of the theory.

The simplest two parameter fits involves allowing the correlation times associated with the scalar and tensor relaxation processes to be different. That is to say, we fix N at zero and allow $\delta = \tau_2/\tau_1$ and $\rho_1 \propto \tau_1^{-1}$ to vary. The physical argument behind such a possibility is that the effective cross section for collisions which result in a change of centrifugal distortion state and the subsequent possibility of spin conversion ($\bar{\sigma}_2 \propto \tau_2^{-1}$) may be different than the effective cross section for collisions that conserve the distortion energy ($\bar{\sigma}_1 \propto \tau_1^{-1}$).

Examples of such two parameter fits are given in Appendix J, Section J.3 for 110 K and 150 K. These fits with $\delta \neq 1$ are in fact poorer than the one parameter fits discussed in the previous Section.

For T = 295 K, the theoretical predictions for $\delta = 0.5$ and $\delta = 0.75$ (N = 0) are shown in Figures 4.16 and 4.17 respectively for different values of ρ_1. The two parameter fit with $\delta = 0.5$ appears to be better than the one parameter fit ($\delta = 1$) shown in Figure 4.11, but there is still too much predicted relaxation in the region between 0.06 and 0.2 amagat although the fit is somewhat improved in the high density region.

The other two parameter fit involves setting $\delta = 1$ and allowing ρ_1 and N to vary. This allows $\tau_1 (=\tau_2)$ to be dependent on J and we must replace ρ_1 in equations 4.5.5 and 4.5.9 with $\rho_1 (J/J_{avg})^N$ in accordance with equation 4.5.10.

The numerical calculations involved in performing these fits are considerably more complicated because the functions A', F' and B' must be replaced with their more general counter parts A, F and B. (See Section 3.8 and Table 3.10).

Several fits for different values of N are presented in Appendix J, Section J.3 for T = 295 K. None of these fits is exceptionally good but we notice that when the absolute value of N is large the relaxation in the region from 0.06 to 0.2 amagat is significantly reduced relative to the high density value. Also, we note that positive values of N weight the higher centrifugal distortion frequencies (associated with the higher J states) too much which manifests itself in the fact that $R_1\rho$ increases too quickly with increasing ρ at high ρ values. The case for N = 2 (Figure J.5) which has been suggested would be the case for weak collisions (8) is clearly a very bad fit. This is not surprising and, in fact, is consistent with the discussion following equations 4.6.8 concerning the strength of collisions.

The agreement between theory and experiment for the case of N = -1 and ρ_1 = 0.0511 shown as the top line in Figure 4.18 is reasonably good below about 2 amagat.

(iii) A Three Parameter Fit

On the basis of the best two, two parameter fits of the 295 K data, (δ = 0.5, ρ_1 = 0.044, N = 0 in Figure 4.16 and δ = 1, ρ_1 = 0.0511, N = -1 in Figure 4.18) we have performed one set of three parameter fits with N = -1, δ = 0.5 and ρ_1 as indicated in Figure 4.19. Three parameter fits must be treated with considerable caution because there is probably more than

one combination of the three parameters that will fit the data. The inter-
pretation of this particular three parameter fit is that all the non-zero
frequency lines (i.e., centrifugal distortion lines) in the spectral den-
sity have one-half the height and twice the width (i.e., $\delta = \frac{1}{2}$) that they
would have if $\tau_1 = \tau_2$. Also, N = -1 implies that all contributions to the
spectral density have a height inversely proportional to J and a width
proportional to J. Because this explanation is not necessary to interpret
the relaxation at 150 K and 110 K, the implication is that N is a decreasing
function of temperature (zero at 110 K to -1 at 295 K) and δ is also a
decreasing function of temperature (1 at 110 K at $\frac{1}{2}$ 295 K). We do not put
a great deal of emphasis on this interpretation other than to say it is
consistent with the experimental results. With respect to the theory, the
big difference between the relaxation at 295 K and the region 110 - 150 K
is that the former involves very many transitions whose combined effect is
important although each transition has a very small effect and the latter
involves considerably fewer transitions some of which are individually
important.

The most successful fit of the 295 K measurements occurs for N = -1,
$\delta = 0.5$ and $\rho_1 = 0.0528$ and is shown in Figures 4.19 and 4.20. Using
equation 4.5.10 this particular fit leads to the following effective cross
sections at 295 K.

$$\bar{\sigma}_1 \sim (24\overset{\circ}{A}{}^2)\left(\frac{J}{J_{avg}}\right)^{-1}$$

$$\bar{\sigma}_2 \sim (12\overset{\circ}{A}{}^2)\left(\frac{J}{J_{avg}}\right)^{-1}$$

$$(4.6.9)$$

J_{avg} at T = 295 K is 6.56. (J = 6 is the most populated state) Equations 4.6.9 are to be compared with $\bar{\sigma}_1 = \bar{\sigma}_2 = 19A^{O2}$ resulting from the one parameter fit.

Figure 4.16. Plot of $R_1\rho$ vs ρ for 295K. The parameters in the theoretical line are $\delta = 0.5$, $N = 0$ and ρ_1 as indicated.

Figure 4.17. Plot of $R_1\rho$ vs ρ for 295K. The parameters in the theoretical line are $\delta = 0.75$, $N = 0$ and ρ_1 as indicated.

Figure 4.18. A plot of $R_1\rho$ vs ρ for 295K. The parameters in the theoretical line are $\delta = 1$, $N = -1$ and ρ_1 as indicated.
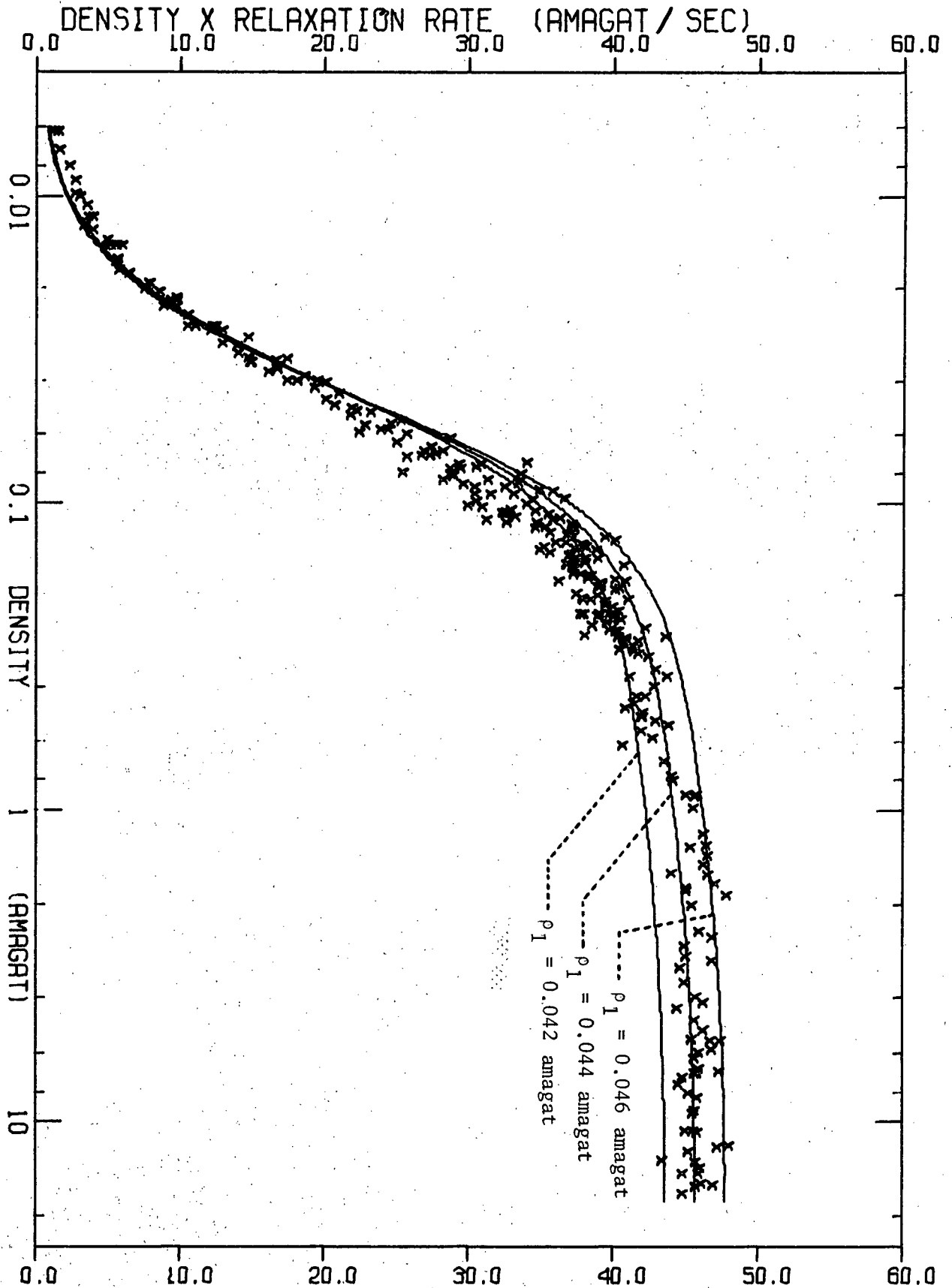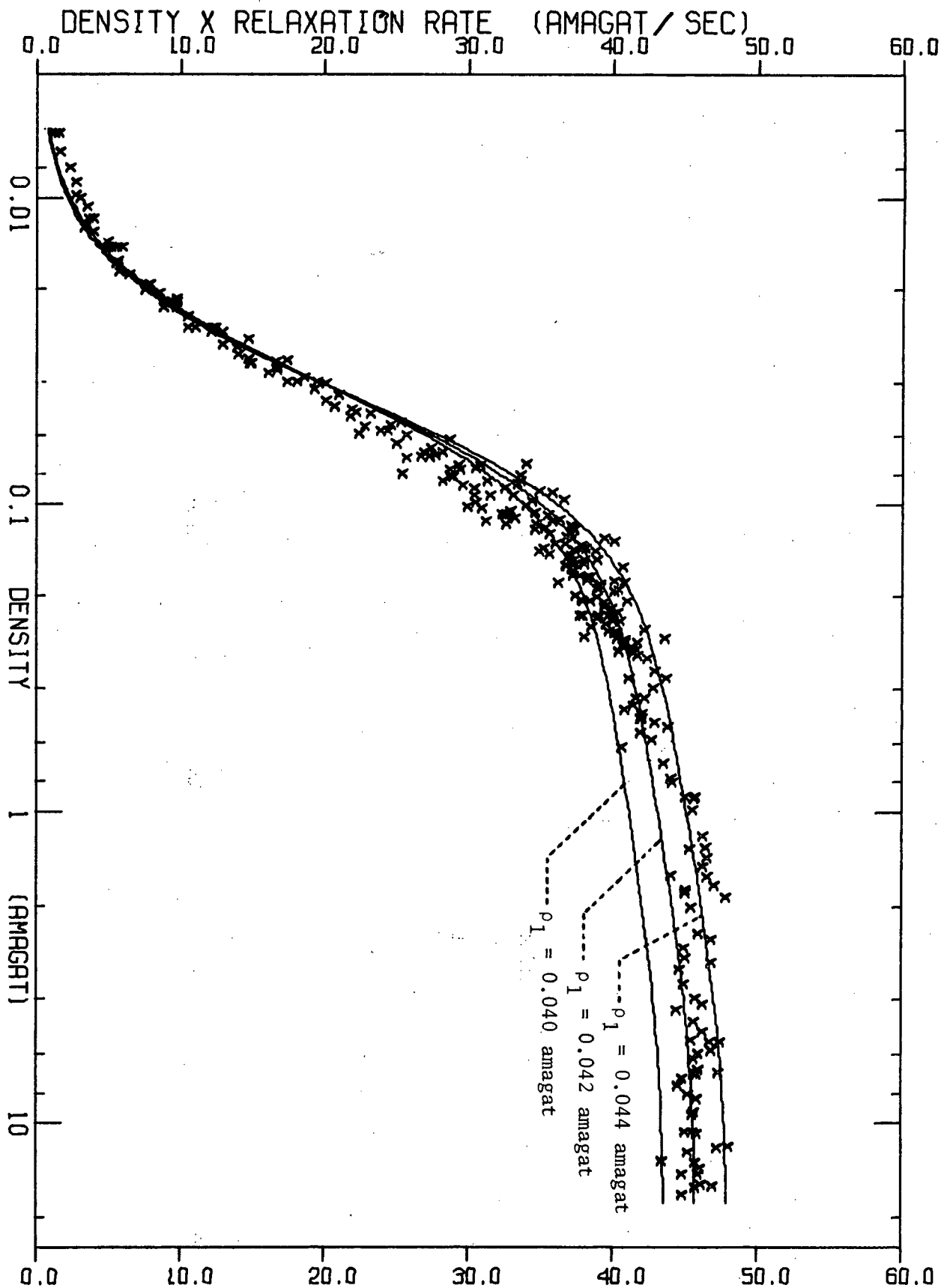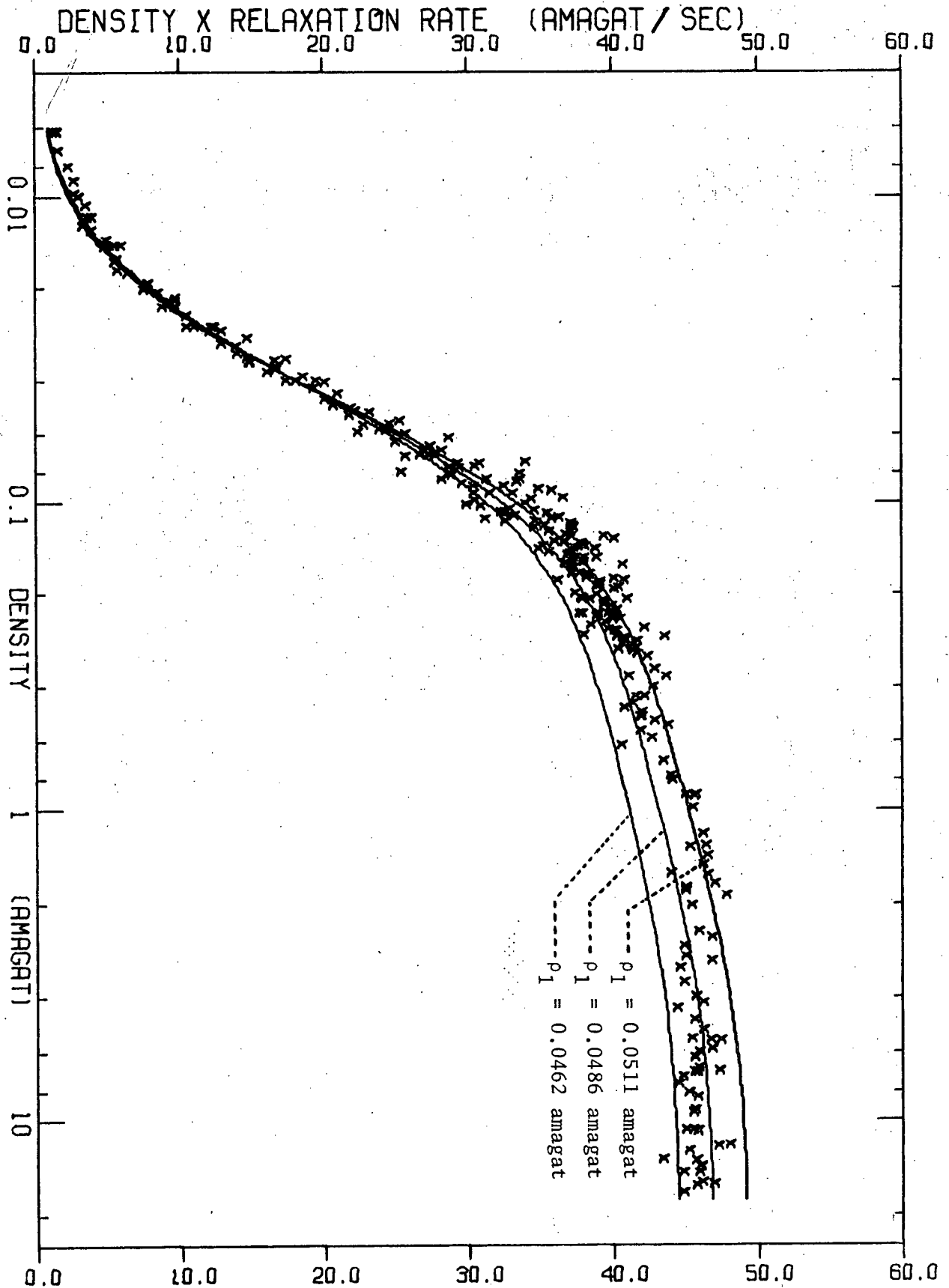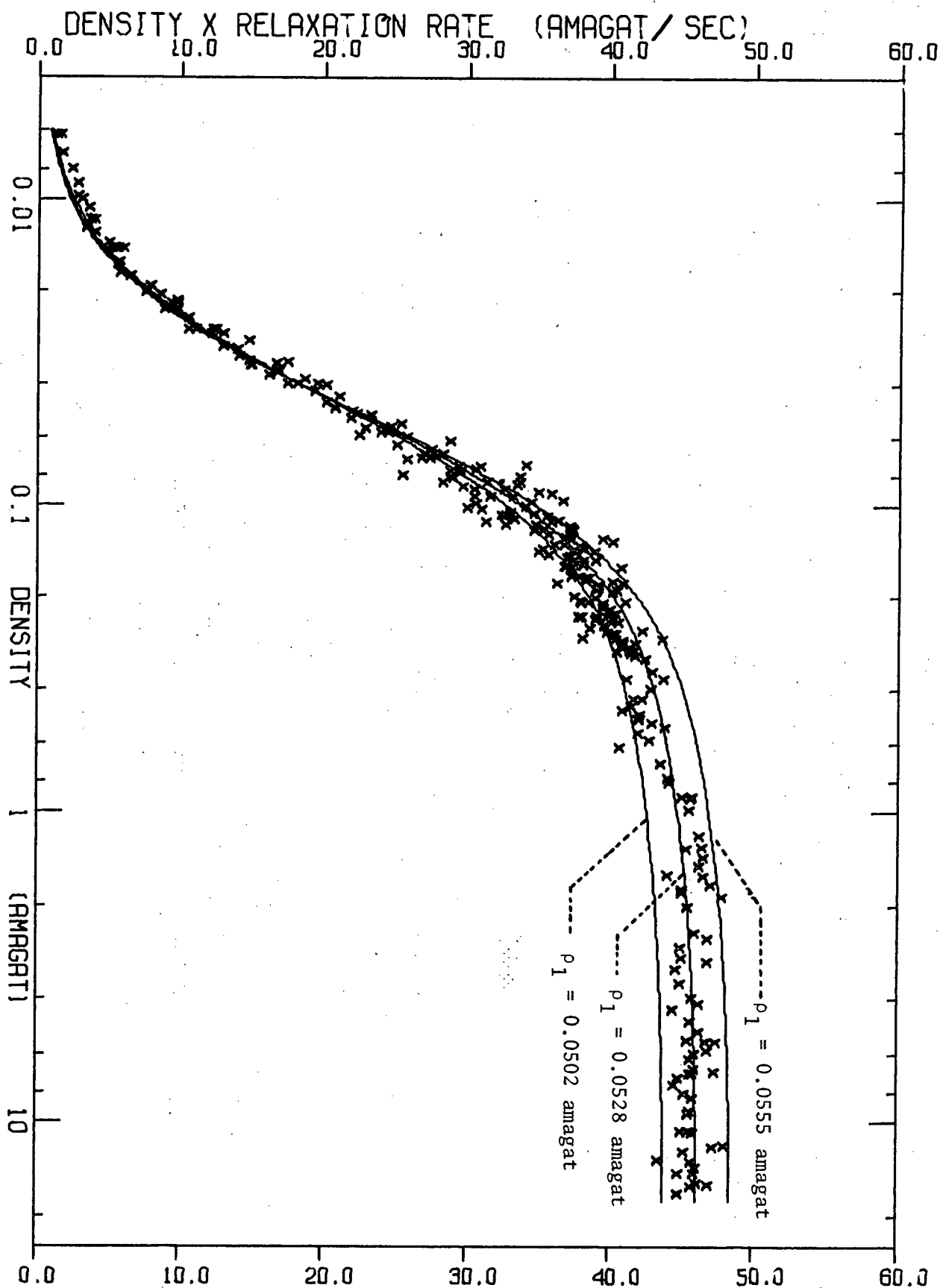
Figure 4.19. A plot of $R_1\rho$ vs ρ for 295K. The parameters in the theoretical line are $\delta = 0.5$, $N = -1$ and ρ_1 as indicated
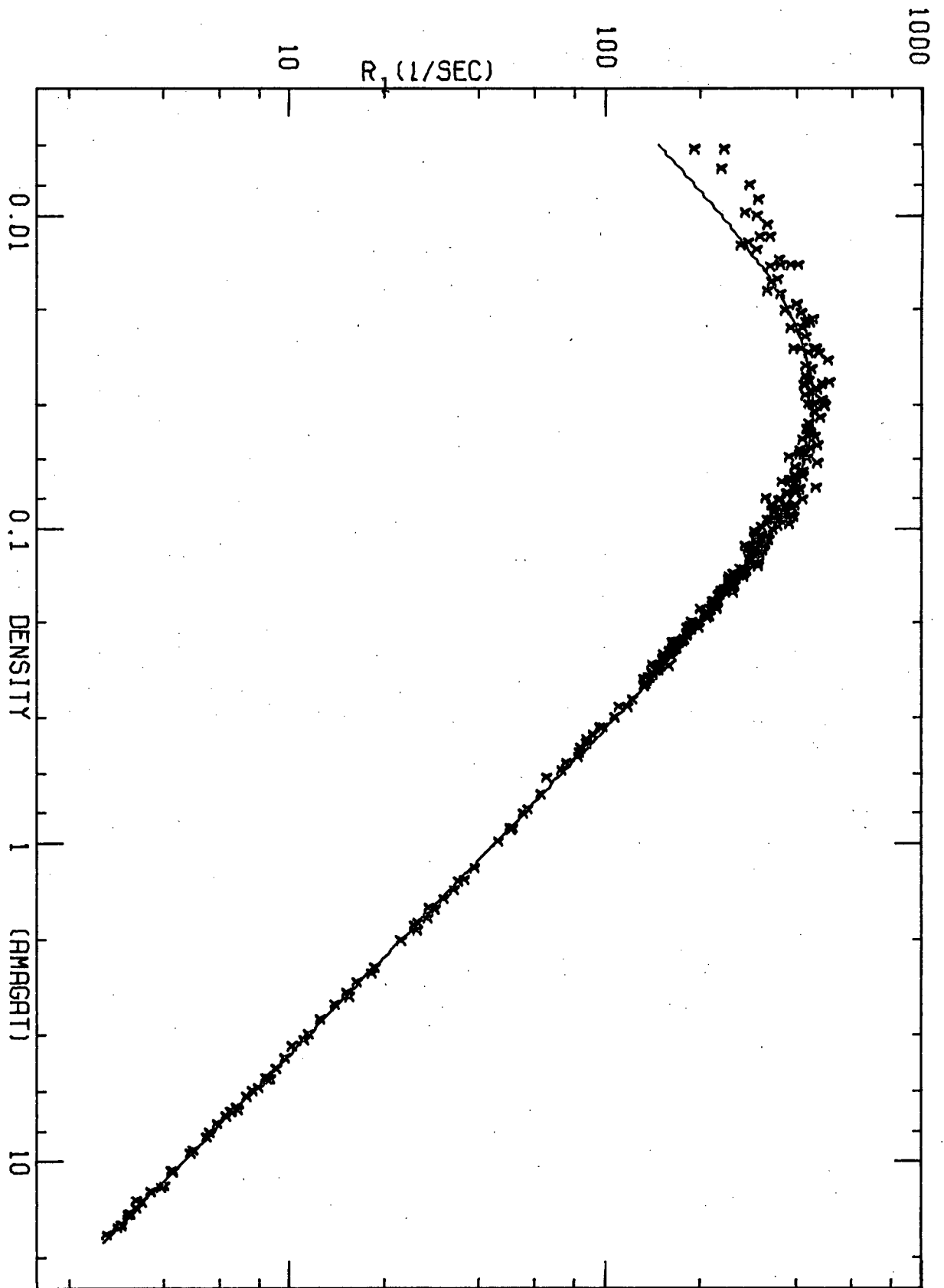
Figure 4.20. A plot of R_1 vs ρ for 295K. The parameters in the theoretical line are $\delta = 0.5$, $N = -1$ and $\rho_1 = 0.0528$ amagat.

4.6.2   GENERAL DISCUSSION

We will assume the relaxation at 30 MHz involves the single para-

meter ρ_1 given by equation 4.6.3. The small discrepancy betwen the result-

ing theory and the 295 K experiments will not seriously affect the discussion

and the large discrepancy at 77 K is almost certainly due to extra relaxa-

tion mechanisms.

The iterative procedure (equation 3.9.7) which determines the time

evolution of the populations of the spin states and therefore the time

evolution of the observed magnetization was used to check that the eigenvalue

procedure discussed in Section 3.9 could be used. These checks were performed

at four densities for each temperature; the lowest density, the density of

the R_1 maximum, a density $\sim \frac{1}{2}$ way between the density of the R_1 maximum

and the highest density, and, the highest density. In all cases, the relaxa-

tion is well represented by a single relaxation rate. The term "well re-

presented" is rigourously defined in Section 4.2. Further, the relaxation

rate calculated by the eigenvalue method resulted in values of R_1 which

agreed with those calculated using the iterative procedure to better than

2%. On inspecting the plots of $R^I(I'm')$ at 30 MHz in Figure 4.1 and 4.2

this result is not surprising for 295 K but is less obvious as temperature

is lowered. On inspecting the $R^I(I'm')$ at 30 MHz at 77 K (Figures 4.7 and

4.8) it is remarkable that the two methods agree. It is, nevertheless, true

and the reason will become clearer in the following discussion.

The relaxation rates λ_α and λ_β and their associated magnetizations

N_α and N_β are shown in Figures 4.21 to 4.24 for 295 K, 150 K, 110 K and 77 K.

The parameters are discussed in section 3.9, defined in Appendix H and an

example calculation of λ_α and λ_β is performed in Appendix I. Also shown in Figures 4.21 to 4.24 is the resulting single relaxation rate computed from an equal weight least squares fit of equation 3.9.20 forced into a single exponential. It is not surprising that this method works and that the observed relaxation is well represented by a single exponential. At high densities where λ_α and λ_β differ considerably, one of them is associated with 103% of the observed magnetization and the other with -3%. At low densities where $N_\alpha/N_\beta \lesssim \frac{1}{2}$, the two relaxation rates λ_α and λ_β differ by less than 15%. The plots of N_α and N_β in Figure 4.21 to 4.24 are associated with the axis at the bottom of the page and the plots of λ_α, λ_β and R_1 are associated with the axis at the top of the page. It is because N_α/N_β is a decreasing function of temperature at fixed density that the relaxation at low temperatures is well represented by a single relaxation rate even though the plots of R^I(I'm') in Figures 4.1 to 4.8 may suggest otherwise. It is also interesting to note that the transition from the limiting low density value of N_α/N_β to the limiting high density value occurs over a density region which decreases with decreasing temperature as indicated in Figure 4.21 to 4.24. It is of interest to compare the higher density values of N_α, N_β, $\lambda_\alpha\rho$, and $\lambda_\beta\rho$, (all of which are approaching limiting values at the higher densities) with the equivalent parameters in the theory that neglects spin symmetry. The limit of high density should correspond to the limit that all the centrifugal distortion frequencies are assigned to zero frequency. This was discussed in Section 4.4 and in fact the high density values of these parameters in Figure 4.21 for 295 K are in agreement with their counterparts in Appendix I.

Figures 4.21 to 4.24

The relaxation rates λ_α and λ_β resulting from the eigenvalue solution of the relaxation problem are plotted as a fuction of density. Also plotted is the total relaxation rate R_1. These three relaxation rates are associated with the top axis in the figures. The density dependence of the magnetizations N_α and N_β associated with the relaxation rates λ_α and λ_β are also shown. These two magnetizations are linear combinations of the I = 1 and I = 2 magnetizations. The low density limit of N_α and N_β are approximately $M^{(1)}$ and $M^{(2)}$ respectively. The high density limiting values are given approximately by equations I.13 and I.15 in Appendix I. In these figures, N_α and N_β are given in terms of the observed magnetization (bottom axis) by employing the analysis discussed at the end of Section 3.9. The parameters δ and N are δ = 1 and N = 0. The remaining parameter ρ_1 is (in amagat) 0.04 at 295K (Figure 4.21), 0.031 at 150K (Figure 4.22), 0.0275 at 110K (Figure 4.23) and 0.024 at 110K (Figure 4.24).
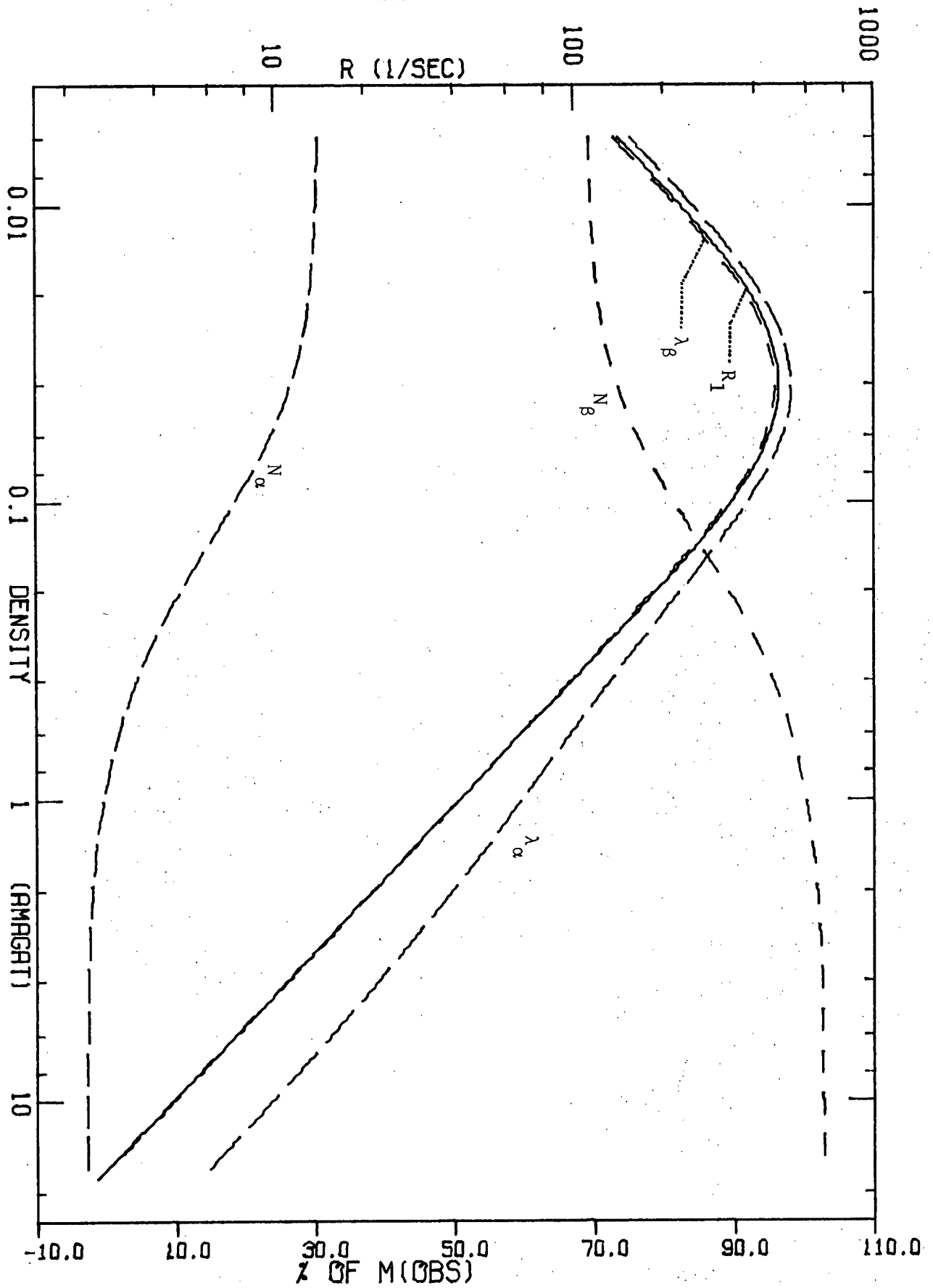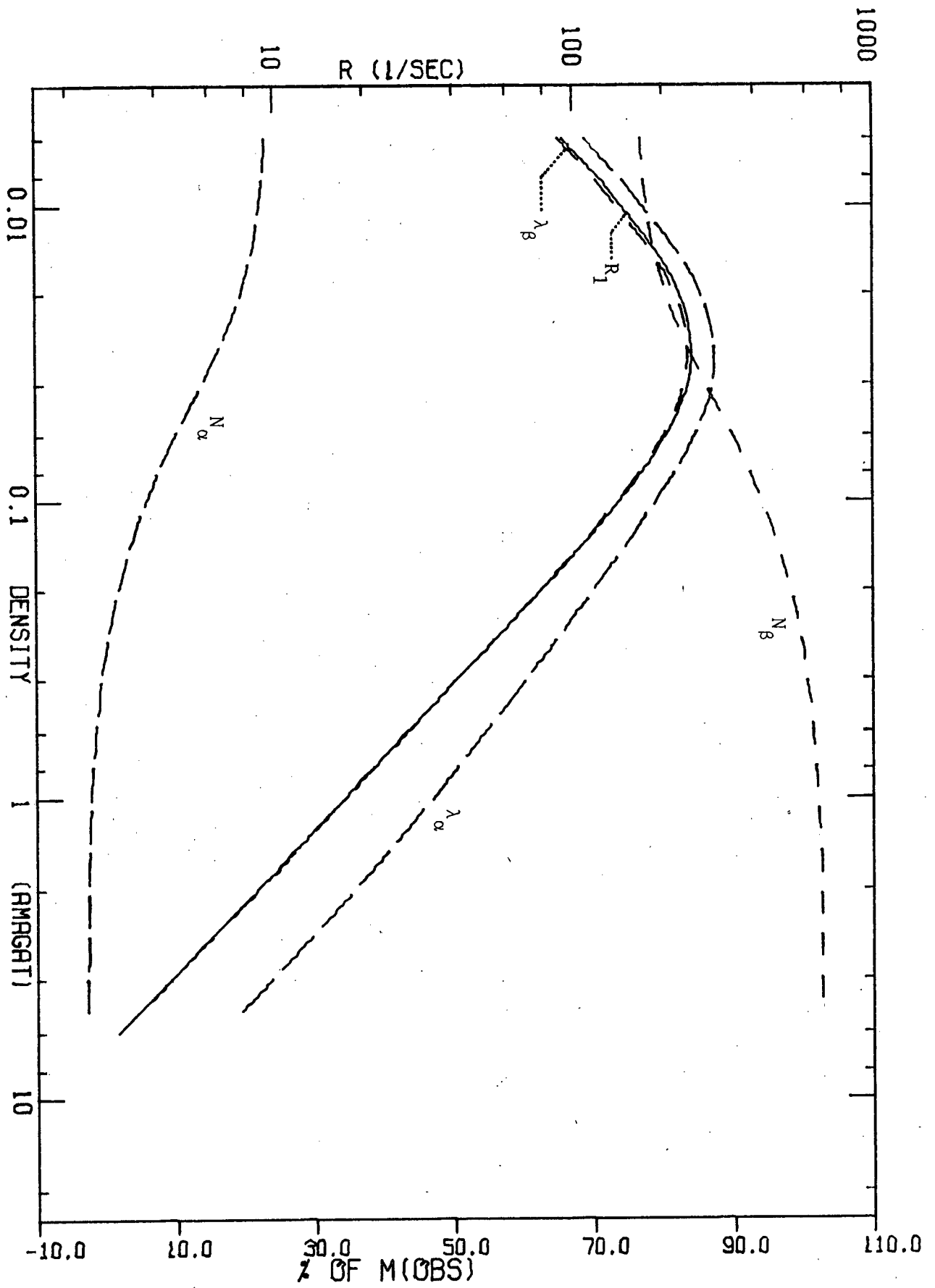
Figure 4.21   (295K)
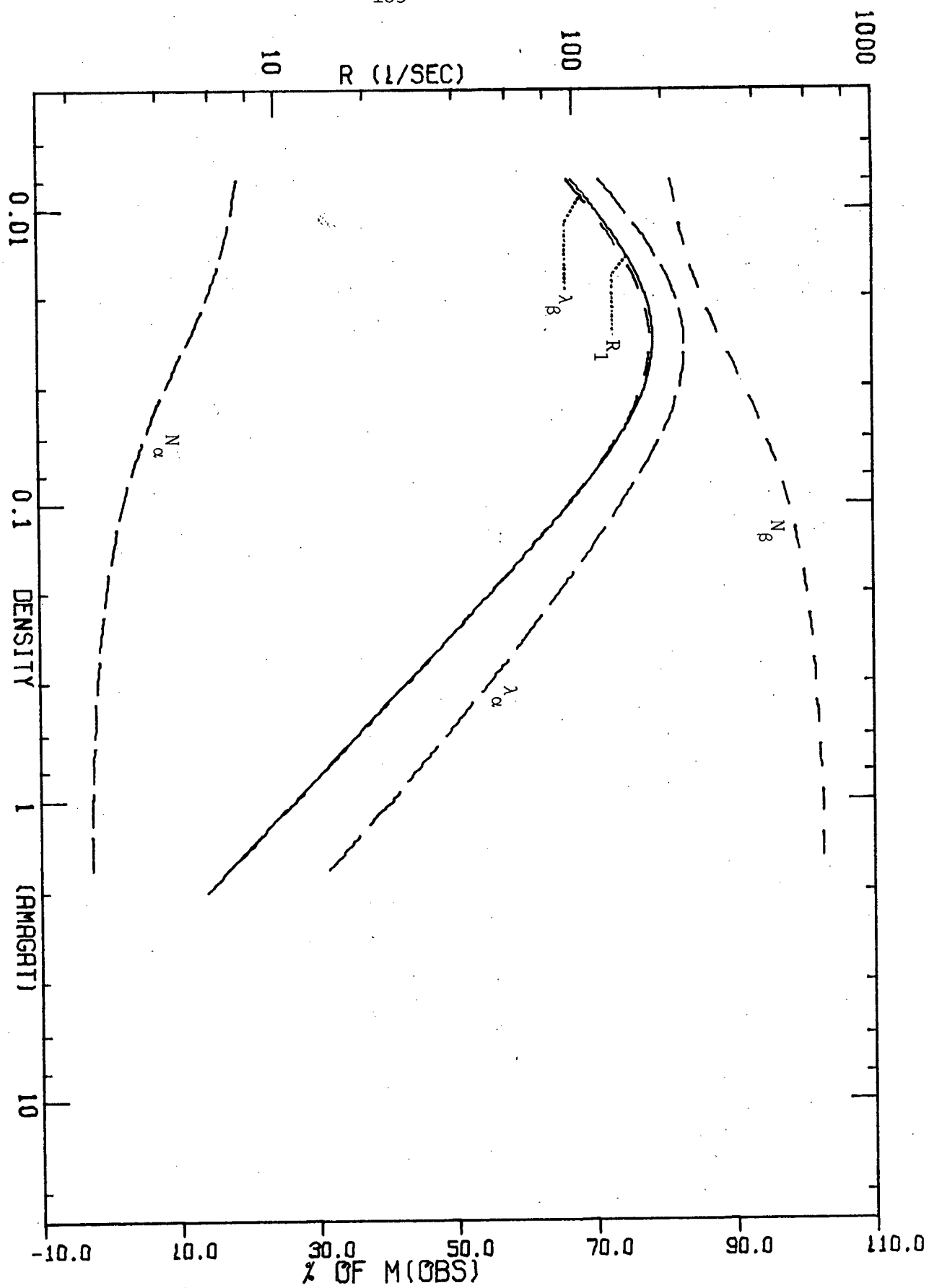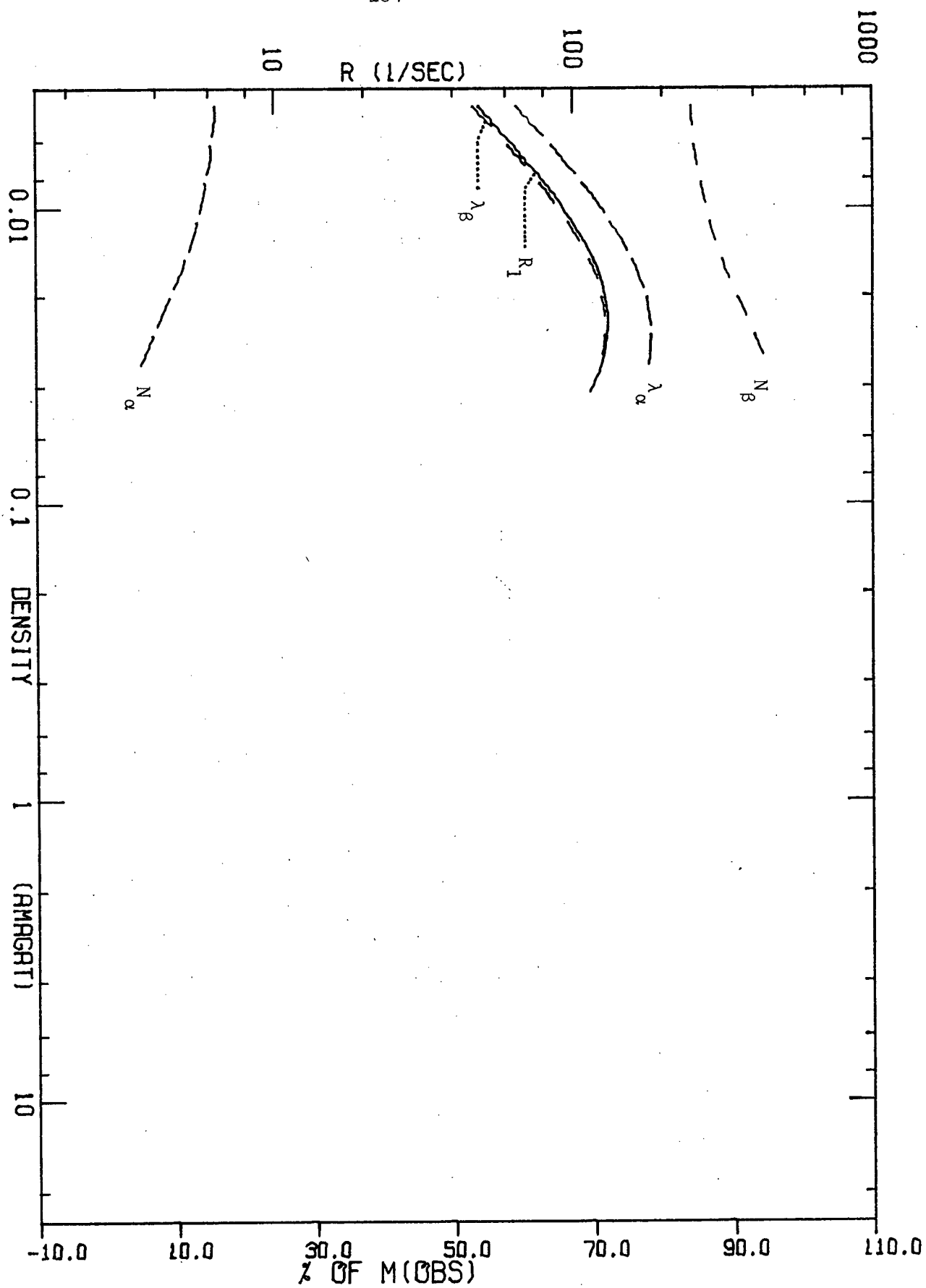
Figure 4.22 (150K)

Figure 4.23 (110K)

Figure 4.24   (77K)

We now investigate what fraction of the relaxation is due to the

different processes. The top theoretical lines in Figures 4.25 (295 K),

4.26 (150 K) and 4.27 (110 K) represent the total relaxation rate R_1. The

bottom curve $R_1^o(C_a)$ in these Figures is obtained by calculating the relaxa-

tion rate with C_d set to zero. We can therefore associate the rate $R_1^o(C_a)$

with that part of the relaxation resulting from the scalar-spin-rotation

interaction. C_d is the coupling constant associated with the tensor spin-

rotation interaction. With $C_d = 0$, the relaxation is strictly exponential

(see Section 4.4 and Appendix I) and so $R_1^o(C_a)$ is well defined. We can

therefore associate that part of the relaxation rate $R_1(C_d)$ resulting from

the tensor spin-rotation interaction through the relation

$$R_1(C_d) = R_1 - R_1^o(C_a) \tag{4.6.10}$$

Because R_1 and $R_1^o(C_a)$ are well defined, so is $R_1(C_d)$. $R_1(C_d)$ is plotted

as a function of density (on a linear scale) in Figures 4.28 (295 K), 4.29

(150 K), 4.30 (110 K) and 4.31 (77 K). The plot of $R_1(C_d)$ is simply the

difference between the top and bottom curves in Figures 4.25, 4.26 and 4.27.

The latter plots can be misleading because R_1 is multiplied by ρ. Note

that the maximum difference between the top and bottom lines on the $R_1\rho$

vs. log ρ plots (Figures 4.25, 4.26 and 4.27) occurs at densities where the

two lines appear to have essentially coalesced. The percentages in the

$R_1(C_d)$ plots (Figures 4.28 to 4.31) are the ratios $R_1(C_d)/R_1$. This ratio

ranges from 4% at 295 K to 9% at 77 K at the density where $R_1^o(C_a)$ has its

maximum, but approaches the limiting value of about 18% at all temperatures

for $\rho \gg \rho_1$. In obtaining $R_1(C_d)$ it must be remembered that we are subtract-

ing two large, not very different, numbers. One of these, $R_1^0(C_a)$, is known

precisely (within the framework of the theory) but the other total relaxation

rate is known only to about ± 2% because of the errors introduced by the

averages involved in the eigenvalue procedure and the least squares fitting

resulting in a single relaxation rate. Thus the error in $R_1(C_d)$ may range

from about 50% at 295 K to about 25% at 77 K. However we rather suspect

that this error has a "one-way-ness" built in, in the sense that if

$R_1(C_d)$ at 295 K is x% too large then so is $R_1(C_d)$ at 77 K. In any event,

this error only affects the scale on Figures 4.28 to 4.31 and not the

relative values of $R_1(C_d)$, $R_1^0(C_d)$ and $R_1^1(C_d)$.

There are two contributions to $R_1(C_d)$, namely those terms involving

the zero frequency transition probabilities for I = I' = 1 (B term) and

those terms involving the non-zero frequency centrifugal distortion transi-

tion probabilities for I' → I of 1 → 1, 2 → 1 and 0 → 1 (E, C and D terms).

We associate $R_1^0(C_d)$ with the former and $R_1^1(C_d)$ with the latter.

Great care must be taken in defining $R_1^0(C_d)$ and $R_1^1(C_d)$. If the

total relaxation rate is computed setting the <u>zero</u> frequency C_d terms to

zero then the resulting time evolution of the magnetization is indeed well

represented by a single exponential. Therefore, if we subtract the well

defined $R_1^0(C_a)$ from this rate then the remainder can be identified with $R_1^1(C_d)$

We can now define $R_1^0(C_d)$ through the relation

$$R_1^0(C_d) = R_1 - R_1^0(C_a) - R_1^1(C_d)$$

(4.6.11)

If, instead of defining $R_1^0(C_d)$ through equation 4.6.11, we calculated the relaxation rate setting the non-zero frequency terms to zero, we would find the resulting relaxation not to be well represented by a single relaxation rate. This is because the only contribution of the remaining C_d terms (i.e., those of zero frequency) is to the relaxation of the I = 1 magnetization and not to the I = 2 magnetization. In this limit the eigenvalue solution is exact with $R^{12} = R^{21} = 0$, $R^{22} = R_1^0(C_a)$ and $R^{11} = R_1^0(C_a)$ plus the zero frequency C_d terms. In this limit 62.5% of the observed magnetization decays with a rate constant R^{22} and 37.5% of the observed magnetization decays with a rate constant R^{11} which is about 15% larger than R^{22}. These percentages are given by equation 3.9.18. It is interesting that when the zero frequency terms are put back in, the relaxation is again well represented by a single relaxation rate. As long as $R_1^1(C_d)$ is defined via the previous page and $R_1^{\,1}(C_d)$ via equation 4.8.11 all the contributions to R_1 are well defined.

$\rho R_1(C_a) + \rho R_1^1(C_d)$ is plotted in Figures 4.25 (295 K), 4.26 (150 K) and 4.27 (110 K). Further $R_1^1(C_d)$ is plotted in Figures 4.28 (295 K), 4.29 (150 K), 4.30 (110 K) and 4.31 (77 K). At the density ρ' where the value of $R_1^1(C_d)$ is a maximum, the ratio $R_1^1(C_d)/R_1$ ranges from 2% at 295 K to 4.3% at 77 K. (This is not the maximum value of $R_1^1(C_d)/R_1$.) In Figures 4.28 to 4.31 the density at which this occurs is given indicated in units of ρ_1. It is interesting to note that this density ρ' is 5 ρ_1 at 295 K but 1.4 ρ_1 at the other temperatures. It is understandable because ρ' is essentially given by some effective average of equation 4.6.1

$$\rho' = \frac{|\omega_d \pm \omega_0|_{avg}}{\omega_0} \rho_1 \qquad (4.6.12)$$

The average value of $|\omega_d \pm \omega_0|$ is $5\omega_0$ at 295 K and will decrease with temperature as fewer J states become effectively populated. However, there is a limit when only a few distortion frequencies constitute the average value of $|\omega_d \pm \omega_0|$. It is a coincidence that the 5 or so relevant distortion transitions which lead to $\rho' = 1.4 \rho$, at 110 and 150 K and the sole important contribution to $|\omega_d \pm \omega_0|_{avg}$ at 77 K, namely the 71 MHz line also leads to $\rho' = 1.4 \rho$. The concept of an average centrifugal distortion transition is useful at high temperatures for practical reasons to be discussed in the next section. This concept breaks down, however, at and below the vicinity of 150 K where the individual contributions to the average value of $|\omega_d \pm \omega_0|$ become significant.

The parameter $\rho R_1^0(C_a) + \rho R_1^0(C_d)$ is given in Figures 4.25 (295 K), 4.26 (150 K) and 4.27 (110 K) and represents the total contribution to the relaxation of zero frequency transitions (i.e., elastic collisions). $R_1^0(C_d)$ is shown in Figures 4.28 (295 K), 4.29 (150 K), 4.30 (110 K) and 4.31 (77 K). It is interesting to note that of the two contributions to $R_1(C_d)$, $R_1^1(C_d)$ dominates at high densities.

Figures 4.25 to 4.27

Different combinations of the three contributions
to the total relaxation rate R_1 are plotted on $R_1\rho$
vs $\log\rho$ plots for 295K (Figure 4.25), 150K (Figure
4.26) and 110K (Figure 4.27). These different
contributions are $R_1{}^0(C_a)$, the contribution of the
scalar spin-rotation interaction; $R_1{}^0(C_d)$, the
contribution of the tensor spin-rotation interaction
involving no change in distortion energy, and; $R_1{}^1(C_d)$,
the contribution of the tensor spin-rotation
interaction involving changes in distortion energy.
The latter relaxation rate includes the effects of
spin conversion transitions. The combinations of
these three relaxation rates are indicated on the
figures and the theoretical parameters δ and N have
been assigned the values of $\delta = 1$ and $N = 0$. The
value of ρ_1 in amagat is 0.04 at 295K (Figure 4.25),
0.031 at 150K (Figure 4.26) and 0.0275 at 110K
(Figure 4.27). The equivalent figure for 77K is not
shown because of the very small density range.
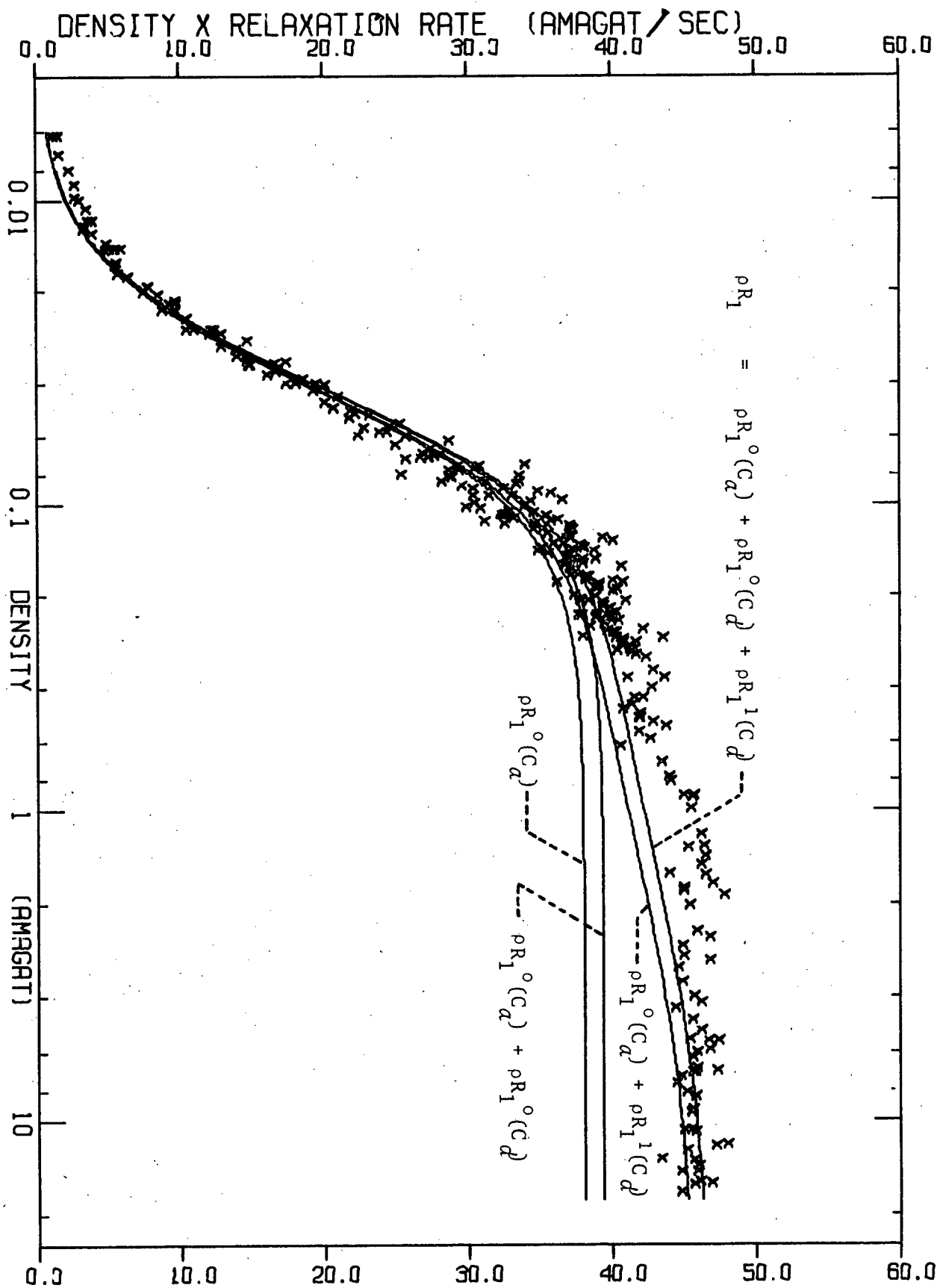
Figure 4.25   (295K)
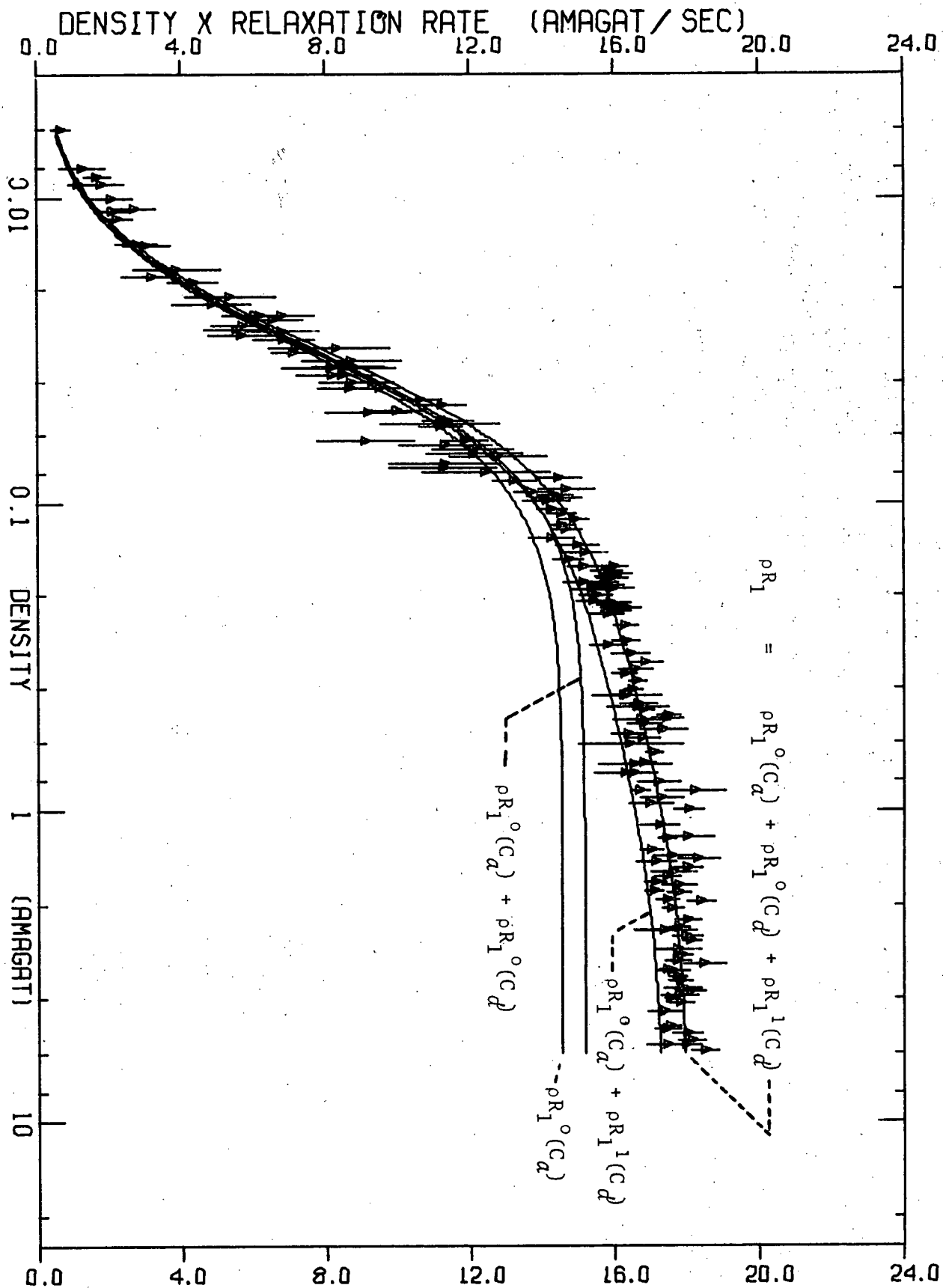
Figure 4.26   (150K)
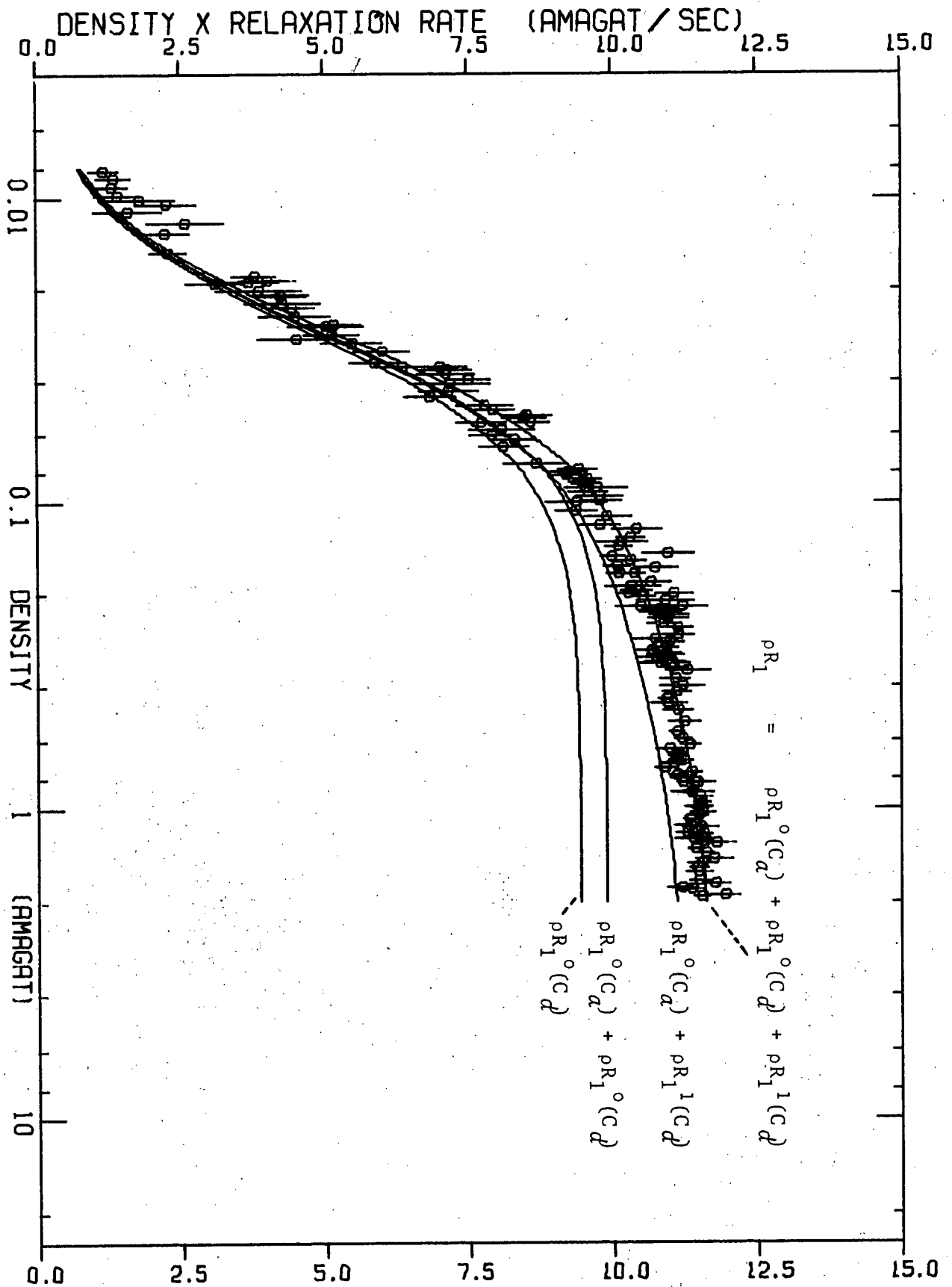
Figure 4.27 (110K)

Figures 4.28 to 4.31

The relaxation rates $R_1{}^0(C_d)$, $R_1{}^1(C_d)$ and their sum
are plotted on a linear scale as a function of density
for 295K (Figure 4.28), 150K (Figure 4.29), 110K
(Figure 4.30) and 77K (Figure 4.31). Both rates
represent relaxation due to the tensor spin-rotation
interaction. $R_1{}^0(C_d)$ is that part which involves no
change in distortion energy (called the zero frequency
contribution) and $R_1{}^1(C_d)$ is that part which involves a
change in centrifugal distortion energy (called the non-
zero frequency contribution). The percentages in square
parenthesis indicate the ratio $R_1{}^1(C_d)/R_1$, the percent-
ages in curly parenthesis indicate the ratios $R_1{}^0(C_d)/R_1$

and the percentages in normal parenthesis indicate the
sum of these ratios. R_1 is the total relaxation rate
given by $R_1{}^0(C_a) + R_1{}^0(C_d) + R_1{}^1(C_d)$. These percentages
are given at the density at which $R_1{}^0(C_a)$ and $R_1{}^0(C_d)$
have their maximum contribution to R_1 and, at the high-
est densities corresponding to the measurements. Also
given is the density ρ' at which $R_1{}^1(C_d)$ makes its
maximum contribution to R_1 and, with no parentheses,
the ratio $R_1{}^1(C_d)/R_1$ at that density. The theoretical
parameters δ and N are $\delta = 1$ and $N = 0$. The values for
ρ_1 (in amagat) are 0.04 at 295K (Figure 4.28), 0.031 at
150K (Figure 4.29), 0.0275 at 110K (Figure 4.30) and 0.024
at 77K (Figure 4.31).

Figure 4.28   (295K)

R1 (1/SEC)
0.0
2.5
5.0
7.5
10.0
12.5
15.0
DENSITY (AMAGAT)
0.01
0.1
1
10
R1 1(Cd)
ρ' = 1.4ρ1
2%
[2%]
{4%}
(6%)
R1 0(Cd)
R1 0(Cd) + R1 1(Cd) = R1(Cd)
(18%)
[15%]
{3%}
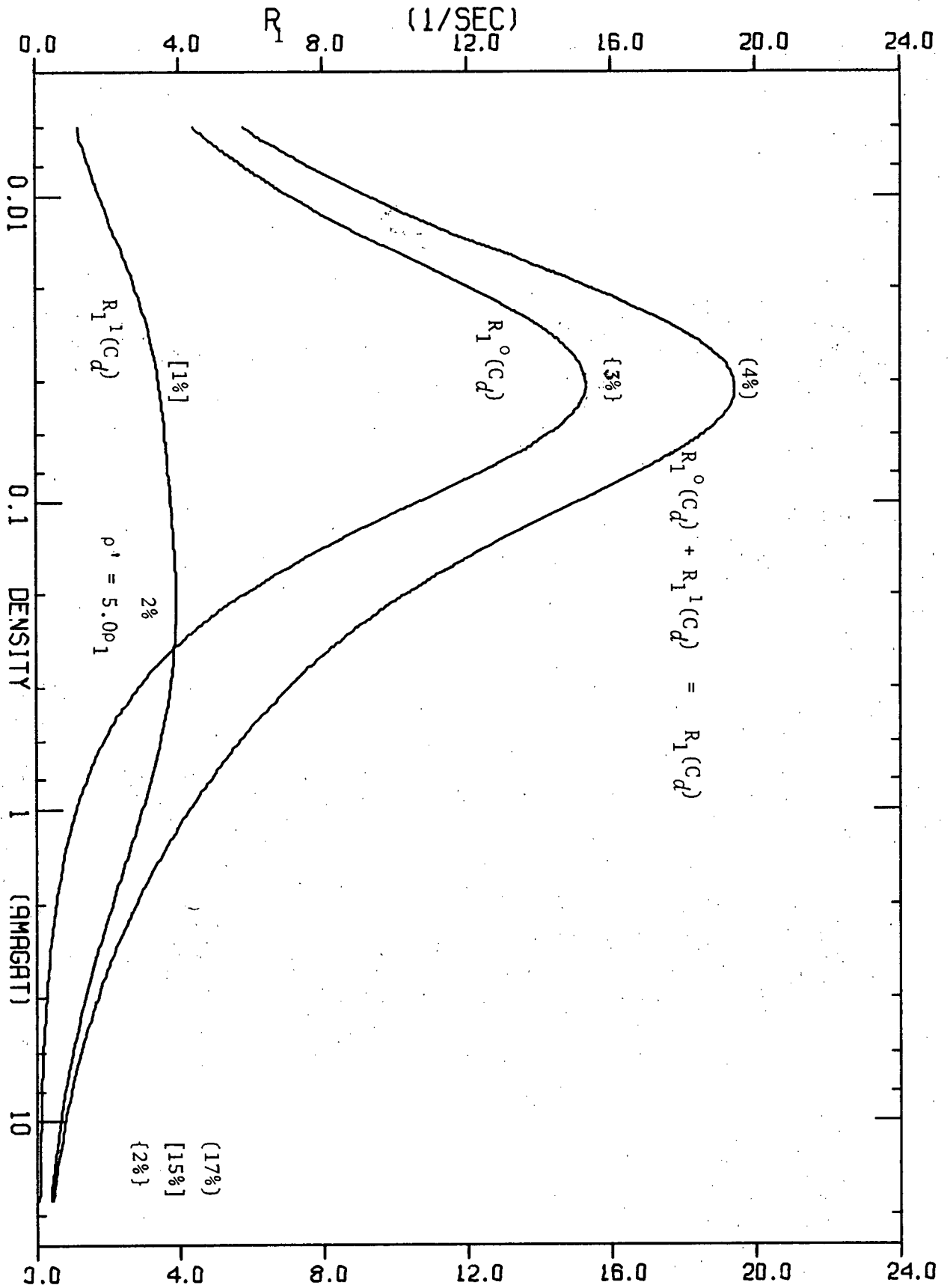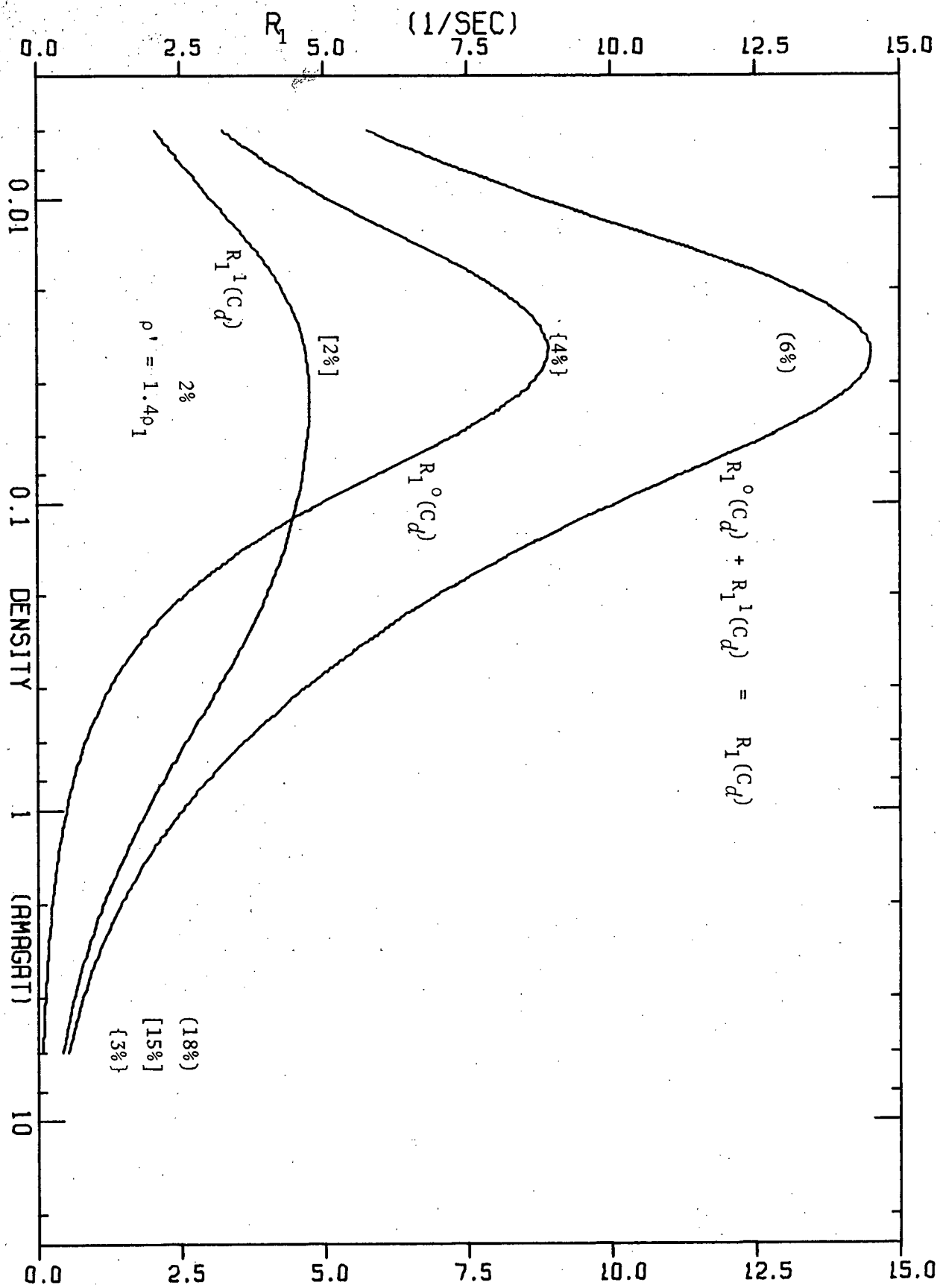
Figure 4.29 (150K)
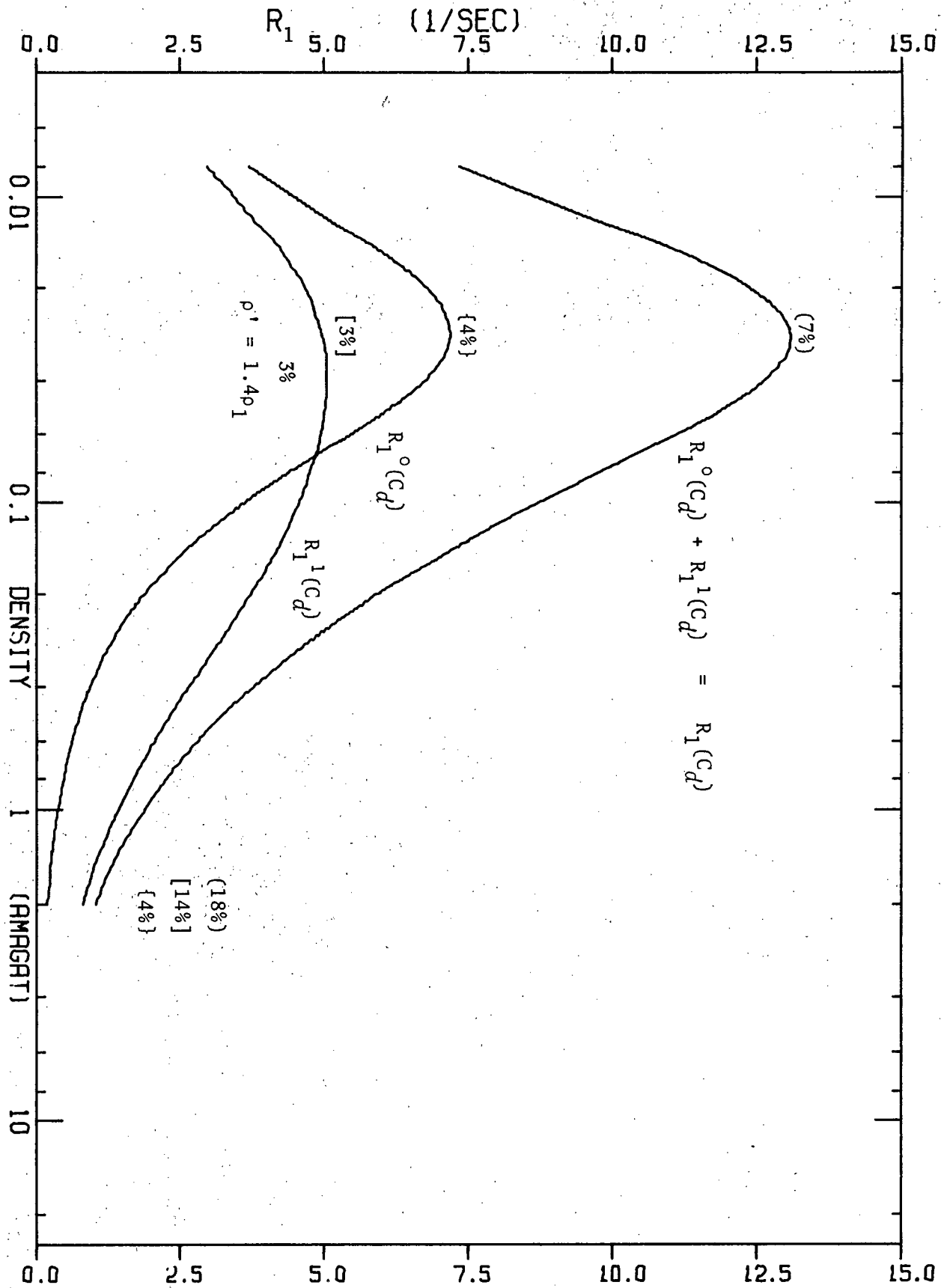
Figure 4.30   (110K)
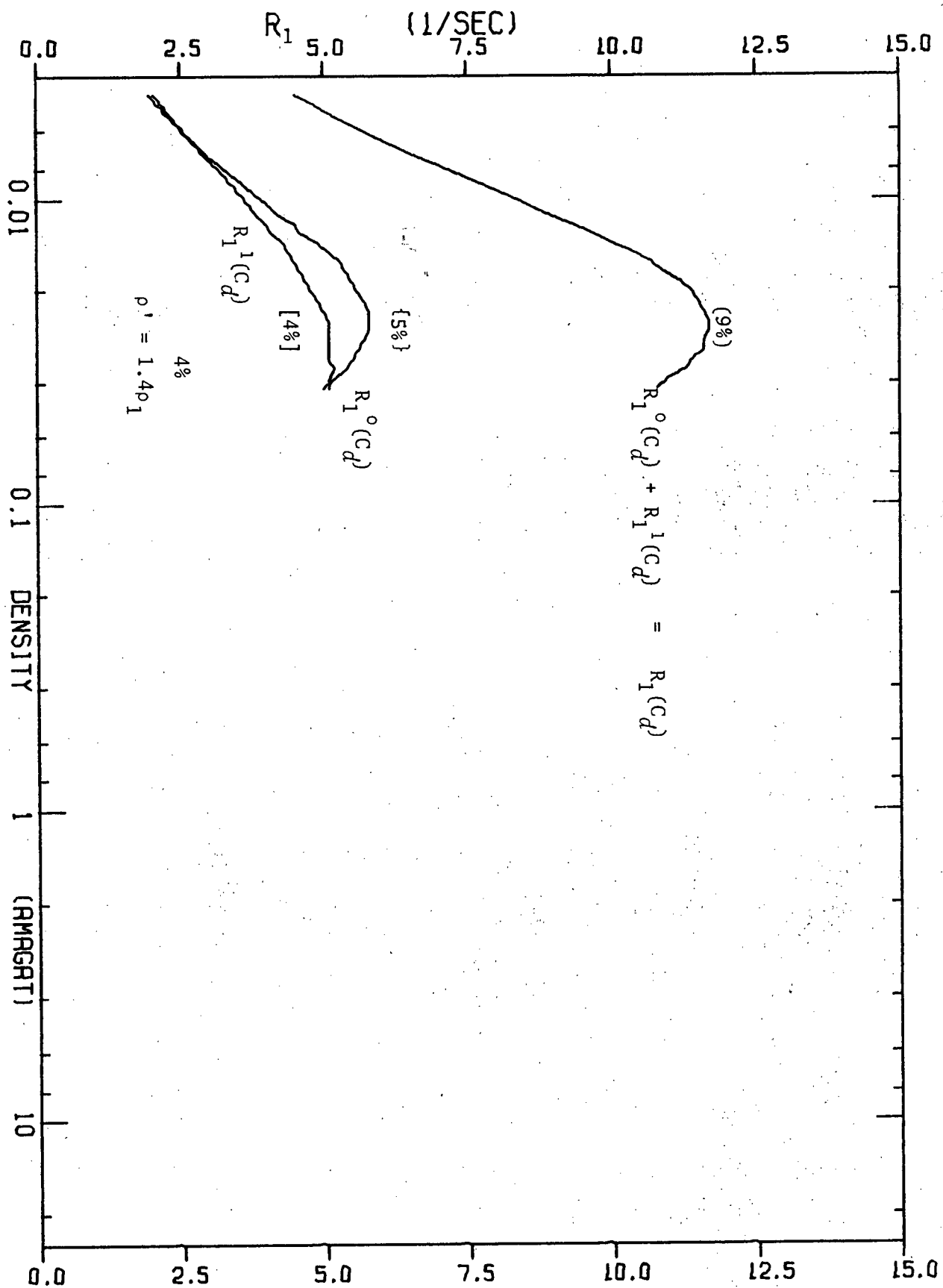
Figure 4.31 (77K)

4.6.3 COMPARISON WITH THE RESULTS OF BBB(25)

It is clear that at room temperature, the effects of centrifugal distortion are small (Figure 4.28). BBB (25) treated this small but not negligible contribution of centrifugal distortion in a phenomenological way. This was done by treating the centrifugal distortion spectrum (Figures G.1 to G.13) as a single line at frequency Ω. Because the contribution of $R_1^0(C_a)$ is the same in the present theory as it is in the "classical" theory employed by BBB (Section 4.4), this term was subtracted from the observed relaxation rate. In the present theory, the resulting relaxation is composed of a single term involving ω_0, namely $R_1^0(C_d)$, and many terms which constitute $R_1^1(C_d)$ involving $\omega_d \pm \omega_0$ for all the distortion frequencies ω_d. BBB, however, fit the remaining relaxation to the single parameter Ω. That is to say they used equation 4.4.1 with $j_2(\omega_0)$ replaced by $j_2(\Omega)$. They find that $5\omega_0 < \Omega < 8\omega_0$ gives "a reasonable fit of the data" although it is clear from Table 4 of BBB that $3\omega_0$ and $9\omega_0$ can not be ruled out. Although this turns out to be an acceptable method at 295 K it should be modified to include a zero frequency term in C_d. At the time, of course, the magnitude of such a term was not known. It was also not known if the factor 4/45 in equation 4.4.1 was accurate, nor was it known that the cross term in $C_a C_d$ was negligible. It has now been established that the 4/45 is reasonably accurate (Section 4.4) and that the cross term is negligible (Section 3.8). This method introduced by BBB has been recently applied to relaxation measurements in methane-helium mixtures (29).

It is not surprising that the two parameter fit of BBB (ρ_1 and Ω)

fit the existing room temperature data (see Appendix A) as well as the two
parameter fits employed here (or even perhaps better), since Ω is allowed
to vary whereas the hundred or so important centrifugal distortion transitions
employed here have both their frequency and relative weights fixed.

At T = 295 K, the value of Ω found by BBB is to be compared with
the average of $|\omega_d \pm \omega_0|$ found here and the agreement is good. It should be
pointed out that the average value of $|\omega_d \pm \omega_0|$ reported here $(5\omega_0)$ is based
on the one parameter fit of the data.

4.7   THE SPECTRAL DENSITY

For nuclear spin relaxation measurements performed at Larmor

frequencies above about 40 MHz and densities near and below the R_1 maximum,

the time evolution of the magnetization is not governed by a single rate

constant. The eigenvalue approach used to describe the relaxation at 30 MHz

is completely inadequate and one must iteratively solve the nine coupled

differential equations for the populations of the nuclear spin states. The

non-exponentiality of the relaxation is most pronounced for experiments per-

formed at low temperatures with a Larmor frequency of 76 MHz. (see Figures

4.1 to 4.8)

The manner in which non-exponential relaxation is characterized is

a matter of convention. We choose to calculate two relaxation rates; one

for the short time evolution of the magnetization and the other for the long

time evolution of the magnetization. The time duration over which these

two relaxation rates are calculated have been defined explicity in Section 4.2.

This is a convenient way to characterize the non-exponentiality of the decay

because these two regions of Δt should be accessible to measurement if

signal to noise is comparable to that realized in the experiments reported

in this project.

These two relaxation rates are plotted as a function of nuclear

Larmor frequency for 295, 150 and 77 K in Figures 4.32, 4.33 and 4.34 res-

pectively. The interesting frequency region (above 50 MHz) is plotted on

an expanded scale in Figures 4.35, 4.36 and 4.37 for the same temperatures.

The density employed in this example is 0.01 amagat. These plots are referred

to as the spectral density $J(\omega)$.

Figures 4.32 to 4.37

The theoretical prediction for the observed
longitudinal relaxation rate resulting from the
spin-rotation interaction is plotted as a function
of nuclear Larmor frequency. The density is 0.01
amagat and the plots are given for T =295K
(Figure 4.32), T = 150K (Figure 4.33) and T = 77K
(Figure 4.34). The parameters in the theory are
δ = 1, N = 0 and ρ_1 = 0.04, 0.031 and 0.024 amagat
for T = 295, 150 and 77K, respectively. At
frequencies where the relaxation is not well
represented by a single relaxation rate, it is
characterized by two relaxation rates as discussed
in the text. The frequency range between 50 and
110 MHz in Figures 4.32, 4.33 and 4.34 is shown
on an expanded scale in Figures 4.35, 4.36 and 4.37
respectively.
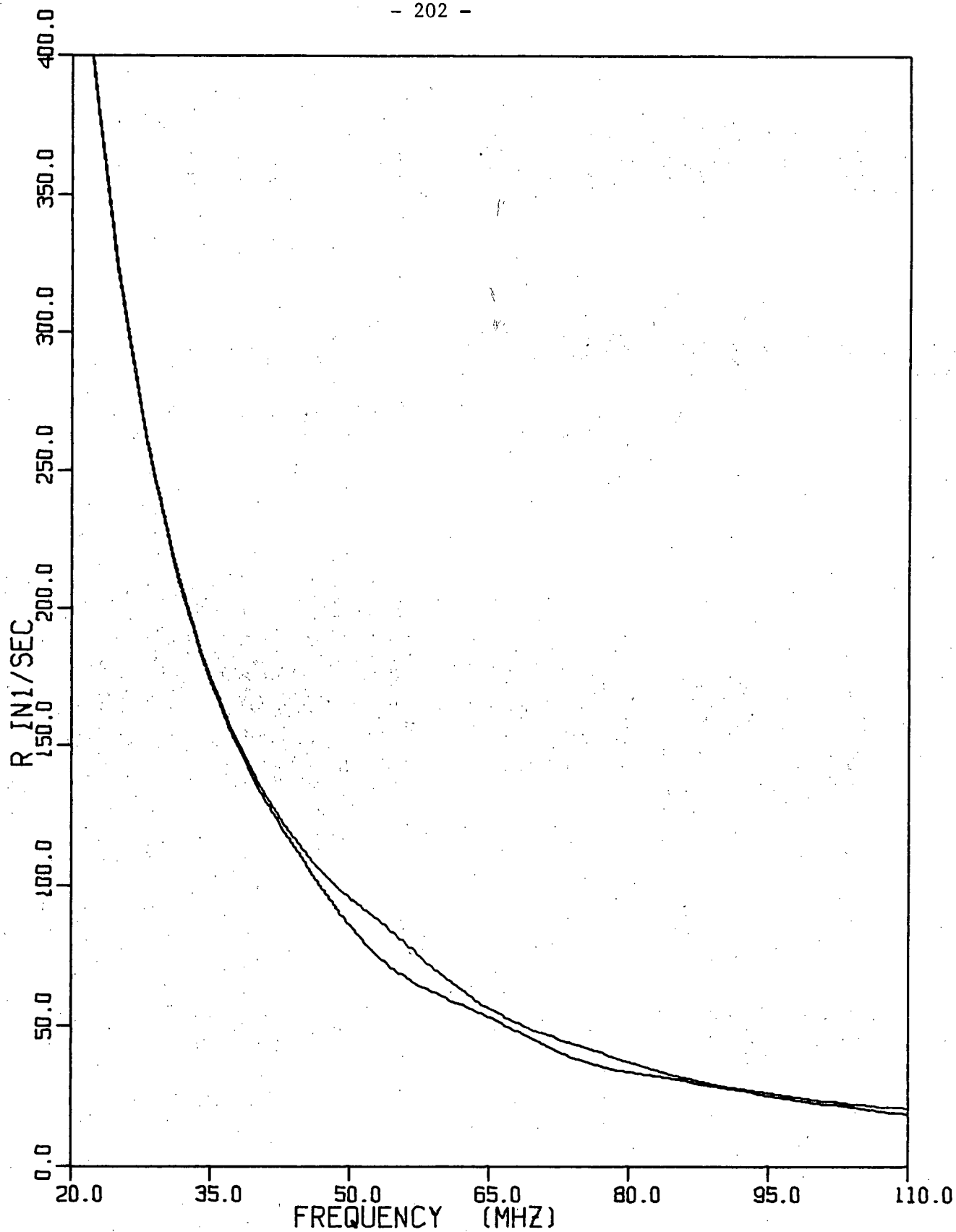
Figure 4.32 (295K)
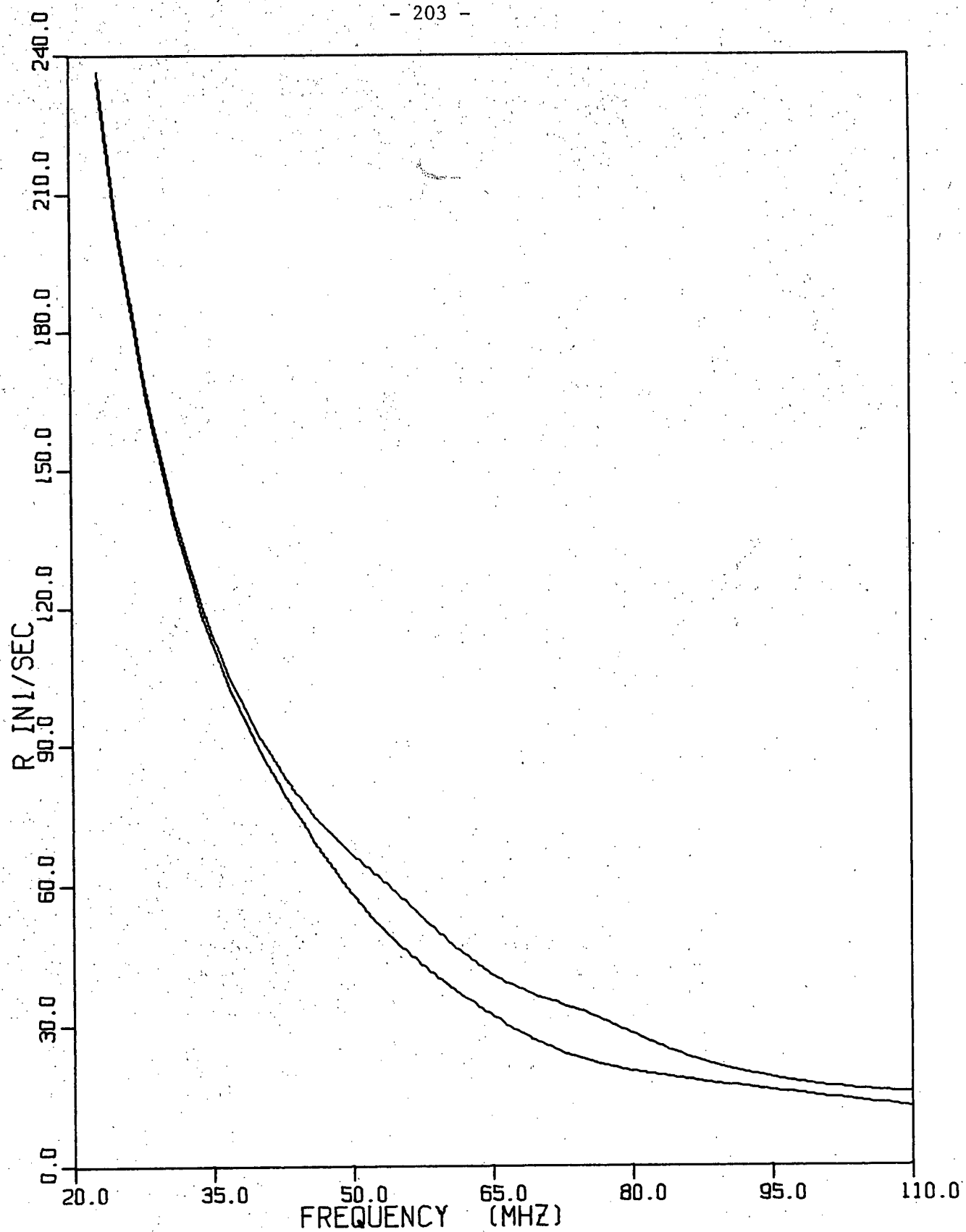
Figure 4.33 (150K)
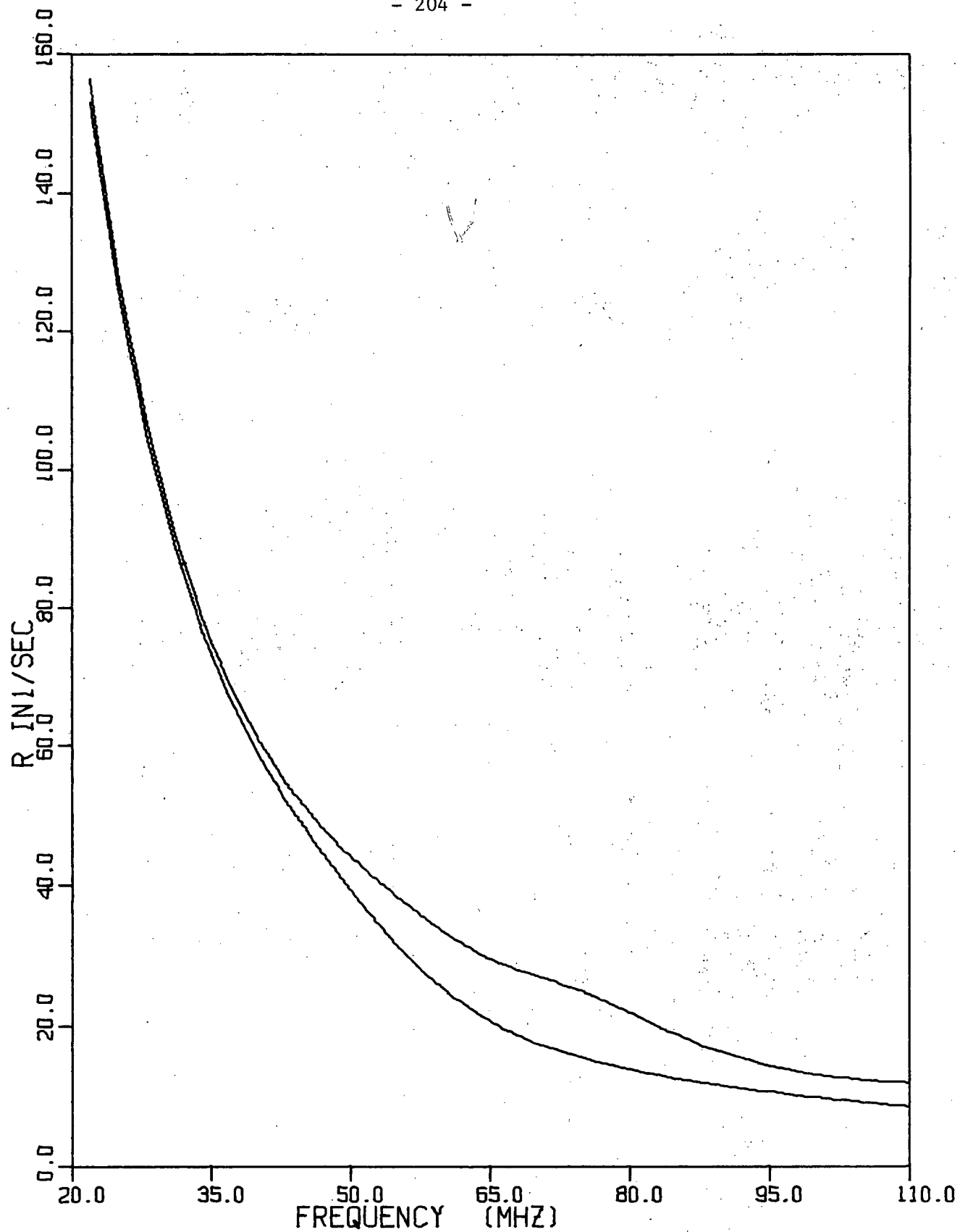
Figure 4.34   (77K)
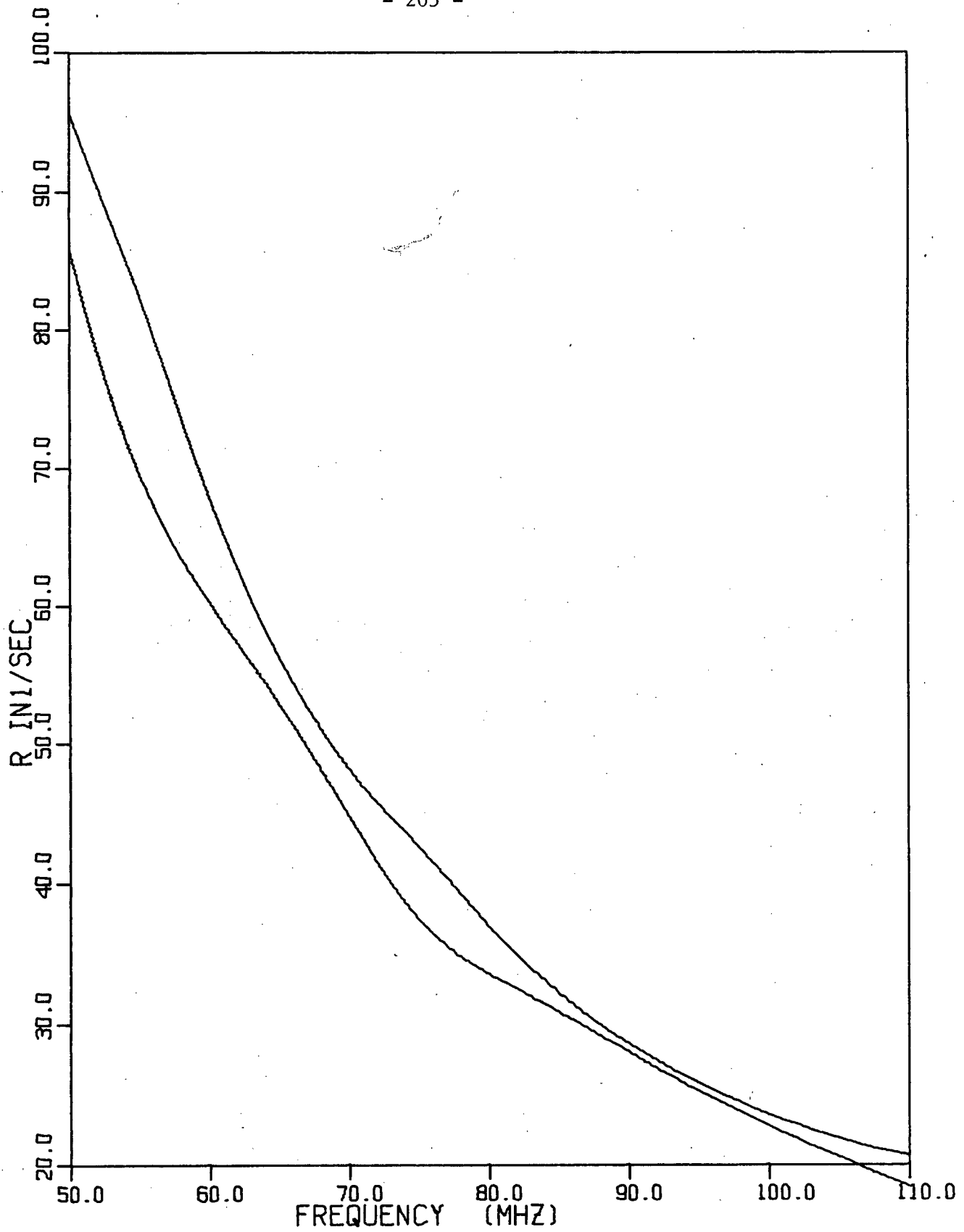
Figure 4.35 (295K)
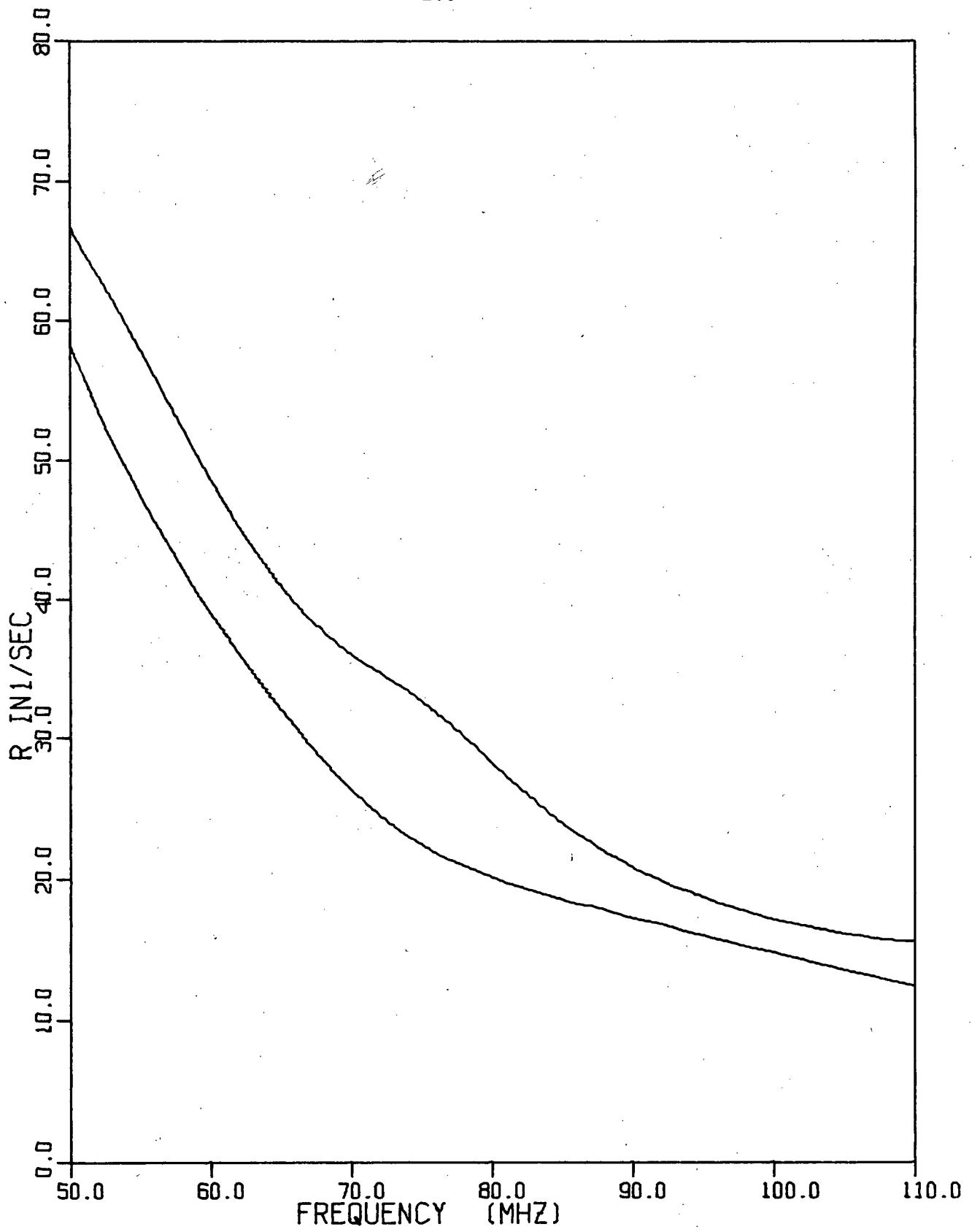
Figure 4.36 (150K)
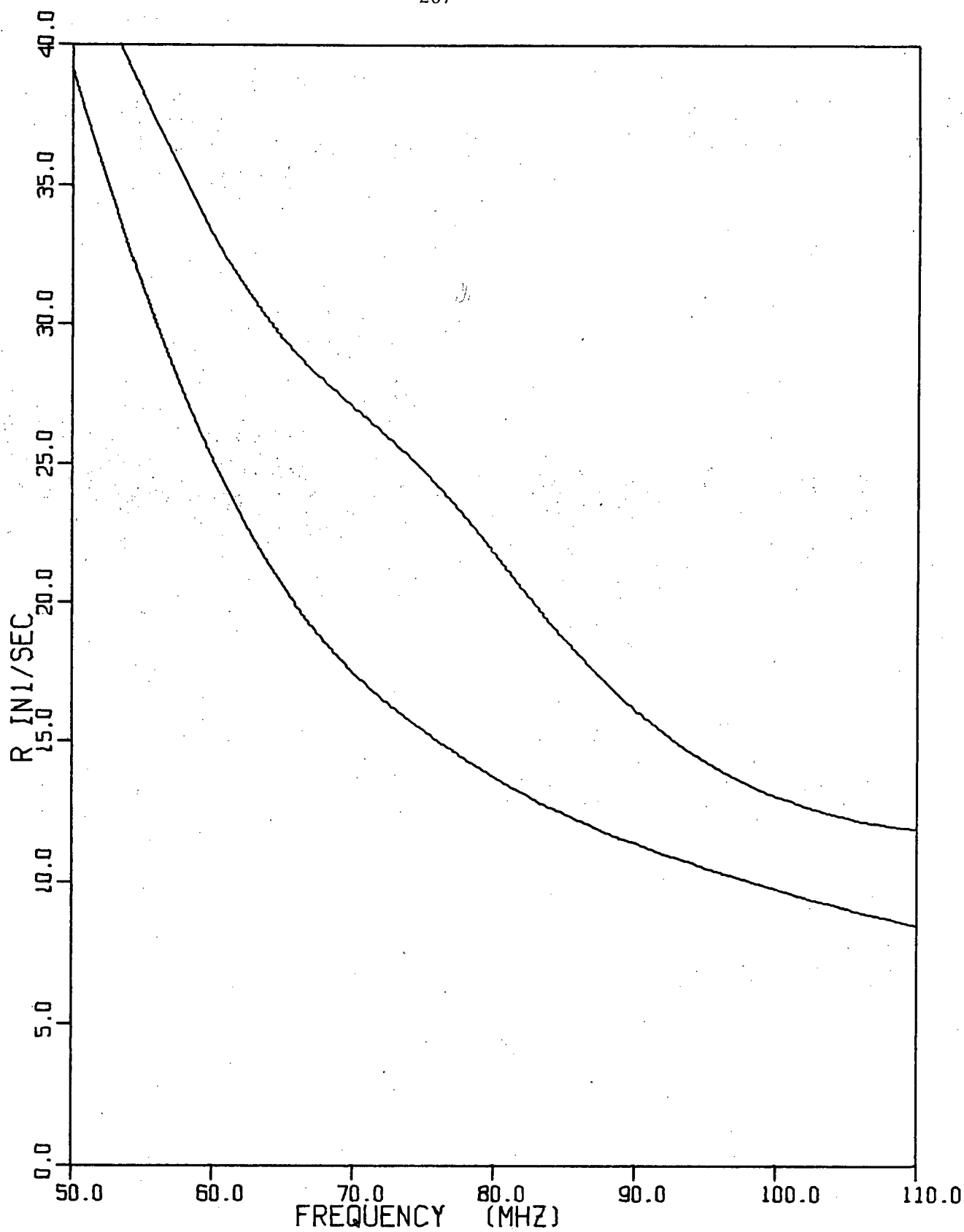
Figure 4.37   (77K)

CHAPTER V

Summary, Conclusions and Proposals

We have examined nuclear spin relaxation in low density methane gas both theoretically and experimentally.

The experiments involve measuring the recovery of the nuclear magnetization after a suitable perturbation by using conventional pulsed nuclear magnetic resonance techniques. Within experimental accuracy, the relaxation process could be characterized by a single rate constant. This longitudinal nuclear spin relaxation rate was measured over a very wide range of density and temperature at a nuclear Larmor frequency of 30 MHz. Considerable effort went into optimizing signal to noise in order that precise measurements could be made in the vicinity of, and well below, the density at which the relaxation rate goes through a maximum.

While the measurements indicate that relaxation rates can be measured at very low densities ($\sim 10^{17}$ molecules/cm^3) there are two problems that should be appreciated before experiments specifically designed for very low density measurements are undertaken. The first problem results from the fact that while R_1, the longitudinal relaxation rate decreases with decreasing density below the density of the R_1 maximum, the transverse relaxation rate R_2 increases with decreasing density. This means that the free induction decay, which at very low densities

has a width of order R_2^{-1} becomes narrower and the time over which the free induction decay can be sampled must be made shorter. Thus the signal to noise will decrease faster than linearly with density as density is decreased. The second problem involves the cleanliness of surfaces. As the density is decreased, the intrinsic relaxation rate resulting from the spin-rotation interaction decreases, but the relaxation resulting from collisions with the walls of the sample chamber continues to increase. Thus a great deal of effort should go into cleaning both the sample chamber and the sample gas. Experiments at very low densities may provide a wealth of information for studies concerning the relationship between the form of the anisotropic intermolecular potential and collision induced changes of molecular angular momentum. Such experiments may also prove to be useful in the study of surfaces, particularly with regard to processes associated with molecular reorientation and diffusion on surfaces. Also, it is possible that Van der Waals complexes could be studied by relaxation measurements at very low densities.

In previous theories of nuclear spin relaxation in polyatomic molecules, the molecular rotation and its modulation by collisions were treated in a phenomenological way and the nuclear spin system was treated quantum mechanically. The experimental results, however, can not be reproduced by such a theory which takes into account only an effective isotropic spin-rotation interaction. That is to say, this "classical" theory accounts for a constant (i.e., zero frequency) local field for the protons which is then modulated by collisons. This theory

neglects the local fields oscillating at characteristic frequencies of the molecular rotation. These fields result from the fact that the anisotropic or tensor spin-rotation interaction gives rise to transitions between the centrifugal distortion states of the molecule. These transitions cover a wide range of frequencies from a few MHz to tens of GHz and must be taken into account. When one thinks of the nuclear spins as relaxing via the Larmor frequency component of the local magnetic fields, this means that one must add up the contributions of many local fields resulting from these centrifugal distortion transitions as well as the contribution of the average local field.

In order to account for the effects discussed in the previous paragraph the theory developed in this work involves treating the composite system, spin plus rotation, quantum mechanically. (The effects of collisions we still treat phenomenologically.) The symmetry of the total (spin plus rotation) wavefunctions results in a one to one correspondence between each rotational state of the molecule and the total nuclear spin of the molecule. Invoking the existence of spin symmetry requires a complete understanding of both the rotational structure of the molecule and the interaction which links the molecular rotation and nuclear spin degrees of freedom. In calculating total transition probabilities for the spin plus rotation system, the matrix elements of the spin-rotation interaction were calculated. This calculation requires extensive use of group theory. In summing over the rotational degrees of freedom to obtain nuclear spin transition probabilities, great care was taken to ensure the requirements of spin symmetry were satisfied.

In performing these calculations it has been assumed that the relaxation process is describable through rates of changes of populations. The present theory should be combined with a complete quantum-mechanical description of the rotation plus spin system which includes off-diagonal elements of the density matrix. It is clear how to perform this calculation, but it would be extremely involved.

Once the nuclear spin transition probabilities are known, one can solve nine coupled equations for the time evolution of the nuclear spin states after a suitable perturbation. Finally, knowing the time evolution of the populations of the spin states, the time evolution of the observed magnetization can be computed. The result of this calculation is that, in general, the relaxation can not be characterized by a single relaxation rate. The departure from exponential relaxation is most pronounced and should be observable for experiments performed at nuclear Larmor frequencies near a characteristic frequency of the rotational system (i.e., a centrifugal distortion frequency). The reason for this is that the nuclear spin transition probabilities W(I'm'Im) become strongly dependent on m' and m. Those transition probabilities involving nuclear spin levels that cross (i.e., a level crossing) dominate the tensor spin-rotation interaction's contribution to the relaxation and lead to non-exponential relaxation.

A major proposal is clearly to measure a departure from exponential relaxation. The suggested experiment involves a temperature of 110K and a density of 10^{-2} amagat at a nuclear Larmor frequency of 75.96 MHz. The temperature and density are not critical, but for these

values numerical predictions of the time evolution of the magnetization are given explicitly in Section 4.7. At this frequency, the level crossing indicated in Figure 3.2 will occur in the J=3 state. If the degree of non-exponential relaxation is observed to peak in the vicinity of the frequency (field) at which level crossings occur then one will have performed spectroscopy on the rotational structure of the molecule by doing a nuclear spin relaxation measurement.

A Larmor frequency of 30 MHz falls in the regime of being "far" from a relevant centrifugal distortion frequency with the result that it would require measurements considerably more precise than those reported here to detect a departure from exponential relaxation. Under these circumstances, certain approximations can be invoked and the problem can be analyzed in terms of the time evolution of the I=1 and I=2 magnetizations instead of the time evolution of the nine spin states. This leads to the prediction of two relaxation rates with the interesting result that at high densities where the rates are quite different, one of them is associated with close to 100% of the observed magnetization and the other with a negligible fraction of the observed magnetization. At low densities, the two relaxation rates are nearly equal. Thus, the theory predicts, within the approximations involved, that a single relaxation rate will be observed.

Comparison of theory and experiment can be used to provide information on that part of the problem we have approached phenomenologically, namely, the manner in which the time dependence of the problem is introduced. In this thesis we have referred to this problem as "the

effects of collisions", "the line shape of the rotational lines" and "the modulation of the local field by collisions". Treating this problem in a more rigorous manner requires the use of a more complete statistical mechanical or kinetic theory description of the molecular system. Considerable headway has been made for the case of diatomic gases and it is felt that this could be extended to polyatomic gases. The present theory, however, simply assumes that the spectral density for each rotational frequency is given by a Lorentzian line shape.

When the theory is fitted to the 30 MHz measurements, the agreement is very good except at the very low densities. The fitting procedure involves one parameter, namely a constant of proportionality which relates the correlation time (time between collisions which effectively reorient the molecule) to the density. This proportionality constant, in turn, can be related to a cross section for molecular reorientation. At room temperature, this cross section is found to be about one third of the kinetic cross section which implies that the strength of collisions is intermediate between strong ($\sigma = \sigma_{KIN}$) and weak ($\sigma << \sigma_{KIN}$). The cross section is found to vary with temperature according to $\sigma \propto T^{-0.9}$. This result may be useful in a theoretical investigation of the anisotropic intermolecular potential responsible for molecular reorientation.

The discussion in the previous paragraph applies to the measurements at 110K and 150K very well. Although the fit to the 295K data is reasonably good, a significant improvement can be obtained by introducing more parameters. One choice of additional parameters has been discussed for illustrative purposes. It was found that when the correlation times for the scalar and tensor parts of the spin-rotation interaction were

allowed to differ and also to be dependent on J, the resulting fit of
the experimental data implied that the cross section associated with
the tensor part is about twice that of the scalar part and both cross
sections vary approximately as 1/J. It is not known whether this
empirical result is meaningful but a more detailed theoretical treat-
ment of the molecular collisions may be worth doing at this time.

APPENDIX A

Experimental Results

Table A.1 and Figures A.1 and A.2 present the experimental results at 295 K from reference (25) and this project. Those values taken from reference (25) are clearly indicated in Table A.1.

The relaxation rates at 150 K, 110 K and 77 K along with random, systematic and total errors are tabulated in Tables A.2, A.3 and A.4 respectively. The 150 K results are plotted in Figures A.3 and A.4, with systematic errors in Figures A.5 and A.6 and with total errors in Figures A.7 and A.8. The equivalent plots for 110 K appear in Figures A.9 to A.14 and for 77 K in Figures A.15 to A.17.

For comparison purposes, all the results are plotted in Figures A.18 and A.19.

These figures are discussed in Chapter II, Section 2.5

TABLE A.1

METHANE RELAXATION RATES AT 295 K AND 30 MHZ

"D" IS THE DENSITY IN AMAGAT
"R" IS THE LONGITUDINAL RELAXATION RATE IN 1/SEC
"DR" IS THE PRODUCT IN AMAGAT/SEC

* DENOTES THIS PROJECT (ROOM TEMP CHAMBER)
** DENOTES THIS PROJECT (VARIABLE TEMP CHAMBER)
ALL OTHER VALUES FROM BECKMANN ET AL (25)

D	R	DR	D	R	DR
0.0062	191.00	1.18	0.0292	505.00	14.75
0.0062	236.00	1.46	0.0302	427.00	12.89
0.0071	231.00	1.64	0.0310	448.00	13.89
0.0080	285.00	2.28	0.0328	426.00	13.97
0.0089	305.00	2.71	0.0337	435.00	14.66
0.0098	274.00	2.69	0.0342	508.00	17.37
0.0100	299.00	2.99	0.0346	481.00	16.64
0.0107	324.00	3.47	0.0348	427.00	14.86
0.0116	308.00	3.57	0.0348	424.00	14.75
0.0117	331.00	3.87	0.0359	465.00	16.69
0.0122	281.00	3.43	0.0370	452.00	16.72
0.0124	267.00	3.31	0.0378	426.00	16.10
0.0129	299.00	3.86	0.0387	481.00	18.61
0.0139	352.00	4.89	0.0400	435.00	17.40
0.0144	407.00	5.86	0.0403	450.00	18.13
0.0144	355.00	5.11	0.0403	485.00	19.54
0.0144	385.00	5.54	0.0407	493.00	20.06
0.0146	330.00	4.82	0.0422	457.00	19.28
0.0161	348.00	5.60	0.0444	474.00	21.05
0.0164	336.00	5.51	0.0461	437.00	20.15
0.0175	323.00	5.65	0.0481	431.00	20.73
0.0180	357.00	6.43	0.0481	431.00	20.73
0.0193	403.00	7.78	0.0494	444.00	21.93
0.0194	402.00	7.80	0.0503	442.00	22.23
0.0202	370.00	7.47	0.0509	455.00	23.16
0.0206	415.00	8.55	0.0520	420.00	21.84
0.0215	452.00	9.72	0.0545	465.00	25.34
0.0219	426.00	9.33	0.0556	442.00	24.57
0.0221	440.00	9.72	0.0560	408.00	22.85
0.0229	385.00	8.82	0.0578	422.00	24.39
0.0230	420.00	9.66	0.0581	412.00	23.94
0.0244	429.00	10.47	0.0590	380.00	22.42
0.0266	415.00	11.04	0.0597	431.00	25.73
0.0266	394.00	10.48	0.0617	465.00	28.69
0.0268	463.00	12.41	0.0634	395.00	25.04
0.0268	455.00	12.19	0.0658	417.00	27.44
0.0274	469.00	12.85	0.0677	417.00	28.23
0.0276	437.00	12.06	0.0677	398.00	26.94

METHANE RELAXATION RATES AT 295 K AND 30 MHZ

	D	R	DR		D	R	DR
*	0.0693	399.20	27.67	*	0.1201	293.80	35.29
*	0.0699	390.10	27.27	*	0.1205	308.30	37.16
	0.0704	379.00	26.68		0.1210	286.00	34.61
	0.0713	360.00	25.67		0.1210	308.00	37.27
	0.0737	461.00	33.98	*	0.1249	296.70	37.07
*	0.0747	411.60	30.76	*	0.1254	284.20	35.63
*	0.0747	392.20	29.31		0.1278	288.30	36.84
	0.0763	400.00	30.52		0.1297	286.00	37.11
*	0.0771	371.60	28.67	**	0.1299	289.80	37.63
	0.0777	378.00	29.37		0.1300	303.00	39.39
*	0.0796	319.50	25.42	*	0.1326	302.30	40.08
*	0.0804	418.00	33.61	*	0.1350	271.50	36.65
*	0.0806	356.40	28.74	*	0.1350	266.30	35.95
*	0.0820	352.30	28.88		0.1360	278.00	37.81
*	0.0844	334.80	28.25	*	0.1374	276.10	37.94
	0.0844	370.60	31.27	*	0.1398	252.10	35.25
	0.0845	398.00	33.63		0.1400	272.00	38.08
*	0.0859	389.00	33.41	*	0.1418	263.00	37.28
*	0.0868	340.60	29.56	*	0.1422	272.90	38.81
*	0.0892	341.20	30.43		0.1430	244.00	34.89
*	0.0892	364.80	32.54		0.1460	244.00	35.62
	0.0910	383.00	34.85	*	0.1470	252.10	37.07
*	0.0916	391.10	35.83	**	0.1493	268.30	41.24
	0.0933	355.00	33.12	*	0.1495	246.60	36.86
*	0.0939	323.90	30.41	*	0.1519	249.90	37.95
*	0.0940	335.50	31.54	*	0.1514	246.10	37.25
	0.0965	379.00	36.57		0.1520	256.00	38.91
*	0.0980	350.60	34.37	*	0.1567	238.20	37.32
*	0.0988	308.80	30.52	*	0.1567	242.70	38.03
**	0.0995	318.40	31.68		0.1590	231.00	36.73
	0.1010	337.00	34.04	*	0.1591	231.00	36.75
*	0.1025	292.20	29.94	*	0.1610	252.60	40.66
*	0.1037	298.50	30.94	*	0.1615	229.80	37.12
*	0.1061	310.10	32.89		0.1639	227.50	37.29
	0.1070	323.00	34.56	**	0.1699	232.30	39.47
*	0.1074	303.80	32.63	*	0.1706	218.30	37.24
	0.1080	299.00	32.29	*	0.1712	220.50	37.74
*	0.1085	299.50	32.49	*	0.1730	222.00	38.41
	0.1090	326.00	35.53		0.1736	220.10	38.20
*	0.1109	299.60	33.22	*	0.1760	216.90	38.17
	0.1130	321.00	36.27	*	0.1784	224.60	40.07
*	0.1134	316.00	35.84	*	0.1808	200.20	36.20
	0.1140	274.00	31.24	*	0.1808	225.50	40.77
*	0.1157	281.60	32.58	*	0.1826	214.10	39.09
*	0.1164	297.70	34.65	*	0.1856	210.50	39.07
*	0.1181	314.00	37.09	*	0.1880	207.00	38.92

METHANE RELAXATION RATES AT 295 K AND 30 MHZ

	D	R	DR		D	R	DR
	0.1890	206.00	38.93		0.3210	132.00	42.37
*	0.1904	212.20	40.41		0.3520	122.00	42.94
*	0.1922	208.50	40.08		0.3700	111.00	41.07
	0.2000	187.00	37.40		0.3700	118.00	43.66
*	0.2018	192.60	38.87		0.4000	107.00	42.80
**	0.2002	191.60	38.36		0.4310	98.00	42.24
*	0.2049	184.60	37.83		0.4320	96.20	41.56
*	0.2066	198.40	40.99		0.4560	90.90	41.45
*	0.2073	185.40	38.44		0.4690	87.00	40.80
	0.2080	182.00	37.86		0.4830	87.00	42.02
*	0.2102	187.50	39.42		0.4990	84.00	41.92
*	0.2170	181.80	39.44		0.5000	84.00	42.00
	0.2190	182.00	39.86		0.5170	82.90	42.86
*	0.2266	177.70	40.27		0.5370	81.50	43.76
*	0.2290	174.60	39.99		0.5570	75.20	41.89
	0.2310	163.00	37.65		0.5890	72.50	42.70
	0.2314	168.70	39.04		0.6210	65.40	40.61
	0.2310	172.00	39.73		0.6960	62.50	43.50
	0.2310	164.00	37.88		0.7750	56.80	44.02
	0.2310	169.00	39.04		0.8030	54.90	44.08
*	0.2362	164.70	38.91		0.9000	50.80	45.72
	0.2380	168.00	39.98		0.9000	50.00	45.00
*	0.2411	168.10	40.52		0.9060	50.30	45.57
*	0.2411	166.10	40.04		0.9910	45.90	45.49
*	0.2471	160.00	39.54		1.2000	38.50	46.20
**	0.2488	164.20	40.85		1.3000	35.70	46.41
*	0.2523	152.60	38.50		1.3200	34.30	45.28
*	0.2583	163.40	42.20		1.4000	33.20	46.48
	0.2610	152.00	39.67		1.5000	30.80	46.20
*	0.2643	152.60	40.33		1.6000	27.50	44.00
	0.2640	152.00	40.13		1.6100	28.90	46.53
*	0.2712	140.20	38.02		1.7200	27.30	46.96
	0.2740	147.00	40.28		1.7800	25.30	45.03
	0.2740	159.00	43.57		1.8200	24.70	44.95
*	0.2763	147.80	40.84		1.8900	25.30	47.82
*	0.2833	144.00	40.79		2.0200	22.50	45.45
*	0.2840	147.00	41.75		2.4700	18.60	45.94
*	0.2883	141.20	40.71	*	2.5700	18.20	46.77
	0.2930	141.00	41.31		2.7400	16.40	44.94
**	0.2997	139.00	41.66		2.9600	15.20	44.99
*	0.3003	138.60	41.63		3.0400	15.40	46.82
*	0.3003	137.50	41.30		3.2100	13.90	44.62
*	0.3037	133.10	40.43		3.5900	12.50	44.87
	0.3040	133.00	40.43		3.9700	11.50	45.65
*	0.3074	134.80	41.43	*	4.1600	11.10	46.18
*	0.3110	134.00	41.67		4.3500	10.20	44.37

METHANE RELAXATION RATES AT 295 K AND 30 MHZ

	D	R	DR			D	R	DR
	4.7400	9.62	45.60		*	9.4400	4.82	45.50
	5.1300	9.00	46.17		*	10.7000	4.25	45.47
*	5.4200	8.38	45.42		*	10.7000	4.21	45.05
*	5.5000	8.62	47.41		*	10.8000	4.24	45.79
	5.5100	8.48	46.72		*	12.0000	4.00	48.00
	5.8900	7.94	46.77		*	12.1000	3.90	47.19
*	6.0100	7.63	45.86		*	12.5000	3.62	45.25
*	6.2700	7.28	45.65		*	13.3000	3.26	43.36
*	6.7800	6.77	45.90		*	13.4000	3.41	45.69
	6.9100	6.85	47.33		*	14.1000	3.26	45.97
	7.0100	6.51	45.63		*	14.7000	3.05	44.83
	7.0100	6.54	45.84		*	14.7000	3.12	45.86
	7.1700	6.25	44.81		*	15.8000	2.92	46.14
*	7.6000	5.85	44.46		*	16.0000	2.93	46.88
*	8.1500	5.55	45.23		*	16.1000	2.84	45.72
*	8.4000	5.45	45.78		*	17.1000	2.62	44.80
*	9.2100	4.95	45.59					
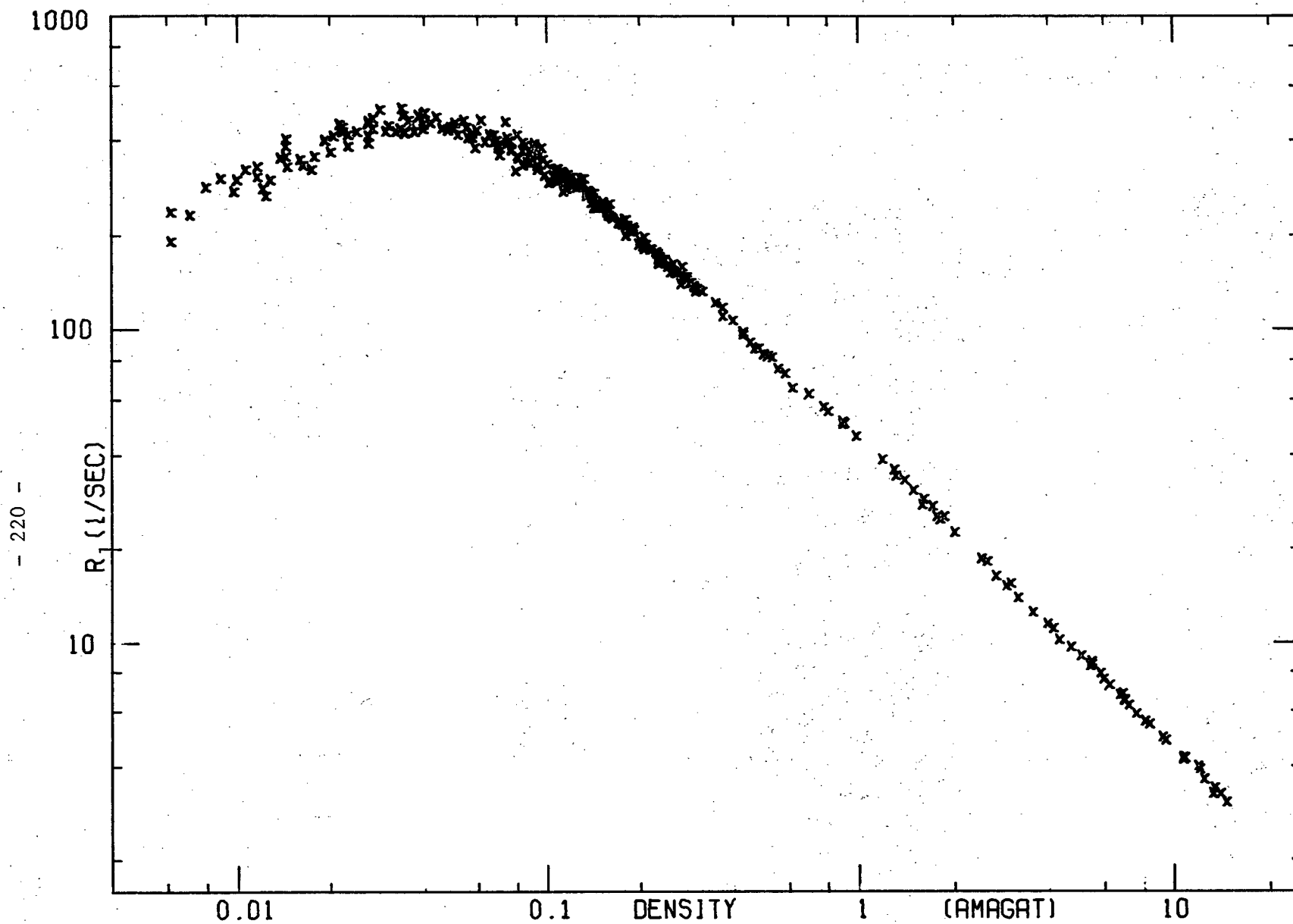
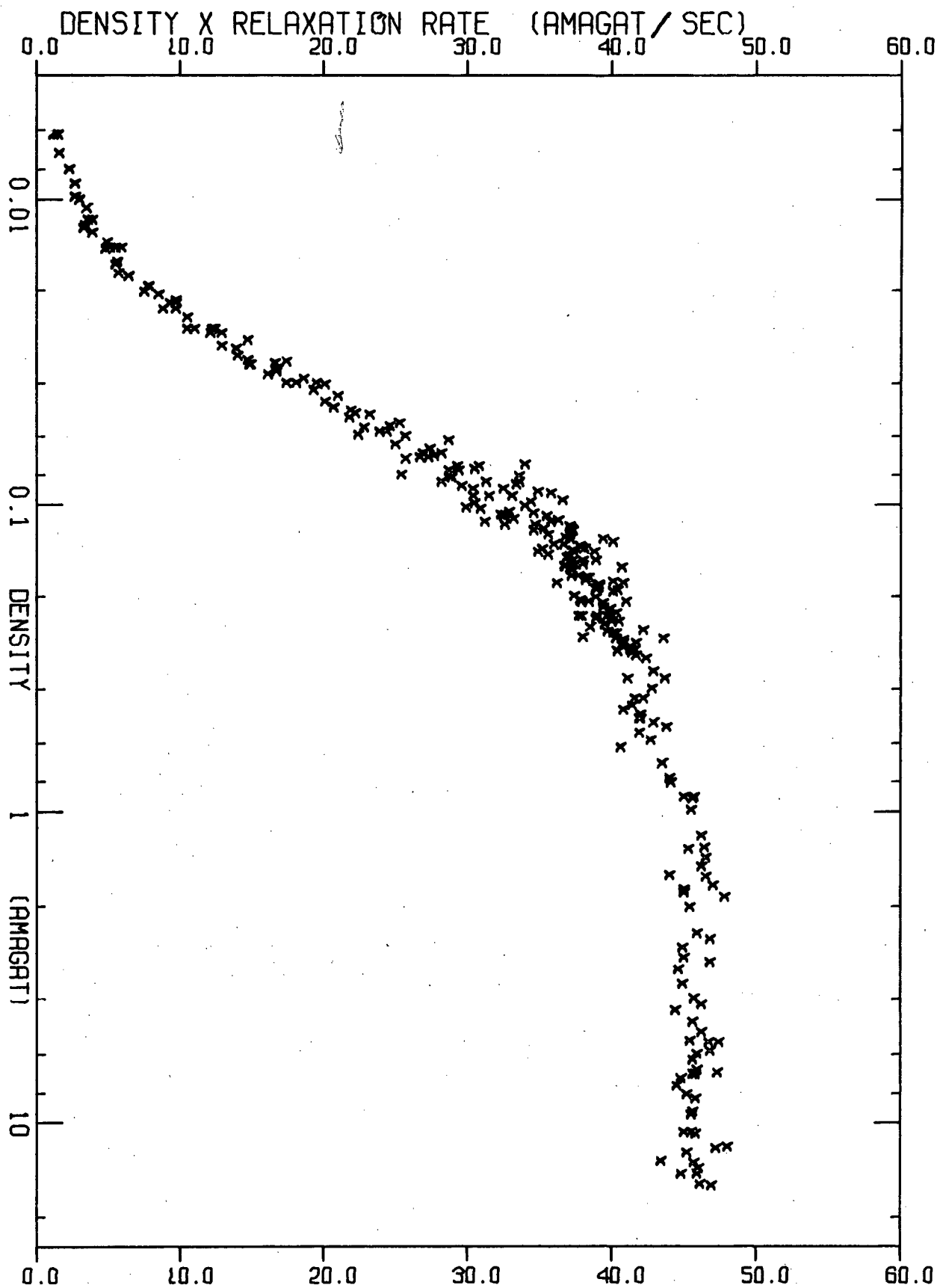Figure A.1. R_1 vs ρ for $T = 295K$

Figure A.2. ρR_1 vs ρ for T = 295K

TABLE A.2

METHANE RELAXATION RATES AT 150 K AND 30 MHZ

"D" IS THE DENSITY IN AMAGAT
"R" IS THE LONGITUDINAL RELAXATION RATE IN 1/SEC
"DR" IS THE PRODUCT IN AMAGAT/SEC
"E(S)" IN % IS THE STATISTICAL ERROR IN R OBTAINED
     BY FITTING THE DATA TO A SINGLE EXPONENTIAL
"E(B)" IN % IS THE ERROR IN R RESULTING FROM THE
     UNCERTAINTY IN THE BASELINE
"E" IN % IS THE TOTAL ERROR

D	R	DR	E(S)	E(B)	E
0.0060	113.50	0.68	22.3	34.6	41.2
0.0080	159.80	1.29	31.7	37.2	48.9
0.0085	199.20	1.70	13.4	18.9	23.2
0.0091	127.80	1.16	14.8	20.1	24.9
0.0091	198.50	1.80	14.1	31.8	34.8
0.0101	207.00	2.08	13.0	25.0	28.2
0.0108	251.50	2.72	11.1	19.9	22.8
0.0111	191.70	2.13	17.9	12.3	21.7
0.0116	193.70	2.25	9.8	16.0	18.7
0.0142	195.50	2.78	9.5	19.1	21.4
0.0142	214.60	3.06	13.6	16.4	21.3
0.0171	227.40	3.89	19.9	24.3	31.4
0.0181	176.50	3.19	16.5	20.2	26.1
0.0189	229.60	4.35	8.9	13.7	16.3
0.0211	254.10	5.37	19.4	13.1	23.4
0.0221	219.70	4.86	12.5	19.0	22.7
0.0241	281.30	6.78	7.3	11.4	13.6
0.0241	257.00	6.20	8.4	9.7	12.8
0.0242	251.60	6.09	7.3	13.5	15.3
0.0249	263.30	6.56	7.0	10.7	12.7
0.0261	218.40	5.70	9.6	11.3	14.8
0.0271	205.50	5.56	9.2	13.4	16.2
0.0271	251.30	6.81	7.6	13.0	15.1
0.0280	203.20	5.69	7.3	14.4	16.1
0.0290	236.20	6.85	5.4	11.5	12.7
0.0309	232.70	7.19	4.5	9.3	10.4
0.0311	267.60	8.33	6.9	16.0	17.5
0.0321	222.50	7.14	4.1	7.5	8.6
0.0342	255.00	8.73	7.0	14.2	15.9
0.0359	237.00	8.51	9.4	14.0	16.9
0.0359	227.10	8.16	8.1	14.4	16.5
0.0357	242.20	8.64	6.3	9.7	11.6
0.0381	215.10	8.19	7.9	9.1	12.0
0.0381	222.30	8.46	7.0	9.1	11.5
0.0400	233.50	9.34	3.6	5.0	6.2
0.0400	218.40	8.73	5.3	8.6	10.1
0.0419	207.30	8.69	5.8	8.4	10.2

METHANE RELAXATION RATES AT 150 K AND 30 MHZ

D	R	DR	E(S)	E(B)	E
0.0419	227.60	9.54	2.5	5.0	5.6
0.0455	233.70	10.63	3.7	4.6	5.9
0.0479	235.00	11.25	3.7	4.6	5.9
0.0498	200.50	9.99	6.4	5.3	8.3
0.0503	182.80	9.19	6.2	11.5	13.1
0.0539	210.40	11.34	2.5	4.9	5.5
0.0539	211.90	11.42	3.1	5.3	6.2
0.0551	203.00	11.18	8.7	11.9	14.7
0.0560	200.10	11.21	3.6	3.9	5.3
0.0620	191.40	11.87	2.3	4.9	5.4
0.0623	146.60	9.13	6.0	13.7	15.0
0.0642	176.50	11.34	5.6	10.1	11.6
0.0666	181.70	12.10	4.9	8.0	9.4
0.0685	177.10	12.14	5.6	9.4	11.0
0.0704	181.70	12.80	5.0	9.4	10.7
0.0740	153.00	11.32	4.9	12.7	13.7
0.0761	148.00	11.27	5.0	12.2	13.2
0.0787	158.20	12.46	5.6	13.1	14.3
0.0826	175.10	14.47	2.3	3.7	4.4
0.0844	157.00	13.26	2.5	4.1	4.8
0.0900	163.20	14.69	2.9	4.3	5.2
0.0920	149.10	13.71	1.3	3.3	3.5
0.0941	152.80	14.38	1.4	3.2	3.5
0.0960	150.40	14.44	1.9	4.4	4.8
0.0979	144.40	14.14	2.1	4.1	4.6
0.1049	136.30	14.30	1.2	2.7	2.9
0.1080	134.80	14.56	1.2	2.4	2.7
0.1121	133.00	14.90	1.5	2.4	2.8
0.1181	123.50	14.58	1.1	2.5	2.7
0.1219	120.60	14.70	1.3	2.5	2.8
0.1300	109.70	14.26	1.7	4.2	4.5
0.1372	109.30	15.00	1.5	3.8	4.1
0.1449	105.00	15.21	1.6	3.9	4.2
0.1525	96.67	14.75	1.1	2.6	2.9
0.1597	94.96	15.17	1.0	2.7	2.9
0.1600	100.10	16.01	0.9	2.2	2.4
0.1650	95.74	15.80	1.1	2.5	2.7
0.1700	94.52	16.07	1.0	2.7	2.9
0.1731	91.52	15.84	1.2	1.9	2.3
0.1753	91.11	15.97	1.1	2.5	2.7
0.1798	87.57	15.75	1.5	1.9	2.4
0.1801	84.19	15.16	1.4	3.5	3.8
0.1851	85.18	15.77	1.4	2.9	3.2
0.1894	84.42	15.99	1.5	3.2	3.5
0.1899	81.09	15.40	1.6	3.4	3.8
0.1997	77.66	15.51	1.2	2.8	3.0

METHANE RELAXATION RATES AT 150 K AND 30 MHZ

D	R	DR	E(S)	E(B)	E
0.2083	74.14	15.45	1.3	2.8	3.1
0.2100	75.89	15.94	1.4	3.1	3.4
0.2148	74.11	15.92	1.4	2.1	2.5
0.2198	74.45	16.37	1.6	1.9	2.5
0.2198	72.79	16.00	0.9	2.1	2.2
0.2249	71.43	16.06	1.0	2.3	2.5
0.2299	68.82	15.82	1.4	2.6	3.0
0.2490	65.61	16.34	0.9	1.8	2.1
0.2802	58.33	16.34	1.0	2.0	2.2
0.2897	54.65	15.83	1.5	3.0	3.3
0.3089	53.30	16.46	1.2	3.1	3.4
0.3305	51.08	16.88	1.3	2.5	2.8
0.3496	47.50	16.61	1.4	2.5	2.9
0.3592	45.38	16.30	0.7	1.9	2.0
0.3807	43.71	16.64	0.6	1.5	1.6
0.4026	41.08	16.54	0.7	1.4	1.5
0.4219	38.58	16.28	0.6	1.5	1.6
0.4243	38.57	16.36	2.2	5.4	5.8
0.4502	37.05	16.68	-1.3	2.9	3.2
0.4622	36.08	16.67	2.1	4.7	5.2
0.4693	35.88	16.84	0.7	1.7	1.8
0.4909	35.69	17.52	0.8	1.7	1.9
0.5029	34.74	17.47	1.3	2.2	2.6
0.5053	33.17	16.76	2.0	4.3	4.7
0.5231	32.20	16.84	1.3	2.6	2.9
0.5460	31.83	17.38	1.4	3.4	3.7
0.5627	29.11	16.38	1.0	2.7	2.9
0.5843	28.77	16.81	1.0	2.6	2.8
0.6112	26.91	16.45	3.7	8.1	8.9
0.6459	26.49	17.11	0.7	1.2	1.4
0.6998	24.09	16.86	0.8	1.7	1.9
0.7073	23.44	16.58	2.1	5.7	6.0
0.7524	22.01	16.56	1.2	2.4	2.7
0.7536	21.65	16.32	2.3	4.9	5.4
0.8063	21.37	17.23	1.7	3.1	3.5
0.8565	21.30	18.24	1.9	4.2	4.6
0.8603	19.42	16.71	0.9	1.4	1.7
0.9067	19.10	17.32	1.3	3.3	3.6
0.9494	17.92	17.01	1.4	3.4	3.7
0.9872	18.31	18.08	1.3	2.0	2.3
1.1081	15.58	17.26	1.6	2.6	3.1
1.2111	14.89	18.03	1.4	3.7	3.9
1.2192	14.34	17.48	0.6	1.3	1.4
1.3393	12.72	17.04	0.8	1.6	1.8
1.3899	12.67	17.61	1.3	2.7	3.0
1.4279	12.84	18.33	1.2	2.9	3.1

METHANE RELAXATION RATES AT 150 K AND 30 MHZ

D	R	DR	E(S)	E(B)	E
1.4533	11.82	17.18	1.4	3.0	3.3
1.5167	11.89	18.03	0.9	2.0	2.2
1.5675	11.26	17.65	1.4	3.2	3.5
1.6183	10.80	17.48	0.8	1.9	2.1
1.6819	10.20	17.16	0.9	1.5	1.7
1.7201	10.34	17.79	1.4	2.3	2.7
1.8093	9.45	17.10	0.6	1.4	1.6
1.8221	9.77	17.81	1.0	1.4	1.8
1.9115	9.15	17.48	0.9	1.5	1.7
1.9371	9.50	18.40	0.9	1.9	2.1
2.0396	8.63	17.61	0.7	1.6	1.8
2.2304	8.09	18.04	0.7	1.9	2.0
2.3483	7.58	17.80	0.8	1.3	1.6
2.4000	7.25	17.40	2.6	4.2	4.9
2.5033	7.20	18.02	1.0	2.1	2.3
2.5940	6.99	18.14	0.6	1.2	1.4
2.7626	6.43	17.76	1.5	3.1	3.5
2.9058	6.15	17.88	0.9	1.2	1.5
3.0171	5.89	17.77	0.7	1.9	2.0
3.0754	6.01	18.50	1.4	2.8	3.1
3.2277	5.41	17.47	0.5	1.0	1.1
3.2501	5.42	17.62	1.1	2.4	2.7
3.3899	5.24	17.75	0.6	1.2	1.3
3.4951	5.10	17.84	0.5	1.7	1.7
3.7062	4.82	17.88	1.0	2.7	2.9
3.7999	4.77	18.13	0.9	1.9	2.1
3.9048	4.55	17.79	1.2	2.6	2.9
3.9977	4.40	17.58	0.5	0.9	1.0
4.1430	4.31	17.85	0.5	1.9	2.0
4.3976	3.95	17.39	1.5	2.4	2.8
4.8679	3.61	17.56	0.7	1.4	1.6
5.0029	3.49	17.48	0.9	1.8	2.1
5.1851	3.48	18.03	0.9	2.2	2.4
5.4284	3.34	18.14	0.7	1.9	2.1
5.6047	3.12	17.47	1.2	3.2	3.4
5.6319	3.20	18.01	0.7	2.0	2.1
5.8497	3.16	18.51	0.7	2.0	2.1

Figure A.3. R_1 vs ρ for T = 150K.
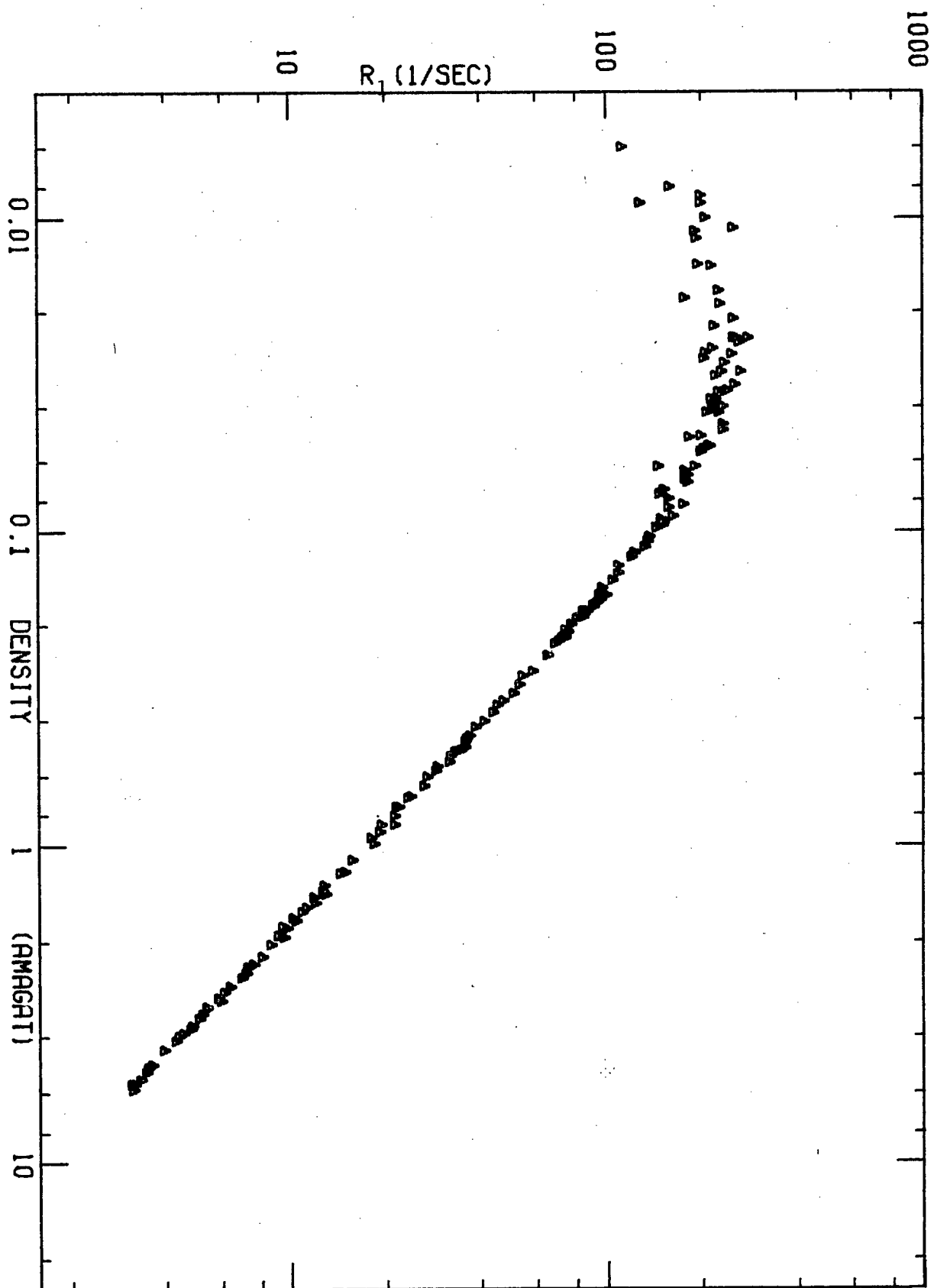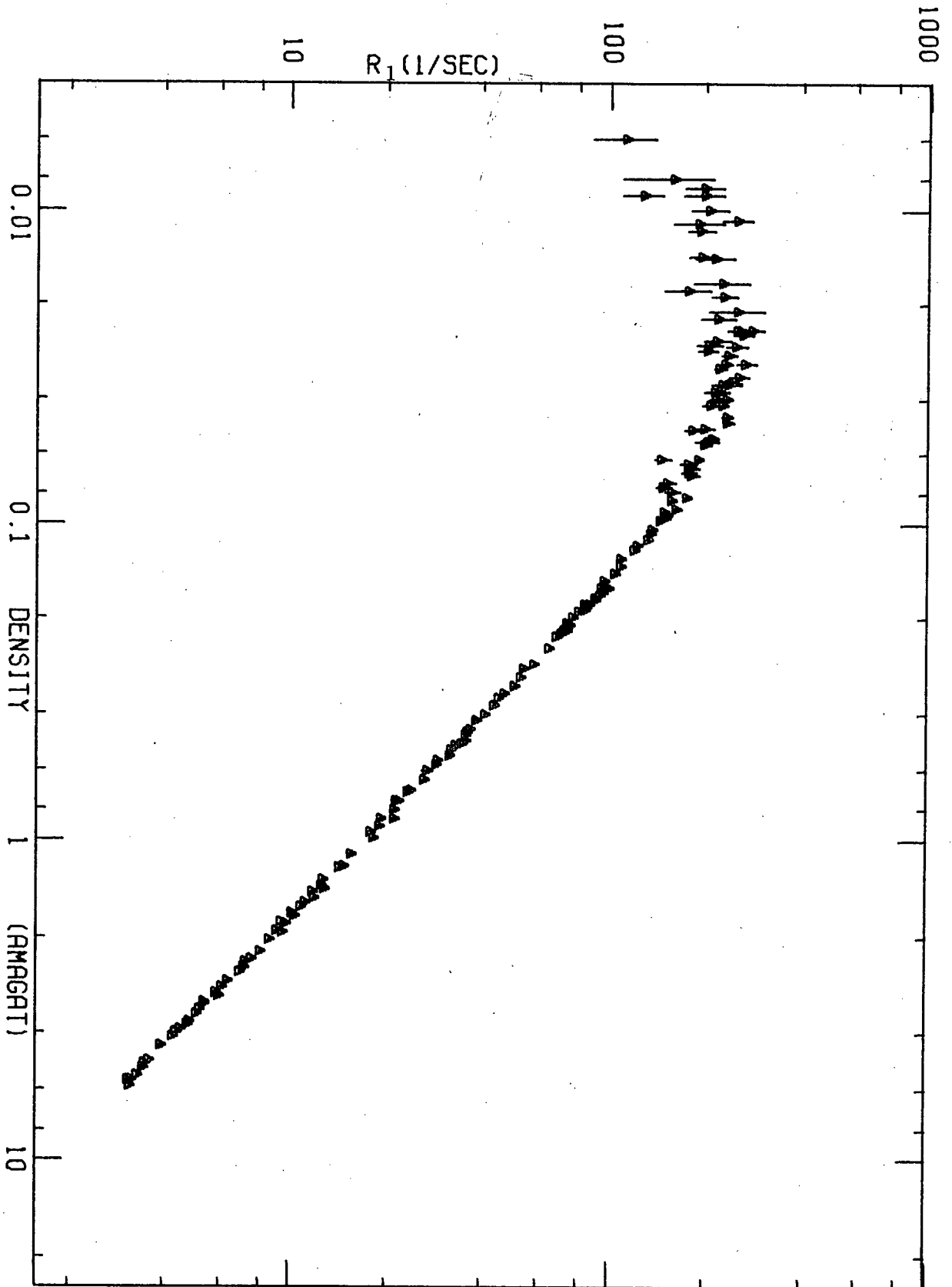
Figure A.4. ρR_1 vs ρ for T = 150K
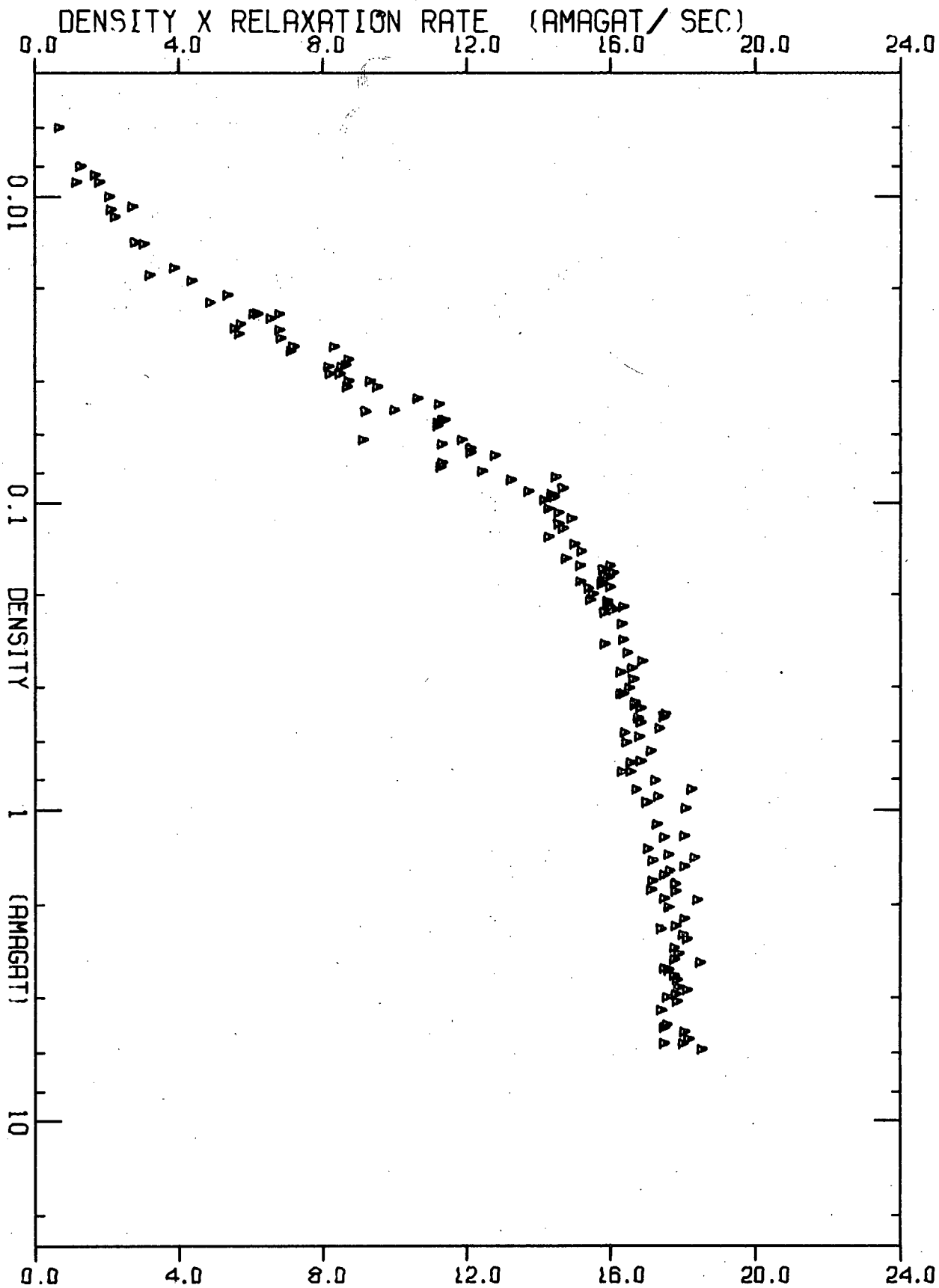
Figure A.5. R_1 vs ρ with statistical errors E(S) for T = 150K
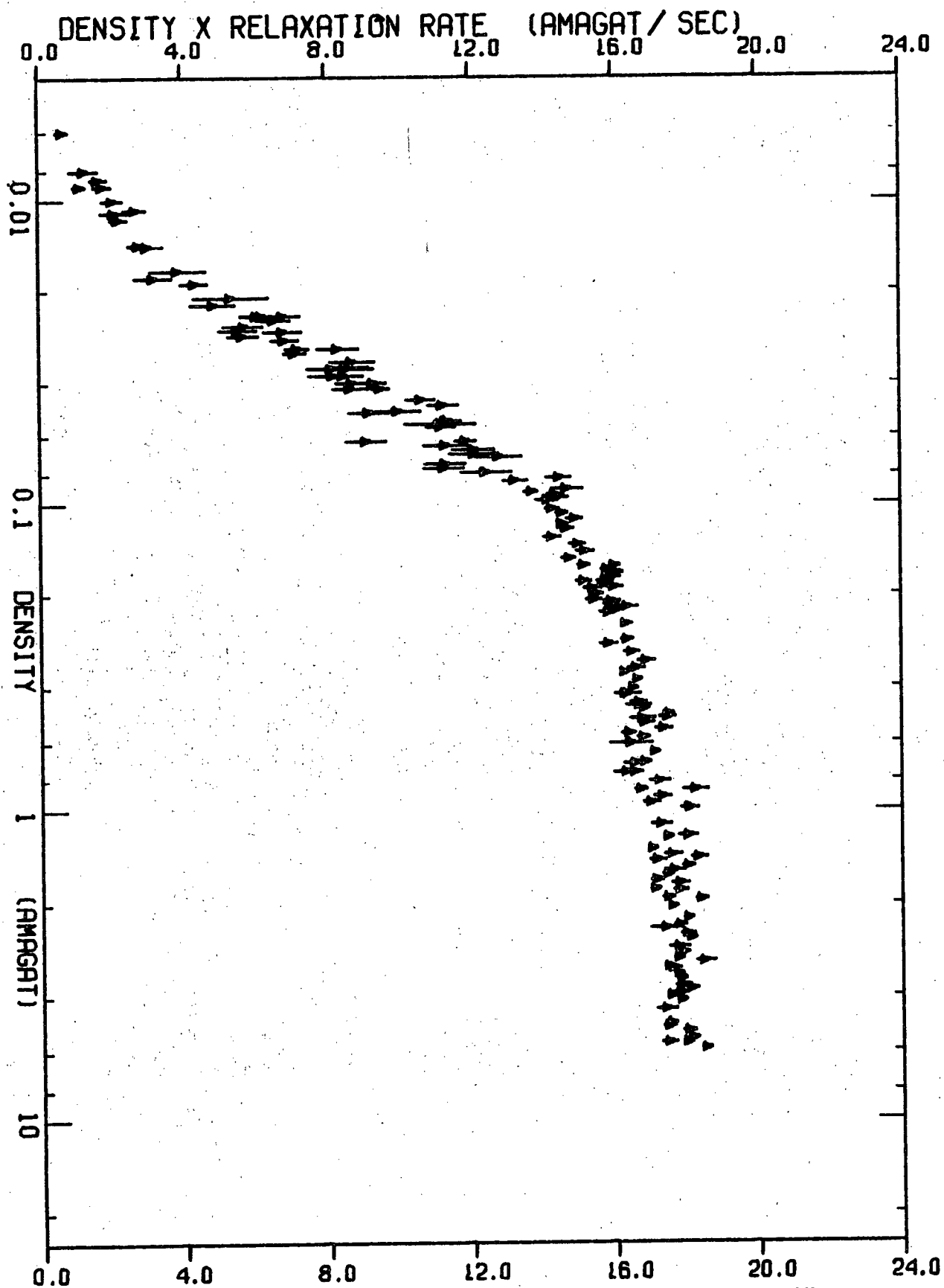
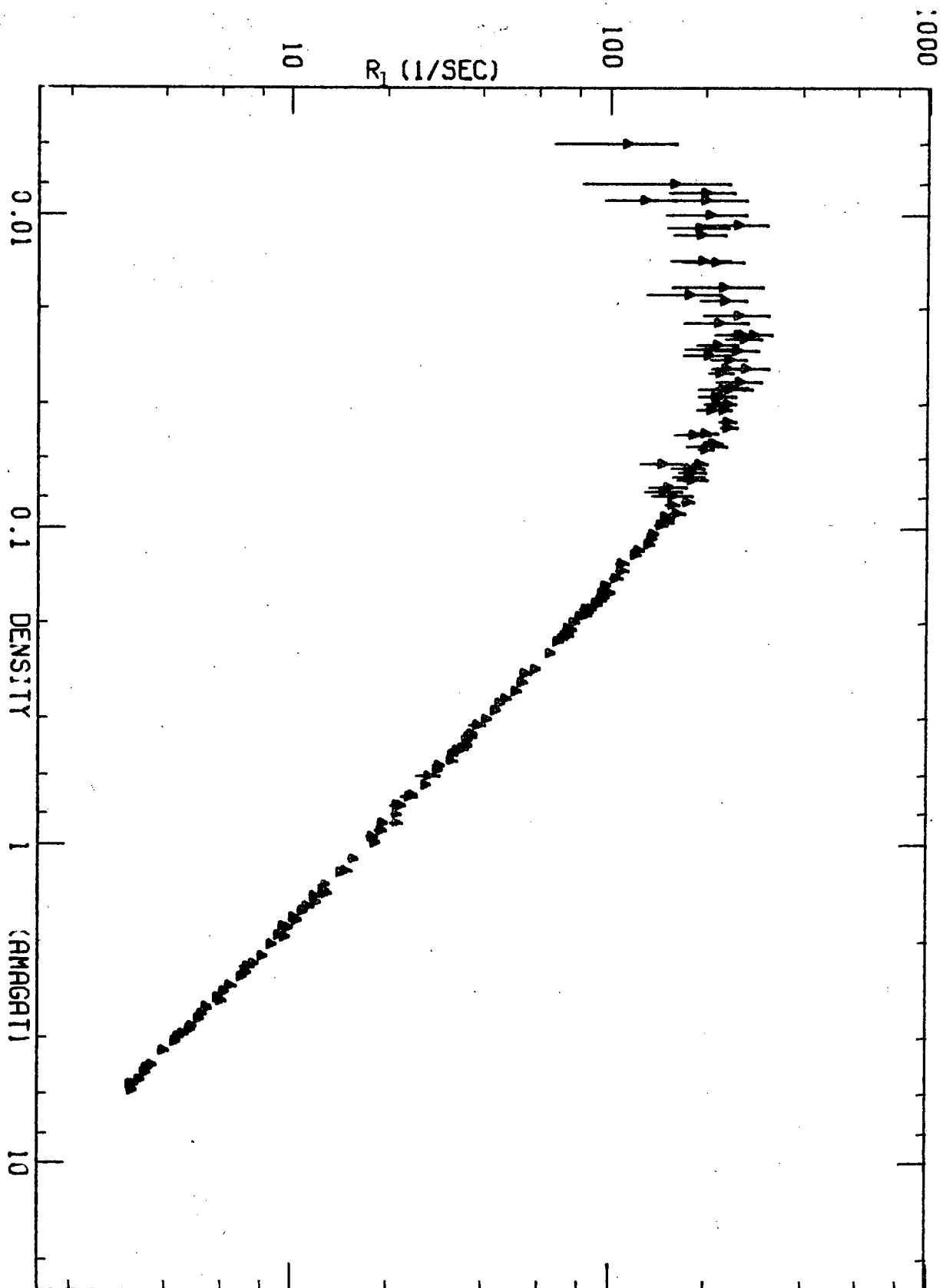Figure A.6. ρR_1 vs ρ with statistical errors E(S) for T = 150K

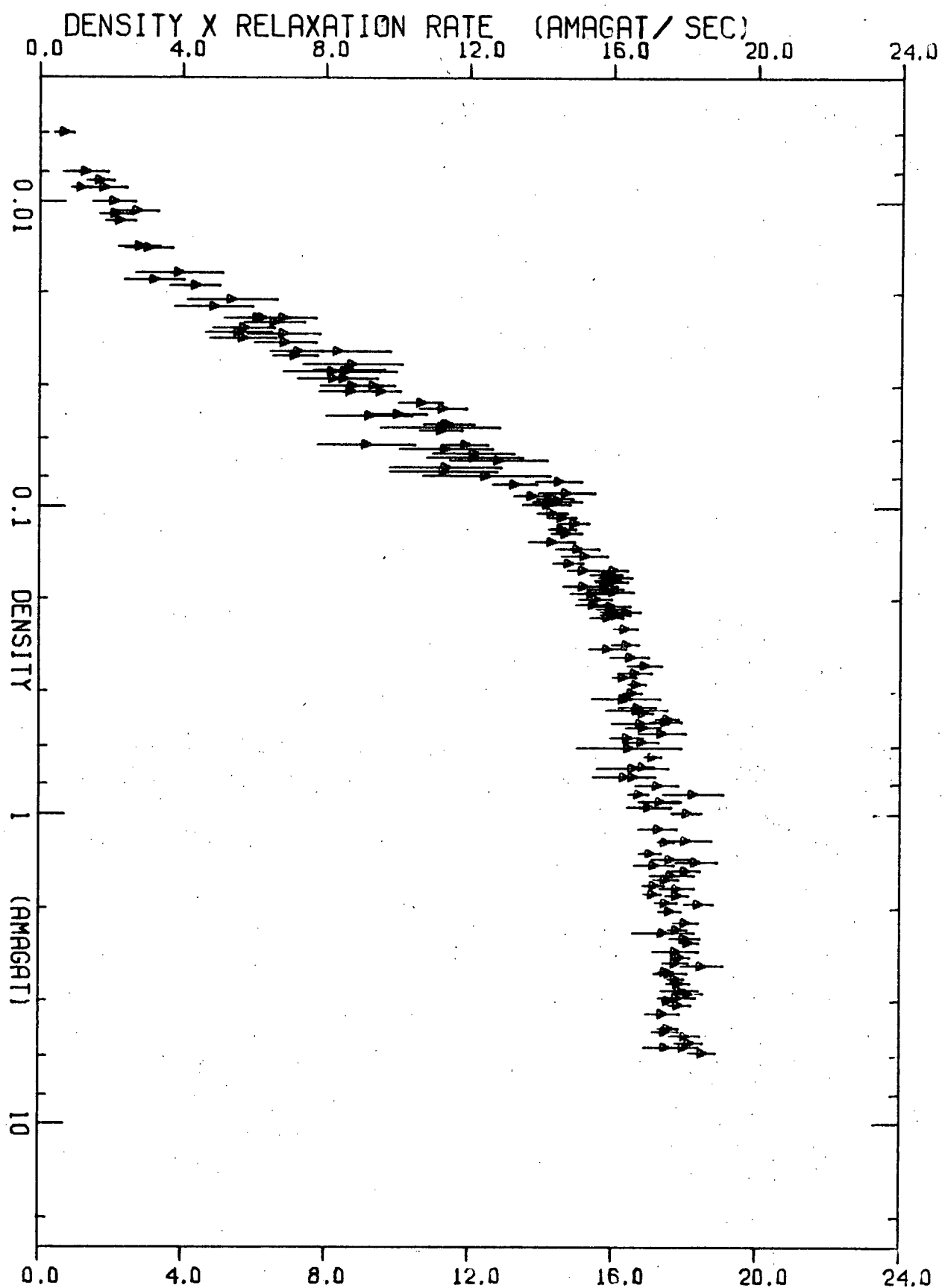Figure A.7. R_1 vs ρ with total errors for T = 150K

Figure A.8. ρR_1 vs ρ with total errors for T = 150K

TABLE A.3

METHANE RELAXATION RATES AT 110 K AND 30 MHZ

"D" IS THE DENSITY IN AMAGAT
"R" IS THE LONGITUDINAL RELAXATION RATE IN 1/SEC
"DR" IS THE PRODUCT IN AMAGAT/SEC
"E(S)" IN % IS THE STATISTICAL ERROR IN R OBTAINED
     BY FITTING THE DATA TO A SINGLE EXPONENTIAL
"E(B)" IN % IS THE ERROR IN R RESULTING FROM THE
     UNCERTAINTY IN THE BASELINE
"E" IN % IS THE TOTAL ERROR

D	R	DR	E(S)	E(B)	E
0.0082	145.30	1.19	14.0	16.0	21.3
0.0086	156.90	1.35	15.7	14.8	21.6
0.0092	142.20	1.31	19.1	9.8	21.4
0.0098	145.50	1.43	19.4	20.6	28.2
0.0101	178.80	1.80	24.2	25.2	35.0
0.0104	217.30	2.26	14.5	19.2	24.1
0.0111	144.60	1.60	17.6	33.1	37.4
0.0120	215.80	2.60	13.2	22.3	25.9
0.0130	172.70	2.25	10.0	15.4	18.4
0.0151	153.10	2.31	11.0	8.9	14.2
0.0180	210.30	3.79	6.5	7.7	10.1
0.0188	214.10	4.03	9.9	7.2	12.2
0.0189	195.90	3.70	11.3	7.9	13.8
0.0192	162.50	3.11	11.2	12.4	16.7
0.0202	191.60	3.86	7.4	18.0	19.4
0.0207	204.70	4.25	8.5	8.2	11.8
0.0210	203.20	4.26	8.0	6.4	10.2
0.0221	193.10	4.28	5.5	14.5	15.5
0.0229	194.50	4.45	4.8	7.6	9.0
0.0244	184.70	4.50	4.6	13.1	13.9
0.0260	198.90	5.18	4.7	7.6	9.0
0.0265	190.30	5.04	4.5	12.2	13.0
0.0282	181.90	5.14	3.9	8.8	9.6
0.0290	156.10	4.53	6.2	13.3	14.7
0.0300	182.70	5.49	4.7	8.8	10.0
0.0319	188.40	6.02	3.8	7.3	8.2
0.0349	168.80	5.90	4.0	6.3	7.4
0.0359	177.60	6.38	3.3	6.6	7.4
0.0359	195.60	7.03	4.2	5.1	6.6
0.0369	193.20	7.13	3.9	4.8	6.2
0.0379	188.30	7.13	4.9	5.0	7.1
0.0398	188.70	7.52	3.3	3.8	5.1
0.0408	176.40	7.20	3.4	9.0	9.6
0.0434	165.50	7.18	2.5	6.9	7.3
0.0451	151.80	6.84	5.2	4.1	6.6
0.0480	162.50	7.80	2.6	6.0	6.5
0.0500	158.90	7.94	2.2	4.3	4.8

METHANE RELAXATION RATES AT 110 K AND 30 MHZ

D	R	DR	E(S)	E(B)	E
0.0519	164.10	8.52	2.4	4.8	5.3
0.0529	160.40	8.49	2.7	3.6	4.5
0.0545	157.90	8.61	2.2	3.0	3.7
0.0549	141.10	7.74	3.1	4.8	5.7
0.0578	140.00	8.09	3.0	6.5	7.2
0.0601	131.70	7.91	3.1	3.6	4.8
0.0626	132.80	8.31	1.8	4.3	4.6
0.0660	123.20	8.13	2.3	4.9	5.4
0.0748	116.30	8.70	2.6	5.9	6.5
0.0780	120.70	9.41	2.0	3.0	3.6
0.0800	115.60	9.25	1.5	3.3	3.6
0.0820	112.70	9.24	1.5	2.6	3.0
0.0839	114.00	9.57	1.1	2.3	2.6
0.0859	110.50	9.49	1.0	2.3	2.5
0.0870	109.70	9.55	1.1	2.3	2.5
0.0898	108.50	9.74	2.7	4.7	5.4
0.0898	106.40	9.55	1.7	3.4	3.8
0.0927	103.50	9.60	1.4	3.2	3.5
0.0957	102.30	9.79	2.2	3.7	4.3
0.0989	99.10	9.81	1.7	3.2	3.7
0.0999	94.00	9.39	3.9	4.3	5.8
0.1068	87.89	9.38	1.9	3.4	3.9
0.1117	88.88	9.93	2.9	2.9	4.2
0.1190	82.41	9.80	1.5	3.3	3.6
0.1223	85.30	10.43	2.1	3.7	4.3
0.1306	79.03	10.32	1.4	2.1	2.5
0.1358	74.83	10.16	1.9	4.2	4.6
0.1401	72.22	10.12	1.1	2.2	2.4
0.1476	74.34	10.97	2.0	3.6	4.2
0.1513	66.17	10.01	1.1	1.9	2.2
0.1554	66.47	10.33	1.2	2.3	2.6
0.1615	62.53	10.10	1.1	2.1	2.3
0.1639	65.64	10.76	1.6	3.3	3.7
0.1714	60.72	10.40	0.8	1.5	1.7
0.1714	59.04	10.12	1.0	1.9	2.1
0.1829	58.44	10.69	1.2	2.8	3.1
0.1891	54.75	10.35	2.8	3.8	4.7
0.1949	53.48	10.43	0.9	2.4	2.6
0.1992	51.68	10.29	0.7	1.9	2.1
0.1992	55.61	11.08	1.2	2.8	3.0
0.2038	51.76	10.55	0.8	1.8	1.9
0.2090	52.25	10.92	1.9	4.1	4.5
0.2191	51.18	11.21	2.0	3.3	3.8
0.2191	47.95	10.51	2.3	3.6	4.2
0.2240	48.37	10.83	1.2	2.7	2.9
0.2289	47.38	10.85	1.4	3.0	3.3

METHANE RELAXATION RATES AT 110 K AND 30 MHZ

D	R	DR	E(S)	E(B)	E
0.2292	47.25	10.83	1.3	2.8	3.0
0.2338	47.01	10.99	1.3	2.7	3.0
0.2390	45.93	10.98	1.2	2.9	3.1
0.2488	43.80	10.90	1.6	2.1	2.7
0.2586	43.14	11.16	0.8	2.0	2.1
0.2712	41.13	11.15	0.7	2.3	2.4
0.2798	38.37	10.74	2.5	3.0	3.9
0.2880	38.16	10.99	1.0	2.2	2.4
0.3005	36.33	10.92	0.9	2.0	2.2
0.3050	35.06	10.69	1.2	2.2	2.6
0.3116	35.17	10.96	1.0	1.9	2.1
0.3151	34.66	10.92	1.3	2.7	3.0
0.3213	33.55	10.78	1.6	2.6	3.1
0.3331	32.81	10.93	1.5	2.9	3.3
0.3363	32.27	10.85	1.4	3.4	3.6
0.3363	32.87	11.06	1.2	2.4	2.7
0.3461	31.96	11.06	1.0	2.3	2.5
0.3559	31.77	11.31	1.3	3.1	3.4
0.3788	29.29	11.09	0.9	2.2	2.3
0.3984	28.16	11.22	1.4	3.1	3.4
0.4180	26.62	11.13	0.8	2.0	2.2
0.4416	24.81	10.96	0.6	1.2	1.3
0.4572	24.03	10.99	1.0	2.6	2.8
0.4811	23.15	11.14	1.0	2.2	2.4
0.5207	21.61	11.25	1.2	2.2	2.5
0.5668	19.64	11.13	0.5	1.0	1.1
0.5943	18.90	11.23	0.6	1.2	1.3
0.6237	18.19	11.34	0.7	1.4	1.5
0.6400	17.17	10.99	1.0	2.0	2.3
0.6596	16.92	11.16	0.6	1.1	1.3
0.6792	16.40	11.14	0.7	1.4	1.5
0.6988	16.03	11.20	0.8	1.5	1.7
0.7184	15.42	11.08	0.9	1.8	2.0
0.7413	14.74	10.93	0.7	1.5	1.7
0.7608	14.94	11.37	0.8	1.4	1.6
0.7804	14.27	11.14	0.7	1.2	1.4
0.8000	14.03	11.22	0.9	1.8	2.0
0.8196	13.70	11.23	0.4	0.7	0.8
0.8229	13.89	11.43	0.8	1.1	1.4
0.8252	13.91	11.48	1.1	2.4	2.6
0.8729	13.05	11.39	0.6	1.3	1.4
0.8823	12.90	11.38	1.6	2.8	3.2
0.9182	12.55	11.52	0.7	1.6	1.7
0.9566	12.08	11.56	0.6	1.1	1.3
0.9986	11.52	11.50	0.5	1.1	1.2
0.9913	11.59	11.49	0.8	1.9	2.0

METHANE RELAXATION RATES AT 110 K AND 30 MHZ

D	R	DR	E(S)	E(B)	E
1.0266	11.26	11.56	0.7	1.7	1.9
1.0494	10.97	11.51	0.5	1.2	1.3
1.0862	10.46	11.36	0.5	1.0	1.1
1.1372	9.98	11.35	1.2	2.2	2.5
1.1495	10.02	11.52	1.2	2.5	2.7
1.2006	9.40	11.29	1.1	1.3	1.7
1.2041	9.62	11.58	0.5	1.2	1.3
1.2387	9.30	11.51	0.6	1.2	1.3
1.2464	9.14	11.39	1.5	2.3	2.7
1.2782	9.07	11.59	0.6	1.0	1.2
1.2959	9.10	11.80	1.4	2.5	2.9
1.3543	8.45	11.45	0.7	1.2	1.4
1.3986	8.31	11.62	0.6	0.9	1.0
1.4502	8.10	11.75	1.2	2.5	2.7
1.5000	7.71	11.56	1.0	1.9	2.2
1.5535	7.39	11.48	0.7	1.3	1.4
1.5999	7.18	11.49	0.9	1.8	2.0
1.7002	6.76	11.50	0.6	1.3	1.4
1.7415	6.77	11.79	1.0	1.7	1.9
1.7954	6.24	11.21	1.3	2.0	2.4
1.8134	6.27	11.36	0.8	1.7	1.9
1.9036	6.27	11.94	0.9	2.0	2.2
1.9217	6.01	11.55	0.4	1.1	1.1
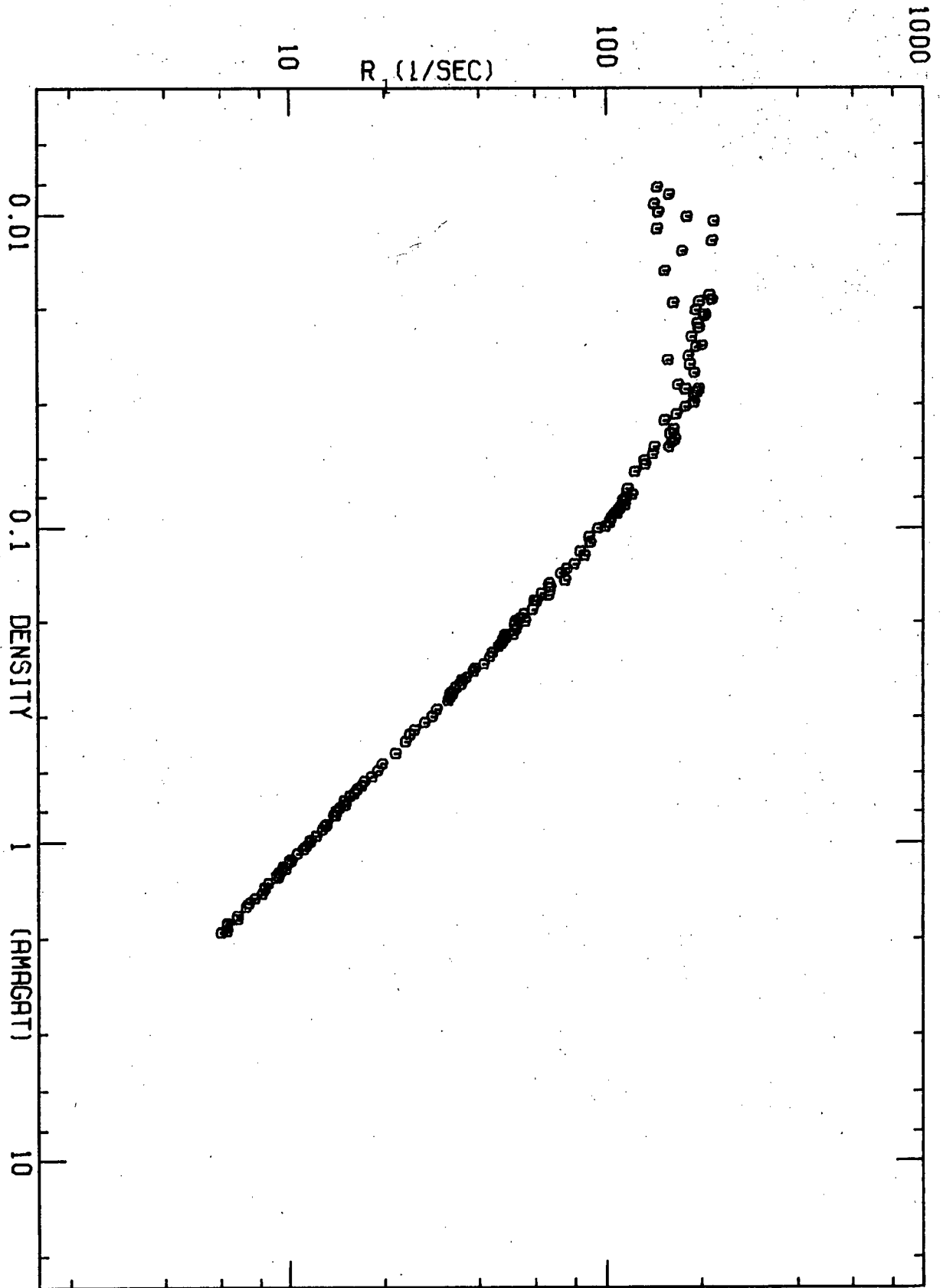
Figure A.9. R_1 vs ρ for T = 110K
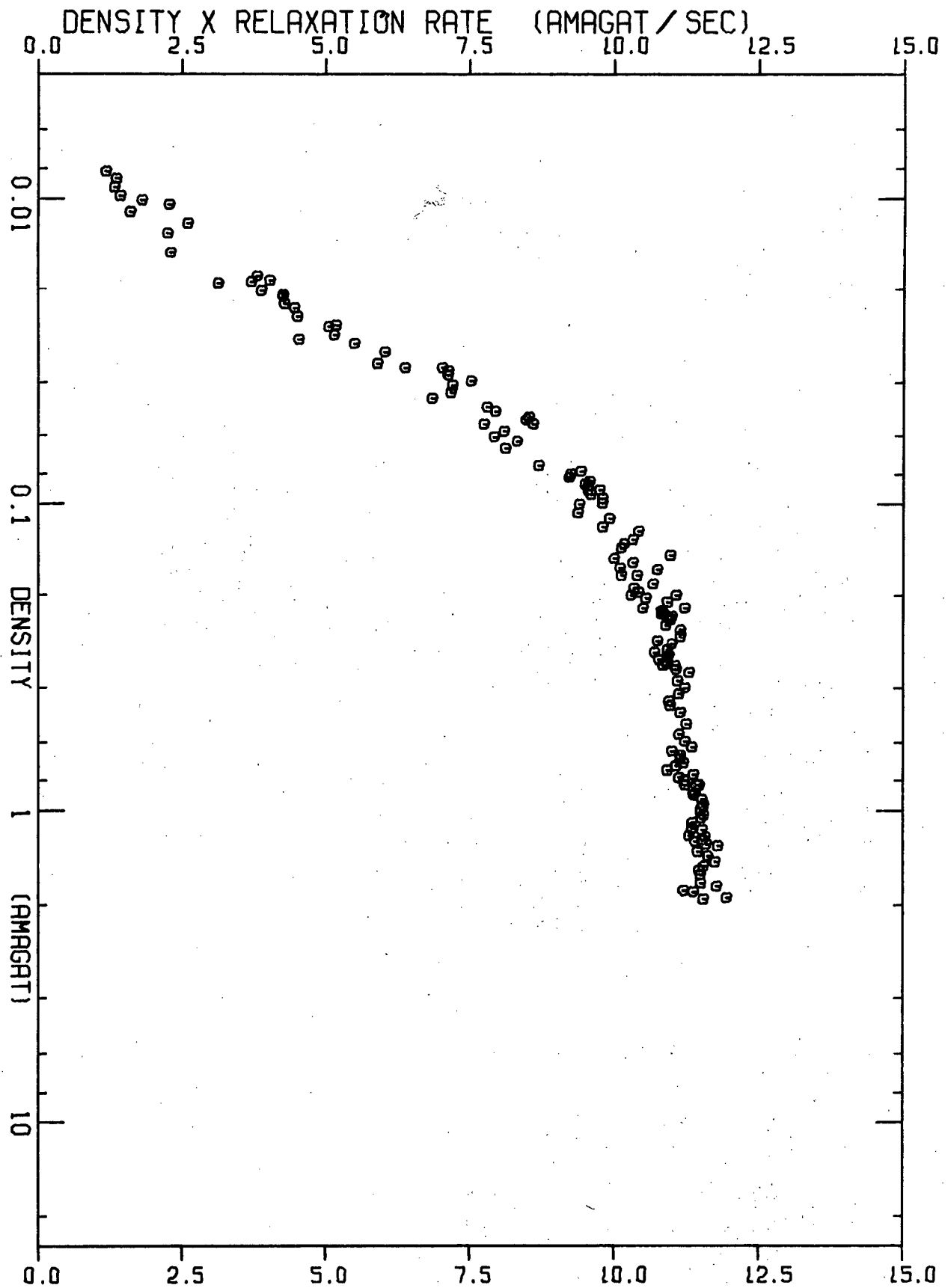
Figure A.10. ρR_1 vs ρ for T = 110K
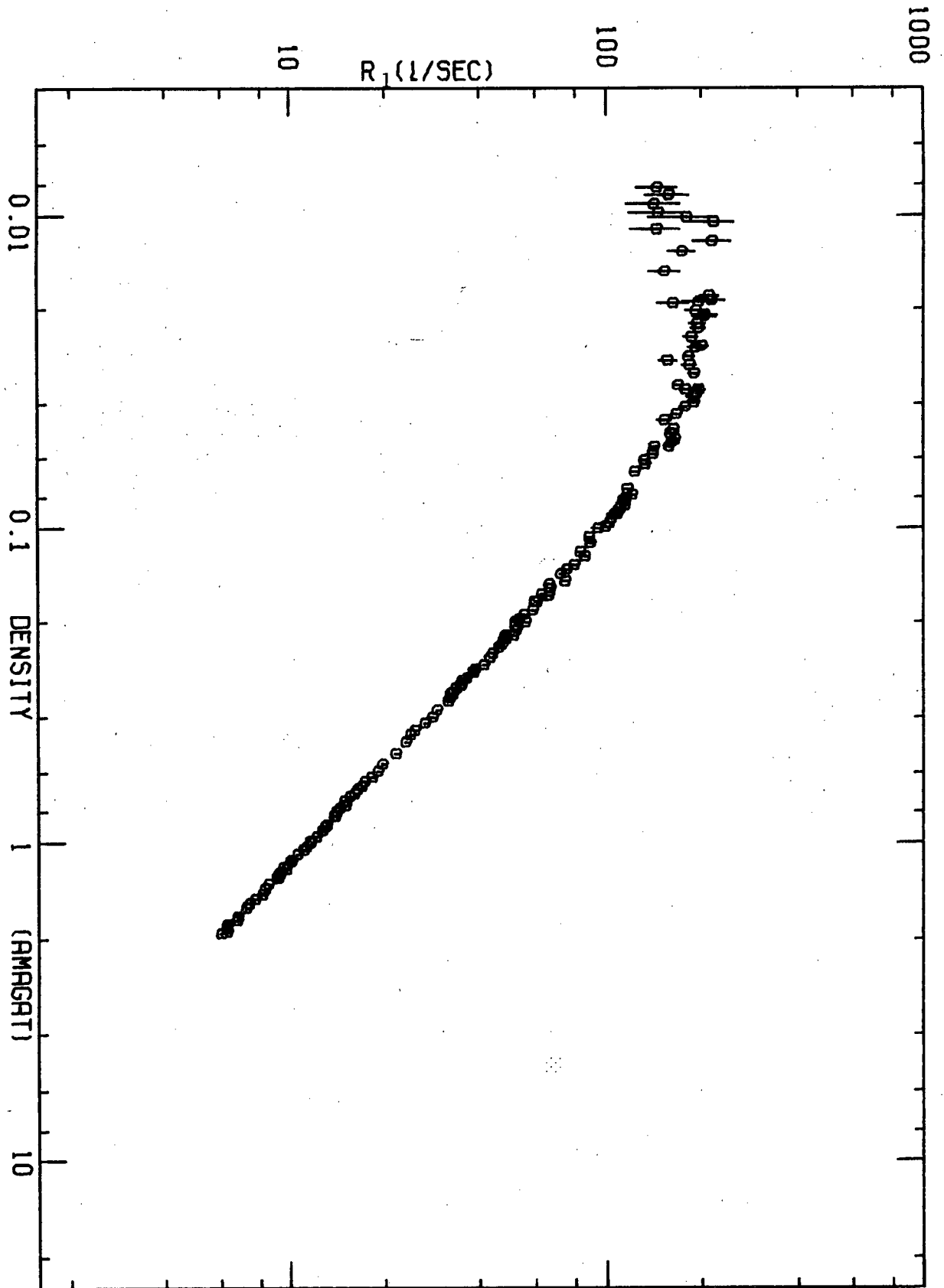
Figure A.11 . R_1 vs ρ with statistical error $E(S)$ for $T = 110K$
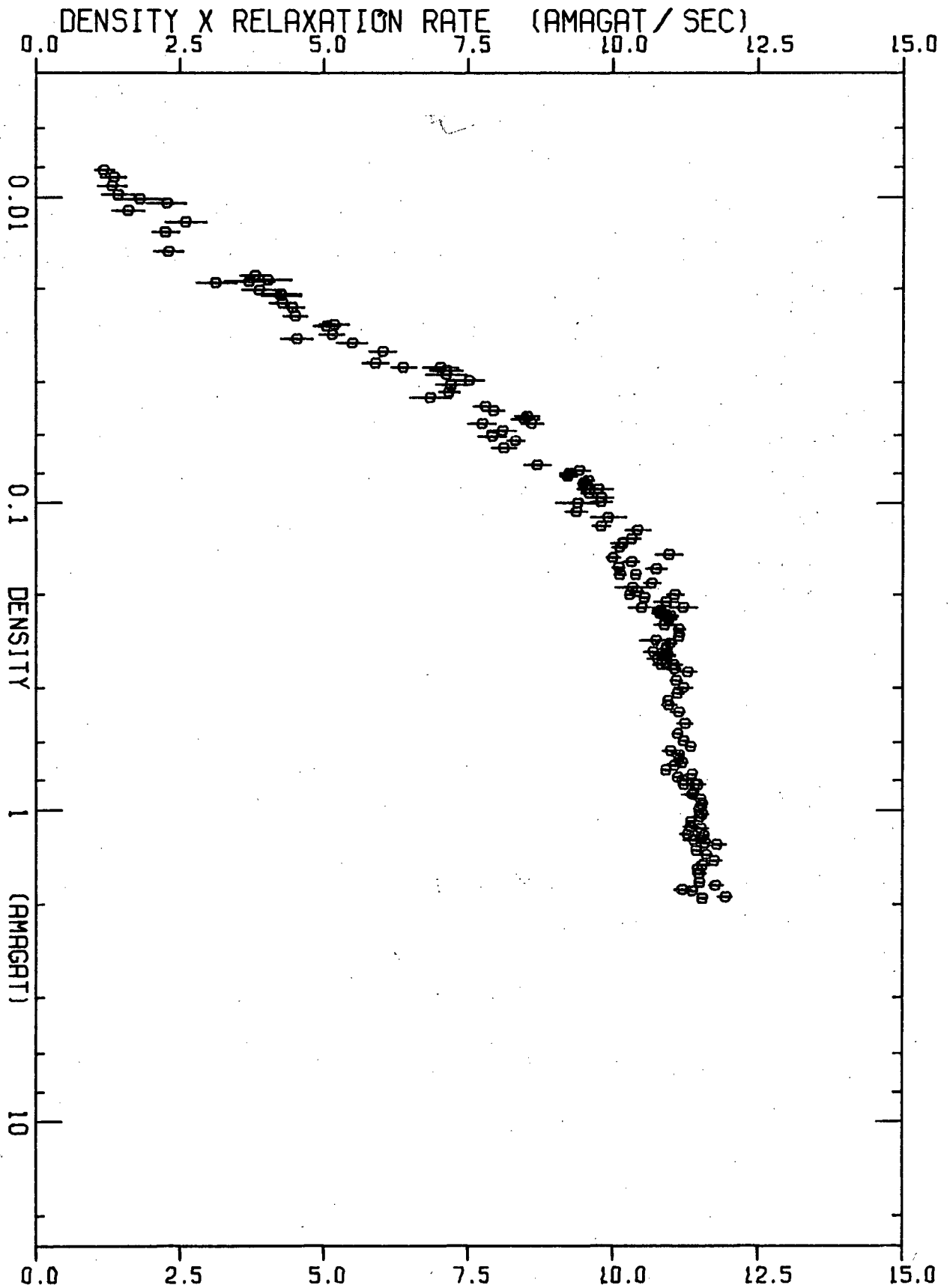
Figure A.12. ρR_1 vs ρ with statistical errors E(S) for T = 110K
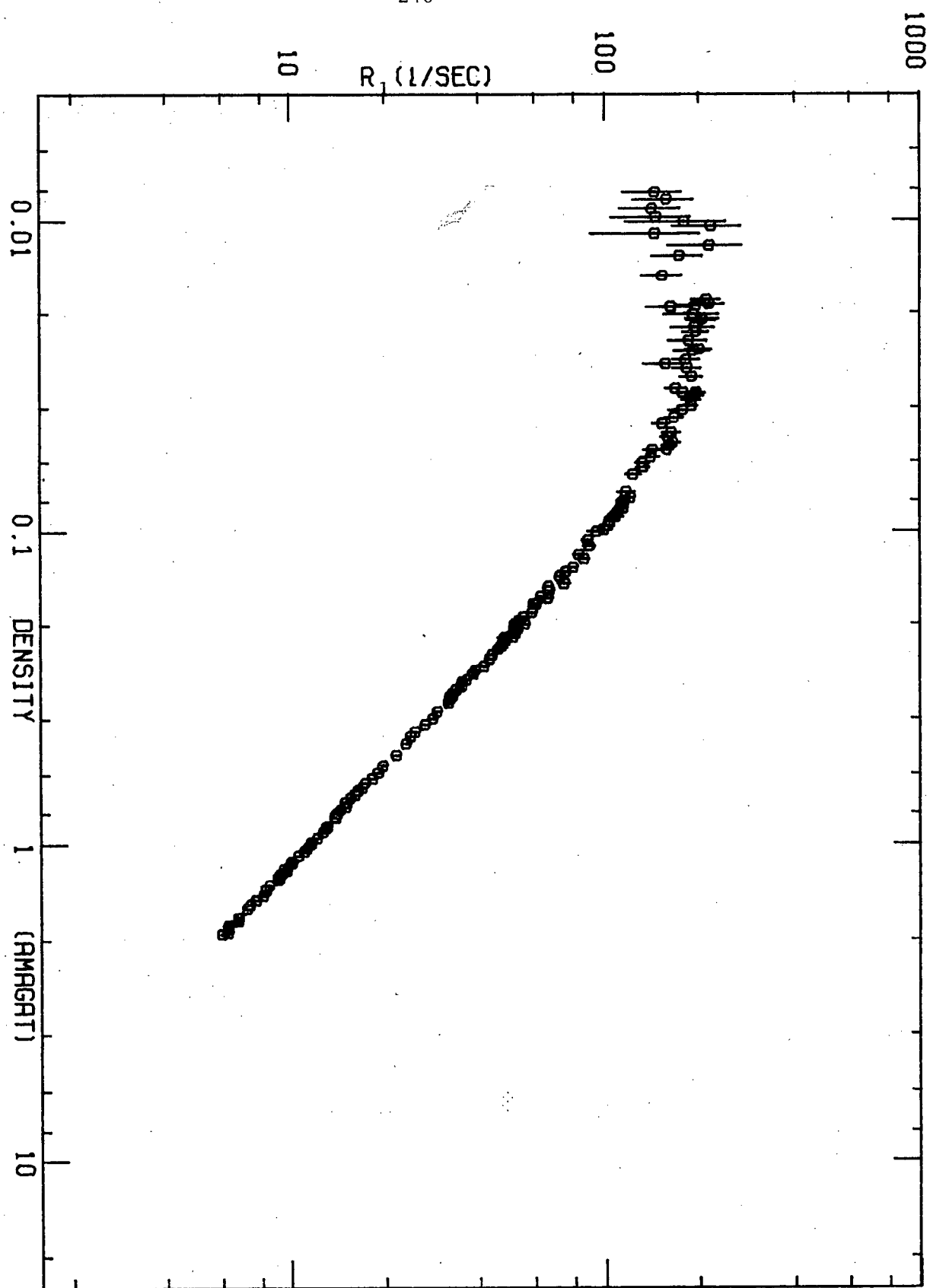
Figure A.13. R_1 vs ρ with total errors for T = 110K
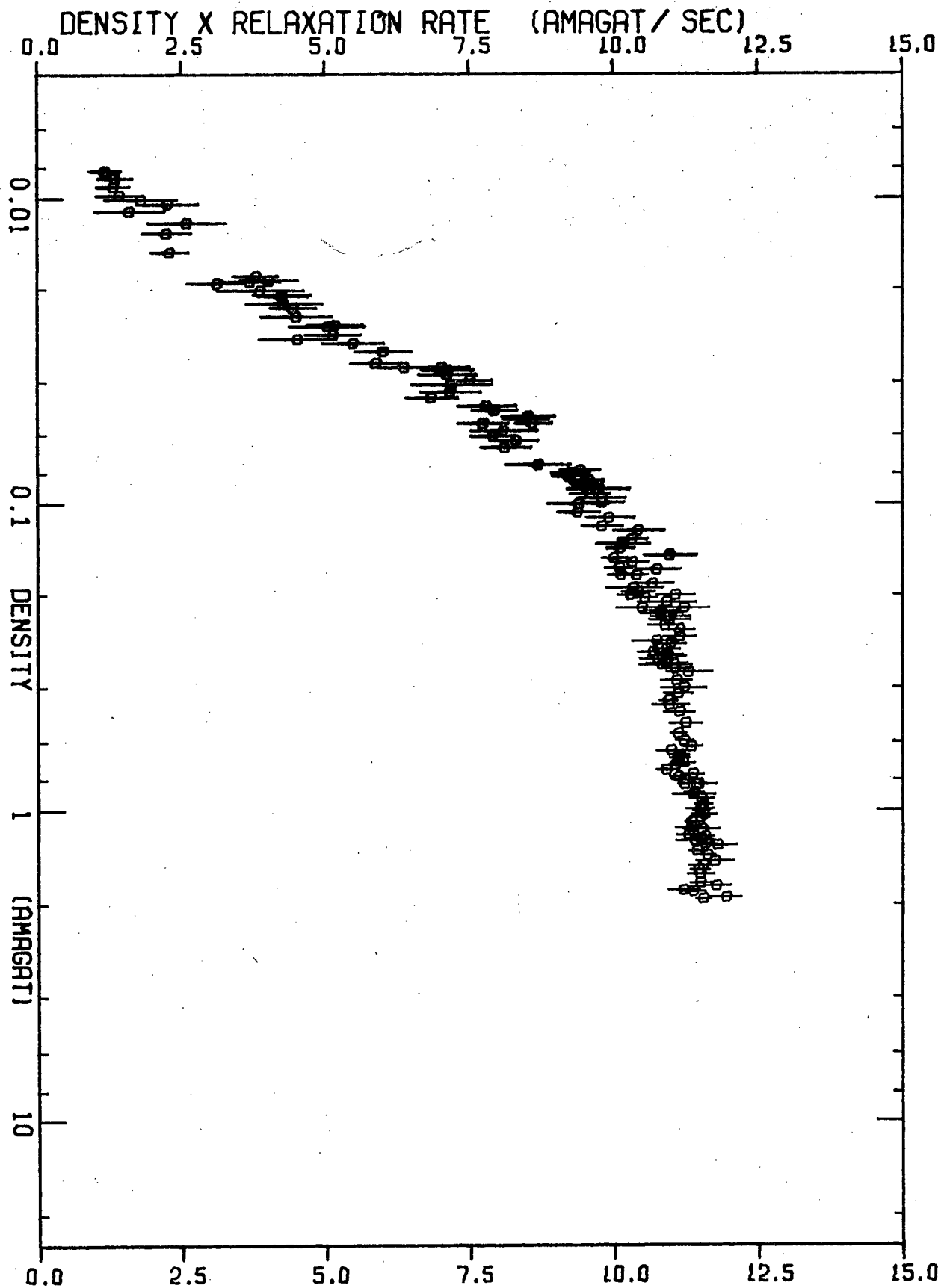
Figure A.14. ρR_1 vs ρ with total errors for T = 110K

TABLE A.4

METHANE RELAXATION RATES AT 077 K AND 30 MHZ

"D" IS THE DENSITY IN AMAGAT
"R" IS THE LONGITUDINAL RELAXATION RATE IN 1/SEC
"DR" IS THE PRODUCT IN AMAGAT/SEC
"E(S)" IN % IS THE STATISTICAL ERROR IN R OBTAINED
      BY FITTING THE DATA TO A SINGLE EXPONENTIAL
"E(B)" IN % IS THE ERROR IN R RESULTING FROM THE
      UNCERTAINTY IN THE BASELINE
"E" IN % IS THE TOTAL ERROR

D	R	DR	E(S)	E(B)	E
0.0046	118.90	0.55	17.3	22.9	28.7
0.0049	121.30	0.60	18.5	25.8	31.8
0.0065	135.30	0.88	18.2	17.1	24.9
0.0070	137.30	0.97	9.7	16.3	18.9
0.0076	140.60	1.06	14.2	12.7	19.1
0.0078	137.90	1.08	11.5	13.4	17.7
0.0082	121.10	0.99	19.2	13.0	23.2
0.0086	108.70	0.94	15.9	12.8	20.4
0.0090	130.30	1.17	10.8	13.6	17.4
0.0094	162.30	1.52	10.2	15.4	18.5
0.0098	117.80	1.16	15.4	15.2	21.6
0.0098	160.20	1.58	7.5	11.8	14.0
0.0112	171.20	1.92	8.3	12.7	15.1
0.0156	143.80	2.25	5.8	6.3	8.5
0.0239	146.70	3.51	4.8	4.8	6.8
0.0260	146.00	3.79	3.1	3.6	4.7
0.0280	136.00	3.81	4.4	3.4	5.5
0.0300	171.50	5.14	3.9	3.8	5.5
0.0319	140.10	4.46	5.3	5.4	7.5
0.0340	153.20	5.21	3.6	5.7	6.7
0.0359	140.20	5.04	3.8	5.1	6.4
0.0378	144.30	5.45	2.9	3.7	4.7
0.0399	111.10	4.43	3.2	4.7	5.6
0.0410	112.80	4.63	2.7	4.3	5.1
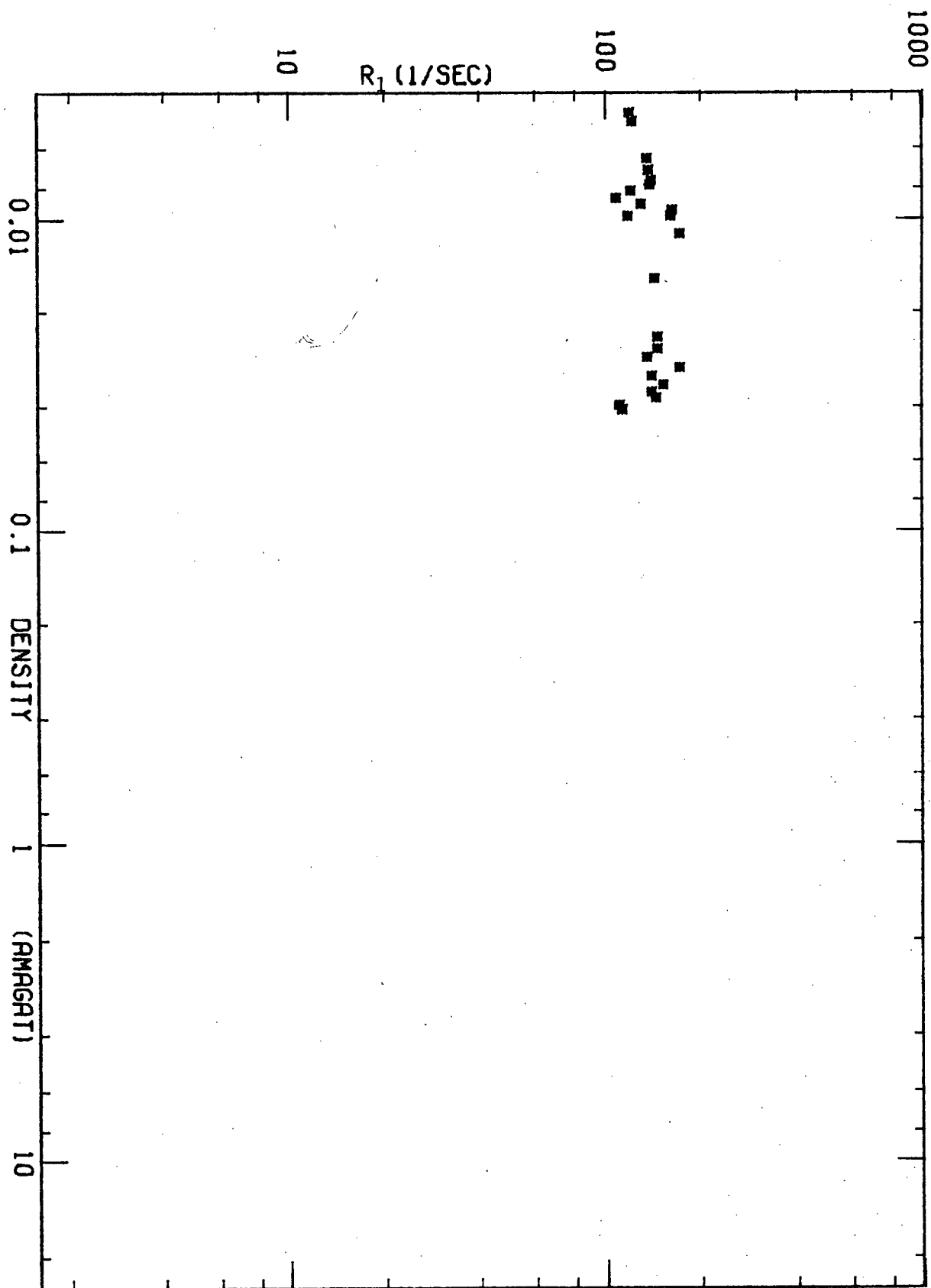
Figure A.15. R_1 vs ρ for T = 77K
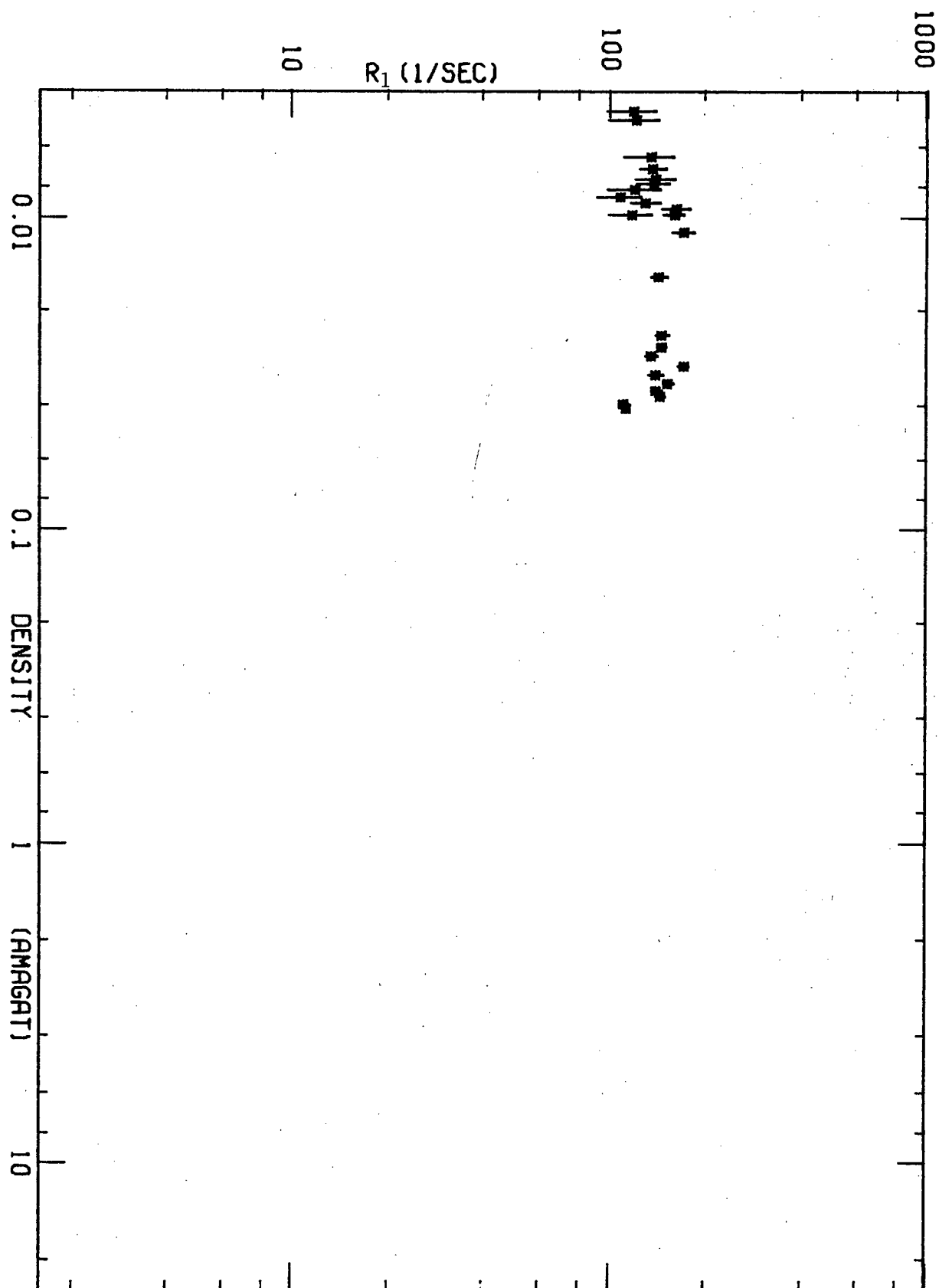
Figure A.16. R_1 vs ρ with statistical error E(S) for T = 77K
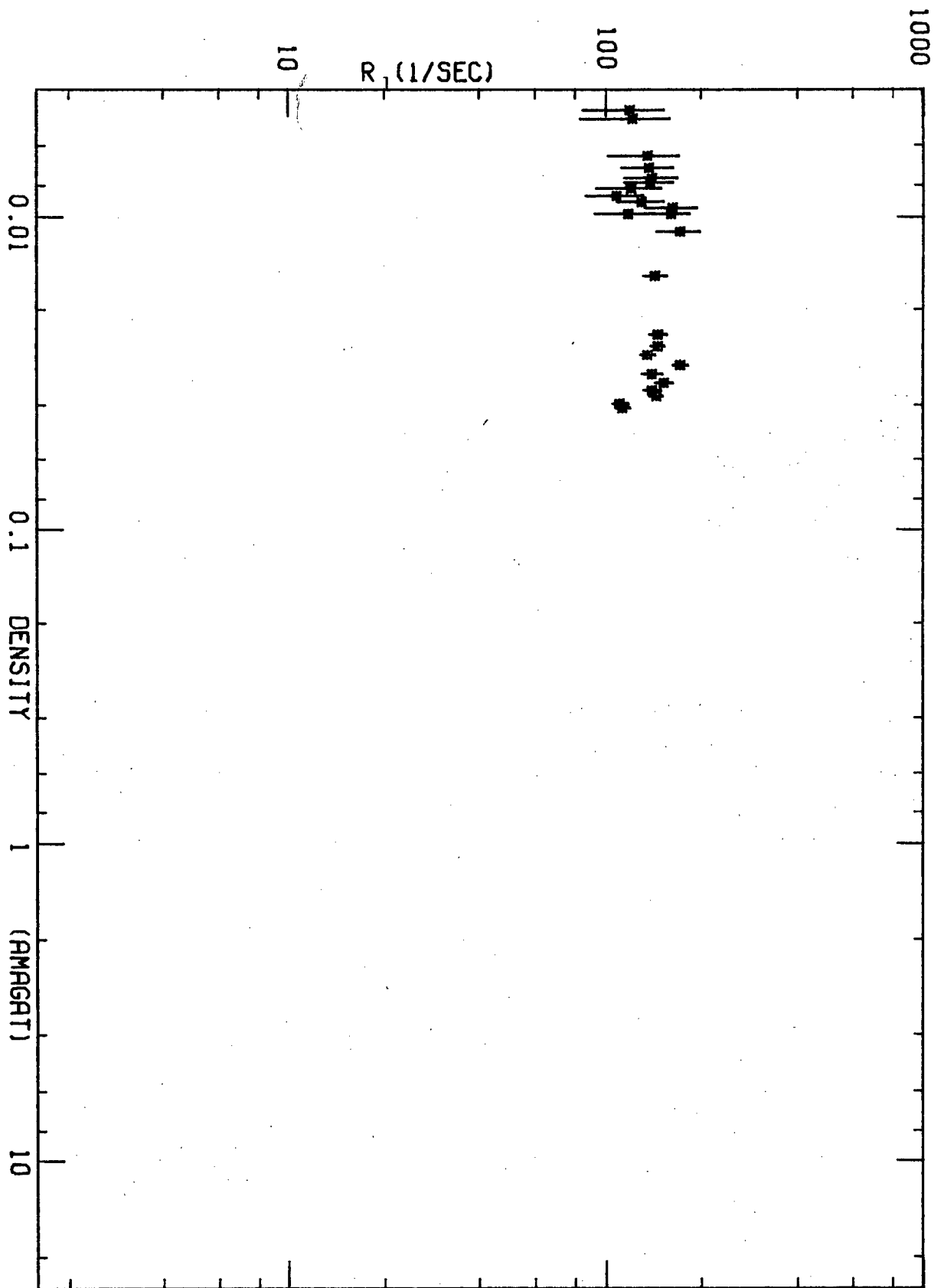
Figure A.17. R_1 vs ρ with total errors for T = 77K

Figure A.18. R_1 vs ρ

Figure A.19. ρR_1 vs ρ
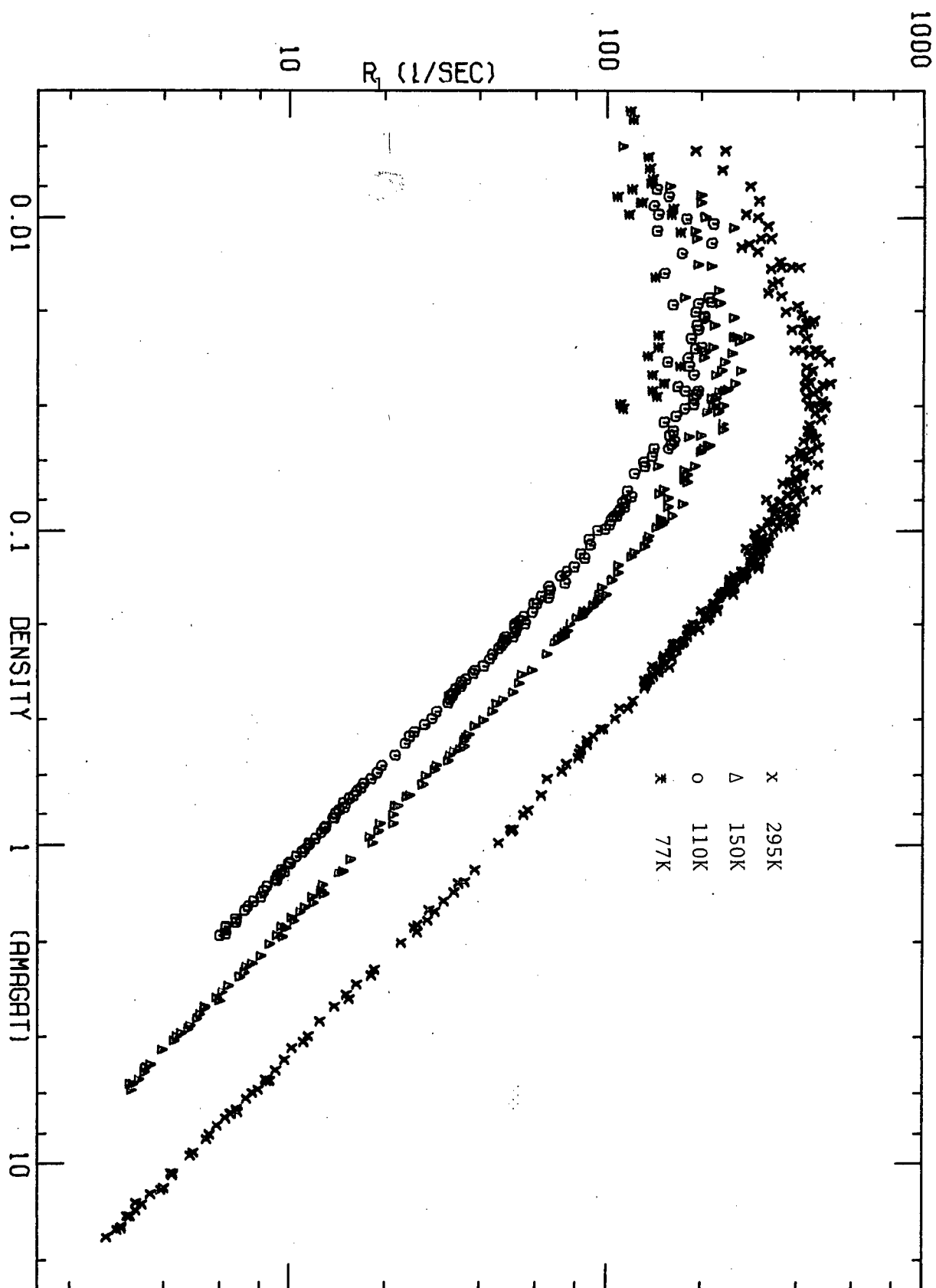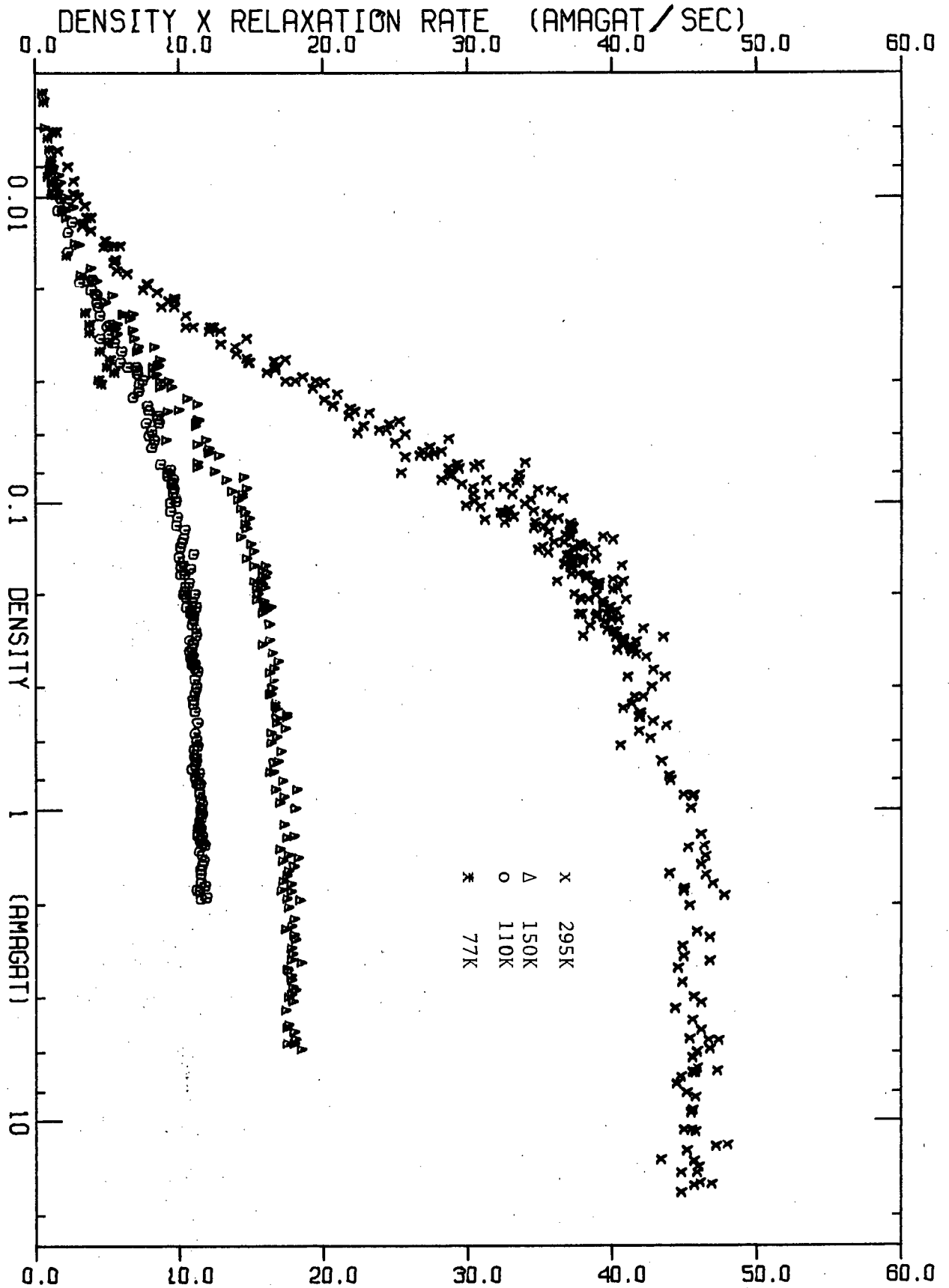
APPENDIX B

CALCULATION OF C_a MATRIX ELEMENTS

Equation 3.7.4 is

$$\langle H^S_{sr}(I \rightarrow I) \rangle = n(\beta) \sum_{\nu} \sqrt{3}\ hC_a C(1,1,0;\nu,-\nu,0)\ B^*(\gamma)\ B(\gamma)$$

$$\chi^*(\beta,\xi;I,m_I')\ I^{A1}_{1,\nu}\chi(\beta,\xi;I,m_I)$$

$$R(\gamma,\xi;J,m_J';t',\rho)\ J^{A1}_{1,-\nu}R(\gamma,\xi;J,m_J;t,\rho) \qquad\qquad B.1$$

The rotational matrix elements are diagonal in γ ξ t and ρ, and are

$$R(\gamma,\xi;J,m_J';t,\rho)\ J^{A1}_{1,-\nu}R(\gamma,\xi;J,m_J;t,\rho)$$

$$= (-1)^{J-m_J'} \begin{pmatrix} J & 1 & J \\ -m_J' & -\nu & m_J \end{pmatrix} \langle J||J^{A1}||J\rangle \qquad\qquad B.2$$

This is the Wigner-Eckart Theorem using the normal 3-j symbols and the reduced matrix element as defined in reference (123)[1].

Choosing $\nu = 0$, $m_J = m_J' = 1$ the left hand side of equation B.2 is one and the right hand side is $[(2J+1)(J+1)J]^{-\frac{1}{2}}\langle J||J^{A1}||J\rangle$. Thus, we have

---

[1] The reduced matrix element as defined in reference (123) differs from the definitions of references (111) and (112).

$$R^*(\gamma,\xi;J,m_J';t',\rho) \quad J_{1,-\nu}^{A1} R(\gamma,\xi;J,m_J;t,\rho)$$

$$= \quad (-1)^{J-m_J'} \begin{pmatrix} J & 1 & J \\ -m_J' & -\nu & m_J \end{pmatrix} [J(J+1)(2J+1)]^{\frac{1}{2}}\delta(t',t) \qquad \text{B.3}$$

The spin matrix element for β = A1 is

$$X(A1;2,m_I') \; I_{1,\nu}^{A1} X(A1;2,m_I) \quad = \quad (-1)^{2-m_I'} \begin{pmatrix} 2 & 1 & 2 \\ -m_I' & \nu & m_I \end{pmatrix} <2||I^{A1}||2>$$

$$\text{B.4}$$

For the choice of $\nu = 0$ and $m_I = m_I' = 1$, the left hand side of equation B.4 is unity and the right hand side is $(30)^{-\frac{1}{2}}$ times the reduced matrix element. The latter therefore equals $(30)^{\frac{1}{2}}$ and equation B.4 becomes

$$\chi^*(A1;2,m_I') \; I_{1,\nu}^{A1} X(A1;2,m_I) \quad = \quad (-1)^{2-m_I'} \sqrt{30} \begin{pmatrix} 2 & 1 & 2 \\ -m_I' & \nu & m_I \end{pmatrix} \quad \text{B.5}$$

The calculation for the β = F2 matrix element proceeds in an identical manner with the result

$$\chi^*(F2,\xi;1,m_I') \; I_{1,\nu}^{A1} X(F2,\xi;1,m_I) \; = \; (-1)^{1-m_I'} \sqrt{6} \begin{pmatrix} 1 & 1 & 1 \\ -m_I' & \nu & m_I \end{pmatrix} \quad \text{B.6}$$

In order to calculate $<H_{sr}^S(2 \to 2)>$, equations B.3 and B.5 are substituted into equation B.1

$$<H_{sr}^S(2 \to 2)> \quad = \quad \sqrt{3} \; hC_a \sum_{\nu=-1}^{+1} C(1,1,0;\nu,-\nu,0) \; B^*(A) \; B(A) \; [\delta(t',t)]$$

$$(-1)^{2-m_I'} \sqrt{30} \begin{pmatrix} 2 & 1 & 2 \\ -m_I' & \nu & m_I \end{pmatrix} (-1)^{J-m_J'} \begin{pmatrix} J & 1 & J \\ -m_J' & -\nu & m_J \end{pmatrix} [J(J+1)(2J+1)]^{\frac{1}{2}}$$

$$\text{B.7}$$

Performing the sum over ν after writing out the Clebsch-Gordan coefficients and the 3-j symbols explicitly (123) is straight forward but tedious. The result is given in equations 3.7.5 and 3.7.6 of the text.

The coupling constant C_a has been measured by molecular beam experiments and is 10.4 ± 0.1 kHz (32).

APPENDIX C

Arrangement of C_d Matrix Elements

The starting point for this appendix is equation 3.7.10.

Substituting $I' = I = 1$ in equation 3.7.10 gives spin matrix elements of

the form $\chi^*(F2,\zeta')\ I^{F2,\eta}\chi(F2,\zeta)$. These are zero unless all three components

(ζ',η,ζ) are different. This can be proved by direct calculation or by

operating on a given matrix element by the elements of T_d. Thus, for instance,

$\chi^*(F2,x)\ I^{F2,y}\ \chi(F2,z)$ can be "rotated" into $\chi^*(F2,y)\ I^{F2,x}\ \chi(F2,y)$ and so on.

This operation is outlined for the more complicated case of $I' = 0$ to $I = 1$

further on in this Appendix. Because these transformations cannot change

the matrix element (a scalar), all the matrix elements can be related to

one, which then must be calculated. Not only are the three matrix elements

with all 3 components the only non-zero ones, they themselves are all equal.

The rotational matrix elements in equation 3.7.10 for the case of

$I' = I = 1$ will be the form as the spin matrix elements discussed in the

previous paragraph, only we can have F1 in both R' and R as well as F2,

depending on whether ρ is 1 or 2. The same rules regarding the components

apply to the rotational matrix elements.

From Table 3.3 we have that $B = 0$ unless $\zeta = \xi$ and $\zeta' = \xi'$. As a

result of this and the preceding paragraphs, out of all 243 terms resulting

from the sums over ζ,ζ',ξ,ξ' and η, only 6 are non-zero and they are all equal.

Equation 3.7.10 becomes

$$\langle H^T_{sr}(1 \rightarrow 1)\rangle = 6[-\frac{1}{3}hC_d] \sum_\nu (-1)^\nu B^*(F) \; B(F) \quad x$$

$$[\chi^*(F2,a;1;m'_I) \; I^{F2,b}_{1,\nu} \; (F2,c;1,m_I)] \quad x$$

$$[R^*(F,a;J,m'_J;t',\rho) \; B^{F2,b}_{1,-\nu} R(F,c;J,m_J;t,\rho)] \qquad C.1$$

In writing equation C.1 we have noted from Table 3.3 that the B's of equation 3.7.10 all completely specified by $B(F) = (3)^{-\frac{1}{2}}$. The representation of the rotational functions is written as F and not F1 or F2 as explained in Section 3.6. We are free to choose a,b and c as any combination of x, y or z as long as they are all different.

For the case of setting I' = 2 and I = 1 in equation 3.7.10, the sums over ξ' and ζ' vanish because the A representation is one-dimensional. By applying the same rules discussed above, one finds that the only non-zero matrix elements involve $\xi = \eta$ and $\zeta = \eta$. Further, from Table 3.3, B = 0 unless $\xi = \zeta$. As a result, the sums over ζ',ζ,ξ',ξ and η in equation 3.7.10 reduce to 3 terms and they are all equal. Equation 3.7.10 can now be written

$$\langle H^T_{sr}(2 \rightarrow 1)\rangle = 3[-\frac{1}{3}hC_d] \sum_\nu (-1)^\nu B^*(A) \; B(F) \quad x$$

$$[\chi^*(A1;2,m'_I) \; I^{F2,\ell}_{1,\nu} \chi(F2,\ell;1,m_I)] \quad x$$

$$[R^*(A;J,m'_J;t',\rho) \; B^{F2,\ell}_{1,-\nu} \; R(F,\ell;J,m_J;t,\rho)] \qquad C.2$$

where ℓ can be x, y or z.

The calculation of the remaining class of matrix elements, that

of I' = 0, I = 1 is more complicated for two reasons. First, we must calculate the matrix elements for $\rho = 1$ and $\rho = 2$ separately and secondly the non-vanishing terms that remain when the components are summed are not equal.

Before proceeding it is convenient to calculate the relationship between the general matrix elements $L(E,\sigma)0^{F2,\omega} M(F2,\omega')$ and $L(E,\sigma)0^{F1,\omega} M(F1,\omega')$ where L and M are arbitrary functions and 0 an arbitrary operator. The former (i.e., with $M(F2,\omega')$ is the form of the spin matrix elements and the $\rho = 2$ rotational matrix elements whereas the latter (i.e., with $L(F1,\omega')$) is the form of the $\rho = 1$ rotational matrix elements. The components ω and ω' can be x, y or z and σ can be 1 or 2.

As an example of such a calculation, let us assume that the matrix element $L(E,1)0^{F2,x} M(F2,x)$ has been calculated. We define the short hand notation;

$$\Delta_{EFF} = L(E,1)0^{F2,x} M(F2,x) \tag{C.3}$$

If we now wish to calculate a similar matrix element only with, say, L(E,1) replaced by L(E,2), we must find a transformation which takes L(E,1) into L(E,2) but does not effect $0^{F2,x}$ or M(F2,x). If this transformation is an element of the tetrahedral point group then the value of the matrix element remains unchanged. Such a transformation is σ_{24} as defined in reference (115) The two dimensional matrix representation of σ_{24} is

$$\sigma_{24} = \begin{pmatrix} \sqrt{3}/2 & -1/2 \\ 1/2 & \sqrt{3}/2 \end{pmatrix} \tag{C.4}$$

where the rows label the components $\sigma = 1$ and 2^1 of the E representation .[2]

This two dimensional matrix σ_{24} leaves operators that transform according to F2,x unchanged. (Note; this is not true for operators that transform according to F2,y and F2,z.) Operating on the matrix elements with σ_{24} gives the result

$$
\begin{bmatrix} \sqrt{3}/2 & -1/2 \\ 1/2 & \sqrt{3}/2 \end{bmatrix}
\begin{bmatrix} L(E,1)0^{F2,x} \; M(F2,x) \\ L(E,2)0^{F2,x} \; M(F2,x) \end{bmatrix} =
$$

$$
\begin{bmatrix} \sqrt{3}/2 \; L(E,1)0^{F2,x} \; M(F2,x) - 1/2 \; L(E,2)0^{F2,x} \; M(F2,x) \\ 1/2 \; L(E,1)0^{F2,x} \; M(F2,x) + \sqrt{3}/2 \; L(E,2)0^{F2,x} \; M(F2,x) \end{bmatrix} \qquad \text{C.5}
$$

This operation cannot change the matrix elements, so the right hand side of equation C.5 must equal the matrix;

$$
\begin{bmatrix} L(E,1)0^{F2,x} \; M(F2,x) \\ L(E,2)0^{F2,x} \; M(F2,x) \end{bmatrix} \qquad \text{C.6}
$$

Equating matrix C.6 with the right hand side of equation C.5 and solving for (the overdetermined) matrix $L(E,1)0^{F2,x} \; M(F2,x)$ one obtains

$$
L(E,2)0^{F2,x} \; M(F2,x) = \sqrt{3} \; L(E,1)0^{F2,x} \; M(F2,x)
$$

$$
= \sqrt{3} \; \Delta_{EFF} \qquad \text{C.7}
$$

---

[1] The <u>component</u> σ should not be confused with the <u>operation</u> σ_{24}.

[2] This matrix has the rows interchanged from that which appears in Table II of reference (115). This results from the definition of the components as discussed in Section 3.6.

Using this procedure, the matrix elements involving all components can be calculated. The results are given in Table C.1.

In the case of $\langle H_{sr}^T(0 \to 1), \rho = 2\rangle$, we note from Table 3.3 that $\xi' = \zeta'$ and $\xi = \zeta$ in equation 3.7.10 for this matrix element to be non-zero. From Table C.1 we have that $\eta = \zeta = \xi$ in order to have non-zero entries. For this case, equation 3.7.10 becomes

$$\langle H_{sr}^T(0 \to 1), \rho = 2\rangle = -\frac{1}{3}hC_d \sum_\nu (-1)^\nu B^*(E) \ B(F) \ \{X\} \qquad C.8$$

where, from Table 3.3

$$B(E,1;E,1;2) = B(E,2;E,2;2) = B(E) = \frac{\sqrt{2}}{2} \qquad C.9$$

and $\{X\}$ is given by the expression

$$\{X\} = \sum_{\sigma=1}^{2} \sum_{\zeta=xyz} [X^*(E,\sigma)I^{F2,\zeta}X(F2,\zeta)][R^*(E,\sigma;2)B^{F2,\zeta}R(F2,\zeta;2)]$$
$$C.10$$

where we have suppressed all but ρ and the group theoretical notation. We can now use Table C.1 to perform the sums in equation C.10

$$\{X\} = (\Delta_{EFF}^S)(\Delta_{EFF}^R) + (\sqrt{3}\Delta_{EFF}^S)(\sqrt{3}\Delta_{EFF}^R)$$

$$+ \ (\Delta_{EFF}^S)(\Delta_{EFF}^R) + (-\sqrt{3}\Delta_{EFF}^S)(-\sqrt{3}\Delta_{EFF}^R)$$

$$+ \ (-2\Delta_{EFF}^S)(-2\Delta_{EFF}^R) = 12 \ \Delta_{EFF}^S \ \Delta_{EFF}^R \qquad C.11$$

TABLE C.1   GENERALIZED E → F MATRIX ELEMENTS

σ	ω	ω'	$L(E,\sigma)O^{F2,\omega}M(F2,\omega')$
1	x	x	Δ_{EFF}
2	x	x	$\sqrt{3}\ \Delta_{EFF}$
1	y	y	Δ_{EFF}
2	y	y	$-\sqrt{3}\ \Delta_{EFF}$
1	z	z	$-2\ \Delta_{EFF}$
2	z	z	0
1	i	≠ j	0
2	i	≠ j	0

σ	ω	ω'	$L(E,\sigma)O^{F1,\omega}M(F1,\omega')$
1	x	x	Δ_{EFF}
2	x	x	$-\sqrt{3}/3\ \Delta_{EFF}$
1	y	y	$-\Delta_{EFF}$
2	y	y	$-\sqrt{3}/3\ \Delta_{EFF}$
1	z	z	0
2	z	z	$2\sqrt{3}/3\ \Delta_{EFF}$
1	i	≠ j	0
2	i	≠ j	0

where the superscripts refer to spin and rotation and Δ_{EFF} is defined in equation C.3 or Table C.1. Substituting equation C.11 into equation C.8 gives

$$\langle H^T_{sr}(0 \to 1), \rho = 2\rangle = 12[-\tfrac{1}{3}hC_d] \sum_\nu (-1)^\nu B^*(E) B(F) \quad \times$$

$$[X^*(E,1;0,0) \; I^{F2,q}_{1,\nu}(F2,q;1,m_I)] \quad \times$$

$$[R^*(E,1;J,m'_J;t',2) \; B^{F2,q}_{1,-\nu} R(F2,q;J,m_J;t,2)]$$

$$\text{C.12}$$

where, in light of entries 1 and 3 of Table 0.1, q can be x or y.

The matrix element $\langle H^T_{sr}(0 \to 1), \rho = 1\rangle$ is even more complicated than the preceding one because the only non-vanishing matrix elements in equation 3.7.10 involve $\zeta' \neq \xi'$ as a result of the second to last entry of Table 3.3. As in the previous case, we have $\xi = \zeta = \eta$. For this particular matrix element, equation 3.7.10 becomes

$$\langle H^T_{sr}(0 \to 1), \rho = 1\rangle = -\tfrac{1}{3}hC_d \sum_\nu (-1)^\nu B^*(E) B(F) \{Y\} \qquad \text{C.13}$$

We write $\{Y\}$ performing the sum over $\zeta' = 1,2$.

$$\{Y\} = \sum_{\zeta=xyz} [X^*(E,1) \; I^{F2,\zeta}(F2,\zeta)][R^*(E,2) \; B^{F2,\zeta} R(F1,\zeta;1)]$$

$$- [X^*(E,2) I^{F2,\zeta}(F2,\zeta)][R^*(E,1) \; B^{F2,\zeta} R(F1,\zeta;1)] \qquad \text{C.14}$$

The minus sign arises as a result of the B values (Table 3.3), namely

$$B(E,1;E,2;1) \quad = \quad -B(E,2;E,1;2) \quad = \quad B(E) \tag{C.15}$$

Using Table C.1 and performing the remaining sum in equation C.14 gives

$$\{Y\} \quad = \quad [(\Delta_{EFF}^{S})(-\frac{1}{\sqrt{3}}\Delta_{EFF}^{R}) \quad + \quad (\Delta_{EFF}^{S})(-\frac{1}{\sqrt{3}}\Delta_{EFF}^{R})$$

$$+ \quad (-2\Delta_{EFF}^{S})(\frac{2}{\sqrt{3}}\Delta_{EFF}^{R})] \quad - \quad [(\sqrt{3}\Delta_{EFF}^{S})(\Delta_{EFF}^{R})$$

$$+ \quad (-\sqrt{3}\Delta_{EFF}^{S})(-\Delta_{EFF}^{R})] \quad = \quad -4\sqrt{3}\Delta_{EFF}^{S}\Delta_{EFF}^{R} \tag{C.16}$$

It is convenient to rewrite $\{Y\}$

$$\{Y\} \quad = \quad 4\sqrt{3} \; (\Delta_{EFF}^{S})(-\Delta_{EFF}^{R})$$

$$= \quad 4\sqrt{3} \; [X^{*}(E,1) \; I^{F2,y}X(F2,y)][R^{*}(E,1) \; B^{F2,y}R(F1,y)] \tag{C.17}$$

The choice of $\zeta = y$ will become clear in the following paragraphs. Substituting equation C.17 in equation C.13 leads to

$$\langle H_{sr}^{T}(0 \rightarrow 1),\rho = 1\rangle \quad = \quad 4\sqrt{3} \; [-\frac{1}{3}hC_{d}] \; \sum_{\nu} (-1)^{\nu} \; B^{*}(E) \; B(F)$$

$$[X^{*}(E,1;0,0) \; I_{1,-\nu}^{F2,y}X(F2,y;1,m_{I})]$$

$$[R^{*}(E,1;J,m_{J}';t',1)B_{1,-\nu}^{F2,y}R(F1,y;J,m_{J};t,1)] \tag{C.18}$$

Summarizing the calculation so far, we have the following expressions for $\langle H_{sr}^{T}(I' \to I)\rangle$: $1 \to 1$ in equation C.1, $2 \to 1$ in equation C.2, $0 \to 1$, $\rho = 2$ in equation C.12 and $0 \to 1$, $\rho = 1$ in equation C.18. We are free to choose some parameters. As discussed in Section 3.7, we make the choice that leads to the same form of the rotational matrix element in all cases. This leads to the following choices: $a = x$, $b = y$ and $c = z$ in equation C.1, $\ell = y$ in equation C.2 and $q = y$ in equation C.12. There are no parameters in equation C.18. On making these choices, equations C.1 and C.2 become equations, 3.7.11 and 3.7.12 respectively. Equations C.12 and C.18 can be incorporated into one equation, namely equation 3.7.13.

The coupling constant C_d used in this calculation has been measured by molecular beam spectroscopy and is 18.5 ± 0.5 kHz (32).

APPENDIX D

Sample Calculation for Tensor spin-rotation spin

matrix elements

As an example, we choose the spin matrix element required in equation 3.7.12. With the conventions adopted in Appendix B,

$$\chi^*(A1;2,m'_I) \, I^{F2,y}_{1,\nu} \chi(F2;1,m_I) = (-1)^{2-m'_I} \begin{pmatrix} 2 & 1 & 1 \\ -m'_I & \nu & m_I \end{pmatrix} \langle A||I^{F2}||F\rangle$$

$$\text{D.1}$$

For the choice of $\nu = 0$ and $m'_I = m_I = 1$, the left hand side of equation D.1 becomes (with the aid of Tables 3.1 and 3.6)

$$[\tfrac{1}{2}(baaa + abaa + aaba + aaab)][-I^{(1)}_0 + I^{(2)}_0 + I^{(3)}_0 - I^{(4)}_0] \quad x$$

$$[\tfrac{1}{2}(aaab + baaa - aaba - abaa)] = 1 \qquad \text{D.2}$$

The right hand side of equation D.1 is

$$(-1)^{2-1} \begin{pmatrix} 2 & 1 & 1 \\ -1 & 0 & 1 \end{pmatrix} \langle A||I^{F2}||F\rangle = -\frac{1}{\sqrt{10}} \langle A||I^{F2}||F\rangle \qquad \text{D.3}$$

Equations D.2 and D.3 are solved for the reduced matrix element. The 3-j symbol is evaluated from Tables in reference (123).

$$\langle A||I^{F2}||F\rangle = \sqrt{10} \qquad \text{D.4}$$

Substituting equation D.4 into equation D.1 gives the desired result, namely equation 3.7.17. Equations 3.7.16 and 3.7.18 are arrived at using the same process.

APPENDIX E

CALCULATION OF C_d ROTATIONAL MATRIX ELEMENTS

The rotational matrix elements required in equations 3.7.11, 3.7.12 and 3.7.13 can be expressed

$$W^*(J,K',m_J^r) \, B_{1,-\nu}^{F2,y} \, U(J,K,m_J) \;=\; (-1)^{J-m_J'} \begin{pmatrix} J & 1 & J \\ -m_J' & -\nu & m_J \end{pmatrix} <JK'||B^{F2}||JK>$$

E.1

Substituting $\nu = 0$ and $m_J' = m_J = 1$, the left hand side of equation E.1 becomes (with the aid of Tables 3.2 and 3.7)

$$W^*(J,K',1) \, B_{1,0}^{F2,y} \, U(J,K,1) \;=\; \left[\{1 + \delta(K',0)\}^{-\frac{1}{2}} \{\tfrac{2J+1}{16\pi^2}\}^{\frac{1}{2}} \{D_{1,K'}^J + (-1)^J D_{1,-K'}^J\} \right]$$

$$\left[\sum_\mu (-1)^\mu C_{2,-\mu}^{F2,y} \{ \tfrac{\sqrt{2}}{2} D_{1,\mu}^2 J_{+1} + \tfrac{\sqrt{6}}{3} D_{0,\mu}^2 J_0 + \tfrac{\sqrt{2}}{2} D_{-1,\mu}^2 J_{-1} \} \right]$$

$$\left[\{1 + \delta(K,0)\}^{-\frac{1}{2}} \{\tfrac{2J+1}{16\pi^2}\}^{\frac{1}{2}} \{D_{1,K}^{J\,*} - (-1)^J D_{1,-K}^{J\,*}\} \right]$$

E.2

The operations $J_\eta \, D_{1,\pm K}^{J\,*}$ are as follows

$$J_1 \, D_{1,\pm K}^{J\,*} \;=\; (-1)^{K+1} \, \frac{1}{\sqrt{2}} \, [(J-1)(J+2)]^{\frac{1}{2}} \, D_{-2,\mp K}^J \qquad\qquad \text{E.3}$$

$$J_0 \, D_{1,\pm K}^{J\,*} \;=\; (-1)^{K+1} \, D_{-1,\mp K}^J \qquad\qquad\qquad\qquad\qquad \text{E.4}$$

$$J_{-1} D_{1,\pm K}^{J\,*} \;=\; (-1)^K \, \frac{1}{\sqrt{2}} \, [J(J+1)]^{\frac{1}{2}} \, D_{0,\mp K}^J \qquad\qquad\qquad \text{E.5}$$

In this calculation, great care must be taken to ensure consistency with respect to definitions of operators and functions. The $D^J_{m_J,K}$ used here are as defined in reference (111) but the expression for the Wigner-Eckart Theorem is as defined in reference (123). The K-dependent phases in equations E.3 to E.5 come from the transformations $D^* \to D$. (Equation 4.2.7 of reference (123).)

When equation E.2 is expanded and equations E.3 to E.5 used, one is left with a sum over μ of triple products like $D^J_{1,\pm K'}$ $D^2_{\eta,\mu}$ $D^J_{\xi,\pm K}$ $\eta = -1, 0 + 1$, $\xi = -2, -1, 0$, and all possible combinations are present. Whereas the D's are functions of the Euler angles measured with respect to the space fixed frame, the matrix element is clearly independent of orientation. The integration over the Euler angles can be expressed by (equation 4.6.2 of reference (123))

$$\frac{1}{8\pi^2} \int_0^{2\pi} \int_0^\pi \int_0^{2\pi} D^{J_1}_{m'_1 m_1}(\alpha\beta\gamma) \, D^{J_2}_{m'_2 m_2}(\alpha\beta\gamma) \, D^{J_3}_{m'_3 m_3} \, d\alpha \, \sin\beta d\beta \, d\gamma \quad = $$

$$\begin{pmatrix} J_1 & J_2 & J_3 \\ m'_1 & m'_2 & m'_3 \end{pmatrix} \begin{pmatrix} J_1 & J_2 & J_3 \\ m_1 & m_2 & m_3 \end{pmatrix} \qquad \text{E.6}$$

On performing the integration, one finds that the resulting products of 3-j symbols factor into two terms; one involving only J and another involving J, K', K, and μ. (A similar result was obtained in reference (117)[1].) After considerable algebraic manipulation, equation E.2 becomes

$$W^*(J',K',1) \, B^{F2,\gamma}_{1,0} \, U(J,K,1) \quad = \quad [f(J)][g(J,K',K)] \qquad \text{E.7}$$

[1]The computation of reference (117) is discussed near the end of Section 3.7.2.

$$f(J) = 8\pi^2 \left[\frac{2J+1}{16\pi^2}\right] \left[(2J+1) \left\{-\frac{1}{4}\left[(J-1)(J+2)\right]^{\frac{1}{2}} \begin{pmatrix} J & 2 & J \\ 1 & 1 & -2 \end{pmatrix} \right.\right.$$

$$\left.\left. -\frac{1}{\sqrt{6}} \begin{pmatrix} J & 2 & J \\ 1 & 0 & -1 \end{pmatrix} + \frac{1}{4}\left[(J)(J+1)\right]^{\frac{1}{2}} \begin{pmatrix} J & 2 & J \\ 1 & -1 & 0 \end{pmatrix} \right\}\right] \qquad \text{E.8}$$

$$g(J,K',K) = \sum_{\mu} (-1)^{\mu} C_{2,-\mu}^{F2,y} (-1)^{K} \left[\{1+\delta(K',0)\}\{1+\delta(K,0)\}\right]^{-\frac{1}{2}} \quad x$$

$$\left[\begin{pmatrix} J & 2 & J \\ K' & \mu & -K \end{pmatrix} - \begin{pmatrix} J & 2 & J \\ -K' & \mu & K \end{pmatrix} + (-1)^{J} \begin{pmatrix} J & 2 & J \\ -K' & \mu & -K \end{pmatrix} - \begin{pmatrix} J & 2 & J \\ K' & \mu & K \end{pmatrix}\right]$$

$$\text{E.9}$$

On expanding the 3-j symbols (123) in equation E.8 and adding terms, one obtains,

$$f(J) = 8\pi^2 \left[\frac{2J+1}{16\pi^2}\right] \left[(-1)^{J} \frac{2}{\sqrt{6}} (2J-1)(2J+3) \left\{(2J+3)(2J+2)(2J+1)(2J)(2J-1)\right\}^{-\frac{1}{2}}\right]$$

$$\text{E.10}$$

Computing g(J,K',K) is somewhat more involved. Using the C-values given in Table 3.5, one sums over μ, which simplifies the problem because only terms with $\mu = \pm 1$ are non zero. Equation E.9 becomes

$$g(J,K',K) = (-1)^{K} \left[\{1+\delta(K',0)\}\{1+\delta(K,0)\}\right]^{-\frac{1}{2}} \quad x$$

$$2\left[\begin{pmatrix} J & J & 2 \\ -K & K' & -1 \end{pmatrix} - \begin{pmatrix} J & J & 2 \\ K & -K' & -1 \end{pmatrix} + (-1)^{J} \begin{pmatrix} J & J & 2 \\ K & K' & 1 \end{pmatrix} - \begin{pmatrix} J & J & 2 \\ K & K' & -1 \end{pmatrix}\right]$$

$$\text{E.11}$$

In performing this last step, the symmetry properties of the 3-j symbols have been used (equations 3.7.4 and 3.7.6 of reference (123)). Both K' and K are greater than or equal to zero so the third 3-j symbol in equation E.11 vanishes because the entries in the second row of a 3-j symbol must add to zero. For this same reason, the 3 remaining 3-j symbols in equation E.11 can be expressed as 3-j symbols involving J and K only times a δ-function in K' and K. For example,

$$\begin{pmatrix} J & J & 2 \\ -K & K' & -1 \end{pmatrix} = - \begin{pmatrix} J & J & 2 \\ -K & K+1 & -1 \end{pmatrix} \delta(K',K+1) \qquad \text{E.12}$$

It should be noted that the last 3-j symbol in equation E.11 is only non-zero when K' = 0, and K = 1 or when K'= 1 and K = 0.

Performing this operation and expanding the resulting 3-j symbols (123) equation E.11 becomes

$$g(J,K',K) = 2(-1)^K [\{1+\delta(K',0)\}\{1+\delta(K,0)\}]^{-\frac{1}{2}} \ x$$

$$[\{(2J+3)(2J+2)(2J+1)(2J)(2J-1)\}^{-\frac{1}{2}} \{(-1)^{J-K} (1+2K) \quad x$$

$$[6(J+K+1)(J-K)]^{\frac{1}{2}} \delta(K',K+1) - (-1)^{J-K} (1-2K) \quad x$$

$$[6(J-K+1)(J+K)]^{\frac{1}{2}} [\delta(K',K-1) + (-1)^J \delta(K',1-K)]\}] \qquad \text{E.13}$$

Substituting equations E.10 and E.13 into equation E.7 and sorting out terms, one obtains

$$W^*(J,K,1) B_{1,0}^{F2,y} U(J,K,1) = \frac{1}{2} [J(J+1)] Q(J,K',K) \qquad \text{E.14}$$

where $Q(J,K',K)$ is given by equation 3.7.20.

The right hand side of equation E.1 with $\nu = 0$ and $m'_J = m_J = 1$ is

$$W^*(J,K',1) \, B^{F2,y}_{1,0} \, U(J,K,1) \quad = \quad (-1)^{J-1} \begin{pmatrix} J & 1 & J \\ -1 & 0 & 1 \end{pmatrix} <JK'||B^{F2}||JK> \qquad E.15$$

With the result that the reduced matrix element is obtained by expanding the 3-j symbol in equation E.16 and equating E.14 and E.15.

$$<JK'||B^{F2}||JK> \quad = \quad \frac{1}{2} \left[\frac{2J+1}{J(J+1)} \right]^{\frac{1}{2}} Q(J,K',K) \qquad E.16$$

Equation E.16 with equation E.1 gives the desired result, namely equation 3.7.19.

APPENDIX F

Sums over m_J' and m_J of the Matrix Elements Squared

We wish to calculate the double sum

$$\sum_{m_J'} \sum_{m_J} \left| \langle H_{sr}^i (I' \rightarrow I) \rangle \right|^2 \qquad\qquad F.1$$

for the four possible types of transitions.

From equation 3.7.5, we have

$$\left| \langle H_{sr}^S (2 \rightarrow 2) \rangle \right|^2 \;=\; h^2 C_\alpha{}^2 \; \delta(t',t) \; [\Gamma]^2 \qquad\qquad F.2$$

where Γ is given by equation 3.7.7. On squaring equation 3.7.7 we have

simply the square of each of the 3 terms[1]. The cross terms are zero because

of the δ-functions in m_J' and m_J. Omitting the $m_{I'}'$, m_I dependence of equation

3.7.7 the first term of $(\Gamma)^2$ will be

$$\sum_{m_J'=-J}^{+J} \;\; \sum_{m_J=-J}^{+J} \; (J+m_J)(J-m_J+1)\; \delta(m_J',m_J-1)$$

$$= \sum_{m_J=-J}^{+J} \; (J+m_J)(J-m_J+1)\; \delta(m_J-1,m_J-1) \qquad\qquad F.3$$

the δ-function in equation F.3 can only take values of unity over the range

$\delta(-J,-J)$ to $\delta(+J,+J)$ so the lower limit in sum becomes $-J+1$.

Equation F.3 is then

---

[1] $\Gamma^2 = \Gamma(m_J';m_J)\Gamma(m_J';m_J)$ is identical to $[\Gamma(m_J;m_J')]^+ \, \Gamma(m_J';m_J)$ which is really
  what we are calculating.

$$\sum_{m_J=-J+1}^{+J} (J+m_J)(J-m_J+1) \quad = \quad \sum_{x=-J}^{J-1} (J+x+1)(J-x) \quad = \quad \frac{2}{3} J(J+1)(2J+1)$$

$$F.5$$

We write the intermediate step in equation F.5 because the square of the third term can be cast into the same form.

The middle term in equation 3.7.7 (again neglecting the nuclear spin quantum numbers) is

$$\sum_{m_J'=-J}^{+J} \sum_{m_J=-J}^{+J} m_J^2 \; \delta(m_J',m_J) \quad = \quad \sum_{x=-J}^{+J} x^2 \quad = \quad \frac{1}{3} J(J+1)(2J+1) \quad F.6$$

Putting the nuclear spin quantum numbers back in and collecting terms, equation F.2 becomes equation 3.8.10.

The computation for $<H_{sr}(1 \rightarrow 1)>$ is more complicated because there are two terms, equations 3.7.6 and 3.7.22. These two equations give

$$\sum_{m_J'} \sum_{m_J} \left| <H_{sr}(1 \rightarrow 1)> \right|^2 \quad = \quad \sum_{m_J'} \sum_{m_J} \left| <H_{sr}^S(1 \rightarrow 1)> + <H_{sr}^T(1 \rightarrow 1)> \right|^2$$

$$= \quad \sum_{m_J'} \sum_{m_J} h^2 \Lambda^2 [C_a \delta(t',t) + \frac{1}{3} \Pi C_d]^2$$

$$= \quad h^2 [C_a \delta(t',t) + \frac{1}{3} \Pi C_d]^2 \sum_{m_J'} \sum_{m_J} [\Lambda]^2 \quad F.7$$

with Λ given by equation 3.7.8 (Π is given by equation 3.7.27 but does not concern us here since it does not involve m_J' or m_J.) The double sum over m_J' and m_J of Λ^2 involves the same kinds of terms as in the previous case and as such, we simply quote the result given by equation 3.8.12.

For the case of $I' = 2$, $I = 1$ equation 3.7.23 results in

$$\sum_{m'_J} \sum_{m_J} \left| <H_{sr}(2\rightarrow1)> \right|^2 = \frac{1}{9} h^2 C_d^2 [\Pi]^2 \sum_{m'_J} \sum_{m_J} [\Omega]^2 \qquad \text{F.8}$$

with Ω given in equation 3.7.25. Again, the double sum is similar to the first case performed in this Appendix and the result is given by equation 3.8.14.

The final case, that of $I' = 0 \rightarrow I = 1$ follows in a similar manner and the result appears in the text as equation 3.8.16.

The coupling constants C_a and C_d are 10.4 ± 0.1 kHz and 18.5 ± 0.5 kHz, respectively (32).

APPENDIX G

Final forms for W_{m_I',m_I}

The starting point for the calculations presented here is equation 3.8.9.

Setting $I' = I = 2$ and using equation 3.8.10, equation 3.8.9 becomes

$$W_{m_2'm_2} = 2\hbar^{-2}[U(2,T)]^{-1} \sum_{J=0}^{\infty} \sum_{\rho=1}^{2} \sum_{t'=1}^{N(A,J,\rho)} \sum_{t=1}^{N(A,J,\rho)} [\frac{1}{2}j_1(\omega_0)] \text{ x}$$

$$[\exp\{-\frac{BJ(J+1)}{kT}\}][\frac{1}{6}h^2C_a^2 \; J(J+1) \; \delta(t',t) \; f^{22}(m_2'm_2)] \qquad \text{G.1}$$

The δ-function eliminates the sum over t' and because there is no explicit dependence on t, the sum over t just adds unity $N(A,J,\rho)$ times in the same manner as outlined at the beginning of Section 3.8 for the calculation of $U(I,T)$. Further, the sum over ρ is as given in equation 3.8.6 and equation G.1 becomes

$$W_{m_2'm_2} = [f^{22}(m_2'm_2')][A(T:C_a^2)] \qquad \text{G.2}$$

with A given by equation 3.8.26 and f^{22} given by equation 3.8.11.

For the case of $I' = I = 1$ we use equation 3.8.12 and equation 3.8.9 becomes

$$W_{m_1'm_1} = 2\hbar^{-2}[U(1,T)]^{-1} \sum_{J=0}^{\infty} \sum_{\rho=1}^{2} \sum_{t'=1}^{N(F,J,\rho)} \sum_{t=1}^{N(F,J,\rho)} \times$$

$$[\frac{1}{6} h^2 J(J+1)(2J+1)\{\delta(t',t) C_a + \frac{1}{3} [\Pi] C_d\}^2 f^{11}(m_1'm_1)] \times$$

$$[\exp\{-\frac{BJ(J+1)}{kT}\}][\frac{1}{2} j\{\omega(J,\rho;F,F;t',t;m_1'm_1)\}]] \qquad \text{G.3}$$

This transition probability is complicated because both the scalar and tensor spin-rotation interactions contribute. We rewrite equation G.3 defining three functions depending on the coupling constant involved.

$$W_{m_1'm_1} = f^{11}(m_1'm_1) [F(T:C_a^2) + G(T:C_aC_d)$$

$$+ H(T:C_d^2;m_1'-m_1)] \qquad \text{G.4}$$

The derivation of $F(T:C_a^2)$ proceeds exactly as that for $A(T:C_a^2)$. $F(T:C_a^2)$ is given by equation 3.8.27. Because the cross term in equation G.3 contains the δ-function in t' and t and because $\gamma' = \gamma = F$, there are no distortion frequencies associated with this term and j is a function of ω_0 only. As discussed in the text we call this j_{12} and $G(T:C_aC_d)$ is given by equation 3.8.28

The final term in equation G.4 involves possible changes in distortion state and is

$$H(T;m_1'-m_1:C_d^2) = [\frac{4}{27} \pi^2 C_d^2][U(1,T)]^{-1} \times$$

$$\sum_{J} \sum_{\rho} \sum_{t'} \sum_{t} [J(J+1)(2J+1)][\Pi(F,F;J,t',t,\rho)]^2 \times$$

$$[\exp \{-\frac{BJ(J+1)}{kT}\}][\frac{1}{2} j_2 \{\omega(J,\rho;F,F;t',t;m_1',m_1)]$$

<div align="right">G.5</div>

It is convenient to split equation G.5 into 2 parts; one involving only zero frequency terms (i.e., $t' = t$) and the other involving only non zero frequency terms (i.e., $t' \neq t$)

$$H(T;C_d^2;m_1'-m_1) = B(T;C_d^2) + E(T;m_1'-m_1;C_d^2)$$

<div align="right">G.6</div>

where $B(T:C_d^2)$ is given by equation 3.8.29 and $E(T:m_1'-m;C_d^2)$ is given by equation G.5 with $t' \neq t$.

The two remaining classes of transitions ($E \rightarrow F$ and $A \rightarrow F$) involve only a change of distortion state accompaning the spin conversion since $\gamma' \neq \gamma$. The derivation proceeds like the H term in equation G.5 and we quote the results in equations 3.8.34 and 3.8.35.

Figures G.1 to G.13

The zero density nuclear spin relaxation rotation
spectrum of methane gas. The factors $Z(T:C_d^2;\gamma',$
$\gamma,J,t',t,\rho)$ are plotted as a function of the
centrifugal distortion frequencies $(1/2\pi)[\omega(J,\gamma',t',$
$\rho) - \omega(J,\gamma,t,\rho)]$. The $Z(T:C_d^2;\gamma',\gamma,J,t',t,\rho)$
are related to the weighted squares of matrix
elements of the tensor spin-rotation interaction.
The various figures correspond to different values
for the temperature, γ' and γ which are indicated
on each figure. The different combinations of
$\gamma' \to \gamma$ are $F \to F$ $(I' =1 \to I = 1)$, $A \to F$ $(I' = 2 \to$
$I = 1)$ and $E \to F$ $(I' = 0 \to I = 1)$. Figures G.1 to
G.5 cover the frequency range from -4000 MHz to
+4000 MHz for 295 and 110K. In these figures, the
magnitude of the largest line is given as a percent
of $A'(T:C_a^2)$. The latter parameter corresponds to
the line at zero frequency (not shown) and is a
measure of the weighted sums of squares of matrix
elements of the scalar spin-rotation interaction.

Figures G.6 to G.13 cover the range from -800 MHz
to +800 MHz at 295, 150, 110, and 77K. In these
figures, the J-level in which the transition occurs
is indicated in brackets for some of the transitions.
The remaining indices in $Z(T:C_d^2;\gamma',\gamma,J,t',t,\rho)$,
namely t', t and ρ for those transitions marked
with an asterisk may be found in Table 4.1 along
with a more precise value of the centrifugal
distortion frequency involved.
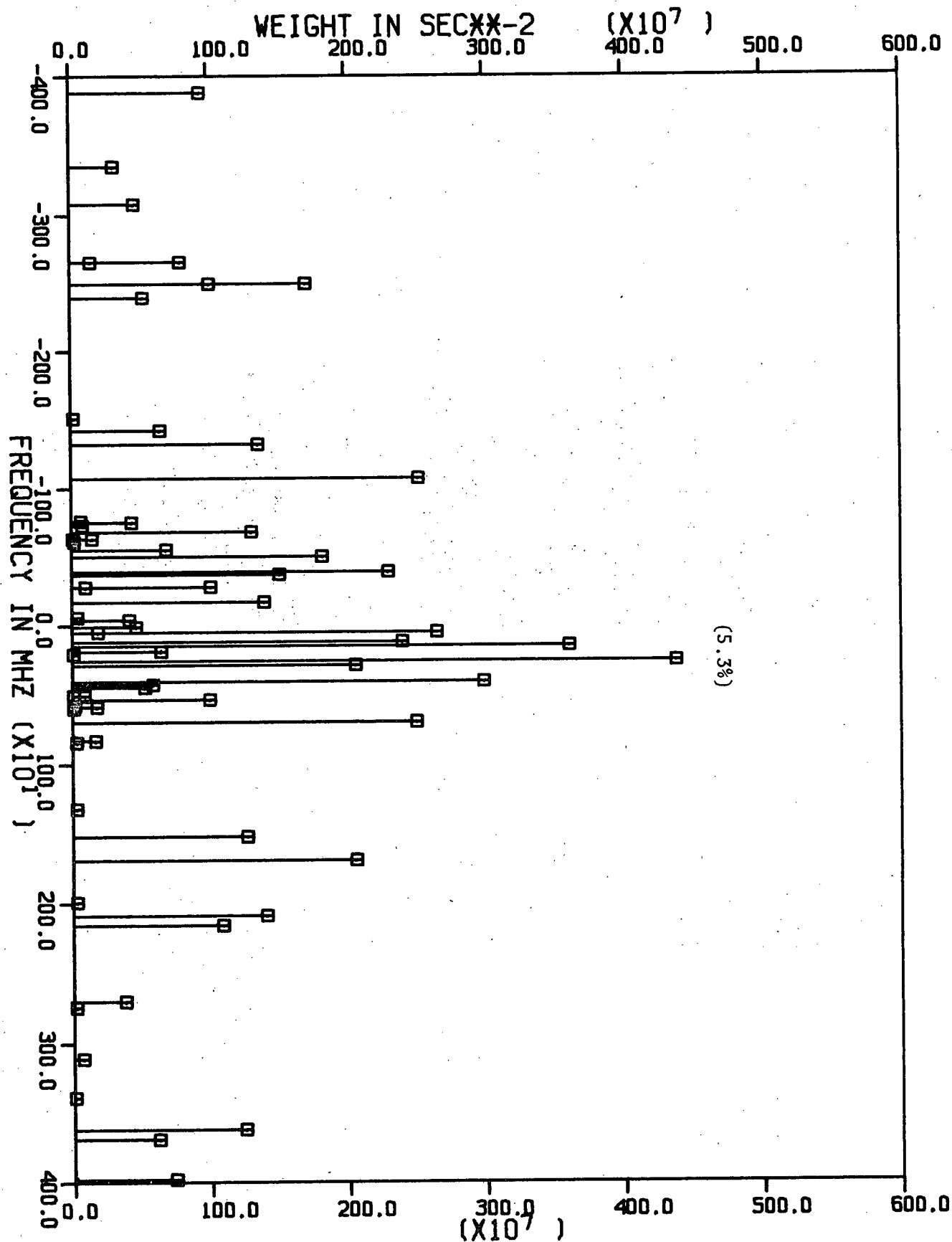
Figure G.1. (T = 295K, γ' = E and γ = F)
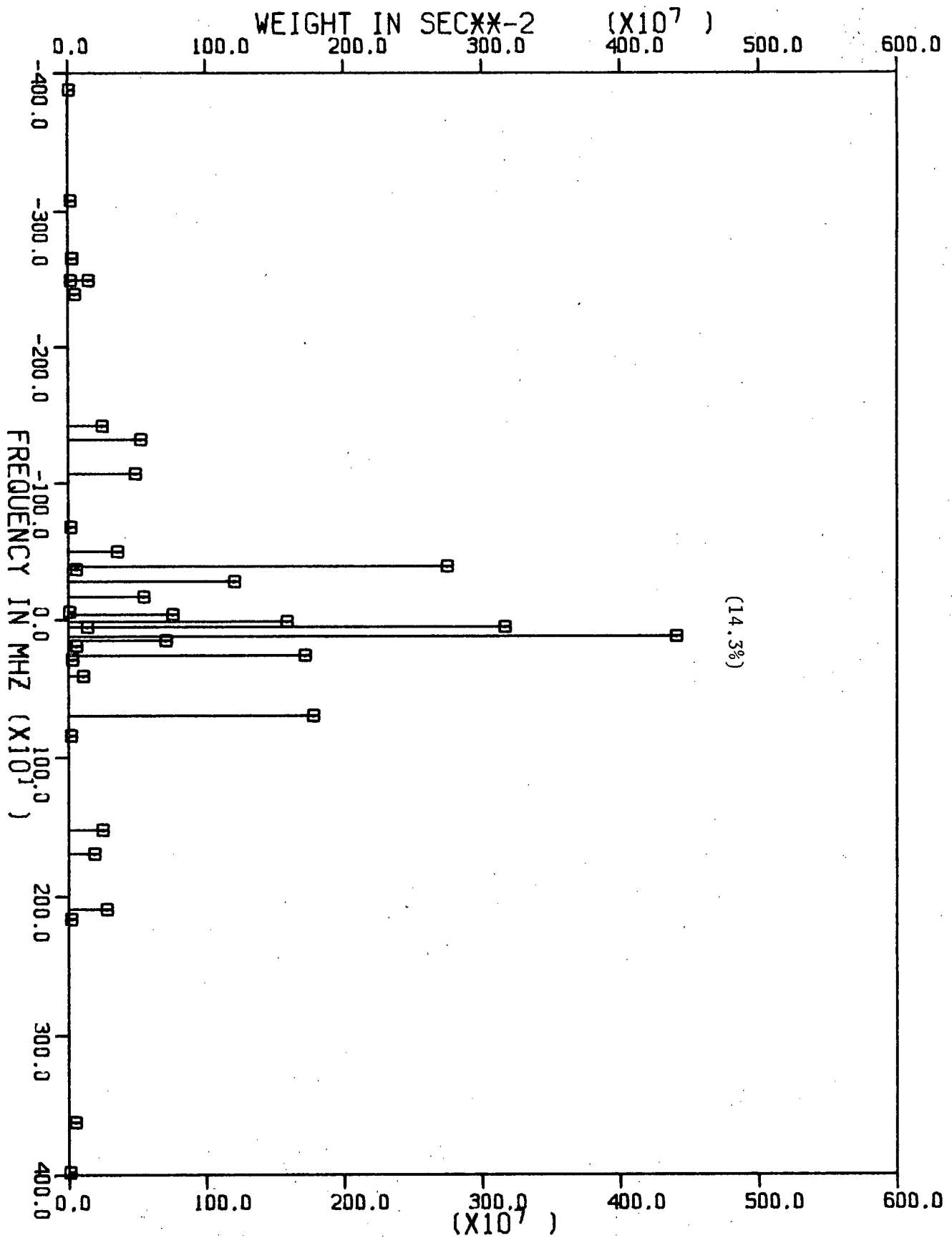
Figure G.2.   (T = 110K, γ' = E and γ = F)

Figure G.3.   (T = 295K, γ' = A and γ = F)
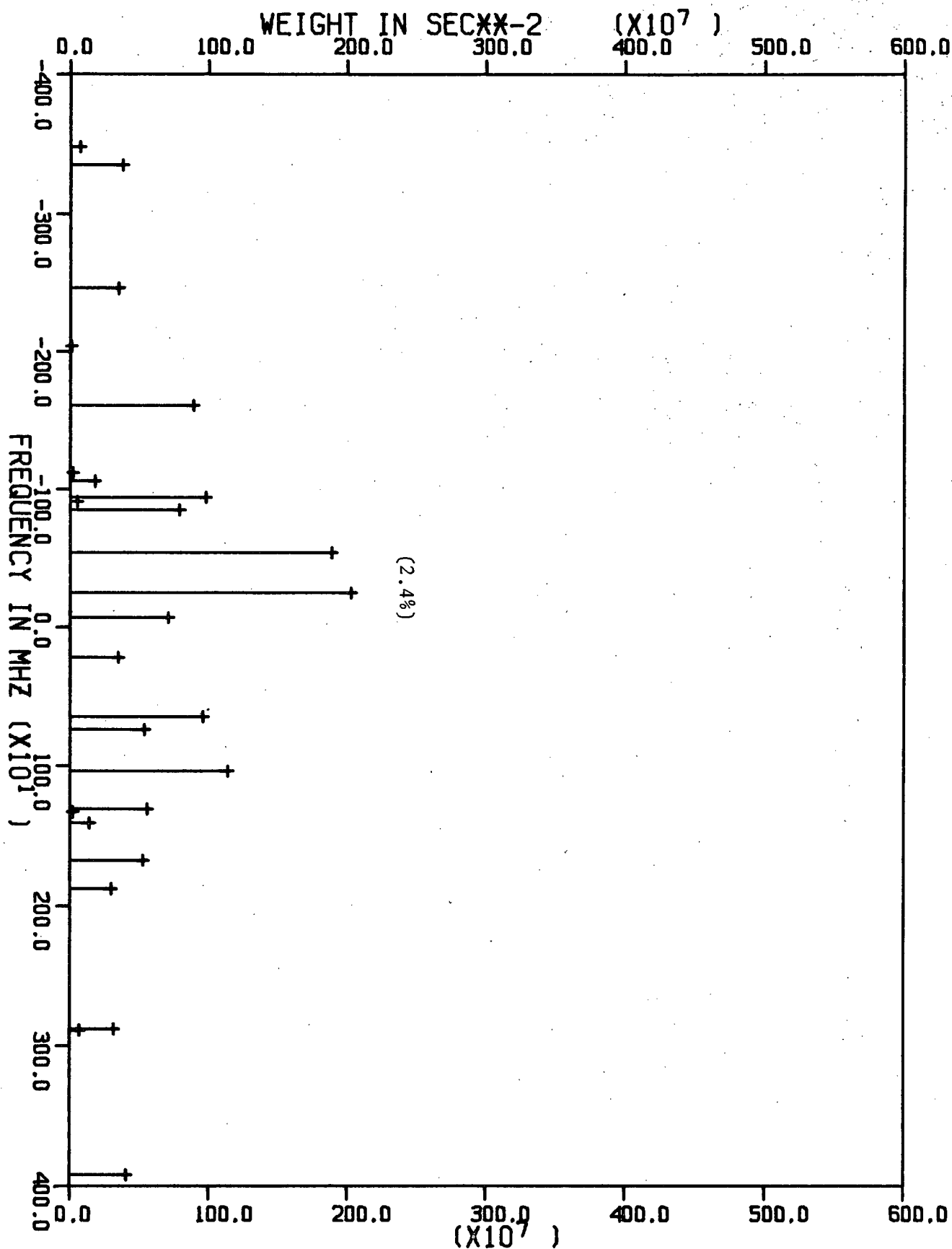
Figure G.4. (T = 110K, γ' = A and γ = F)
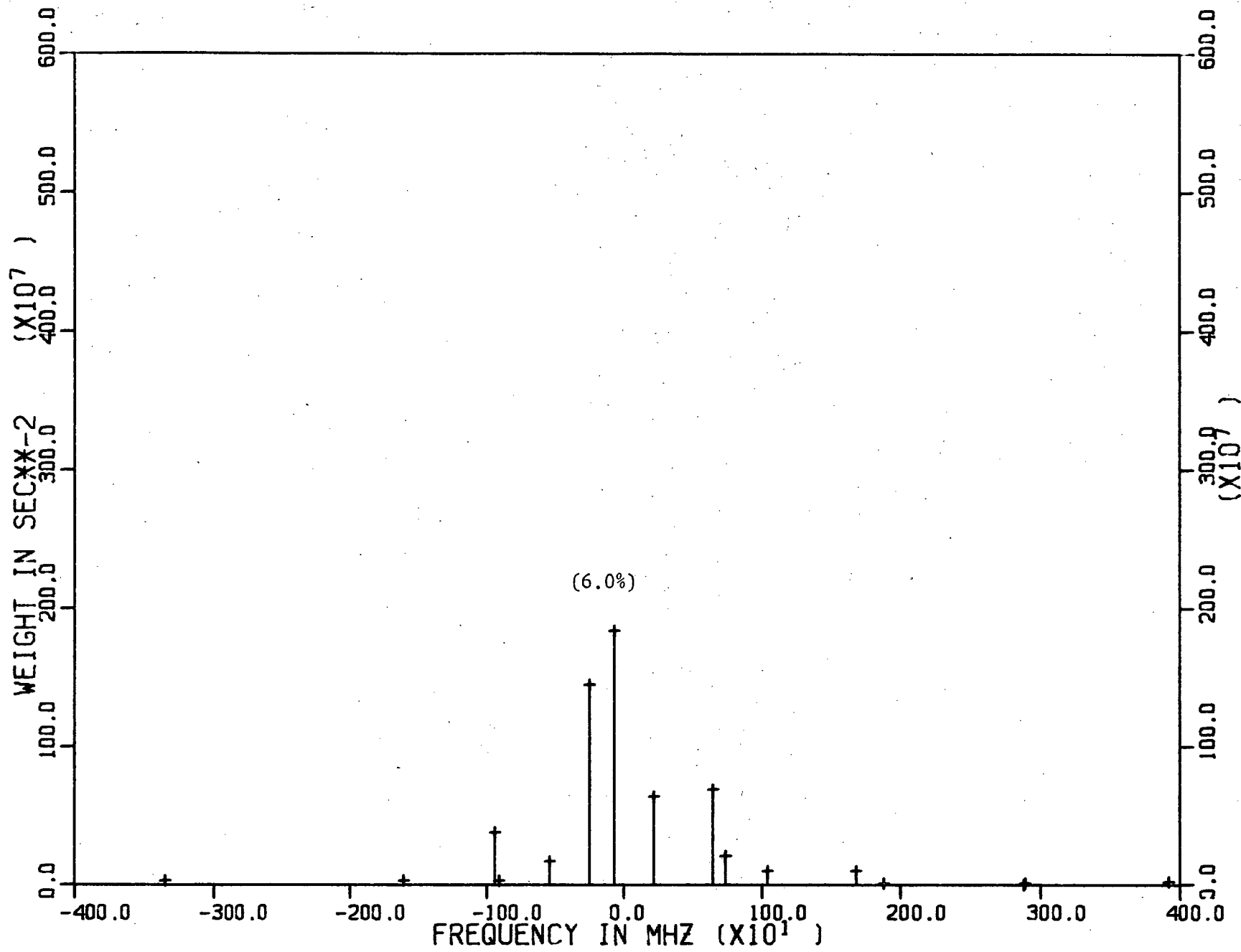
Figure G.5.   (T = 295K, γ' = F and γ = F)
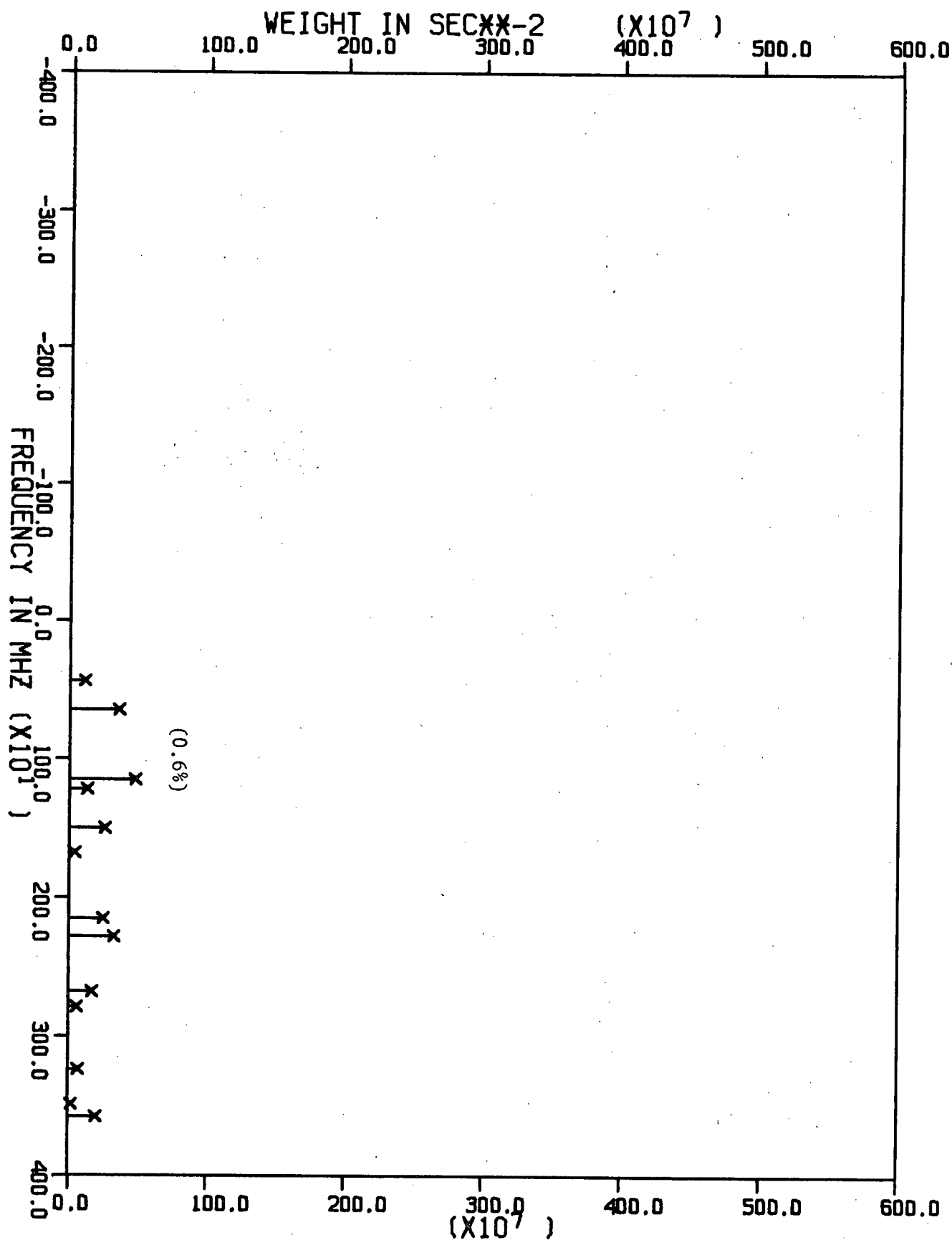
Figure G.6.   (T = 295K, $\gamma' = E$ and $\gamma = F$)
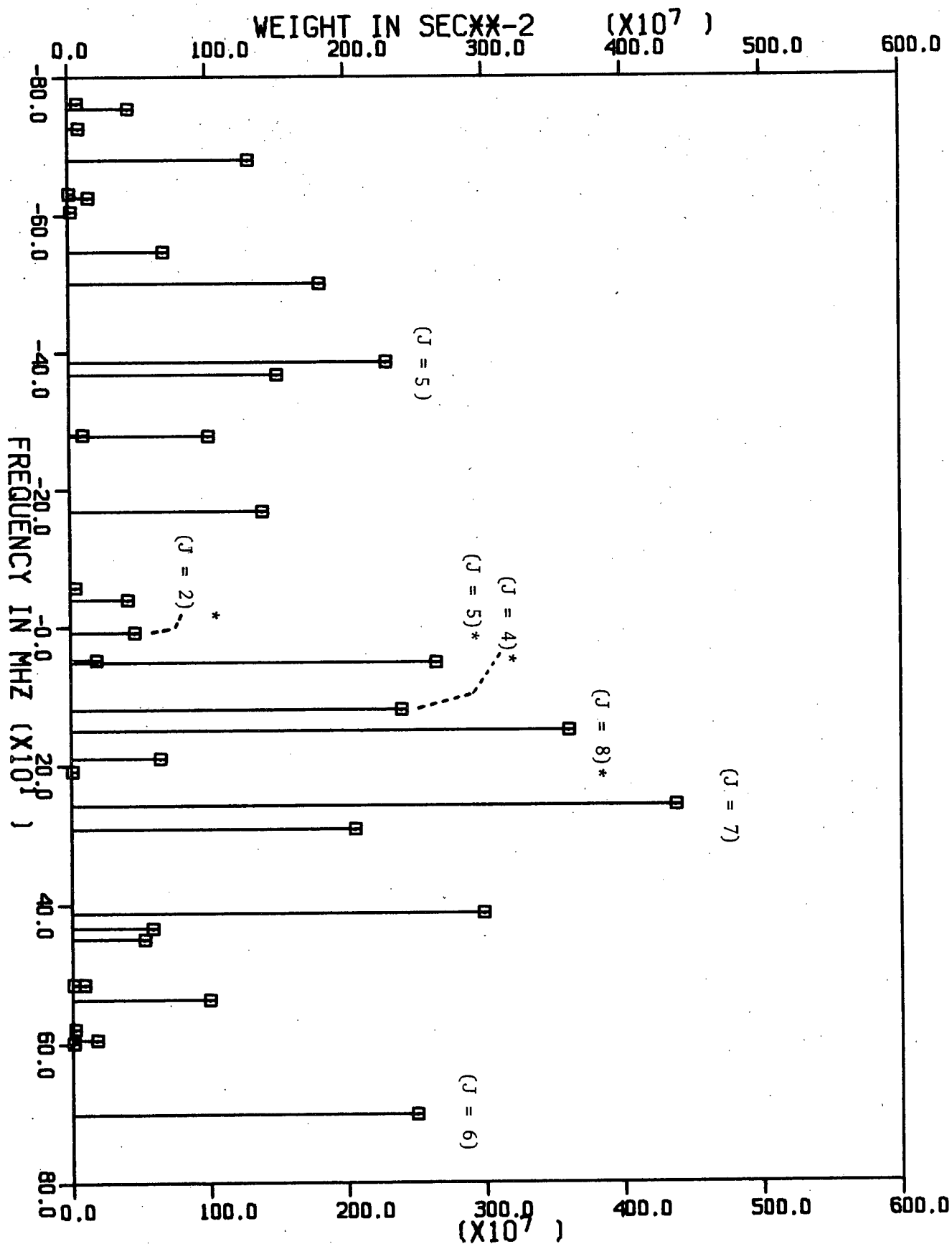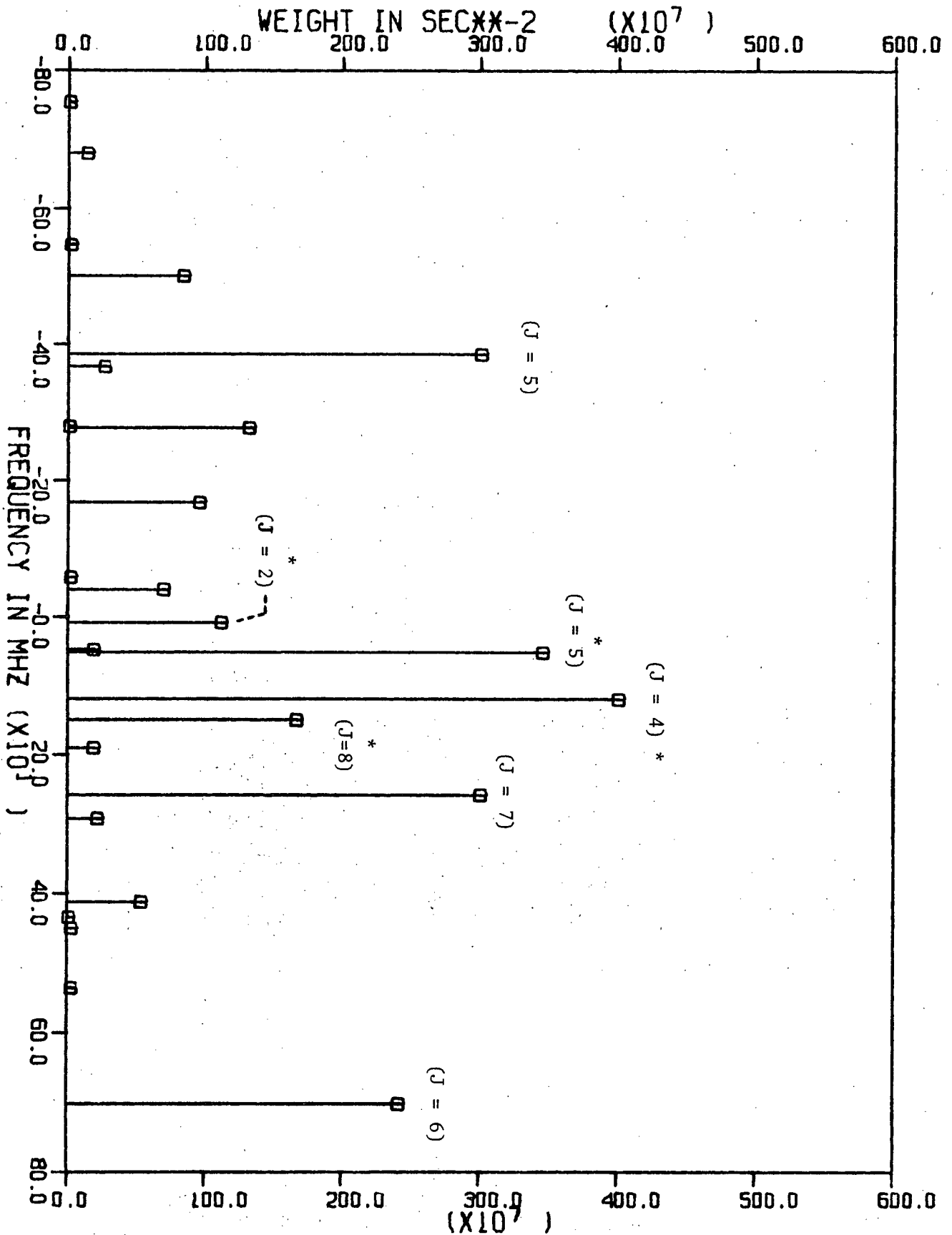
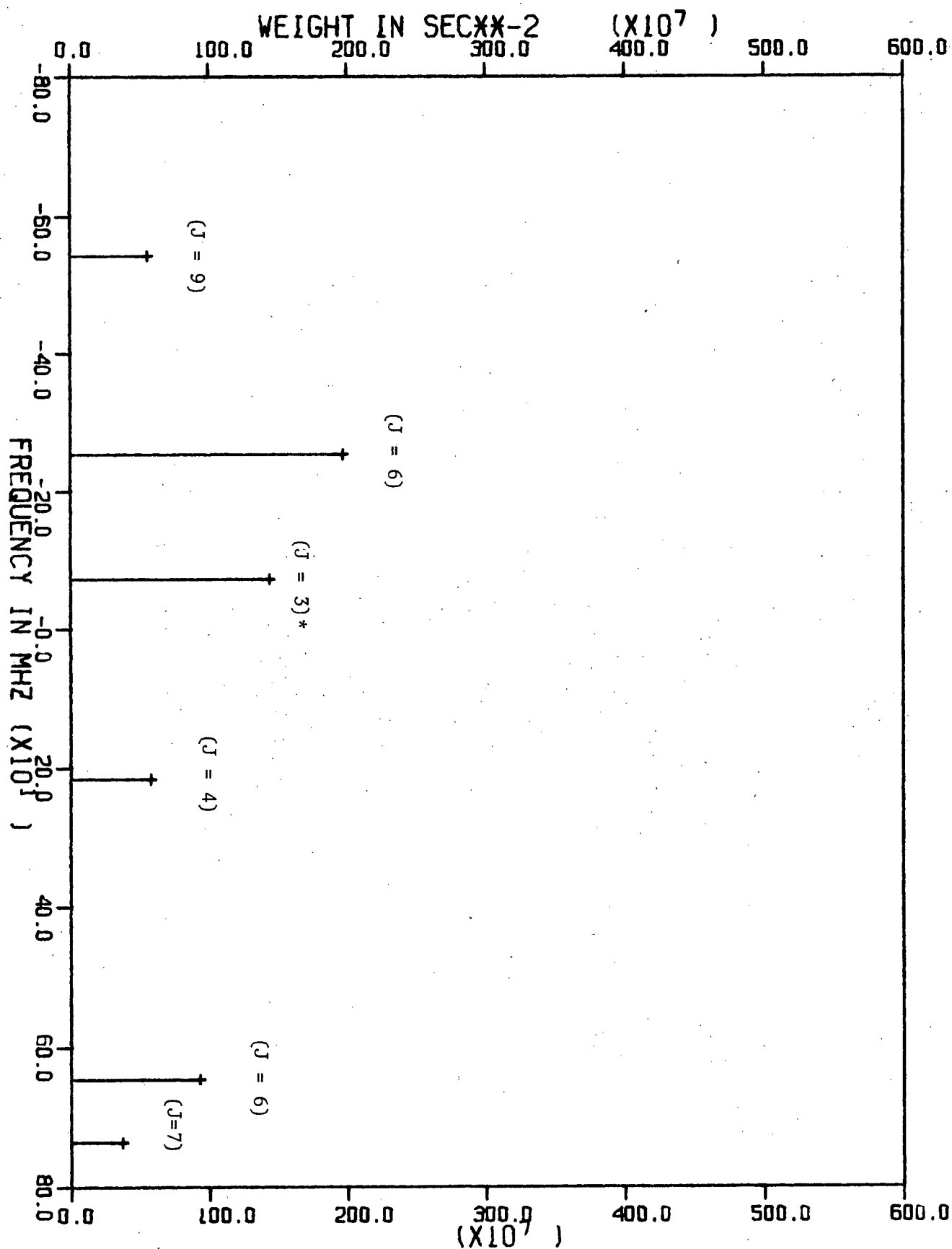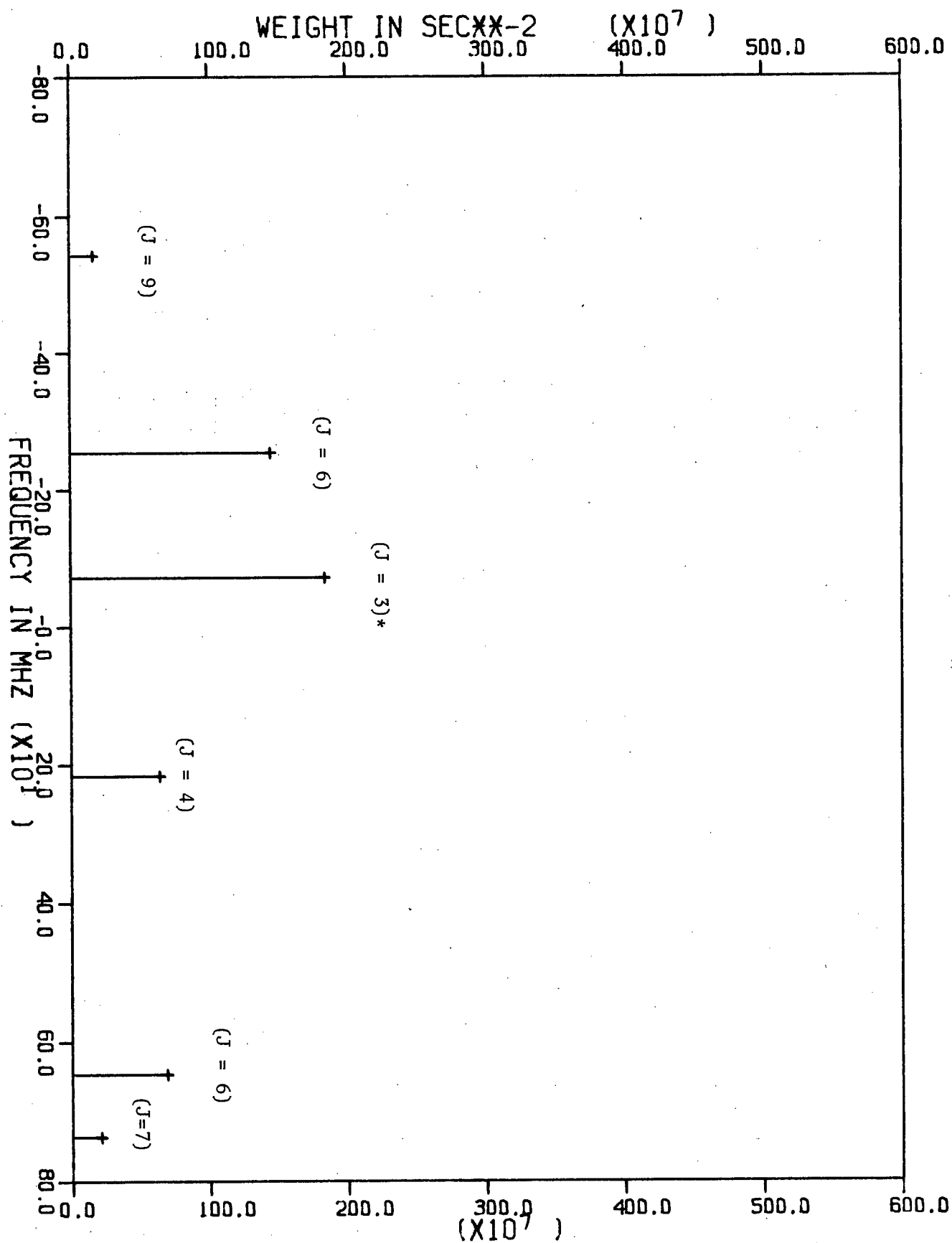Figure G.7. (T = 150K, γ' = E and γ = F)
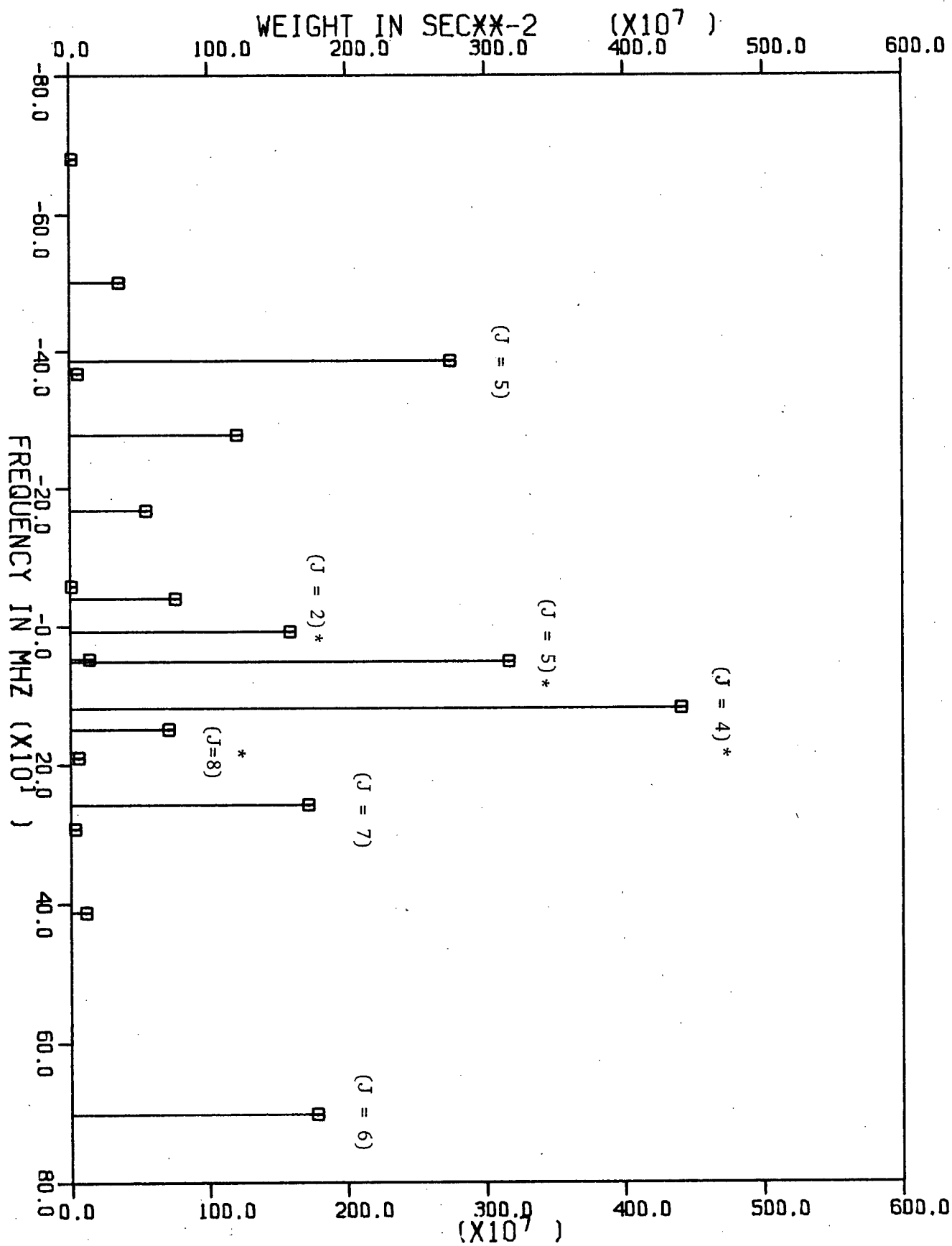
Figure G.8. (T = 110K, $\gamma' = E$ and $\gamma = F$)
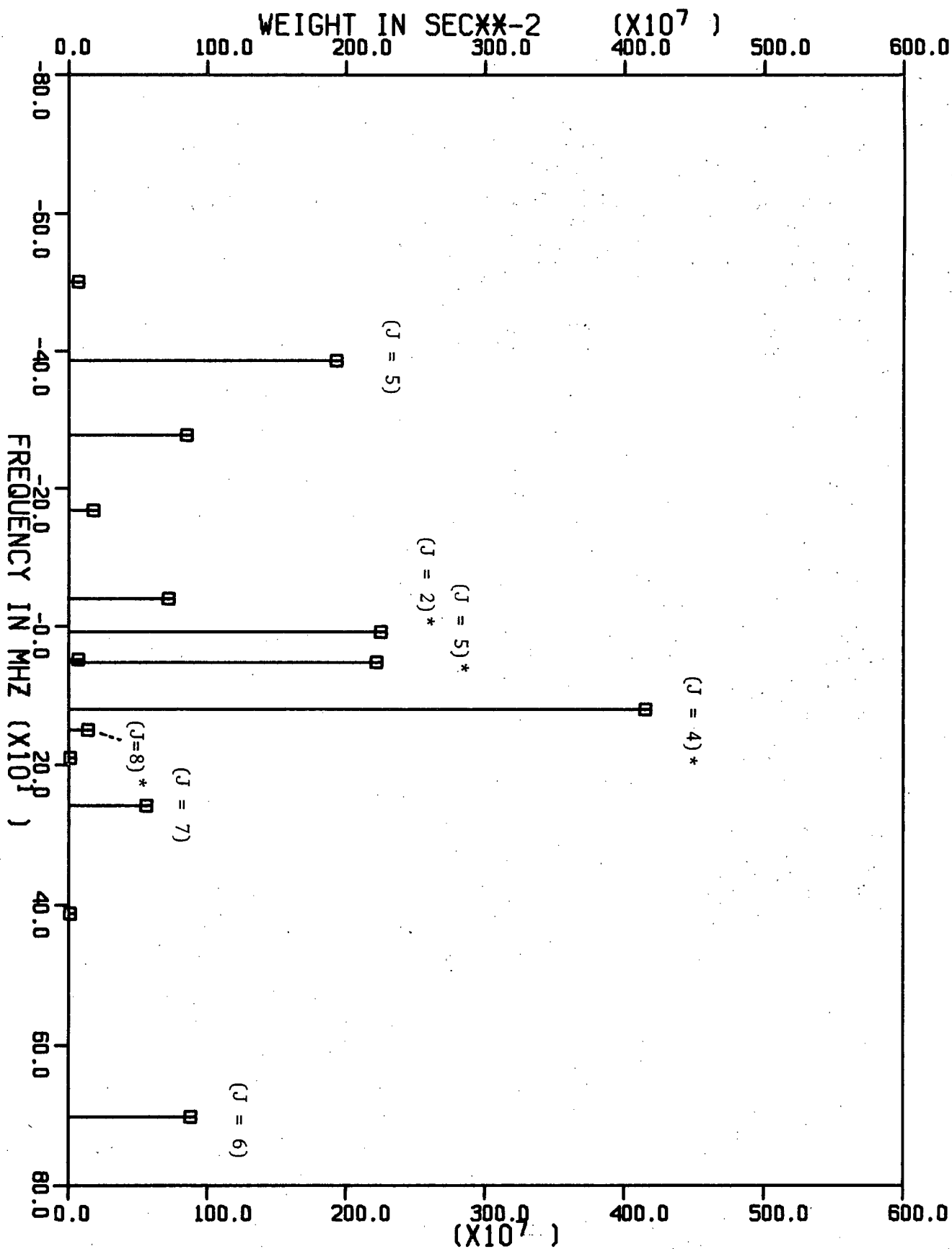
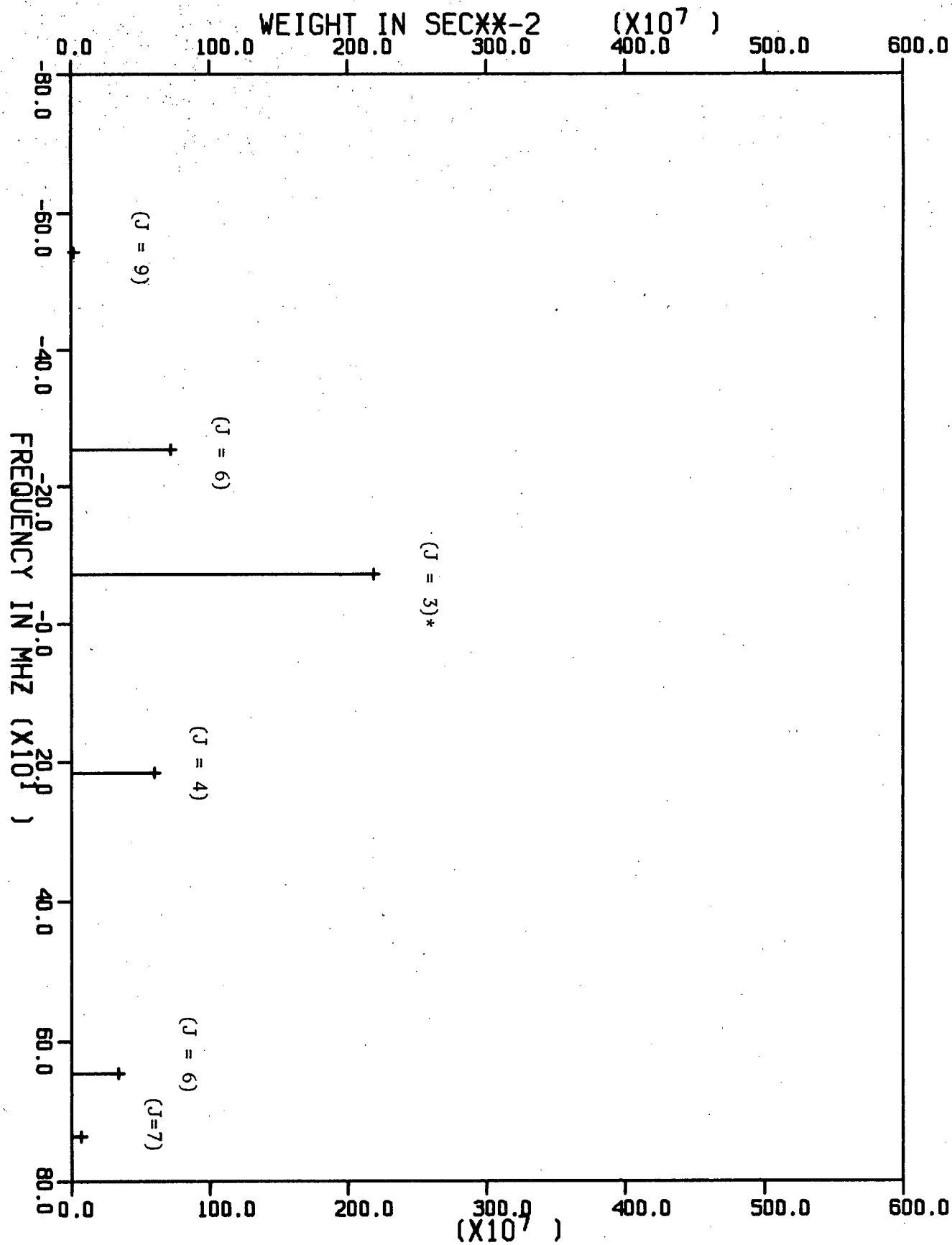Figure G.9. (T = 77K, $\gamma' = E$ and $\gamma = F$)
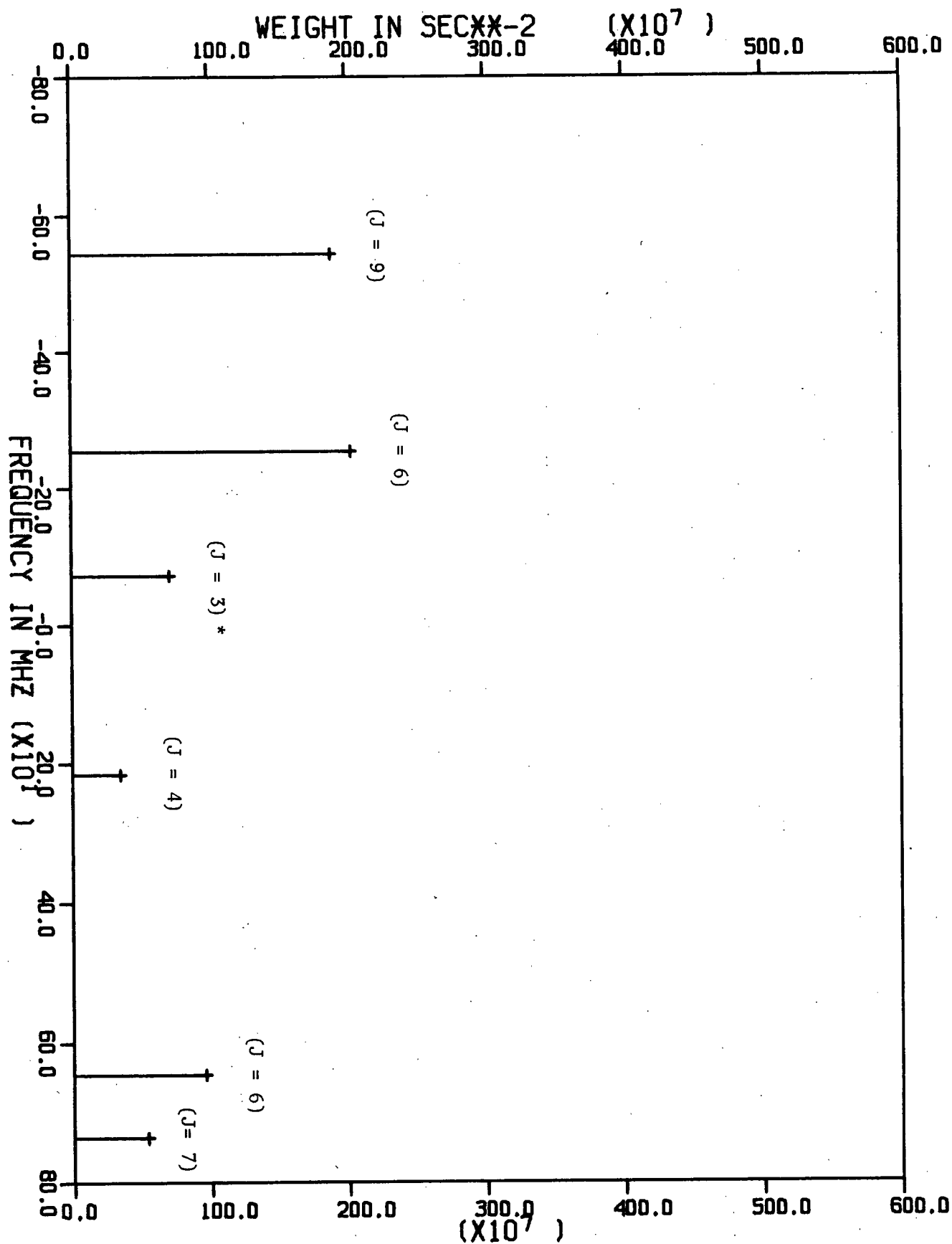
Figure G.10. (T = 295K, γ' = A and γ = F)

Figure G.11. (T = 150K, γ' = A and γ = F)

Figure G.12. (T = 110K, γ' = A and γ =F)

Figure G.13.   (T = 77K, γ' = A and γ = F)

APPENDIX H

Relaxation Matrix Algebra

The values of $\underline{M}$, $\overset{\sim}{\underline{M}}$ and $\underline{\underline{R}}$ in equation 3.9.14 are

$$\underline{M}(t) \quad = \quad \begin{bmatrix} M^{(2)}(t) \\ M^{(1)}(t) \end{bmatrix} \qquad \overset{\sim}{\underline{M}}(t) \quad = \quad \begin{bmatrix} M^{(2)}(\infty) - M^{(2)}(t) \\ M^{(1)}(\infty) - M^{(1)}(t) \end{bmatrix}$$

$$\underline{\underline{R}} \quad = \quad \begin{bmatrix} R^{22} & R^{21} \\ R^{12} & R^{11} \end{bmatrix} \qquad \text{H.1}$$

The superscripts on $\underline{\underline{R}}$ refer to the species of magnetization and should not be confused with the normal procedure for numbering the components of a matrix. Equation H.1 means that there is a basis such that the two magnetizations in this basis decay exponentially.

$$\frac{d}{dt} \underline{N} \quad = \quad \underline{\underline{\lambda}} \, \overset{\sim}{\underline{N}} \qquad \text{H.2}$$

where

$$\underline{N} \quad = \quad \begin{bmatrix} N_\alpha \\ N_\beta \end{bmatrix} \qquad \underline{\underline{\lambda}} \quad = \quad \begin{bmatrix} \lambda_\alpha & 0 \\ 0 & \lambda_\beta \end{bmatrix} \qquad \text{H.3}$$

Equations 3.9.4 and H.2 are related through the matrix $\underline{\underline{\Lambda}}$ defined by

$$\underline{M} \quad = \quad \underline{\underline{\Lambda}} \, \underline{N} \qquad \text{H.4}$$

where

$$\underline{\underline{\Lambda}} \quad = \quad \begin{bmatrix} \Lambda_{2\alpha} & \Lambda_{2\beta} \\ \Lambda_{1\alpha} & \Lambda_{1\beta} \end{bmatrix} \qquad \text{H.5}$$

The matrix $\underline{\underline{\Lambda}}$ is not unitary. It must satisfy the conditions imposed by

$$M^{obs} = M^{(1)} + M^{(2)} = N_\alpha + N_\beta \qquad \text{H.6}$$

which means that its columns must add to unity. The matrix $\underline{\underline{\Lambda}}^{-1}$ satisfies the same criteria. Substituting equation H.4 into equation 3.9.14 and using equation H.2 leads to the condition

$$\underline{\underline{\lambda}} = \underline{\underline{\Lambda}}^{-1} \underline{\underline{R}} \, \underline{\underline{\Lambda}} \qquad \text{H.7}$$

and one then finds $\underline{\underline{\lambda}}$ by solving the normal eigenvalue problem. The solution for a 2 x 2 matrix system is just

$$\lambda_{\alpha,\beta} = \frac{1}{2}(R^{22}+R^{11}) \pm \frac{1}{2}[(R^{22}-R^{11})^2 + 4\, R^{21}R^{12}]^{\frac{1}{2}} \qquad \text{H.8}$$

Although it is not obvious, R^{21} and R^{12} are always the same sign with the result that the λ's are real. The matrix $\underline{\underline{\Lambda}}$ can then be deduced from equation H.7. The solution to equation H.2 is

$$N_i(t) = N_i(\infty) - [N_i(\infty) - N_i(0)]e^{-\lambda_i t} \qquad i = \alpha, \beta$$

and $M^I(t)$ is given by

$$M^I(t) = \sum_{i=\alpha\beta} \Lambda_{Ii}[N_i(\infty) - \{N_i(\infty) - N_i(0)\}\, e^{-\lambda_i t}] \qquad \text{H.10}$$

Using equation H.4 to eliminate N_i gives

$$M^I(t) = \sum_{i=\alpha\beta} \sum_{I'=2,1} \Lambda_{Ii} \Lambda^{-1}_{iI'}[M^{I'}(\infty) - \{M^{I'}(\infty) - M^{I'}(0)\}e^{-\lambda_i t}]$$

$$\text{H.11}$$

In order to obtain the observed magnetization equation H.11 is summed over I and the result is equation 3.9.15.

A numerical example of this matrix algebra is given in the next Appendix where the present theory is compared with the theory that neglects spin symmetry effects.

APPENDIX I

Comparison with the theory of Dong and Bloom

The C_a term of DB (see equation 4.4.1) can be compared directly with the present theory by setting $C_d = 0$. In this case, the functions B, C, D and E in equations 3.8.21 to 3.8.24 are identically zero and the relaxation is exponential with

$$R_1 = 2A'(T:C_a^2) \{ \tfrac{1}{2}j_1(\omega_0) \} \tag{I.1}$$

Using the values of A' in Table 3.11 and evaluating $4\pi^2(C_a{}^2/\alpha)$ in equation 4.4.1, it is found that

$$2A'(T:C_a^2) = \frac{4\pi^2}{\alpha} C_a^2 \tag{I.2}$$

to better than 1.7% at all four temperatures employed in the experiment. The left hand side of equation I.2 is in fact 0.4% smaller than the right hand side at 295 K and 1.6% smaller at 77 K. (see Table 3.11) It is clear that the parameter 2A' should be smaller since it involves numerical summations over J up to a finite J value whereas the DB theory includes J up to J = ∞. The uncertainty in the measured value of C_a (32) does not enter here because the same value is used on both sides of equation I.2.

If C_d is not zero, it is not at all obvious how the two theories should be compared. The most reasonable interpretation of the DB theory is

that it corresponds to assigning all the non-zero frequency terms to zero frequency. One can imagine the factor 4/45 in equation 4.1.1 as correcting for the fact that this process will clearly lead to too great a relaxation rate otherwise. This amounts to keeping all the terms in the present theory but now the expressions E, C and D in equations 3.8.33 to 3.8.35 are greatly simplified. They can now be written (using equation 3.8.25)

$$E(T:C_d^2;m_1'-m_1) \quad = \quad E'(T:C_d^2)[\tfrac{1}{2}j_2\{(m_1'-m_1)\omega_0\}] \tag{I.3}$$

$$C(T:C_d^2;m_1'-m_1) \quad = \quad C'(T:C_d^2)[\tfrac{1}{2}j_2\{(m_2'-m_1)\omega_0\}] \tag{I.4}$$

$$D(T:C_d^2;0-m_1) \quad = \quad D'(T:C_d^2)[\tfrac{1}{2}j_2\{0-m_1)\omega_0\}] \tag{I.5}$$

The functions E', C' and D' are the sums over J, t', t and ρ of $Z(T:C_d^2; \gamma',\gamma,J,t',t,\rho)$. This can be seen by comparing equations I.3 to I.5 with equations 3.33 to 3.35. In this limit, equation 3.9.10 for both I = 1 and 2 is

$$
\begin{aligned}
\frac{dM^2}{dt} \quad = \quad & 2(\tilde{n}_{22}-\tilde{n}_{2-2})[2A'\{\tfrac{1}{2}j_1(\omega_0)\} + 6C'\{\tfrac{1}{2}j_2(\omega_0)\}] \\[2mm]
+ \quad & (\tilde{n}_{21}-\tilde{n}_{2-1})[2A'\{\tfrac{1}{2}j_1(\omega_0)\} + 3C'\{\tfrac{1}{2}j_2(0)\} + 3C'\{\tfrac{1}{2}j_2(\omega_0)\}] \\[2mm]
+ \quad & (\tilde{n}_{11}-\tilde{n}_{1-1})[-12C'\{\tfrac{1}{2}j_2(\omega_0)\} - 3C'\{\tfrac{1}{2}j_2(0)\}]
\end{aligned}
\tag{I.6}
$$

$$\frac{dM^1}{dt} = 2(\tilde{n}_{22} - \tilde{n}_{2-2})[-3C'\{\tfrac{1}{2}j_2(\omega_0)\}]$$

$$+ \quad (\tilde{n}_{21} - \tilde{n}_{2-1})[-3C'\{\tfrac{1}{2}j_2(0)\}]$$

$$+ \quad (\tilde{n}_{11} - \tilde{n}_{1-1})[2A'\{\tfrac{1}{2}j_1(\omega_0)\} + 2B'\{\tfrac{1}{2}j_2(\omega_0)\}$$

$$+ \quad 2E'\{\tfrac{1}{2}j_2(\omega_0)\} + 7C'\{\tfrac{1}{2}j_2(\omega_0)\}$$

$$+ \quad 3C'\{\tfrac{1}{2}j_2(0)\} + D'\{\tfrac{1}{2}j_2(\omega_0)\}] \qquad (I.7)$$

In order to carry this calculation to a meaningful degree we must now limit ourselves to the short correlation time limit in order to equate $j_2(\omega_0)$ and $j_2(0)$ because of the $\Delta m = 0$ terms which arise in the A-f transition probabilities. Thus we assume $\omega_0\tau \ll 1$ which corresponds to densities well above the observed relaxation rate maximum.

With this approximation, equation 3.9.13 (or 3.9.14) can be used with

$$\underline{\underline{R}} = 2A'\{\tfrac{1}{2}j_1(\omega_0)\}\underline{\underline{E}} + \{\tfrac{1}{2}j_2(\omega_0)\}\underline{\underline{Q}} \qquad (I.8)$$

where $\underline{\underline{E}}$ is the unit matrix and $\underline{\underline{Q}}$ is given by

$$\underline{\underline{Q}} = \begin{bmatrix} 6C' & -15C' \\ -3C' & 2B' + 2E' + 10C' + D' \end{bmatrix} \qquad (I.9)$$

The functions C', D' and E' have been evaluated numerically both in absolute units (S^{-2}) and in units of $(4/45)$ $(4\pi^2/\alpha)C_d^2$ and appear in Table I.1 A' and B' have also been evaluated in units of $(4\pi^2/\alpha)C_a^2$ and $(4/45)(4\pi^2/\alpha)C_d^2$ respectively and are given in Table 3.11. It is interesting to note the functions C' and D' are almost proportional to temperature. (i.e., they are almost constant when expressed in DB units). The terms B' + E' should now be regarded as a single term because they both correspond to I' = 1 → I = 1 transitions and they are both zero frequency. Because one decreases with temperature (in DB units) and the other increases with temperature, the sum does not vary much with temperature. The result is, that if we express equation I.8 in DB units we have

$$\underline{\underline{R}} \quad = \quad \frac{4\pi^2}{\alpha} C_a^2 \{\tfrac{1}{2}j_1(\omega_0)\}\underline{\underline{E}} + \frac{4}{45} \frac{4\pi^2}{\alpha} C_d^2 \{\tfrac{1}{2}j_2(\omega_0)\}\underline{\underline{S}} \tag{I.10}$$

where, to a good approximation $\underline{\underline{S}}$ is temperature independent

$$\underline{\underline{S}} \quad \sim \quad \begin{bmatrix} 2 & -5 \\ -1 & 5 \end{bmatrix} \tag{I.11}$$

Solving the eigenvalue problem, we find that eigenvalues of $\underline{\underline{S}}$ are about 6 and 0.8. Further, the matrix $\underline{\underline{\Lambda}}^{-1}$ is approximately,

$$\underline{\underline{\Lambda}}^{-1} \quad \sim \quad \begin{bmatrix} 0.03 & -0.1 \\ 0.97 & 1.1 \end{bmatrix} \tag{I.12}$$

TABLE I.1 TABULATION OF C', D' AND E'

Temp. (K)	x $10^8 S^{-2}$			x $\frac{4}{45} \frac{4\pi^2}{\alpha} C_d^2$		
	$C'(T:C_d^2)$	$D'(T:C_d^2)$	$E'(T:C_d^2)$	$C'(T:C_d^2)$	$D'(T:C_d^2)$	$E'(T:C_d^2)$
295	154	615	35.1	0.329	1.310	0.0749
150	78.1	305	13.2	0.327	1.279	0.0551
110	57.5	219	7.28	0.329	1.250	0.0416
77	41.2	146	3.02	0.336	1.192	0.0247

$$C_a = 10.4 \pm .1 \text{ kHz} ; \quad C_d = 18.5 \pm .5 \text{ kHz} \quad (32)$$

This is an interesting result because equation I.12 implies that there is

a magnetization

$$N_\alpha \quad \sim \quad (0.03)M^{(2)} + (-0.1)M^{(1)} \qquad (I.13)$$

that relaxes with the rate

$$\lambda_\alpha \quad \sim \quad \frac{4\pi^2}{\alpha} C_a^2 \{½j_1(\omega_0)\} + [6] \frac{4}{45} \frac{4\pi^2}{\alpha} C_d^2 \{½j_2(\omega_0)\} \quad (I.14)$$

and the other magnetization

$$N_\beta \quad \sim \quad (0.97)M^{(2)} + (1.1)M^{(1)} \qquad (I.15)$$

decays with the rate

$$\lambda_\beta \quad \sim \quad \frac{4\pi^2}{\alpha} C_a^2 \{½j_1(\omega_0)\} + [0.8] \frac{4}{45} \frac{4\pi^2}{\alpha} C_d^2 \{½j_2(\omega_0)\}$$

$$(I.16)$$

We note, using equations 3.9.17 and 3.9.18 that to within 2% the equilibrium

value of N_α is zero and the equilibrium value of N_β is M^{obs}. Thus it is

clear that the observed relaxation rate is given by equation I.16.

It is actually quite surprising that the theory of nuclear spin

relaxation which includes spin symmetry agrees so well with the theory of Dong and Bloom in the limit that all the centrifugal distortion transitions are assumed to be zero. The reason that it is surprising is because this process does not really neglect spin symmetry. The process described here is only a special case of the spin symmetry theory.

For completeness, we note that in numerically solving an eigenvalue problem, great care must be taken in order that round-off errors do not accumulate. The actual matrices and vectors used in equations I.11 and I.12 are as follows. At 295 K, $\underline{\underline{S}}$ and $\underline{\underline{\Lambda}}^{-1}$ are

$$\underline{\underline{S}} \;=\; \begin{bmatrix} 1.974 & -4.935 \\ -0.987 & 5.110 \end{bmatrix} \;;\quad \underline{\underline{\Lambda}}^{-1} \;=\; \begin{bmatrix} 0.0281 & -0.1216 \\ 0.9719 & 1.1216 \end{bmatrix} \quad (I.17)$$

The eigenvalues of $\underline{\underline{S}}$ are 6.249 and 0.835. At 77 K $\underline{\underline{S}}$ and $\underline{\underline{\Lambda}}^{-1}$ are

$$\underline{\underline{S}} \;=\; \begin{bmatrix} 2.016 & -5.040 \\ -1.008 & 5.205 \end{bmatrix} \;;\quad \underline{\underline{\Lambda}}^{-1} \;=\; \begin{bmatrix} 0.0307 & -0.1329 \\ 0.9792 & 1.1329 \end{bmatrix} \quad (I.18)$$

and the eigenvalues of $\underline{\underline{S}}$ are 6.371 and 0.850. In actual fact then, the agreement is better, in that the factor 0.8 in equation I.16 ranges from 0.835 at 295 K to 0.850 at 77 K.

The result of this comparison may very well be interesting but

the neglect of the centrifugal distortion frequencies is not justified.

We indicate this by fitting equation 4.4.2 to our present data in Figures

I.1 to I.6. These fits are made to agree at the high densities. If

the region near the R_1 maximum were fit, the fits would be just as poor.

They would, in fact be very similar to the bottom plots in Figures 4.25, 4.26

and 4.27. If equation 4.4.1 is used with $\tau_1 \neq \tau_2$ instead of equation

4.4.2, the fits are equally as poor. This is discussed extensively

elsewhere (25). DB were able to fit their 295 K data to equation 4.4.2

mainly because the data was less precise. This is also discussed ex-

tensively in reference (25). (see also the discussion in Section 2.4)

To put it in purely mathematical terms, the data simply can

not be fit by a single Lorentzian function (i.e. $j(\omega)$) centered around

zero frequency nor can it be fit by a sum of two Lorentzians of different

width ($\tau_1 \neq \tau_2$) both of which are centered around zero frequency.
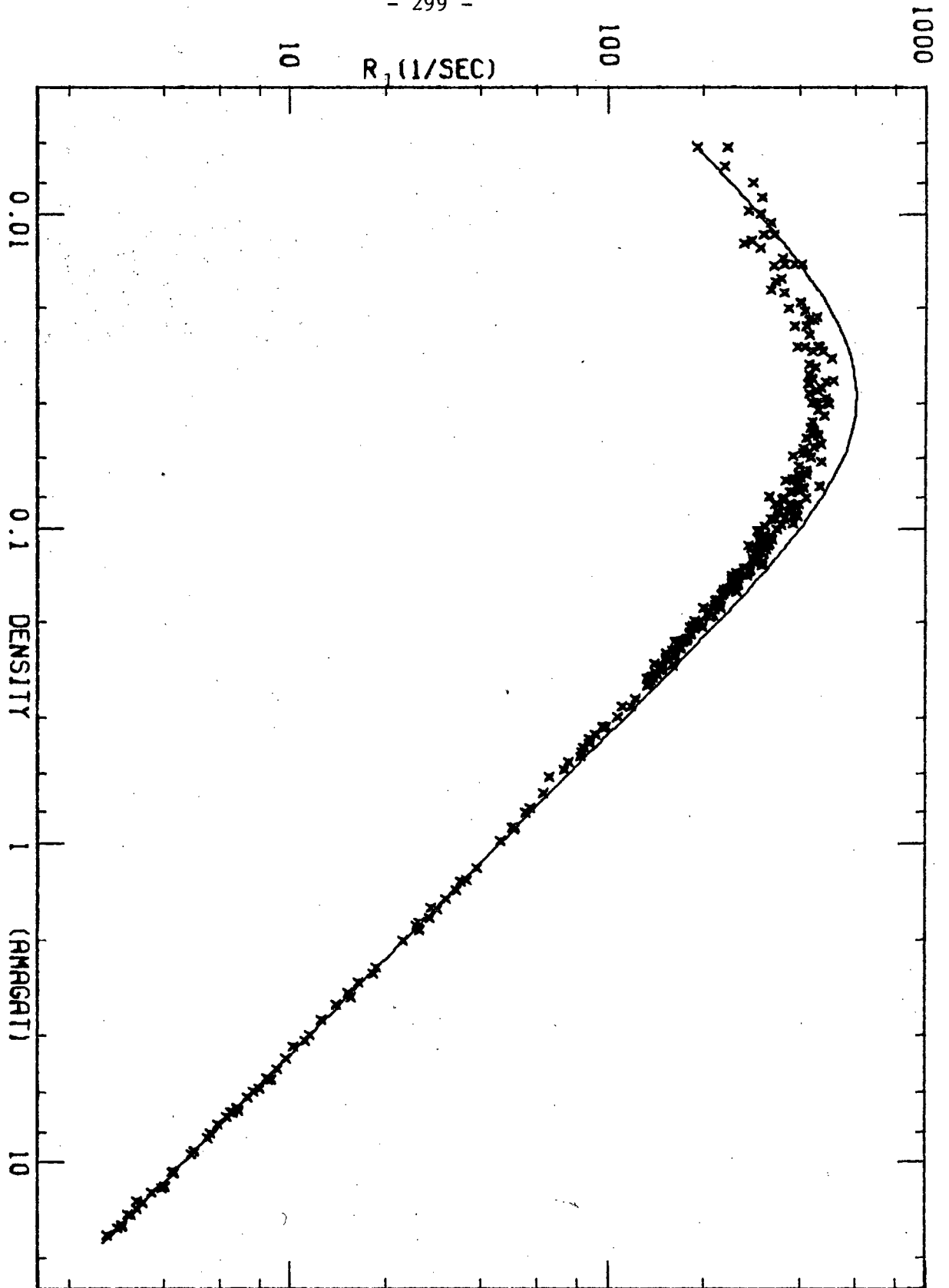
Figure I.1. A plot of R_1 vs ρ for 295K. The parameter in the theoretical line is $(R_1\rho)_{LIM}$ = 45.8 amagat/sec.
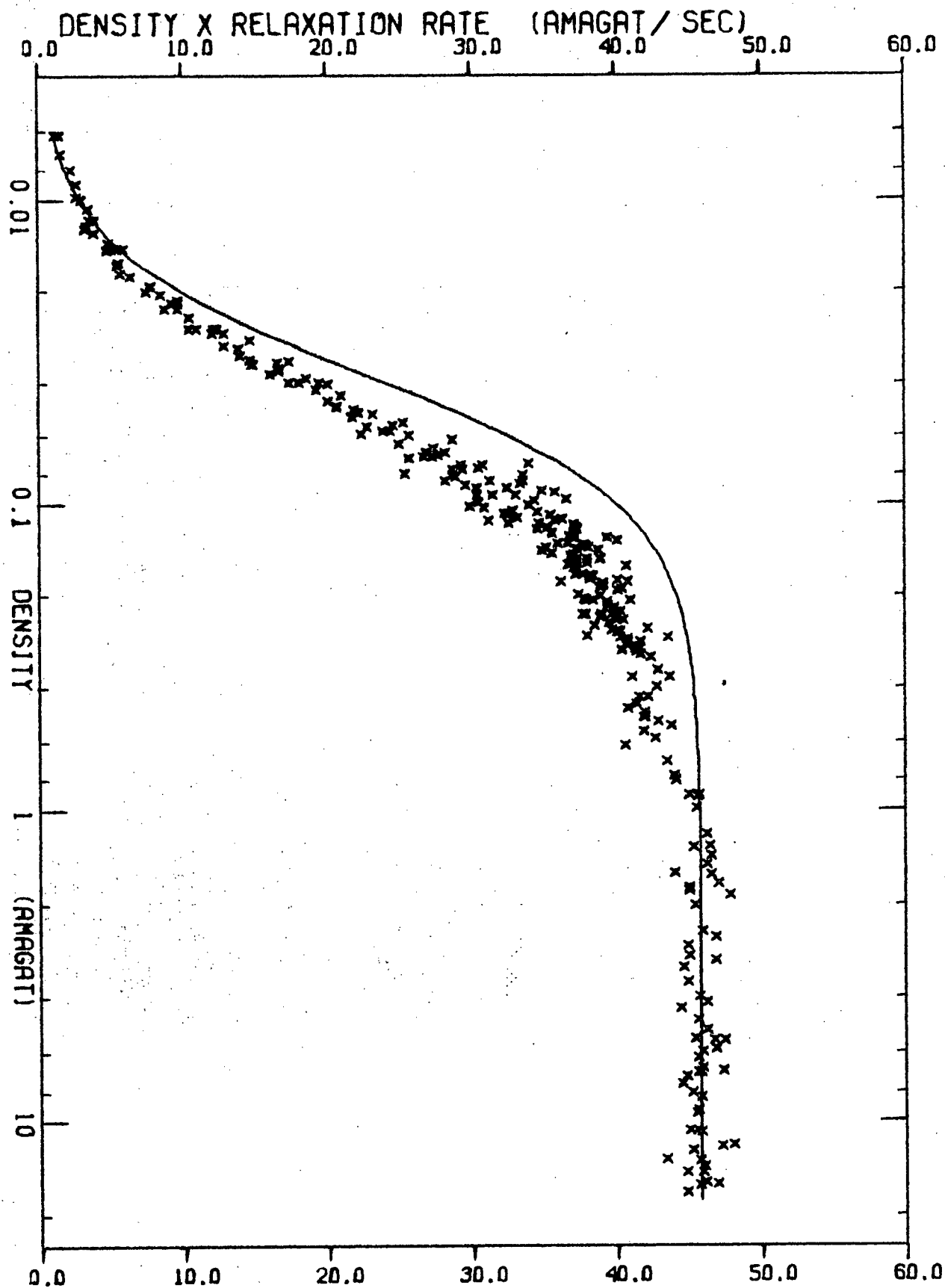
Figure I.2. A plot of $R_1\rho$ vs ρ for 295K. The parameter in the theoretical line is $(R_1\rho)_{LIM}$ = 45.8 amagat/sec.
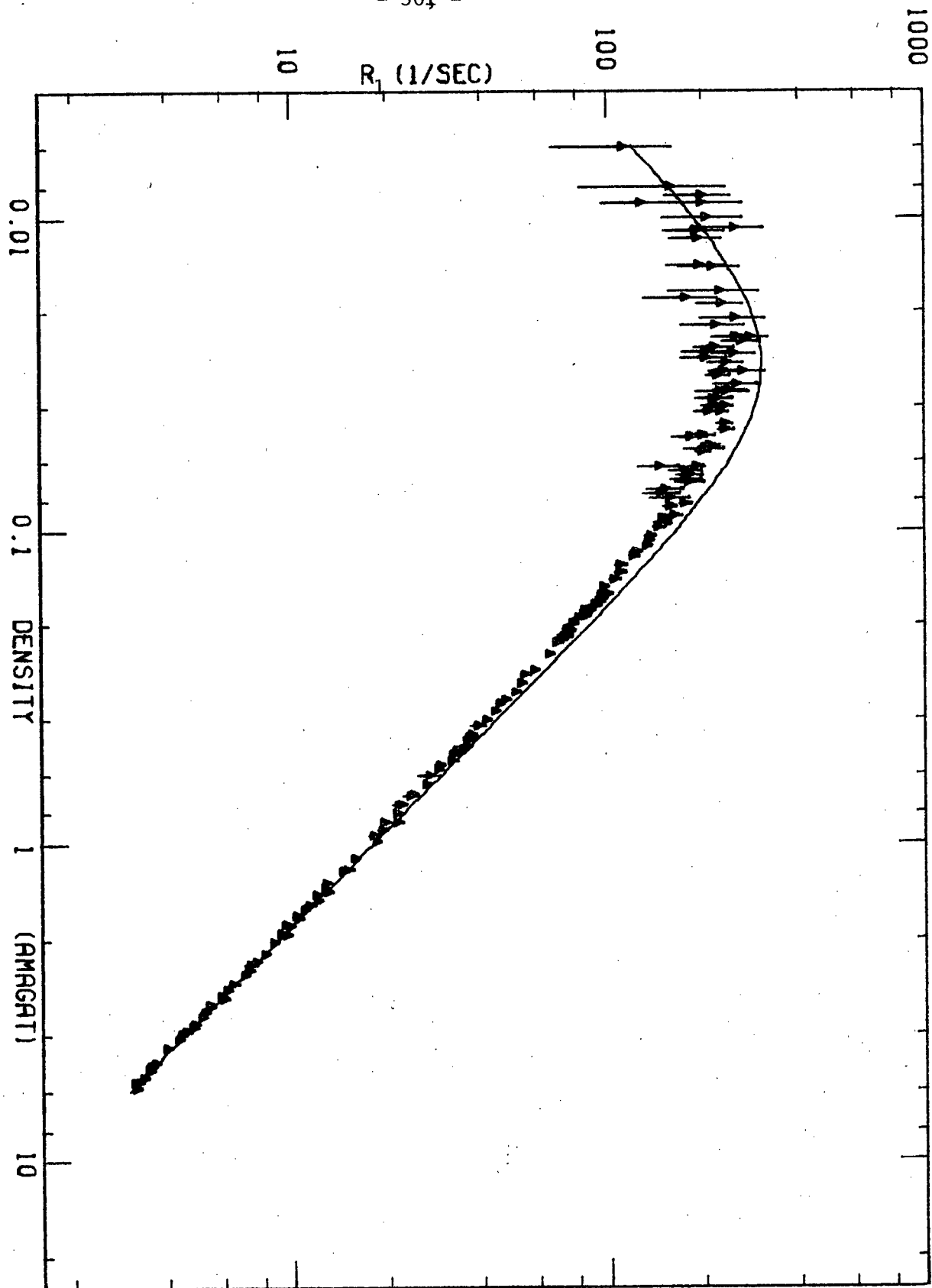
Figure I.3. A plot of R_1 vs ρ for 150K. The parameter in the theoretical line is $(R_1\rho)_{LIM}$ = 17.9 amagat/sec.
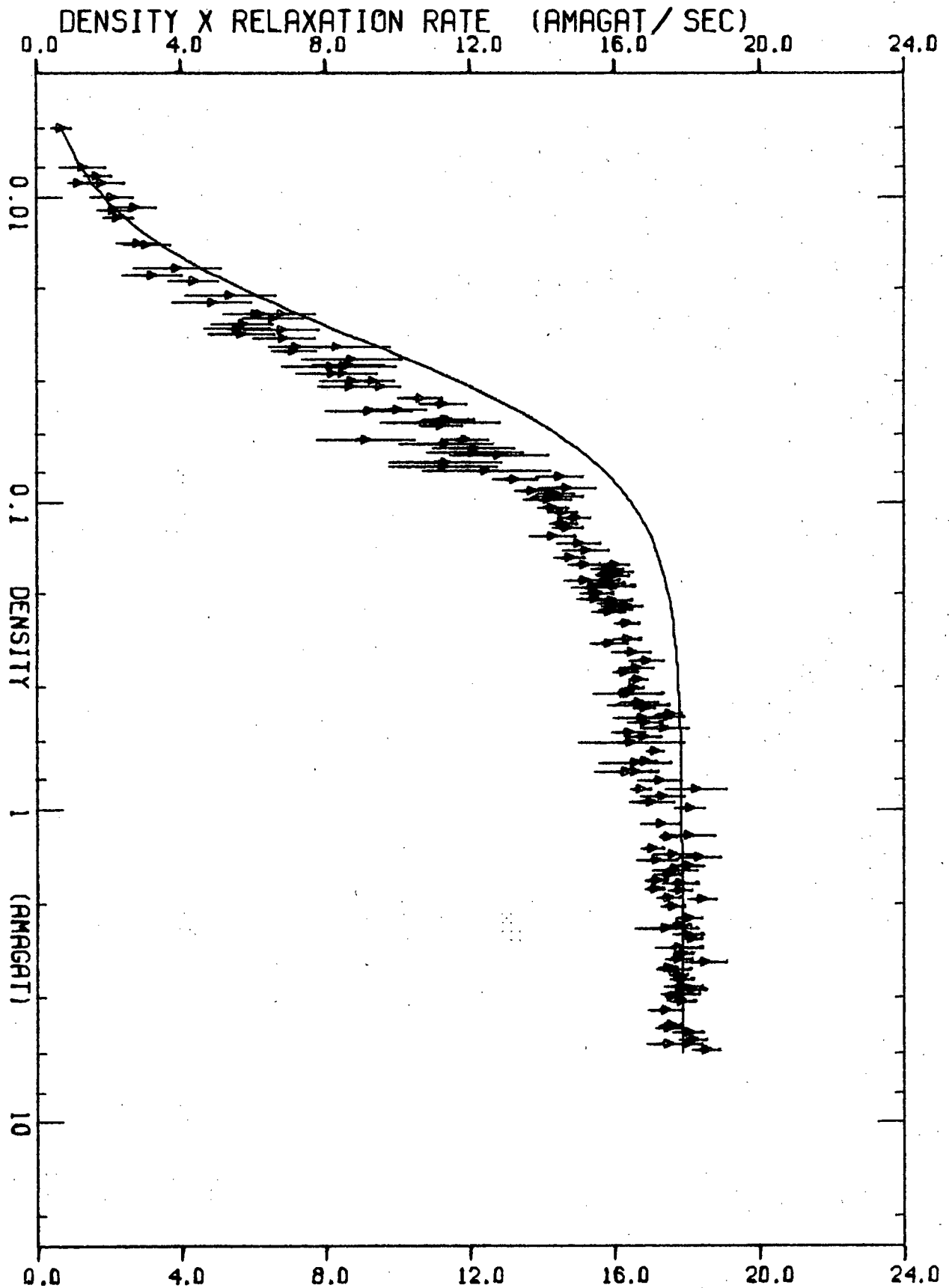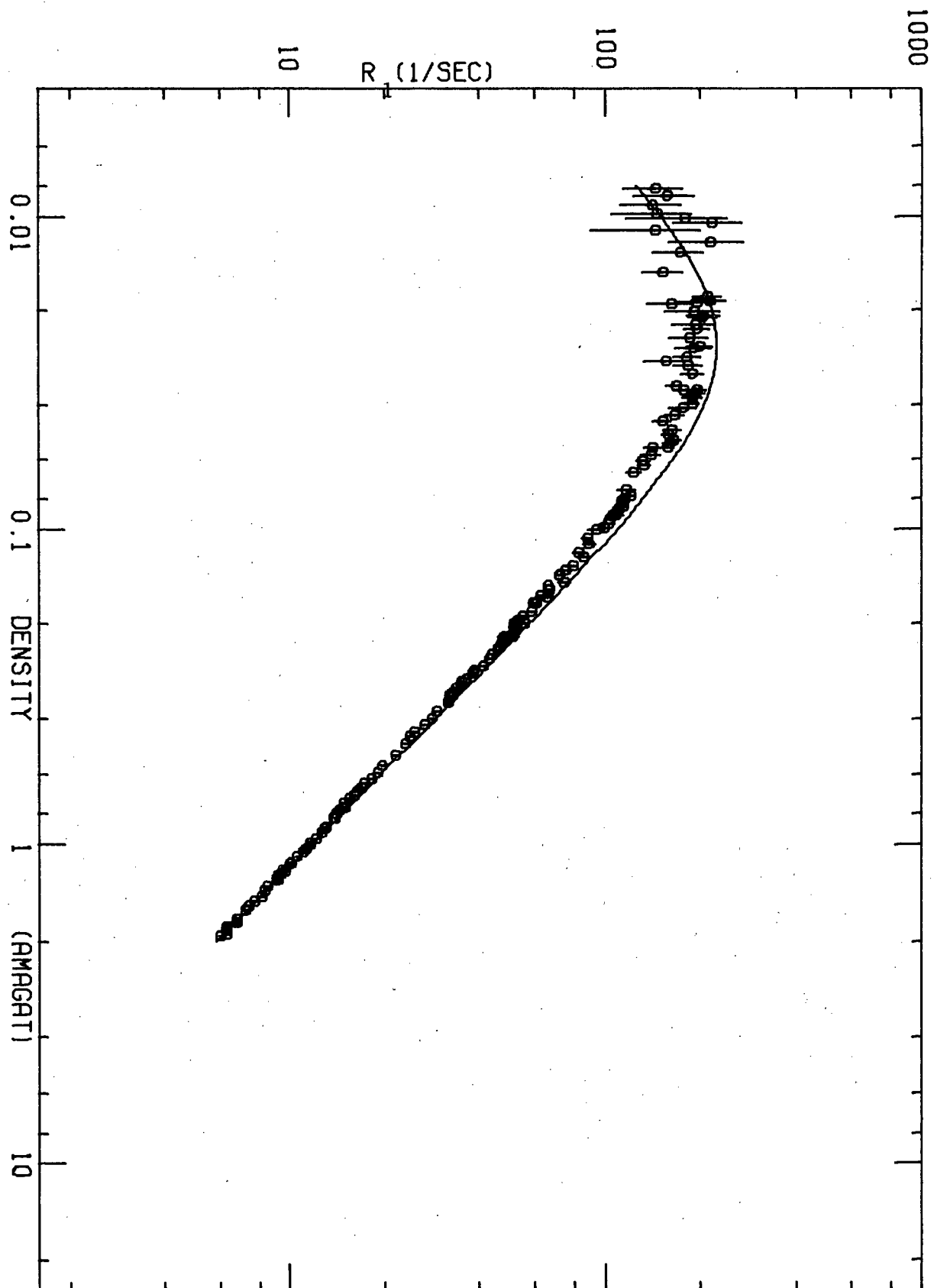
Figure I.4. A plot of ρR_1 vs ρ for 150K. the parameter in the theoretical line is $(R_1\rho)_{LIM} = 17.9$ amagat/sec.

Figure I.5. A plot of R_1 vs ρ for 110K. The parameter in the theoretical line is $(R_1\rho)_{LIM}$ = 11.6 amagat/sec.
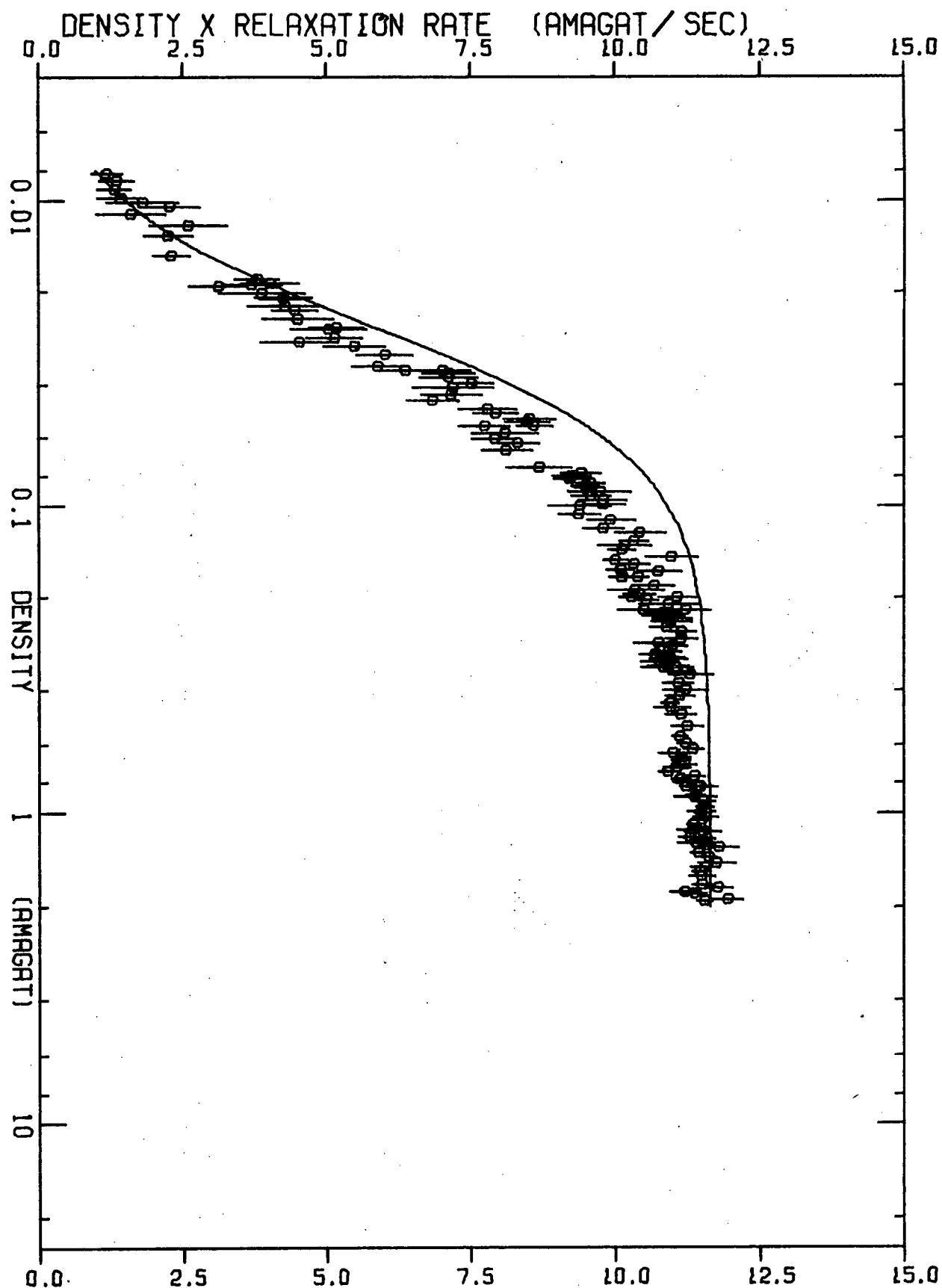
Figure I.6. A plot of ρR_1 vs ρ for 110K. The parameter in the theoretical line is $(R_1\rho)_{LIM}$ = 11.6 amagat/sec.

APPENDIX J

Numerical Fits of the 30 MHz Measurements

J.1   Fitting Procedure

The normal fitting procedure for comparing experimental results with theoretical predictions involves the various methods of least squares. The numerical calculations involved for each determination of R_1 are both complicated and relatively expensive in terms of computer dollars. Because of the vast range in density employed in the experiments, this procedure must be performed for between about 30 (77 K) and 100 (295 K) densities equally spaced on a logarithmic scale. This must be done for each numerical fit at each temperature. The reason for requiring this many density values is a practical one. The plots presented in this thesis were generated by a Calcomp Plotter on line to the I.B.M. 370/168 computer. The pen movements employed in this plotter are "quantized" and if the $\Delta \log \rho$ units employed are too large, the effect is noticeable. As discussed in the text, the fitting procedure involves estimating values for the parameter or parameters in the theory and converging on a best fit on the basis of previous fits.

J.2   Values of ρ_1 for the Single Parameter Fits

We can obtain an estimate for the accuracy to which ρ_1 can be determined from Figures 4.9 to 4.11. At 110 K, (Figure 4.9) the fits for

ρ_1 5% smaller and larger than the best fit are clearly outside the limit of the standard deviation one would obtain from a least squares fit of the region above the R_1 maximum. In fact, neither line goes through any of the 71 high density points $(0.22 < \rho < 2.1$ amagat) and both go through on about six of the 71 error bars. We will ascribe an error of 3% to the value of $\rho_1 = 0.0275$ amagat at 110 K. This would be close to, or somewhat larger than, one standard deviation. Using similar procedures, we ascribe an error of 4% to the value of $\rho_1 = 0.031$ amagat at 150 K. This is based on Figure 4.10. On the basis of Figure 4.11, it is extremely difficult to ascribe an error to ρ_1 at 295 K because of the poorness of fit. The error on $\rho_1 = 0.04$ would, however, be less than about 10%. These values are summarized in equation 4.6.2.

J.3   Two Parameter Fits

As discussed in Section 4.6.1 (ii), the two parameter fits with N = 0 for T = 110 and 150 K result in a poorer agreement between theory and experiment than do the one parameter fits with N = 0 and $\delta = 1$. Figures J.1 (110 K) and J.2 (150 K) show fits for $\tau_2 = 0.5 \tau_1$ ($\delta = 0.5$) and Figures J.3 (110K) and J.4 (150 K) for $\tau_2 = 0.75 \tau_1$ ($\delta = 0.75$), all for three choices of ρ_1. The equivalent fits for 295 K are presented and discussed in Section 4.6.1 (ii).

Only at 295 K were two parameter fits performed with δ fixed at unity. These are presented in Figures J.5, J.6, J.7, J.8, 4.22 and J.9 for N = 2, 1, 0.5, -0.5, -1, and -2 respectively, each for 3 values of ρ_1.
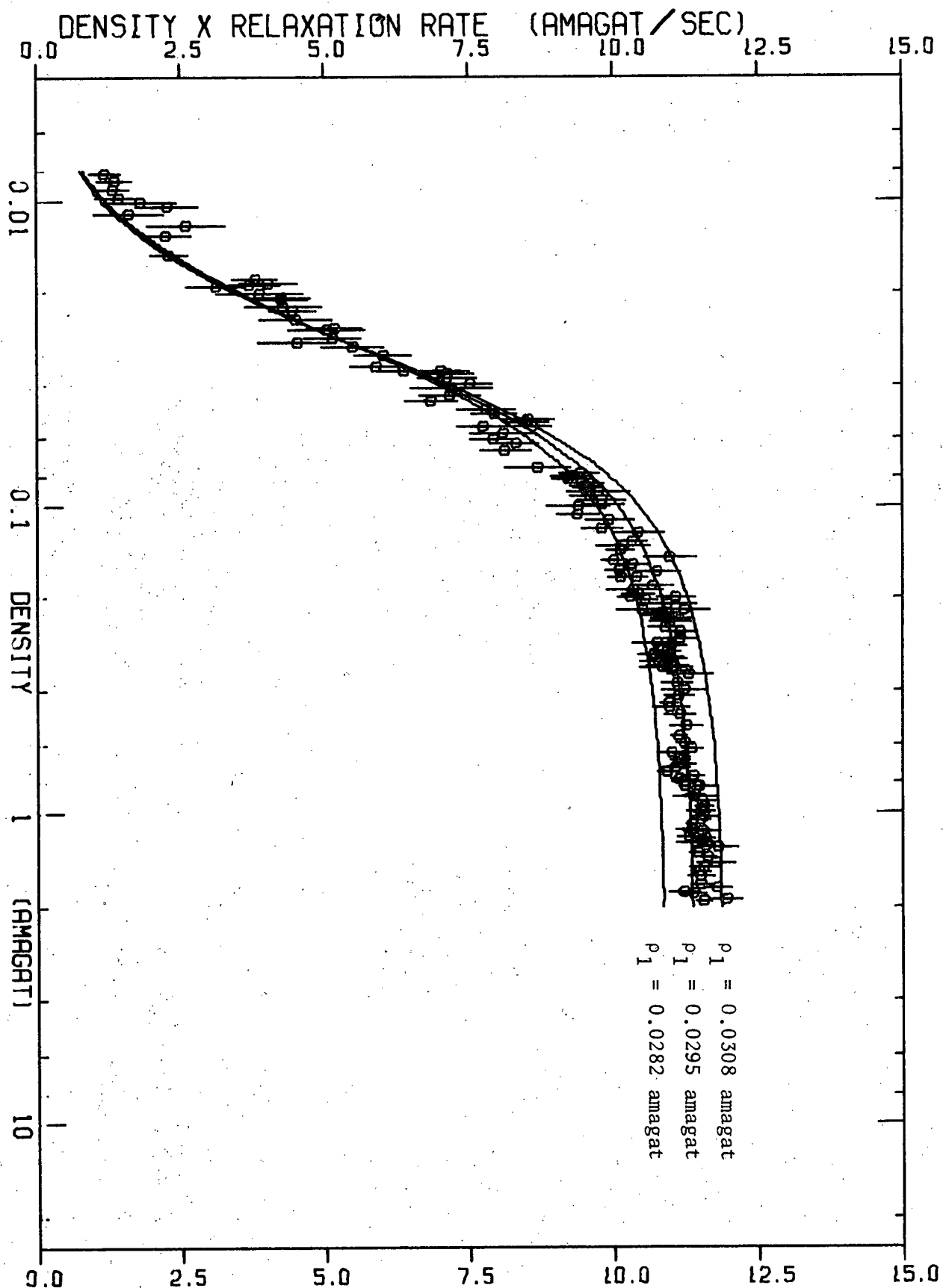
Figure J.1. A plot of ρR_1 vs ρ for 110K. The parameters in the theoretical are $\delta = 0.5$, $N = 0$ and ρ_1 as indicated.

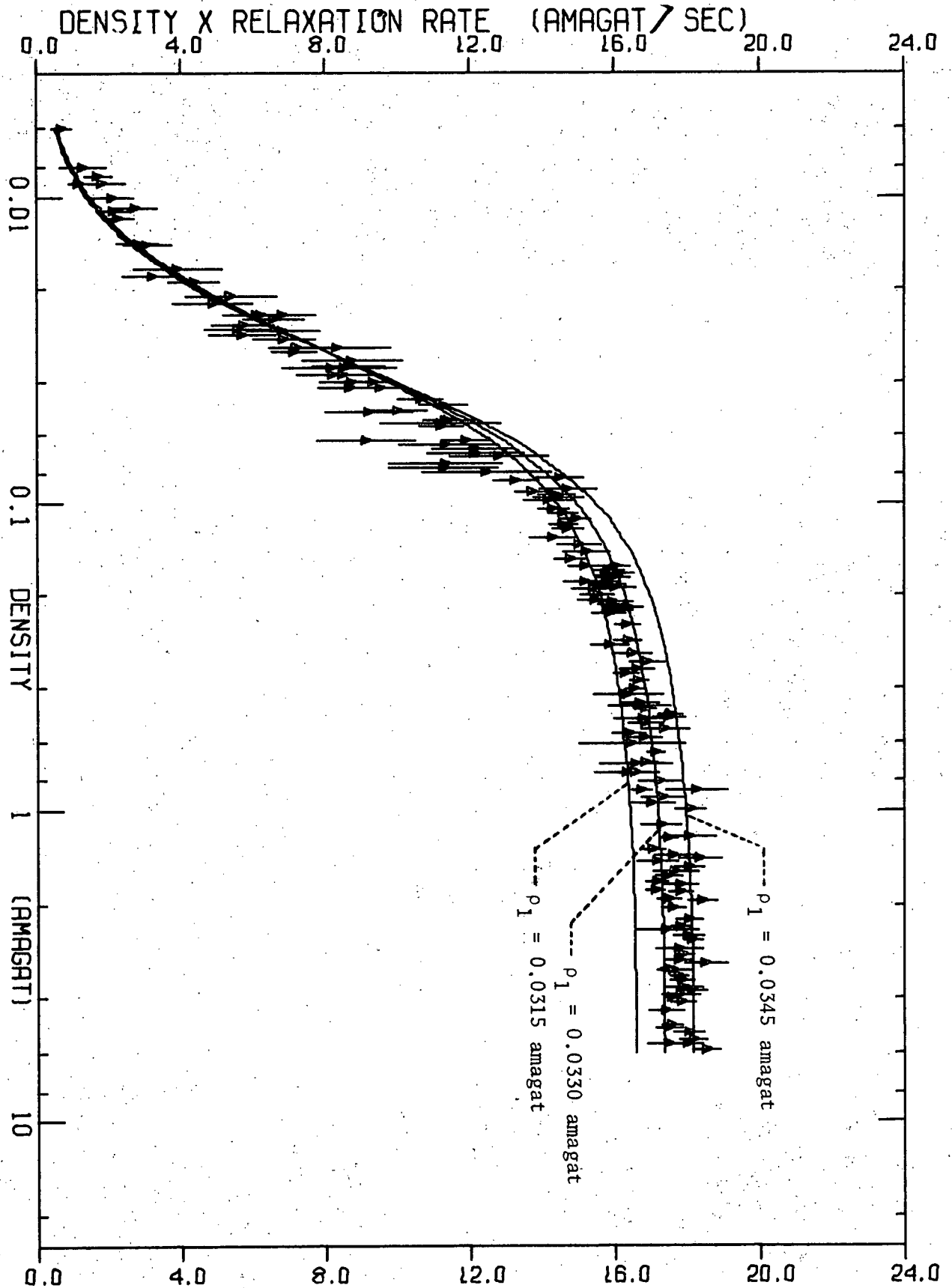Figure J.2 A plot of ρR_1 vs ρ for 150K. The parameters in the theoretical line are $\delta = 0.5$, $N = 0$ and ρ_1 as indicated.
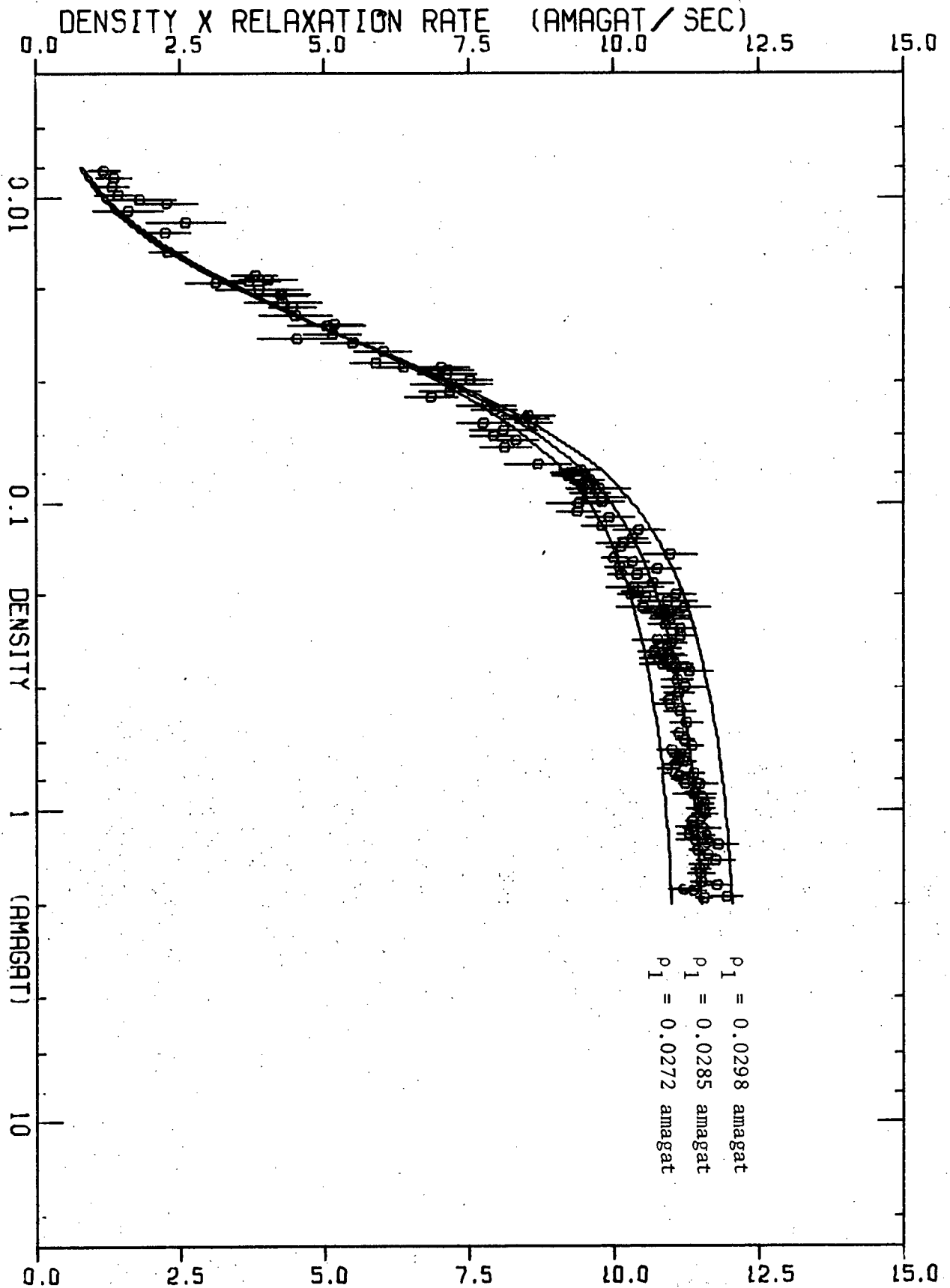
Figure J.3. A plot of ρR_1 vs ρ for 110K. The parameters in the theoretical
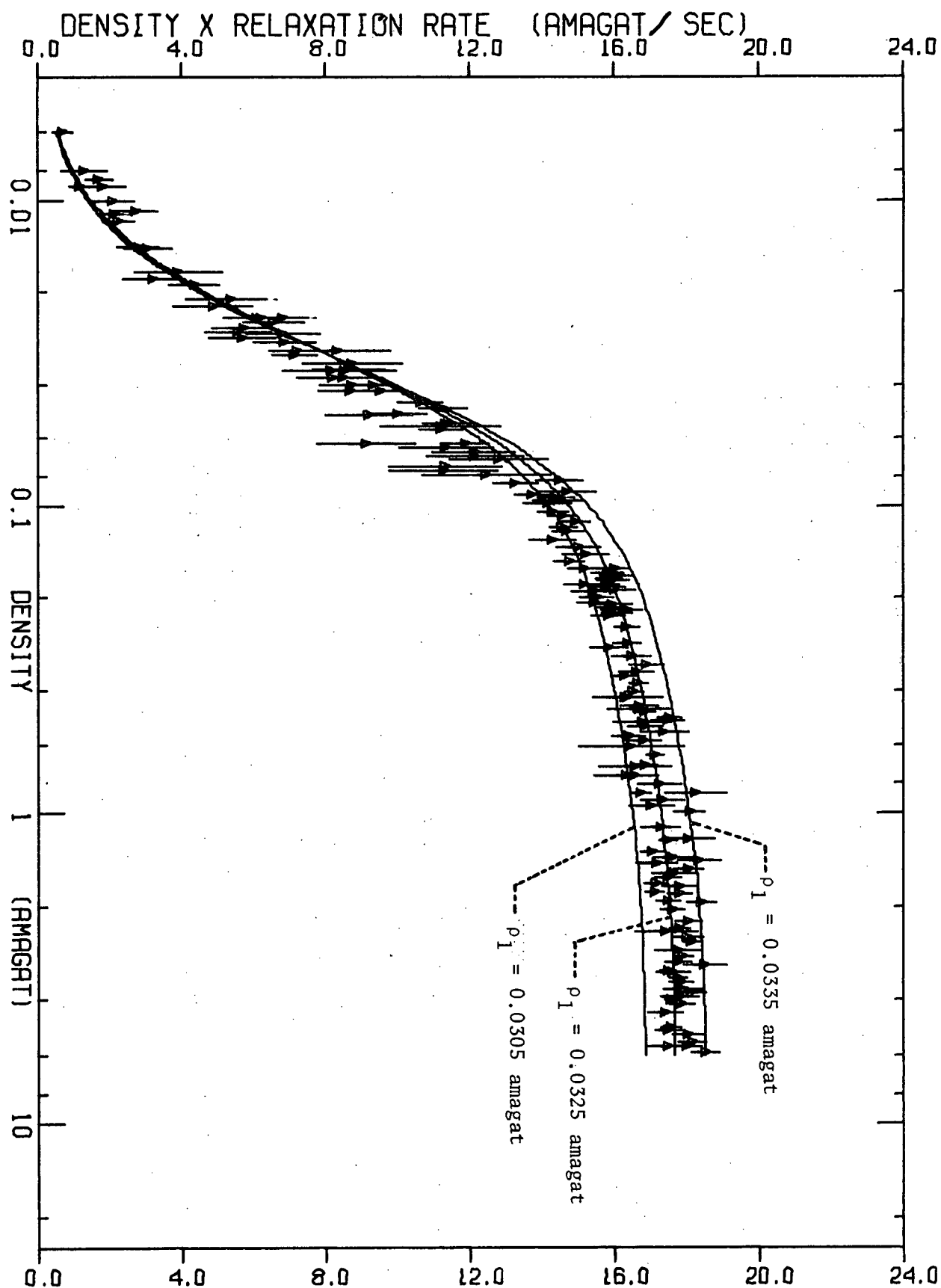line are $\delta = 0.75$, $N = 0$ and ρ_1 as indicated.

Figure J.4. A plot of ρR_1 vs ρ for 150K. The parameters in the theoretical line are $\delta = 0.75$, $N = 0$ and ρ_1 as indicated.
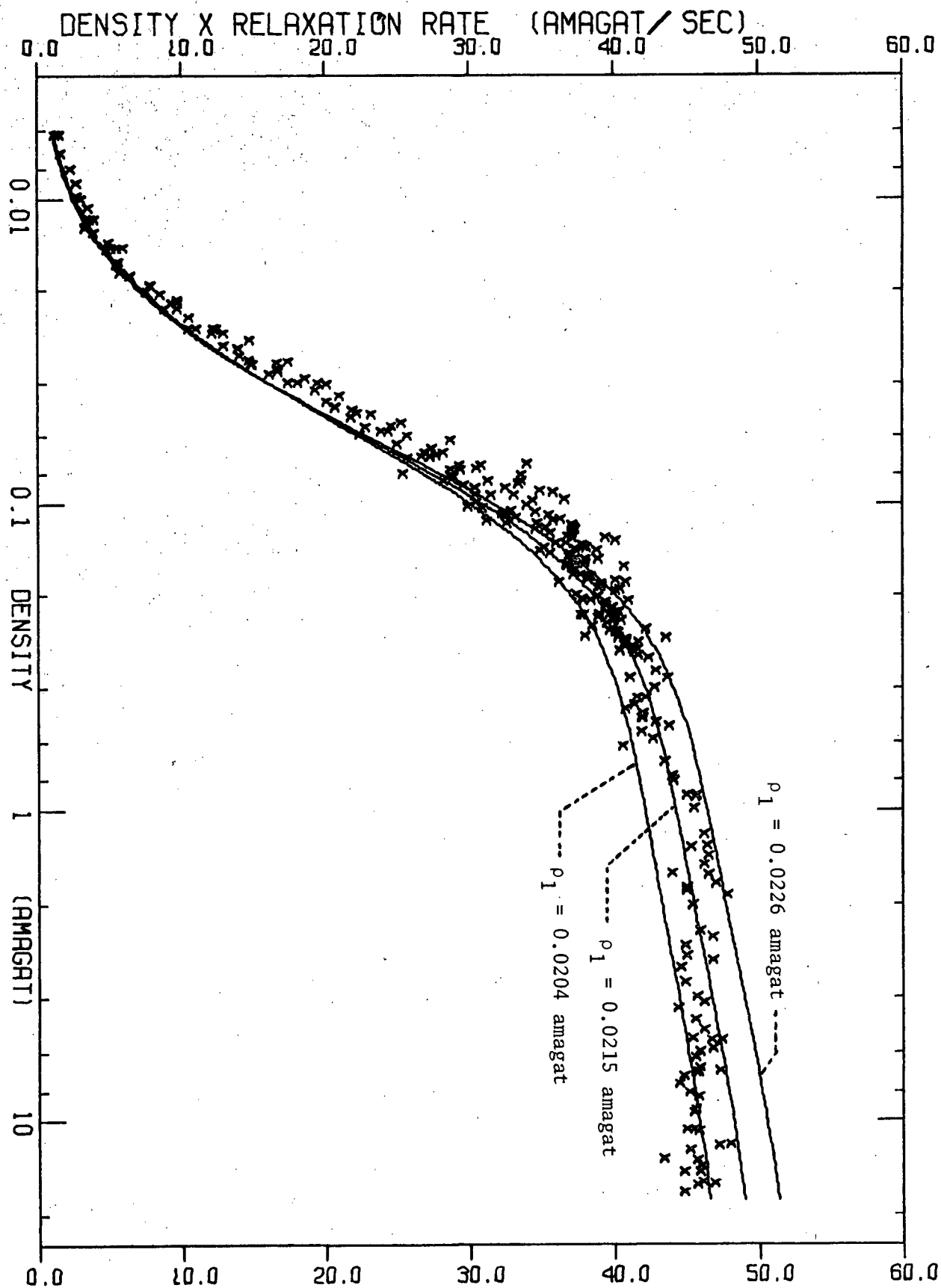
Figure J.5. A plot of ρR_1 vs ρ for 295K. The parameters in the theoretical line are $\delta = 1$, $N = 2$ and ρ_1 as indicated.
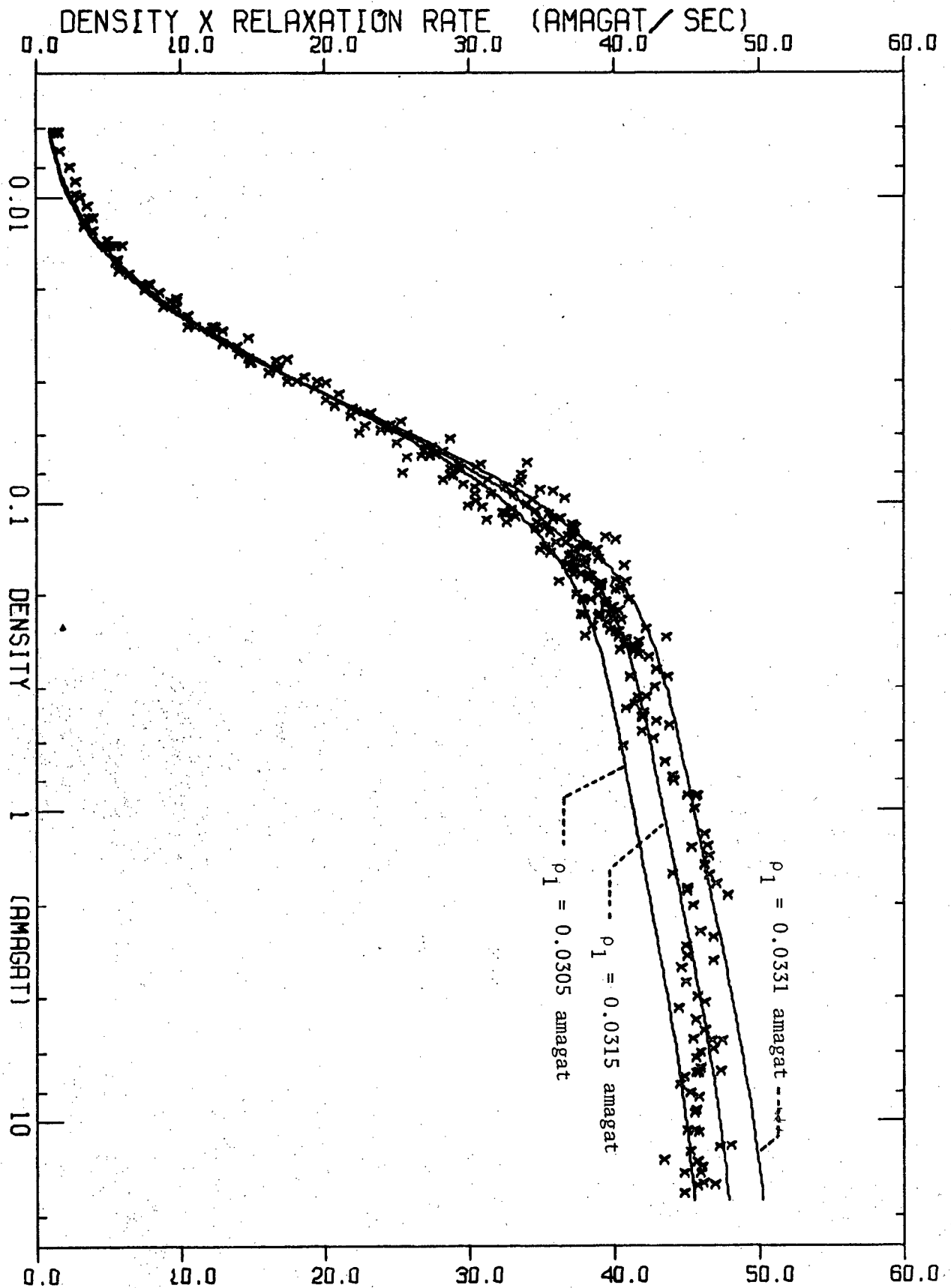
Figure J.6. A plot of ρR_1 vs ρ for 295K. The theoretical parameters are $\delta = 1$, $N = 1$ and ρ_1 as indicated.

Figure J.7. A plot or ρR_1 vs ρ for 295K. The parameters in the theoretical line are $\delta = 1$, $N = 0.5$ and ρ_1 as indicated.
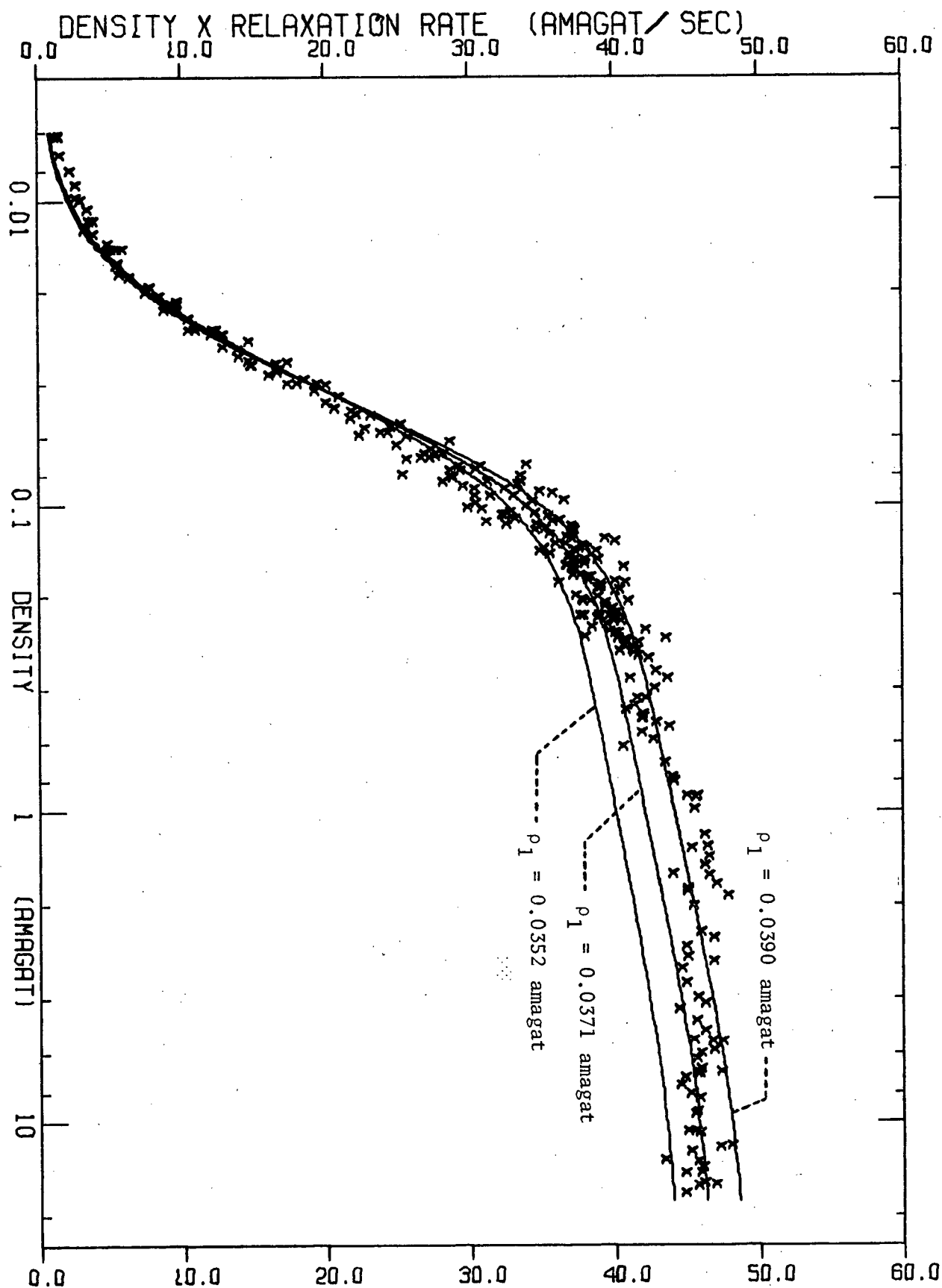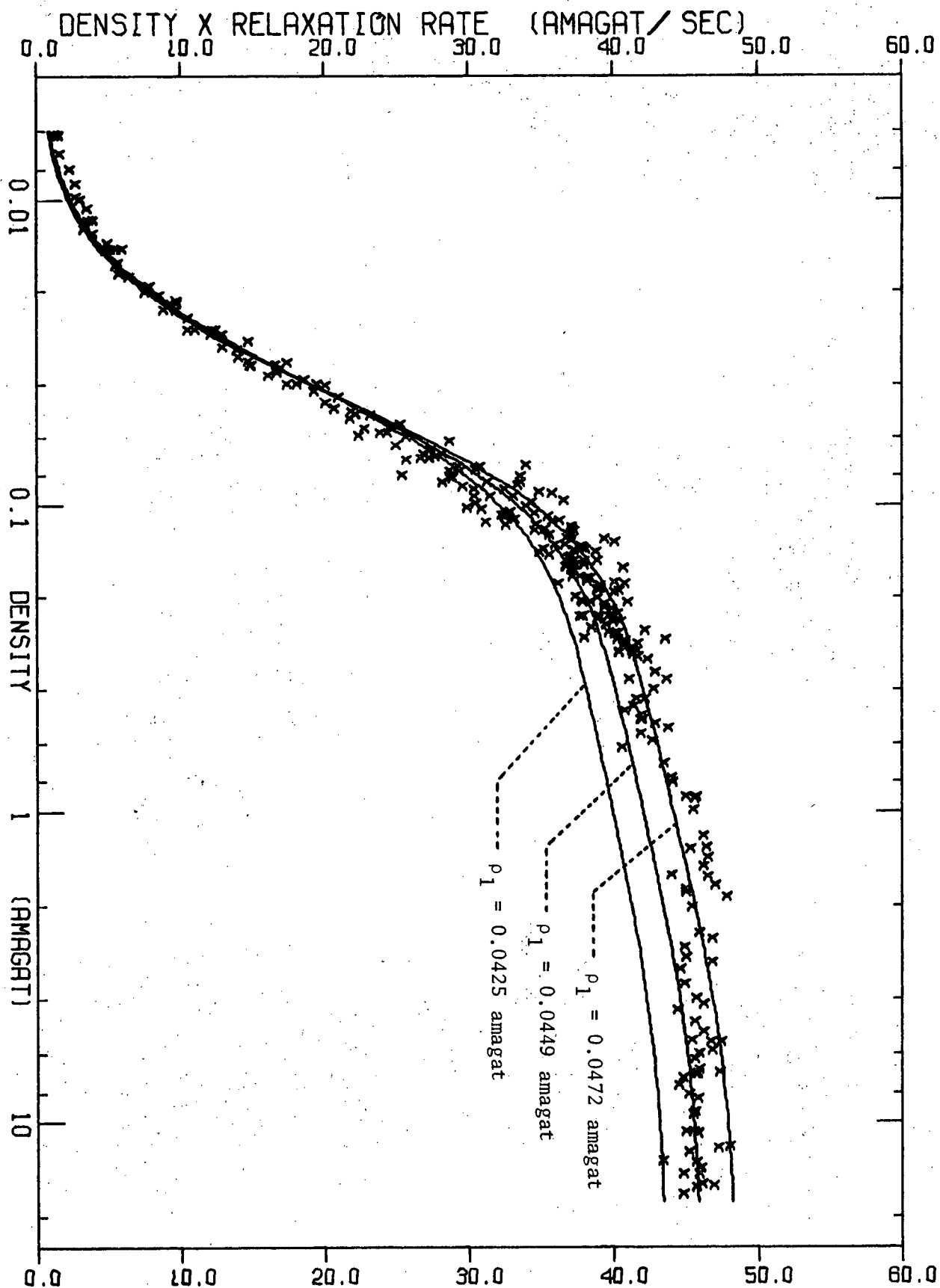
Figure J.8. A plot of ρR_1 vs ρ for 295K. The parameters in the theoretical line are $\delta = 1$, $N = -0.5$ and ρ_1 as indicated.
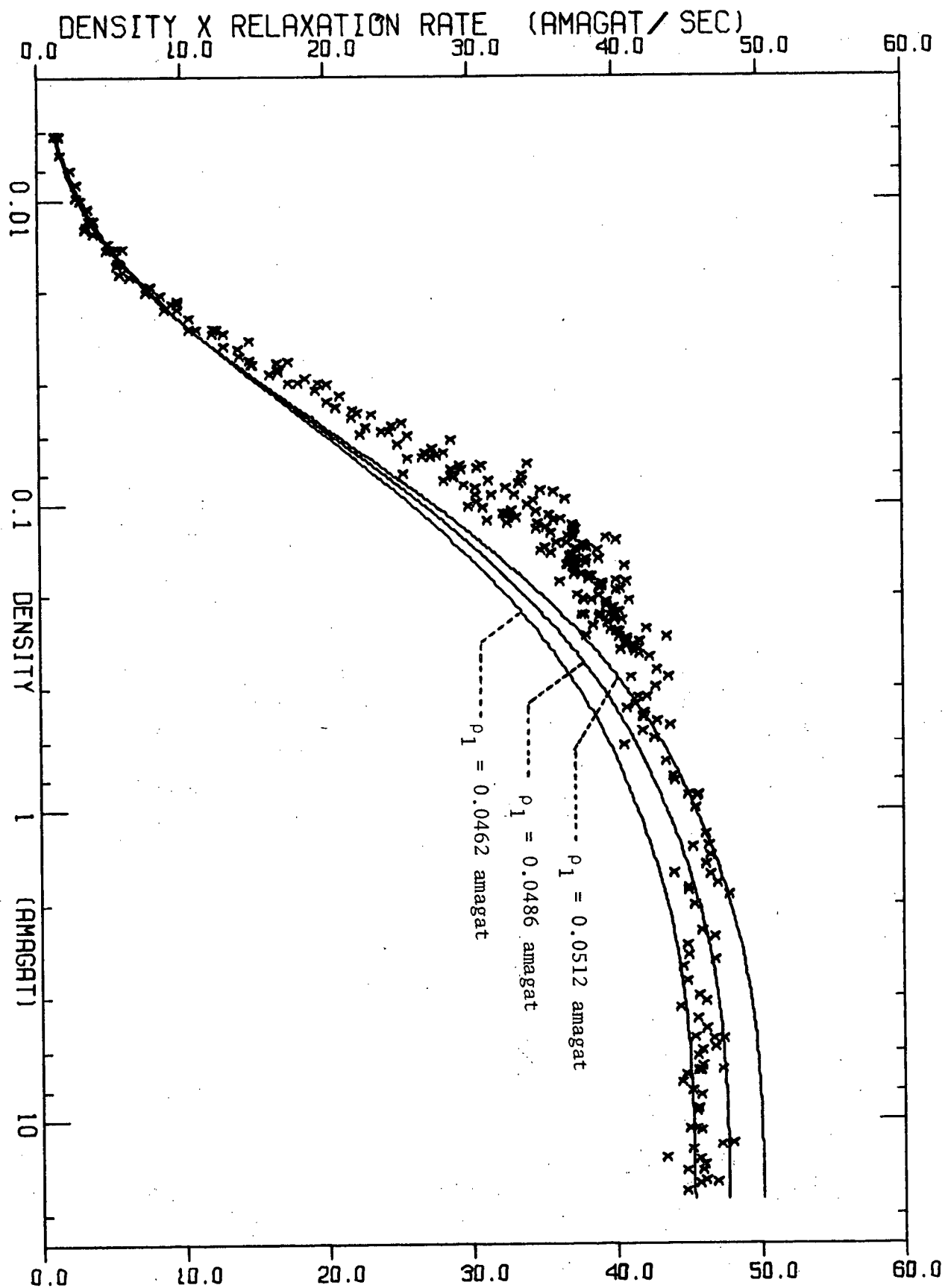
Figure J.9. A plot of ρR_1 vs ρ for 295K. The parameters in the theoretical line are $\delta = 1$, $N = -2$ and ρ_1 as indicated.

BIBLIOGRAPHY

1   Leonas, V.B., and Sermygin , A.V. 1973 Chem. Phys. $\underline{2}$, 462.

2   Shizgal, B. 1973 J. Chem. Phys. $\underline{58}$, 3424.

3   Chapman, R.N. and Richards , M.G. 1974 Phys. Rev. Lett. $\underline{33}$, 18.

4   Beckmann, P.A., Burnell, E.E., Lalita, K., Armstrong, R.L., Kisman, K.E. and McCourt, F.R. 1972 Phys. Rev. A $\underline{60}$, 1684.

5   Hardy, W.N. 1966 Can. J. Phys. $\underline{44}$, 265.

6   Kisman, K.E. and Armstrong, R.L. 1974 Can. J. Phys. $\underline{52}$, 1555.

7   Lalita, K., Bloom, M. and Noble, J.D. 1969 Can. J. Phys. $\underline{47}$, 1355.

8   Bloom, M. and Oppenheim, I. 1963 Can. J. Phys. $\underline{41}$, 1580.

9   Bloom, M. and Oppenheim, I. 1967 Advances in Chem. Phys. Vol. 12, edited by J. Hirschfelder, Interscience publishers, New York.

10   Armstrong, R.L. and Courtney, J.A. 1972 Can. J. Phys. $\underline{50}$, 1262.

11   Armstrong, R.L. and Courtney, J.A. 1969 J. Chem. Phys. $\underline{51}$, 457.

12   Armstrong, R.L. and Hanrahan, T.A.J. 1968 J. Chem. Phys. $\underline{49}$, 4777.

13   Courtney, J.A. 1971 Ph.D. Thesis, U. Toronto, unpublished.

14   Dong, R.Y. 1969 Ph.D. Thesis, U.B.C., unpublished.

15   Dong, R.Y. and Bloom, M. 1968 Phys. Rev. Lett. $\underline{20}$, 981.

16   Dong, R.Y. and Bloom, M. 1970 Can. J. Phys. $\underline{48}$, 793.

17   Hinshaw, W.S. and Hubbard, P.S. 1971 J. Chem. Phys. $\underline{54}$, 428.

18   Sanctuary, B.C. 1971 Ph.D. Thesis, U.B.C., unpublished.

19   Sanctuary, B.C. 1974 Can. J. Phys. $\underline{52}$, 387.

20   Waugh, J.S. 1972 Advances in Mol. Rel. Processes $\underline{3}$, 315.

21   Armstrong, R.L. and Tward, E. 1968 J. Chem. Phys. $\underline{48}$, 332.

22   Courtney, J.A. and Armstrong, R.L. 1972 Can. J. Phys. 50, 1252.

23   Mohanty S. and Bernstein, H.J. 1970 J. Chem. Phys. 53, 461.

24   Beckmann, P.A. 1971 M.Sc. Thesis, U.B.C., unpublished.

25   Beckmann, P.A., Bloom, M. and Burnell, E.E. 1972 Can. J. Phys. 50, 251.

26   Bloom, M., Bridges, F. and Hardy, W.N. 1967 Can. J. Phys. 45, 3533.

27   Bloom, M. and Dorothy, R. 1967 Can. J. Phys. 45, 3411.

28   Gerritsma, C.J., Oosting, P.H. and Trappeniers, N.J. 1971 Physica 51, 381.

29   Lalita, K. 1974 Can. J. Phys. 52, 876.

30   Lalita, K. and Bloom, M. 1971 Chem. Phys. Lett. 8, 285.

31   Rajan, S., Lalita, K. and Babu, S.V. 1974 J. Mag. Res. 16, 115.

32   Yi, P., Ozier, I. and Ramsey, N.F. 1971 J. Chem. Phys. 55, 5215.

33   Yi, P., Ozier, I. and Anderson, C.H. 1968 Phys. Rev. 165, 92.

34   Fox, K. 1972 Phys. Rev. A 6, 907.

35   Hecht, K.T. 1960 J. Mol. Spectros. 5, 355.

36   Hecht, K.T. 1960 J. Mol. Spectros. 5, 390.

37   Hougen, J.T. to be published, MTP Int. Rev. Sci., Phys. Chem., Series Two, Spec., ed. D.A. Ramsey.

38   Jahn, H.A. 1938 Proc. Roy. Soc. (London) Ser. A. 168, 469.

39   Kirschner, S.M. and Watson, J.K.G. 1973 J. Mol. Spectros. 47, 347.

40   Michelot, F., Moret-Bailly, J. and Fox, K. 1974 J. Chem. Phys. 60, 2606.

41   Ozier, I., Yi, P., Khosla, A. and Ramsey, N.F. 1970 Phys. Rev. Lett. 24, 642.

42   Holt, C.W., Gerry, M.C.L. and Ozier, I. 1973 Phys. Rev. Lett. 31, 1033.

43   Husson, N. and Dang Nhu, M. 1971 J. Phys. 32, 627.

44   Rosenberg, A., Ozier, I. and Kudian, A.K. 1972 J. Chem. Phys. 57, 568.

45   Tarrango, G. Dang Nhu, M. and Paussigue, G. 1974 J. Mol.
            Spectros. 49, 322.

46   Curl, R.F., Jr., 1973 J. Mol. Spectros. 48, 165.

47   Curl, R.F., Jr., and Oka, T. 1973 J. Chem. Phys. 58, 4908.

48   Vehara, K., Sakurai, K. and Shimoda, K. 1969 J. Phys. Soc.
            Jpn. 26, 1018.

49   Hougen, J.T. 1971 J. Chem. Phys. 55, 1122.

50   American Petroleum Institute Research Project 44. 1957.

51   Gordon, R.G. 1965 J. Chem. Phys. 42, 3658.

52   Gordon, R.G. 1966 J. Chem. Phys. 45, 1635.

53   Oka, T. 1972 Mémoires Société Royale des Sciences de Liège, 6,
            37.

54   Black, J.H. 1974 Nature, 248, 319.

55   Pasachoff, J.M. and Fowler, W.A. 1974 Sci. Amer. 230, 108.

56   Reeves, H. 1974 Nature, 248, 398.

57   Evenson, K. M., Wells, J.S., Peterson, F.R., Danielson, B.L., Day,
            G.W., Barger R.L. and Hall, J.L. 1972 Phys. Rev. Lett., 29, 1346.

58   Evenson, K.M. N.B.S., Boulder, Colorado, private communication.

59   Anderson, C.H. and Ramsey, N.F. 1966 Phys. Rev. 149, 14.

60   Fox, K. 1970 J. Quant. Spectros. Radiative Transfer 10, 1835.

61   Hougen, J.T. 1973 J. Mol. Spectros. 46, 490.

62   Code, R.F. and Noble, J.D. 1972 J. Chem. Phys. 57, 2160.

63   Van Hecke, P., Grobet, P. and Van Gerven, L. 1972 J. Mag. Res.
            7, 117.

64   Van Hecke, P. and Van Gerven, L. 1973 Physica. 68, 359.

65   Wong, K.P., Noble, J.D., Bloom, M. and Alexander, S. 1969
            J. Mag. Res. 1, 55.

66   Glättli, H., Sentz, A. and Eissenkremer, M. 1972 Phys. Rev. Lett.
            28, 871.

67   Alexander, S. and Lerner-Naor, M. 1972 Can. J. Phys. 50, 1568.

68   Bloom, M. 1971 Proc. IVth Int. Symp. N.M.R., Israel.

69   de Witt, G.A. and Bloom, M. 1969 Can. J. Phys. 47, 1195.

70   Abragam, A. 1961   The principles of nuclear magnetism,
            Oxford University Press, London.

71   Pegg, D.T. 1973 J. Phys. B, 6, 246.

72   Slichter, C.P. 1963 Principles of magnetic resonance,
            Harper and Row, New York.

73   Rhim, A., Pines, A. and Waugh, J.S. 1971 Phys. Rev. B, 3, 684.

74   Muller, B. and Bloom, M. 1960 Can. J. Phys. 38, 1318.

75   Murday, J.S. 1973 J. Mag. Res. 10, 111.

76   Bloch, F. 1946 Phys. Rev. 70, 460.

77   Bloembergen, N., Purcell, E.M. and Pound, E.M. 1948 Phys. Rev.
            73, 679.

78   Hahn, E. L. 1950 Phys. Rev. 80, 580.

79   Guyer, R.A., Richardson, R.C. and Zane, L.I. 1971 Rev. Mod. Phys.
            43, 532.

80   Hardy, W.N. 1964 Ph.D. Thesis, U.B.C., unpublished.

81   Clark, W.G. 1964 Rev. Sci. Instrum., 35, 316.

82   Pegg, D.T. 1973 J. Phys. B, 6, 241.

83   Rhiel, J.W. 1966 Ph.D. Thesis M.I.T., unpublished.

84   Gerritsma, C.J. and Trappeniers, N.J. 1971 Physica, 51, 365.

85   Solomon, I. 1972 unpublished lecture notes, Ecole Polytech-
            nique; translated by W. N. Hardy.

86   Hardy, W.N. private communication.

87   Bull, T.E. 1974 Rev. Sci. Instrum. 45, 232.

88   Bloom, M. 1972 M.T.P. International Reviews of Science,
            Butterworths, London; edited by
            C.A. McDowell.

89   Kumar, A. and Johnson, C.S. 1972 J. Mag. Res. 7, 55.

90   Pausak, S. and Waugh, J.S. 1974 J. Chem. Phys. 61, 2165.

91   Courtney, J.A., private communication.

92   Okazaki, E.A. and Fowler, J.K. 1969 Library programmes for the
            A.E.C.L. G-20 computer, CRT-1149, Part B.

93   Rose, M.E. 1953 Phys. Rev. 91, 610.

94   Moore, W.S. and Yalcin, T. 1973 J. Mag. Res. 11, 50.

95   Zemansky, M.W. 1957 Heat and thermodynamics, McGraw Hill,
        Toronto.

96   Redfield, A.G. 1957 I.B.M. Journal 1, 19.

97   Zussman, A. and Alexander, S. 1968 J. Chem. Phys. 49, 5179.

98   Hubbard, P.S. 1958 Phys. Rev. 109, 1153.

99   Gordon, R.G. 1968   Advances in Mag. Res. Vol. 3 edited by
        J.S. Waugh, Academic Press, New York.

100   Schiff, L.I. 1968 Quantum mechanics, McGraw Hill, New York.

101   Alekseyev, V., Grasuik, A., Ragulsky, V., Sobelman, I. and
        Farzalov, F. 1968 IEEE J. Quant. El., 4, 654.

102   Ben-Reuven, A. 1966 Phys. Rev. 145, 7.

103   Chen, F.M. and Snider, R.F. 1967 J. Chem. Phys. 46, 3937.

104   Chen, F.M. and Snider, R.F. 1968 J. Chem. Phys. 48, 3185.

105   Chen, F.M. and Snider, R.F. 1969 J. Chem. Phys. 50, 4082.

106   Kisman, K.E. 1974 Ph.D. Thesis, U. Toronto, unpublished.

107   Sanctuary, B.C. and Snider, R.F. 1975 Can. J. Phys. (in press).

108   McCourt, F.R. and Hess, S. 1970 Z. Naturforsch., 25a, 1169.

109   Ozier, I. 1971 Z. Naturforsch., 26a, 1232.

110   McCourt, F.R. and Hess, S. 1971 Z. Naturforsch., 26a, 1234.

111   Rose, M.E. 1957   Elementary theory of angular momentum,
        Wiley, New York.

112   Tinkham, M. 1964   Group theory and quantum mechanics,
        McGraw Hill, Toronto.

113   Ozier, I., private communication.

114   Hamma, J. and Miyagi, H. 1973 Prog. Theor. Phys. 50, 1142.

115   Fox, K. and Ozier, I. 1970 J. Chem. Phys. 52, 5044.

116   Ozier, I. and Rosenberg, A. 1973 Can. J. Phys. 51, 1882.

117   Ozier, I., Crapo, L.M. and Lee, S.S. 1968 Phys. Rev. 172, 63.

118   Hougen, J.T. 1974 J. Mol. Spectros. 50, 485.

119   Sanctuary, B.C. 1973 Can. J. Phys. 51, 2488.

120   Moret-Bailly, J. 1974 J. Mol. Spectros. 50, 483.

121   Ozier, I. and Fox, K. 1970 J. Chem. Phys. 52, 1416.

122   Bloom, M., Beckmann, P.A. and Sanctuary, B.C. to be published.

123   Edmonds, A.R. 1957   Angular momentum and quantum mechanics,
            Princeton University Press, Princeton.

124   Hirschfelder,J.O., Curtiss, C.F. and Bird, R.B. 1954
            Molecular theory of gases and liquids, Wiley, New York.